UNIVERSITAT DE BARCELONA

Nanoscale dielectric mapping of biomembranes with in-liquid Scanning Dielectric Microscopy

Martina Di Muzio

Doctoral thesis

Nanoscale dielectric mapping of biomembranes with in-liquid Scanning Dielectric Microscopy

Author: Martina Di Muzio

Director: Gabriel Gomila Lluch

UNIVERSITAT DE BARCELONA

Universitat de Barcelona

Facultad de Física

Departamento de Ingenieria Electrónica y Biomédica

Nanoscale dielectric mapping of biomembranes with in-liquid Scanning Dielectric Microscopy

Autora: Martina Di Muzio

Programa de Doctorado: Nanociencias

Línea de Investigación: Nanobiotecnología

Director y tutor de tesis: Gabriel Gomila Lluch

Barcelona 2021

UNIVERSITAT DE BARCELONA

Table of Content

Summary

The structure and physicochemical properties of biomembranes are fundamental for the functioning of cells, and many pathologies have been associated with their alterations (cancer, neurodegenerations, obesity, etc.) [1, 2]. For this reason, biomembranes have been the subject of intensive research. Yet, there is only limited knowledge of biomembranes, which show a heterogeneous structure at the nanoscale that is naturally present in cells, and determines many of the phenomena occurring through them at the molecular level [3, 4].

Due to their prominent role in Electrophysiology, electrical properties are among the more relevant physical properties of biomembranes. Most often, attention is paid to biomembranes' conduction properties, and the role played in them by ionic channels. However, biomembranes' dielectric properties are also of central interest in bioelectric phenomena, and a powerful reporter of membranes' composition, which can be exploited to develop label-free mapping methods. Yet, most of the available techniques have addressed the dielectric membrane properties in bulk solutions and at the level of single cells (micrometers), thus lacking spatial resolution. In other cases, they make use of exogenous labels, as in the case of spin paramagnetic resonance [5, 6] and fluorescence microscopy [7, 8, 9, 10, 11].

In recent years, the Nanoscale Bioelectric Characterization group at IBEC, as well as other groups, have developed some Scanning Probe Microscopies (SPMs) based techniques to attempt the dielectrical characterization at the nanoscale [12, 13, 14, 15, 16] and applied them to biomembranes [17, 18, 19, 20, 21] and other biosystems [12, 22, 23, 24, 25, 26, 27]. Initially, these techniques were implemented to be operated in air environment, but lately they were also extended to liquid environment [28, 29]. The implementation of in-liquid Scanning Dielectric Microscopy (SDM) paved the way to the accurate dielectric characterization of biomembranes at the nanoscale, in their physiological environment and in a label-free way [28, 29].

In-liquid SDM is based on measuring the electrostatic force acting on a nanometric probe under application of a modulated voltage between the tip and a conductive substrate, on top of which the sample is sitting. As compared to the standard SDM in air, operation in liquid environment requires several modifications. In terms of set-up, one needs to apply frequencies above the dielectric relaxation frequency of the electrolyte. Significant changes are also necessary for the modelling part [30].

This work of thesis takes advantage of the latest developments of in-liquid SDM to characterize the dielectric properties of heterogeneous model and natural purified membranes systems in liquid. In this framework, new knowledge has been gained about imaging in liquid conditions with SDM, e.g. about the prominent electrostatic finite size effect and different models have been tested and optimized for the analysis of the measurements.

First, I focused on characterizing mono- and bicomponent planar supported bilayer lipid mixtures containing cholesterol, providing a first proof-of-concept of the label-free mapping capabilities of the technique in liquid media, extending earlier work done in air on nanoparticles [12]. This study allowed gaining information on the composition of sub-micrometric membrane domains in liquid environment [31] and to provide reliable values of the intrinsic dielectric properties of DOPC and DOPC:cholesterol compositions, about which there was some debate in the literature. The low values obtained are responsible for membranes' low permeability to ions, in agreement with previous studies on monocomponent biomembranes [29]. Our results allow speculating on fundamental properties of lipid bilayers like viscosity and hydration of cholesterol-containing layers.

Afterwards, we extended the methods to deal with more complex biomembrane 3D structures, such as liposomes [32]. Liposomes with few hundred nanometers in height have been successfully imaged by in-liquid SDM, showing a sensitivity comparable to the one for flat biomembranes only a few nanometers thin. Once again, the dielectric properties of the liposomes' membrane were precisely extracted, this time in a more natural configuration of the

biomembrane. This study also highlighted the technique's sub-surface capabilities in the liquid environment, demonstrated earlier only in air measurements [33, 34, 35, 36, 37, 38, 39]. This capability enabled to obtain in a label-free way the lamellarity of liposomes, a crucial parameter in liposomes technology. The developed methodology has the potential to be used to screen a myriad of different compositions of liposomes (shell and core), since in-liquid SDM was shown to be sensitive to the dielectric properties of the membrane, but also to the conductivity of the medium inside the liposomes. This accomplishment was essential to evaluate its future application to living cells and constitutes one of the main achievements of this thesis.

During the thesis, I also draw my attention to the dielectric characterization of natural purified membranes in liquid environment. As a test example, we focused on the case of the purple membrane (PM), which had previously been studied in air environment [19, 20, 40]. PMs are constituted by the protein bacteriorhodopsin (BR) arranged in a crystal lattice, and lipids in a ratio 10:1 lipids:proteins. However, there is an unsolved uncertainty in determining the real topography of supported PM patches in the liquid environment, which can also display a concave surface. This made the dielectric quantification problematic, and further explorations will be necessary to provide reliable values of the permittivity of these layers in liquid media.

In summary, the objective and common thread connecting all the chapters of this work has been implementing and demonstrating the capabilities of in-liquid SDM in the dielectric characterization of bio-membranes, model and natural systems, with nanoscale spatial resolution.

I believe that this work laid the ground for elucidating the structure and dielectric properties of more complex membranes systems and their associated electric phenomena, e.g. conduction. Preliminary studies of the cell membrane directly on living neuroblastoma cells, in low concentration MOPS buffer, were carried out in collaboration with Maria Elena Piersimoni, PhD student at Imperial College, London. The group is now collaborating with experts in the field and trying to develop new algorithms, fundamental to extend the methods to living cells.

In addition to the main objective of my thesis, I also participated in a side project concerning the in-liquid SDM characterization of an operative EGOFET transistor [41], crucial for optimizing the devices and gain a better understanding of the transduction mechanism with biological entities. One of the newest frontiers of such technology is indeed to use supported lipid bilayers for bio-sensing purposes [42].

Motivation

In terms of well-being, diseases like cancer, neurodegenerations, and ageing are just some of the main focuses of current research. It is rather unrealistic to challenge them without coming into terms with multidisciplinary science. The complexity of the problem benefits from the exploitation of many different approaches, especially needed to delineate a fully understood picture.

In this work, the tools of biology, chemistry, and physics will be used to explore the dielectric properties of some simple membrane systems. Biomembranes alterations are at the origin of many pathologies [1, 2] and much could be understood by disposing of label-free techniques to characterize them at the nanoscale.

Membranes dielectric properties, in particular, are responsible for the interactions between cells and with different molecular complexes [43], they also regulate transport processes inside and outside the cell [44, 45], action potentials formation and propagation in electroactive cells [46, 47, 48, 49], and can be used to characterize membranes composition and associated bioelectric processes. In-liquid Scanning Dielectric Microscopy (SDM) [28, 50] has a huge potential to be exploited in their characterization at the nanoscale.

However, even if SDM is operative, its application to in-liquid measurements has just begun. Nanoscale measurements of the dielectric constant of synthetic DPPC lipid membranes in diluted ionic media were only reported in Ref. [29]. Further investigations are required to confirm the permittivity range for lipid bilayers in water and the reproducibility of the results, but also to test the sensitivity of the technique, its limits, and evaluate the most suitable conditions of operation depending on the specific system under analysis. Lipid model systems are not only good test samples but also of great interest. For instance, the effect of cholesterol on the specific capacitance of biomembranes, investigated during this thesis project, continues to be an object of debate. Liposomes constitute another example as they are one of the technologies

with the highest number of patents for pharma applications up to date. In addition to lipids, proteins are fundamental units of natural membranes. Their electrical characterization in liquid has not been achieved yet by SDM, and it could potentially provide traces of their activity.

The generated knowledge aims to lay the foundation for characterization of natural systems (natural vesicles, cells, etc.) under various conditions, with the scope of elucidating interesting bioelectric phenomena.

Objectives and structure of the thesis

The main objective of this work of thesis is to take advantage of the latest developments of in-liquid Scanning Dielectric Microscopy to characterize the dielectric properties of heterogeneous lipid model systems and natural purified membranes in liquid. This thesis intends to provide increased understanding about lipids and proteins dielectric properties, intrinsically linked to phase behaviours and membranes' hydration and propose new methods for screening the structure and composition of membrane systems.

First, we aim to confirm the range of permittivity values for lipid bilayers in water and the reproducibility of the results, to test the sensitivity of the technique, its limits and evaluate the most suitable conditions of operation depending on the specific system under analysis. Second, we aim to demonstrate the possibility of using membranes' dielectric properties as reporters of their composition as a first step towards the development of a label-free composition mapping method for biomembranes. Third, we aim to advance the fundamental understating of SDM for measurements on more complex systems than planar lipid bilayers, such as 3D model membranes systems with celluloid-like geometries like liposomes. In particular, we want to investigate the capability of in-liquid SDM methods to provide the dielectric properties of single liposomes, together with information on their internal structure (e.g. lamellarity). Finally and forth, we aim to show that in-liquid SDM can also be applied to characterize the dielectric properties of natural membrane systems containing both lipids and proteins.

The thesis is organized into eight chapters. The **first chapter** presents an introduction to the structure of the cell membrane and its dielectric properties. It revises the methods developed to model membranes on planar surfaces, including conductive ones, required for SDM characterization.

Chapter two introduces Scanning Probe Microscopy methods, explaining the basis of Atomic Force Microscopy and presenting Scanning Dielectric Probe Microscopies, among which SDM.

Chapter three is the last introductory chapter and describes in detail in-liquid Scanning Dielectric Microscopy, underlining the differences with respect to the implementation in air, in terms of operation and modelling.

Chapter four and **chapter five** contain the main experimental body of the thesis and present the studies conducted on the planar heterogeneous lipid systems and liposomes.

Chapter six reports the dielectric imaging and preliminary characterization of natural PM samples and discusses the problematics that arise when the membranes are topographically complex.

The seventh chapter exposes the conclusions and future perspectives of this work, including an exploratory application of in-liquid SDM to living cells, and to the characterization of EGOFET transistor under operation.

1. Introduction to bio-membranes

1.1 The cell membrane

Biomembranes are two-dimensional, highly anisotropic systems held together by non-covalent forces that resembles no other biological organization (Figure 1). They are very soft (Young' modulus below 1 kPa range [51, 52]) and thin structures (only ~ 5 nm thick) that define the cell's boundary and delimit cytoplasmatic compartments into which certain activities are segregated and/or carried out more efficiently [53]. Biomembranes act as both physical and chemical barriers, by protecting the integrity of the cellular material but still providing some flexibility and regulating the uptake of nutrients and signalling molecules [54].

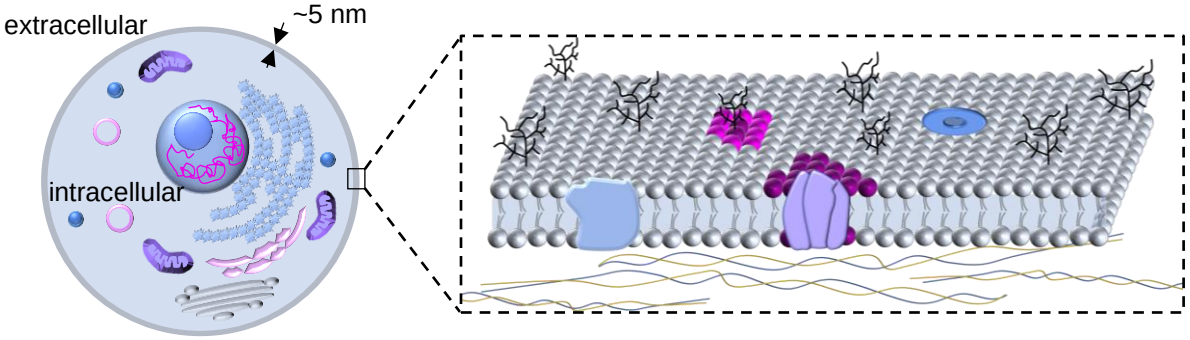

Figure 1: Schematic representation of the cell membrane and its heterogeneous nature.

Biological membranes are also the interfaces responsible for cells communication with their environment and other units, which is achieved through molecular exchanges, resulting in pH regulation and osmotic homeostasis, but also transduction of mechanical stimuli into cell signals [54].

Membranes detailed structure is key for their function. They are mainly composed of lipids (Phospholipids, Cholesterol, Glycolipids), proteins (Integrals, Peripheric) and carbohydrates (Glycolipids, Glycoproteins). These constituents can be arranged in compositional domains

which are very dynamic and sometimes only ~ 100 nm in lateral extension [55]. The interplay between membrane's components regulates phenomena like recognition, signaling, endocytosis and exocytosis and thus, any alteration of such equilibrium can lead to structural changes responsible for serious pathologies. Among them we find cancer, neurodegenerations (Alzheimer's and Parkinson's disease), metabolic and cardiovascular diseases which can originate in individual cellular compartments, including the cell membrane [2].

In particular, lipid composition was shown to alter protein's structure/activity and location (i.e. G-protein coupled receptors [56]) as well as defining membrane microdomains that constitute spatiotemporal platforms for proteins. Membrane lipids are also crucial in the fission and fusion of lipid bilayers and they also act as sensors to control environmental or physiological conditions. Furthermore, lipids and lipid structures participate directly as messengers or regulators of signal transduction [53]. In conclusion, the modulation of the membrane lipid levels is another way for a given organism to respond to environmental stimuli.

As membranes composition affects the membranes overall activity [1, 57], its modulation was proposed for new therapeutic avenues [1, 58, 59].

Interestingly, biomembranes are also explored as platforms for the fabrication of biosensing devices [42].

Therefore, characterization of membranes composition at the nanoscale and the study of lipid–lipid and lipid-protein interactions have attracted great interest over the years, and yet it is an evolving field.

1.1.1 From early models to the modern structure

The cell was discovered in the XVII century and cell research began with the invention of the light microscope, giving access for the first time to the microscopic world. However, it would

take another 200 years for the boundaries of the cell to be thoroughly investigated. Charles Overton started a series of studies to determine which molecules were able to cross this boundary layers [60] and suggested their lipidic nature.

In 1925, Gorter and Grendel performed some key experiments using a Langmuir trough and blood cells [61] and brought up the concept of lipid bilayer, which laid the foundation for future membranes models. Nevertheless, the very firsts direct observations of the cell membrane were possible only in the 50s, thanks to the improved resolution of Electron microscopy (emerged already 20 years before) [62, 63, 64]. Yet, the interpretation of the images obtained was difficult and naturally influenced by former conceptions of membrane structure.

In 1972, as a result of the combination of previous models, the *fluid mosaic hypothesis* was formulated by Singer and Nicolson [65]. The model depicts biological membranes as 2D dynamic structures of proteins and lipids, whose arrangement in domains is driven by thermodynamic principles. The importance of hydrophobic forces in determining the arrangement of the molecules was also emphasized. In addition, the model is intrinsically fluid, and predicts the lateral distribution of most molecules to be essentially random; however, it also suggests the formation of specific clusters (microdomains) [66, 67]. The formulation of the fluid mosaic model has been nowadays modernized, but it has barely been altered, and it remains the most explanatory hypothesis to understand biological membranes [65].

1.1.2 Membrane components

Biomembranes are structured as a bilayer of phospholipids (glycerophospholipids and sphingolipids) and glycolipids with proteins incorporated. Carbohydrates, which account for about 10% of the weight of plasma membranes, are invariably covalently bound to either protein or lipid. The relative amount of protein and lipids varies widely.

Phospholipids are a class of lipids consisting of a wide range of amphiphilic compounds. Glycerophospholipids are the most important type of phospholipids. From a chemical point of view, they consist of a glycerol esterified with two fatty acids (tails) and a hydrophilic polar head. The polar head is exposed toward the aqueous medium, while the hydrocarbon chains are oriented toward the central region of the bilayer. The head may be formed by a choline, in the case of phosphocholines, or alcohols such as ethanolamine or serine, or derivatives of sugars such as inositol. The hydrocarbon chains usually consist of between 12 and 24 carbon atoms and may be unsaturated or saturated, i. e. present, or not, double bonds, or may have a chain of each type. Phospholipids can differ a lot in their physicochemical behavior, e.g. vary considerably in their interaction with water and in their spreading properties at the air–water interface. A major representative of this category and constituent of animal cell membranes is the 1,2-Diacyl-sn-glycero-3-phosphocholine (DOPC) (Figure 2).

Sphingolipids are another important class of phospholipids, with sphingomyelin (SM) as a major representative, which contains sphingosine esterified with choline instead of glycerol.

Besides, it is relevant to mention cholesterol (Figure 2), pertaining to the category of sterols (20−50% of membranes composition) [68], which are membrane fluidity regulators [69]. Cholesterol is widely abundant in eukaryotic cells and modulates consistently the physical properties of the membrane. The molecule is formed by a hydro-carbonated chain and four rigid rings; one of them carrying a hydroxyl group that confers amphiphilic character. Given its chemical nature, cholesterol does not form a bilayer itself in solution but tends to intercalate among the hydrocarbon chains of the membrane, with the hydroxyl group near the phospholipid polar head.

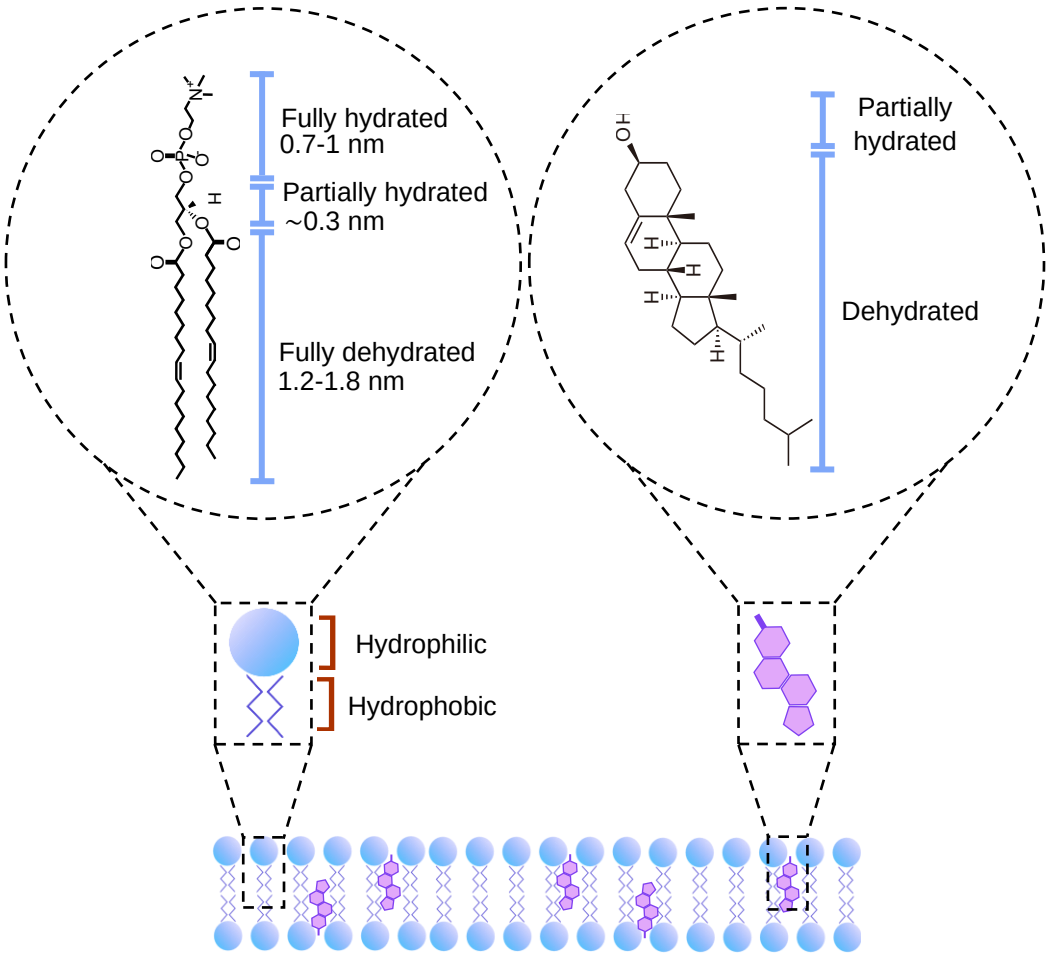

Figure 2: DOPC and cholesterol molecules. Chemical structure and schematic of their insertion in the bilayer.

Among the main components of biomembranes there are also glycolipids, glycoconjugates of lipids generally found on the extracellular surface of eukaryotic cell membranes. They help maintaining the stability of the membrane and facilitate cell-cell interactions. Gangliosides and cerebrosides are two important classes of glycolipids.

In nature, every type of cell is distinctive: lipids' identity and their abundance vary widely from organism to organism [70, 71], from organ to organ [72], within the same cell [73] (see [72] for a review) and between leaflets (Figure 3).

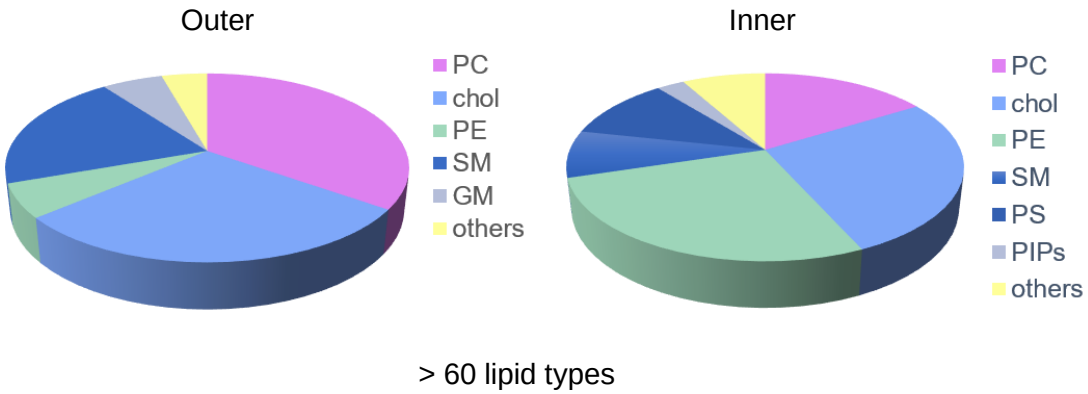

Figure 3: Simplified composition of the outer and inner leaflet of the membrane of a eukaryotic cell, adapted from Ref. [74]. Phosphatidylcholines (PC), sphingomyelin (SM), and gangliosides (GM) are found predominantly in the outer leaflet and phosphatidylethanolamine (PE), phosphatidylserine (PS), and other charged lipids in the inner leaflet. The charged species are PS, phosphatidic acid (PA), phosphatidylinositol (PI), and the PI- phosphate, -bisphosphate, and -trisphosphate (PIPs).

As mentioned earlier, under physiological conditions, most membrane lipids exist in the lamellar or bilayer structure. Lipids can adopt different phases and conformations depending on their chemical nature, concentration, temperature (and pressure), and solution environment.

Several behaviors have been identified, among which the most common ones are solid or gel phase (L_β or S) and fluid or liquid-disordered (L_α or L_d), but also liquid-ordered (L_o), interdigitated (L_β I or L_β I_T) and ripple phase (P_β), which arises in intermediate transition states and temperature conditions depending on the composition.

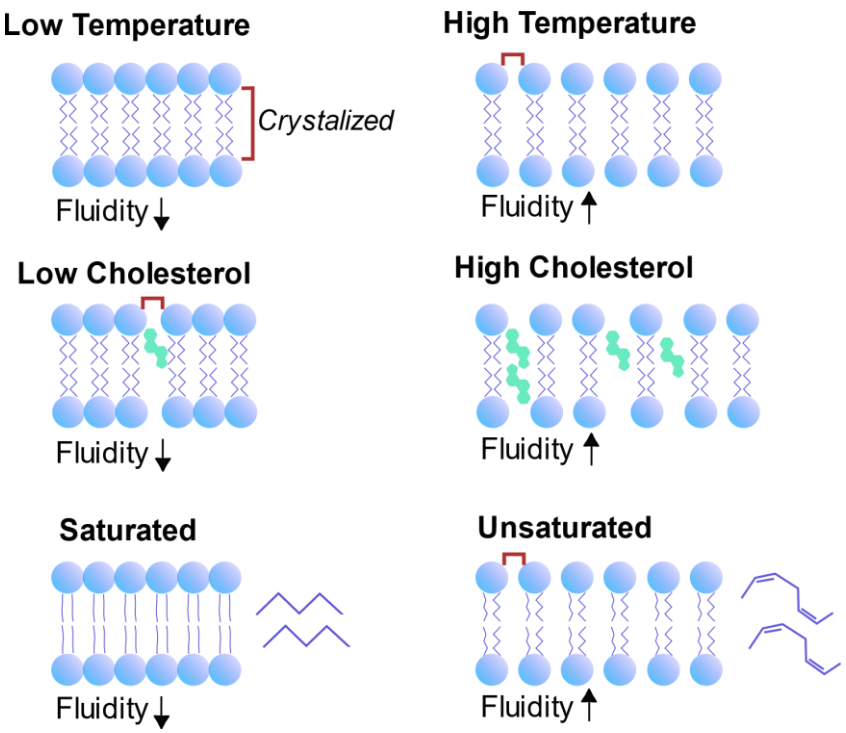

Figure 4: Effect of the temperature, cholesterol content and degree of unsaturation in the hydrocarbon lipid tail on the fluidity of the layer. A temperature rise leads to an increase in fluidity of the bilayer. The same effect is observed with high cholesterol (when the lipid layer is in gel phase, otherwise the opposite happens) and/or when double bonds are present in the lipidic tail. All these three factors tend to increase the distance between the lipid molecules and weaken their capabilities of packing.

Figure 4 provides a simplified picture of the effect of temperature, cholesterol content and unsaturation of the lipid chains on the response of the lipids, that originates the phase behavior of the bilayer.

An increase of temperature normally results in the gain of rotational degrees, to which a higher fluidity of the membrane follows. Every lipid has a specific transition temperature (T_m), required to induce a change of phase in the lipids. The transition gel to liquid–crystalline (or chain-melting) phase has probably been the most intensively studied. The gel to liquid–crystalline phase transition is favored by entropic gain [75], and it is accompanied by a relevant lateral expansion and a parallel decrease in the thickness of the bilayer. There is also evidence that, upon chain melting, the number of water molecules bound to the surfaces of the lipid bilayer increases.

The presence of cholesterol is another important determinant of the lipids' phases; its influence on the fluidity of the bilayer depends on the composition of the system and can be very complicated. Cholesterol is known to increase the fluidity of gel-phase bilayers and to increase instead the rigidity of fluid membrane lipids by intercalating between the molecules. The presence of high levels of cholesterol in many eukaryotic membranes, particularly plasma membranes, was shown to abolish a discrete cooperative gel to liquid–crystalline membrane lipid phase transition in these systems.

Finally, since the phase of a lipidic system is largely determined by the strength of attractive Van der Waals forces, we have to consider intrinsic lipid characteristics. Lipids with longer tails will tend to pack better together and consequently decrease lipid mobility. On the contrary, lipids with short chains have less interaction area and, at the same temperature, will tend to be more fluid. Besides the chain length, transition temperature and thus the lipid phase can also be affected by the degree of unsaturation of the lipid tails. The presence of double bonds produces a kink in the alkane chain which interrupts the regular periodic structure. The free space generated within the bilayer allows higher mobility in the adjacent chains. In general, lipids with low melting temperature have short or unsaturated acyl chains (e.g. DOPC, T_m=−20ºC) whereas lipids with high melting temperature present long, saturated acyl chains (e.g. DPPC, T_m=41ºC, or Sphingomyelin (SM), T_m=~37ºC).

Embedded into this lipidic matrix there is a high amount of membrane proteins. Proteins account roughly for half of the mass of most cellular membranes. Although scientists model membranes as a fluid mosaic where proteins can move laterally, in living cells many proteins are not free to move and they are anchored in place within the membrane by tethers to proteins outside the cell, cytoskeletal elements inside the cell, or both.

Membrane proteins can be classified in integral and peripheral (see Figure 5 (b) later in the text). Additionally, proteins, like lipids, can be glycosylated.

Integral proteins are embedded in the lipid bilayer matrix where they establish hydrophilic and hydrophobic interactions with their respective lipid counterparts. Among integral proteins we underline the category of transmembrane proteins, known to have communication-related jobs. Some of these proteins can bind signals, such as hormones or immune mediators, to their extracellular portions. Binding normally causes conformational changes in the protein that transmit a signal to intracellular messenger molecules. These receptor proteins are specific and selective for the molecules they bind.

Peripheral membrane proteins, on the other hand, are not inserted into the bilayer but are associated with the membrane and often bound to other membrane proteins. Some peripheral proteins can actually form a network underneath the membrane which provides attachment sites for integral proteins. Some other peripheral proteins are secreted by the cell and form an extracellular matrix that functions in cell recognition. Peripheral proteins can also be associated transiently with the membrane surface through weak interactions and carry on the transport of some molecules across the membrane.

The distribution of membrane components in the bilayer is asymmetric; there can be differences between leaflets as well as laterally within the same leaflet. The lateral organization is the results of thermodynamically stable configurations leading to preferential packing (lipid rafts) described in modern works [67, 76].

1.2 Model bio-membranes

1.2.1 Introduction

The inherent complexity of biological membranes and their interactions with intra- and extracellular networks make direct investigations difficult and motivated the development of model systems that can be tailored with great precision [62].

Simplified model membranes, with known composition and global structure, in the form of planar lipid bilayers or vesicles (tethered or in suspension) are widely used to simulate the properties of natural membranes and to investigate on specific mechanisms such as membrane fusion, proteins interaction or phase behavior of specific components, interactions, etc. Such processes are often difficult to study in natural systems, since it is not trivial to obtain good natural preparations, and even when that is achieved, it is hard to characterize the main actuators involved in a dedicated function.

Besides, the properties of model membranes and lipid systems can be tuned for diverse purposes, such as design of biosensors for membrane proteins interactions and high-throughput drug screening. New frontiers are open for building biosensors using biomembranes-based organic transistors [42]. Also in this case, membranes configurations for building biosensors can be planar or in the form of vesicles called liposomes.

1.2.2 Liposomes

Liposomes are spherical enclosed structures of lipid bilayers that are formed spontaneously under certain conditions, due to the amphiphilic character of the lipids used (e.g. when water is added to dried layers of phospholipids).

They can be formed by one or a series of concentric lipid bilayers, so-called lamellae, and span variable ranging sizes. According to their size and lamellarity, liposomes are usually

classified in: Giant Unilamellar vesicles (GUVs) (1-10 µm), Large Unilamellar vesicles (LUVs) (50-200 nm), Small Unilamellar Vesicles (SUVs) (18-20 nm) and Multilamellar Vesicles (MLVs).

The structural characteristics of the vesicle obtained depend on the specific preparation method. Conventionally, liposomes are obtained by gently hydrating a phospholipid film with the desired buffer. By simply doing that, normally a mixture of SUVs, LUVs and MLVs is obtained. For the purpose of synthesizing instead more homogeneous populations of liposomes, some extra steps or different procedures are often required. For example, SUVs vesicles are obtained by extruding the liposome suspension through a porous filter (100 nm to ensure mono-lamellarirty). GUVs instead, can be obtained by electro-formation [77] or inverted emulsion method [78].

Liposomes can be functionalized and loaded with both hydrophilic (in the internal aqueous solution) and hydrophobic molecules (inserted in the carbonyl band). They became extensive drug delivery platforms with more than 59 patents and 15 lipid based therapeutics approved for clinical use [79]. They are important structures in the study of membrane permeability and allowed a fruitful comparison to the biological membranes.

Besides being modulated for obtaining various drug delivery systems, the bilayer properties of GUVs can be carefully tuned to allow their use as microreactors with confined volume [80] and finally, GUVs of different composition can serve as cell model systems [81].

Liposomes, as compared to extended membranes, have the advantage of being much less affected by the presence of the substrate (they anchor the substrate on one side but expose a free-standing bilayer on the other), thus, the proteins embedded in these systems are normally more stable and can retain their fully functional form.

Another type of unsupported membranes are the so-called black lipid membranes [82, 83, 84], obtained by painting with a lipid solution over a hole in a hydrophobic support separating aqueous compartments. The so-formed bilayer is also free standing and thus very fragile [85].

1.2.3 Supported lipid bilayers

Lipid-bilayer membranes supported on solid substrates are widely used as cell-surface models, and they are at the intersection between biological and artificial materials. Supported lipid bilayers (SLBs) are typically formed by Langmuir transfer to a suitable substrate surface or by vesicle fusion. The Langmuir-Blodgett technique [86] consists of depositing successive monolayers on a substate by dipping it in a lipid suspension. With this technique, the lateral pressure of the layers can be very well controlled and the composition of the different leaflets can be tuned to be different.

SLBs are instead formed by vesicle fusion when LUVs or SUVs suspensions are deposited onto a substrate and incubated under certain conditions [87]. The time of incubation, the required temperature and the concentration of lipids depend upon the vesicle lipid composition and surface properties of the solid support [87, 88], which can affect lateral mobility and when present, proteins' functionality. Original methods have been proposed to reduce the coupling with the substrate surface. Yet, in the majority of the cases, a trade-off between stability of the membranes and the retention of their natural properties is still sought.

Substrates of choice for bilayers formation normally meet the conditions of hydrophilicity and surface smoothness. The former is normally required for a good interaction with lipids polar heads, which can be eventually mediated by some water layers (for a better retention of membrane's natural properties) and when requested, by cations or anions in solution, such as Ca^{2+} or Mg^{2+}. Atomically or almost atomically flat surfaces are also fundamental, given the small thickness of the bilayers (~ 5 nm), which can present microdomains with height difference of less than 1 nm. Given these requirements, the most common substrates used to support lipid bilayers are mica (easy to cleave, atomically flat and hydrophilic), glass and SiO_2 (with similar characteristics).

SLBs offer many advantages to an experimentalist, including ease of preparation, stability, patterning [89], and the availability of a wide variety of surface sensitive techniques for their characterization, among which Atomic Force Microscopy.

For the simplest cases of study, the composition of model membranes can be simply lipidic (mono, bi- or multicomponent). When the composition of the membranes is purely lipidic, the most common practice is to extend the bilayers directly on a hydrophilic solid substrate. In this case, few water layers (5–20 Å) mediating the membranes-substrate interaction can be enough to allow a good mobility and formation of microdomains.

However, membranes can also be synthesized to contain some proteins or fragments of natural membranes [90]. This results in sophisticated interfaces that can be used to control, organize and study the properties and function of membranes and membrane-associated proteins [72]. Current strategies for proteins inclusion are the direct incorporation into supported lipid bilayers destabilized with detergents [91, 90], or stabilization in surfactant micelles, followed by incorporation into lipid vesicles which are later spread on a substrate [92]. However, many of the surfactants used for protein purification disrupt the membrane so that the incorporated proteins are randomly orientated [93]. Furthermore, it is difficult to approach the natural proteins/lipids molar ratio of 1:5000.

In the perspective of carrying out more biologically relevant studies, nowadays biomimetic interfaces strive to be capable of reproducing the biological function of cell-membrane *in vitro.* Indeed, advances in complexity of membrane models are being sought with respect to architecture, size, and composition, accompanied as well by advanced computer simulations of their properties and dynamics. Thus, isolation of native membrane fractions directly from a cell source, constitutes one of the preferred approaches to achieve complexity, as it provides the same lipidic environment found in the native cell, which prevents the possible protein denaturation during the insertion into an artificial membrane [94, 95].

When working with membrane proteins spanning the whole thickness of the membranes and which domains can extend to several tens of nanometers (i.e. cell adhesion receptors), it becomes necessary to space the proteins from direct contact with the substrate, in order for them to remain stably anchored to the bilayer and retain their functionality. This can be achieved by using ultrathin soft polymer supports [96, 97], e.g. cellulose [98], which mimics the intracellular matrix and remove proteins-substrate frictional coupling [99, 100, 101, 102, 103], tether molecules [104, 105] or directly lipopolymer tethers [103], linking covalently some of the lipid molecules in the proximal monolayer to the substrate and establishing an ion reservoir.

1.2.4 Strategies for deposition of lipid bilayers on conductive substrates

Sometimes, it is necessary to obtain lipid membranes on conductive substrates, e.g. for building biosensors or perform electrical measurements, for instance by Scanning Dielectric Microscopy (SDM), which is the technique of choice for this work of thesis.

In this case, bilayers cannot be obtained by simple vesicle fusion method, because metal surfaces are often hydrophobic and not prone to interact with the lipid heads.

On materials like gold, titanium oxide and aluminum oxide, zwitterionic lipid vesicles tend to adsorb and remain intact on the substrate surface. To overcome this limitation, optimization of experimental conditions like ionic strength, pH, osmotic shock or addition of specific peptides [106] can be attempted to promote vesicle rupture. One can also try to play with vesicle properties (size, lipid composition and lamellarity [107]). However, given the wide range of experimental parameters, it can be difficult to identify the right set of conditions to make a planar bilayer [108].

Several other approaches have been developed to achieve SLBs extension on conductive substrates, including some of the methods previously mentioned, i.e. deposition on ultrathin soft polymer supports or tethers.

Recently, also solvent-assisted lipid bilayer (SALB) fabrication protocols [108, 109] and dip-pen nanolithography (DPN) methods [110, 111] have been proposed. However, these two procedures also require the optimization of several parameters [112], which is often difficult.

Finally, Self-assembled monolayers (SAM) of organic molecules can be used to tune the wetting properties and the interface of several metallic materials to promote SLBs formation [113, 114]. Surface hydrophilicity or hydrophobicity can be wisely modified by introducing terminal net charges or polar moieties, that will interact with the lipid polar heads. Self-assembled monolayers (SAMs) have also emerged as promising tool to mimic the extracellular matrix as they can be precisely tailored for specific cell culture applications [115]. Additionally, they can be incorporated in the fabrication of organic electronic devices, not only enhancing their stability and performance, but sometimes also conferring new types of behaviours [116].

SAMs are molecular assemblies formed by molecule absorption on the substrate in a single monolayer, from either the vapor or liquid phase, and are generally organized into quite large and ordered domains [117], depending on the incubation time. They can also be patterned on the surface in well-defined domains [118, 119].

In some cases, the molecules that form the monolayer do not interact strongly with the substrate and form two-dimensional supramolecular networks [120]. In others, they bind to the substrate thanks to a strong chemical affinity; this is, for instance, the case of thiol molecules on noble metals. Gold can be an optimal choice to carry out electrical studies, thanks to its biocompatibility and outstanding conductive properties. SLBs can be obtained on gold by exploiting the well-known chemistry between gold (Au) and sulfur (S), which results in a covalent interaction.

SAMs are the technology selected in the framework of this thesis project to obtain SLBs and immobilize liposomes over gold chips for electrical characterization.

1.3 Electric properties of membranes

1.3.1 Conduction and capacitance

Membranes bioelectrical activity regulates the functions of cells and organisms and it is thus one of the most fascinating characteristics of the membranes. The cell membrane possesses both capacitive and conducting properties, which determine the transport of several types of molecules across this semi-permeable barrier.

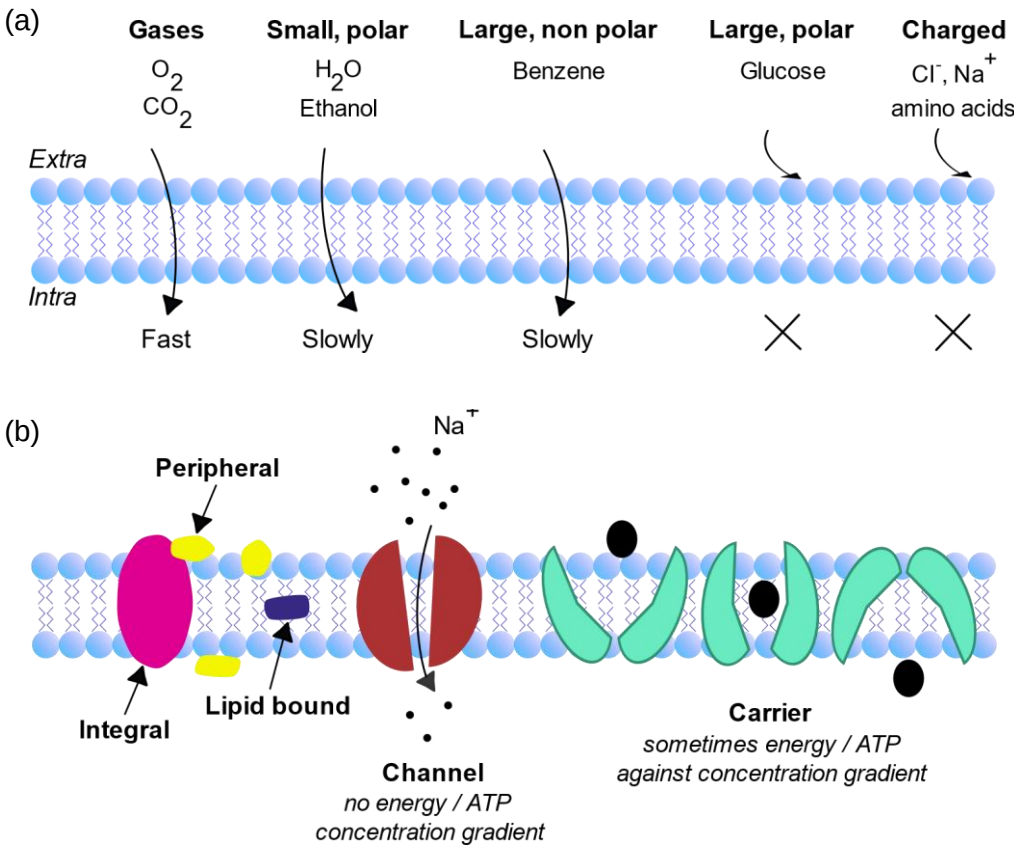

Figure 5: Transport phenomena. (a) Passive transport: schematic of membranes permeability to several kind of molecules. Small hydrophobic molecules and gases (O_2, CO_2) can cross the membranes rapidly. Small polar molecules (H_2O, EtOH) can also pass through the membrane, but they do it more slowly. The diffusion of ions and large molecules, i.e. sugars and amino acids, is instead restricted. Transport of these molecules relies on specific membrane proteins called transporters (ion channels, carriers), which are the main players in bioelectrical activity (b).

Lipid membranes behave like insulators with respect to ions transport, maintaining charge separation between the two interfaces. Their very low ionic conductivity is determined by the dielectric properties of the lipids, far different from that of the aqueous environment (Figure 5 (a)). However, when specific proteins are present (e.g. ion channels, transporters), biomembranes are also able to establish conduction phenomena.

The ability of cell membranes to polarize or accumulate charges under the application of an externally applied field is reflected in its capacitive, passive properties, reported by the dielectric constant (ε_r) (see following section).

Instead, the ability of cells membranes to conduct electricity is an active property, which exploits membrane proteins called ion channels [121], i.e. responsible for conduction of ions in excitable cells like neurons. They normally work under passive conditions, allowing ions to flow by simple gradient diffusion.

To maintain the ionic balance, vital to cell health and maintenance, there are other specialized proteins called carriers, able to work against the concentration gradient and thus responsible of the active transport. For this reason, they require energy, which we consume in all our bioelectrical processes.

Thanks to membrane barriers and transport proteins, the cell can accumulate nutrients in higher concentrations than existing in the environment and, conversely, dispose of waste products (Figure 5 (b)).

The main physical magnitudes involved in these transport phenomena consist of ions concentrations inside, outside and at the cell membrane, ionic currents (J), electrical potentials (f), conductivities (σ) which give the measure of how much easily an ion move in response to an electric field, and dielectric constants (ε_r) (Figure 6). All these quantities are in general space, time, voltage and ligand dependent.

Bioelectricity is the study of electrical phenomena taking place in biological systems. Two type of phenomena are typically analysed in bioelectricity: the active electrical response of cells to chemical or electrical stimulation (active response) [122], and its passive response in an external electric field (passive response), (Figure 6). The passive response is measured when the cell is considered like a material; an external electric field is applied through a source and we can measure for instance the current passing through the system.

On the other hand, to measure active response a source is not needed; since the system itself acts as one, only a meter for recording is required. An active response can be produced chemically or using electrical stimulation; for this second case, a source must be also present in the circuit (Figure 6).

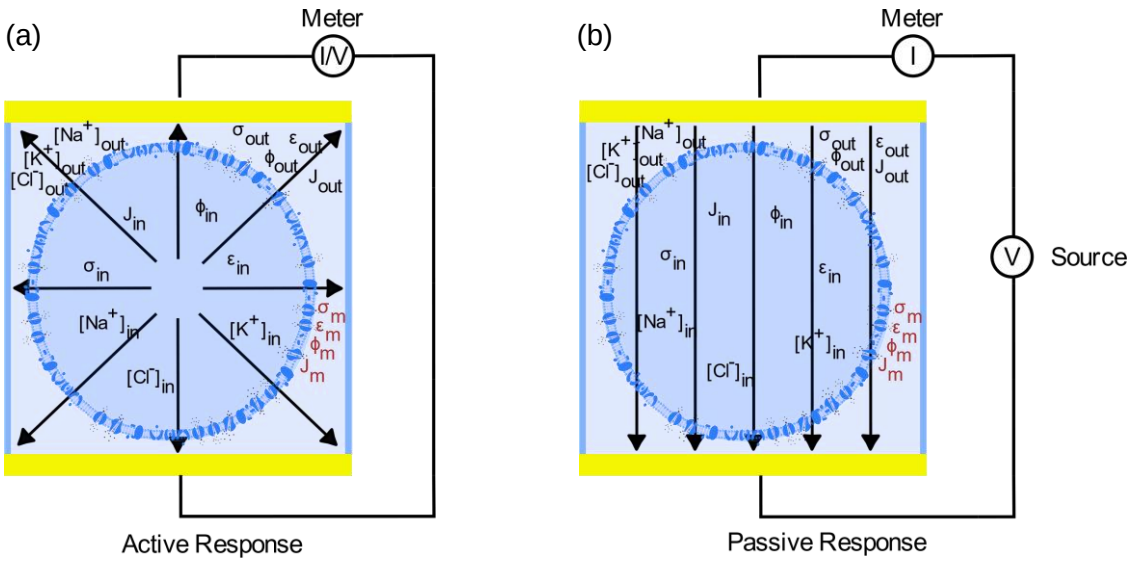

Figure 6: Schematic of an active (a) and passive (b) response measurement. The physical magnitudes involved in the bioelectrical phenomena are highlighted, in red the ones of the membrane.

The electrophysiological signal recorded will strongly depend on the composition of the membrane and also on its physicochemical conditions that will affect its conducting and/or insulating behavior. Our work is mainly focused on the measure of membranes' passive response, even though the possibility of monitoring active responses can be explored.

1.3.2 The dielectric constant (ε_r) of the membrane

When an external electric field is applied to a cell or membrane, its electric dipoles reorient according to it and generate an additional electric field that opposes to the external one (Figure 7).

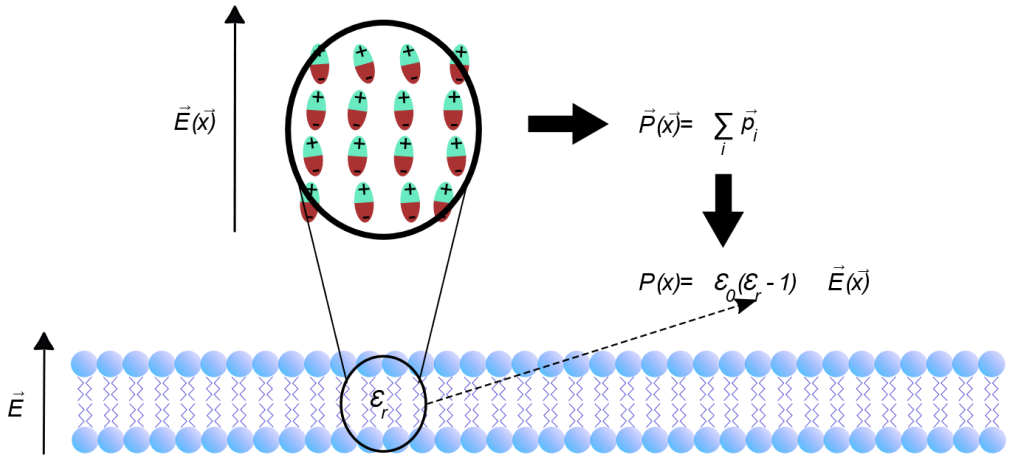

Figure 7: Polarization of a membrane by an externally applied electric field.

The overall dipole moment of the membrane is represented by the polarization vector $\vec{P}$. In linear systems the polarization is proportional to the internal electric field according to the relation:

$$\vec{P}=\varepsilon_0(\varepsilon_r - 1)\vec{E} \quad (1)$$

where, $\vec{E}$ is the internal electric field, $\vec{P}$ the polarization vector, ε_0 the vacuum permittivity and ε_r the relative permittivity of the membrane, also referred to as the dielectric constant for low frequencies.

As can be observed from Eq. (1), a material with high dielectric constant polarizes more in response to an electric field than a material with lower electrical permittivity; and hence, it screens more the external electric field.

The permittivity is treated often as a complex function of the frequency of the applied electromagnetic field, as complex numbers allow to include both electric polarization and losses (including conduction) in a single magnitude.

The fundamental equation for the complex permittivity of a material (ε_r) is given by:

$$\varepsilon_r = \varepsilon_r'(\omega) - i\varepsilon_r''(\omega) \quad (2)$$

where ε_r' and ε_r'' are the real and imaginary components, respectively.

Specifically, the real and imaginary parameters defined within the equation of the complex permittivity describe how a material stores electromagnetic energy and dissipates it as heat.

The processes influencing the material response to a time-varying electromagnetic field depend on the frequency and are generally classified as either ionic, dipolar, vibrational, or of electronic nature (Figure 8).

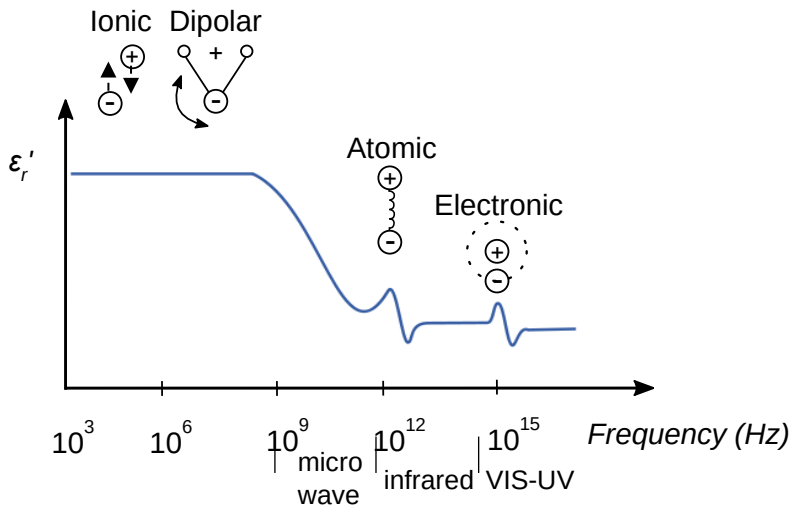

Figure 8: Frequency dependence of the dielectric constant: ionic relaxation (kHz) and dipolar relaxation (MHz), also referred to as dielectric relaxation, vibrational relaxation (THz), electronic relaxation (PHz).

Ionic polarization processes refer to the general case of a charged ion moving back and forth in response to a time-varying electric field; they dominate at low frequencies. Interface

polarization (kHz range) happens when charge carriers are trapped at interfaces of heterogeneous systems; the Electric Double Layer is a good example of it. Dipolar or orientational polarization (MHz - GHz range) originates from the alignment of the permanent or induced electric dipoles with respect to an electric field. This orientation is perturbed by thermal noise, and the time required for the dipoles to relax back to the initial conditions is determined by the local viscosity. These two factors make dipolar relaxation highly dependent on temperature and chemical characteristics of the medium.

At higher frequencies, we find vibrational processes (THz range), including molecular vibrations and associated vibrational-rotation states that are infrared (IR) active. Finally, electronic processes (PHz range) take place in a neutral atom when an electric field displaces the electronic density around the nucleus. They include optical and ultra-violet (UV) absorption and scattering phenomenon seen across the UV-visible range.

Although the relative permittivity is in fact a function of frequency, the dielectric constants are mostly expressed for low frequency electric fields, where the electric field is essentially static in nature.

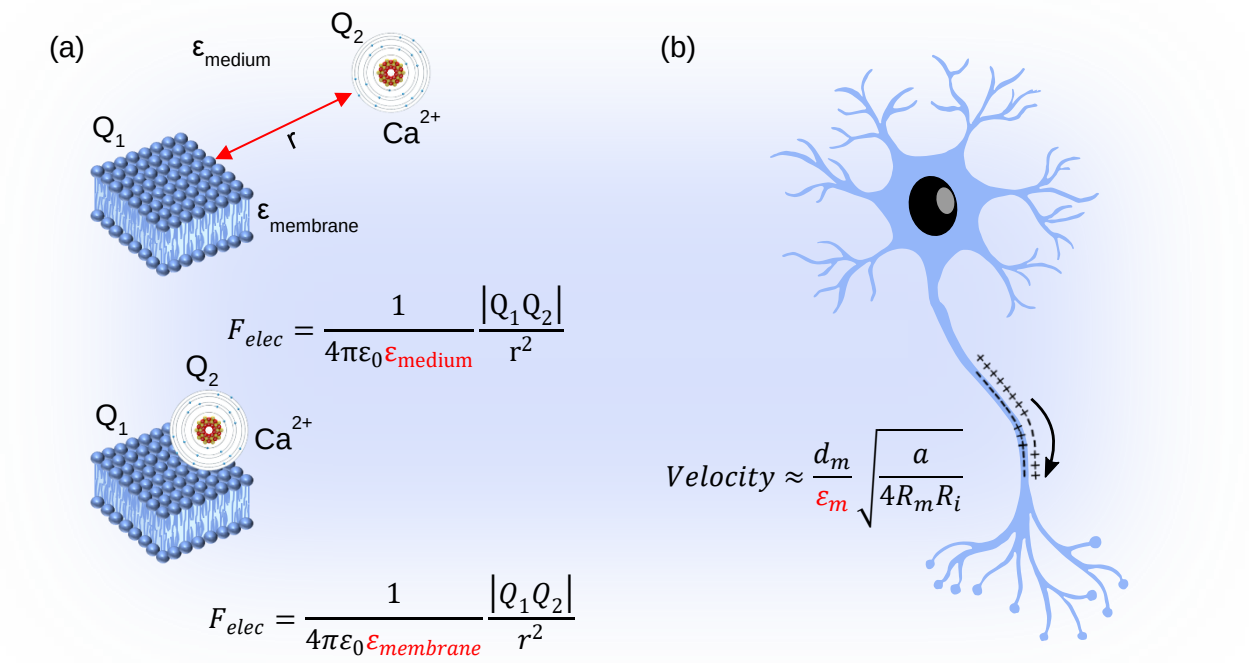

Figure 9: Examples of the relevance of ε_r in biology. (a) Schematic of the interaction lipid bilayer-ion. It is regulated, at long distance, by the dielectric constant of the medium (ε_{medium}), while at short distance, by the dielectric properties of the membrane ($\varepsilon_{membrane}$). (b) Propagation velocity in neurons, given by the dielectric constant of the myelin sheets (ε_m) and their thickness.

The dielectric constant (ε_r) is one of the main actors governing electrostatic interactions in biological systems. Electrostatic interactions are fundamental for protein folding and protein interactions [22, 123, 124], for clustering of lipid molecules held together in a double bilayer configuration and for the integration of all the membrane components with one another [43]. The magnitude of the dielectric constant determines the strength of such interaction when the interacting objects are at very close distance and the medium is no longer present (Figure 9 (a)).

Furthermore, the dielectric constant is also an important parameter in electrophysiology, as it ultimately determines membranes' permeability to ions and charged molecules distribution into the cell membrane [44, 45]. It also affects the action potential generation (charging time) and propagation velocity in electroactive cells [46, 47, 48, 49]. For instance, the difference in the

propagation speed between myelinated and non-myelinated axons in neurons is largely due to the dielectric constant of the myelin sheets (Figure 9 (b)).

Besides, the permittivity also determines the cell's and membrane's response to externally applied electric fields (dielectrophoresis [125], impedance spectroscopy [126], or electroporation [127]), which can in turn be used to gain information about the system or used in technological applications.

For these reasons, the measurement and quantification of such parameter in biological systems is of great interest.

1.3.3 Bioelectrical measurements

Technology has been an important driving force for bioelectrical measurements; new tools and methods constantly allow us to understand bioelectrical phenomena more deeply. As compared to the past, where only very simple apparatuses were available, electronically complex source-meters and modern microelectrodes have been developed, together with amplifiers and computers to acquire and post-process the information recorded.

Finally, also microscopes came to play an important role in bioelectrical studies because they allow to visualize the structures of interest. The modern set-up for bioelectrical studies is composed by an optical microscope coupled to micro-electrodes that can be positioned with micrometric precision in/on the membrane of single cells (Figure 10 (a)). Alternatively, planar microelectrodes can be exploited, being the cell seated on top of them, and with the cells electrical activity being sometimes amplified with in-situ transistors [128, 129] (Figure 10 (b)).

(a) (b)

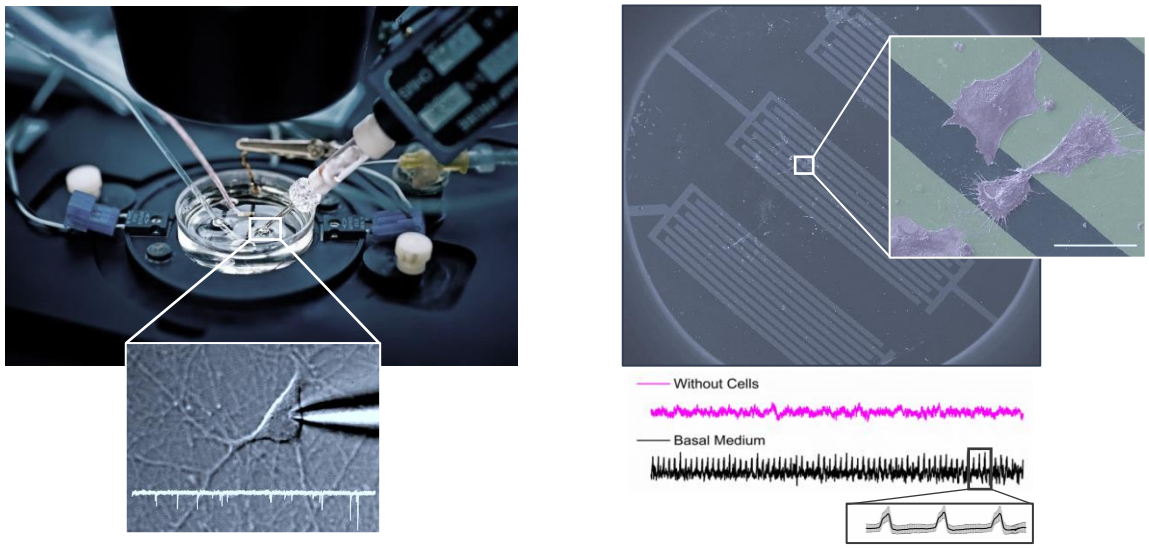

Figure 10: (a) Microscopy set-up with micromanipulators (adapted from: Charles river, "Find a Cell Line - ChanTest Cell Lines", Accessed on February 2021, <https://www.criver.com/find-cell-line>); (b) Microelectrodes array of an EGOFET transistor for extracellular recording (courtesy of A. Kyndiah and H. Lozano).

With these setups, intracellular [130] or extracellular [131] electrical recordings can be performed, depending on the electrode type and what is to be measured.

However, to scale down the electrodes to less than ~1 µm is complex and costly, and makes parasitic effects to dominate their response; this constitutes a limitation to measure samples like membranes, whose heterogeneity is in the nanoscale range, or when addressing small scale biological objects like bacterial cells or viruses.

Nowadays, single channel recording has become experimentally accessible with the development of the patch clamp technique, which realized the idea of electrically isolating a very small membrane patch, where only very few channels are present, and achieved single channel current resolution [132, 133, 134, 135]. Yet, the technique still suffers from mechanically fragile connections which makes long term recordings extremely difficult, and is in essence a blind technique, in the sense that the presence of the ion channel is not visualized previously to the measurement.

Most efforts in bioelectric technologies have been made to measure the active cell response. In these measurements, the main physical quantities involved are electrical potentials (either extracellular or intracellular) or ionic electric currents across the cell membrane. The most widely known bioelectric recording is the action potential in neurons [136].

Besides technologies to address the active properties of excitable cells, specific technologies to measure the passive properties (e.g. permittivity, ε_r) have been developed. One of such techniques, for the past century, has been impedance spectroscopy (IS), which has led to the dielectric characterization of tissues [137], cells [138], synthetic and natural membranes [139, 126, 139, 140, 141] and ion channels or upon addition of drugs to the bilayer [142] in a non-invasive way.

Impedance spectroscopy measures the impedance of a system over a wide range of frequencies, in order to analyse its frequency dispersion. The measurements are carried out normally by placing the object of study (e.g. a membrane, a whole cell or an ensemble of cells) immersed in an electrolyte solution, between two electrodes. A small alternating ac potential is applied to the system and leads to an ac electrical current flowing through the object, of which the amplitude and phase difference are measured. From the ratio of the applied potential to the measured current, the impedance is derived. The impedance can be expressed as a complex number:

$$Z = R + jX \tag{3}$$

where $j=\sqrt{-1}$. The real and imaginary parts of Z describe respectively the resistance (R) and reactance (X) and can be represented by equivalent electrical circuit elements. An equivalent permittivity including both dielectric properties of the sample and of the interfacial regions can be then obtained. Equivalent electric circuits, which are needed to extract the object's electric properties, can be however very difficult to set for complex systems.

Impedance measurements [143] have given us the very first evidence that living cells were contained by a membrane with low permeability to ions [144]. Furthermore, they also provided the first estimation of the thickness of a cell membrane [145, 146], which was very close to the one determined by electron microscopy three decades later [147]. Impedance measurements can be carried out on solid supported lipid bilayers, or on suspended bilayers (e.g. black lipid bilayers). Since IS allows to resolve different processes of electrical polarization, natural membranes can be characterized directly on intact cells, so that each frequency range informs about the property of a specific part of the cell (Figure 11).

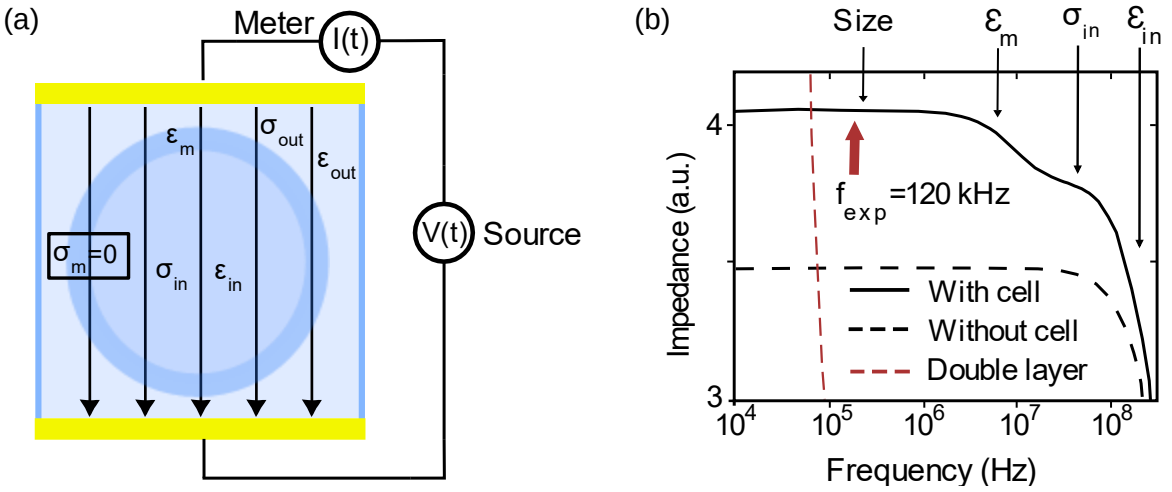

Figure 11: Impedance spectroscopy measurements of intact cells. (a) Schematic of the setup. A cell is introduced between a pair of electrodes to which an alternating voltage is applied. The presence of the cell modifies the electric field in that region, this physically imply a modification of the impedance between the electrodes [148, 149, 150]. (b) Electric polarization processes are resolved in each frequency range. Information about size (in the kHz range), permittivity of the membrane (ε_m), conductivity of the interior (σ_{in}) and permittivity of the interior (ε_{in}) can be extracted [151].

The techniques reported mostly provide averaged values of the electrical properties of biological systems. To address systems like heterogeneous biomembranes, it is important to resort to characterization techniques with nanoscale spatial resolution. This opportunity is provided by Scanning Probe Microscopies (SPMs).

2. Nanoscale dielectric characterization of membranes

2.1 Introduction to Scanning Probe Microscopies (SPMs)

Scanning Probe Microscopies identify an ensemble of techniques which shares a number of common features. They all make use of a sharp probe that scans over the sample surface in the x and y direction, thanks to a piezoelectric scanner that changes its geometry with sub-nanometric precision, according to an applied voltage. The probe-sample distance in the z axis is controlled by a feedback-loop, which adapts it as a function of the interaction sensed by the probe, maintaining it constant. The movement of the z piezo is recorded and correlated with the X, Y position of the tip. By doing so, SPMs can access to the sample surface topography at the nanoscale and sometime even sub-nanometer length scales. Besides topography, SPMs can be customized to measure a number of physical and chemical properties of the sample.

SPMs techniques differ from each other depending on the interaction they probe, which has to be recorded at a typical distance and can benefit from operating in different modes, i.e. applying a feedback on different quantities. Some SPMs techniques can also image different interactions simultaneously.

The properties recorded are later displayed as images, where every pixel returns the measured quantity at that specific position on the sample surface. The spatial resolution approached varies from technique to technique and from sample to sample.

In the case of membranes, for instance, mechanical properties such as force of rupture, adhesion, Young modulus; electrical properties such as electrical conductivity, surface charge, dielectric constant; or chemical properties such as material composition can be provided with

a resolution down to the nanometric level. Every of these properties is given by a physical interaction and reveal local characteristics of the sample.

Since the implementation of the first SPM, named Scanning Tunnelling Microscope [152], SPM has proved to be an invaluable tool of investigation in all areas of science starting from solid state physics to molecular biology.

The invention of the STM triggered the development of the Atomic Force Microscope a few years later [153] and a series of ground breaking results in various fields, all based on the strength of SPM techniques to work under natural ambient conditions with resolutions down to the sub-nanometer scale. Membrane's understanding grew exponentially.

2.2 Atomic Force Microscopy (AFM)

2.2.1 Introduction to AFM

Atomic Force Microscopy is an SPM technique that senses the short-range dipolar forces, e.g. Van der Waals forces of attraction, or short range repulsion forces between the sample and a sharp probe (Figure 12). The AFM probes has a long, micrometric cantilever accessorized with a sharp tip located at the extremity, which interacts with the sample. The interaction force between the sample and the tip induces the bending of the cantilever that can be measured by an optical detection system called photodiode, although some kind of samples (turbid liquids) require a different approach [154, 155]. The change in cantilever deflection as the probe approaches the surface is measured as a voltage difference by the photodiode (ΔV). The cantilever deflection in length units can be calculated by simply dividing for the sensitivity (m), extracted from a mechanical approach curve over a stiff surface. Hooke's law allows to further transform deflection in force (N):

$$F = k \times \Delta V \tag{4}$$

where k (N/m) is the equivalent spring constant of the lever.

AFM can work with both conductive and insulating samples and can be operated both in air and liquid conditions (and also in vacuum). The probes can be made of insulating or conductive materials and are easily available from probe manufacturers. Usually, AFM is used to image the topography of the sample, as well as to determine its mechanical properties through force spectroscopy measurements. The mechanical properties of supported lipid membranes have been largely investigated by AFM [156, 157, 158, 159]. The development of high-speed AFM [160] provided access to their dynamics and allowed to visualize processes never observed before [161].

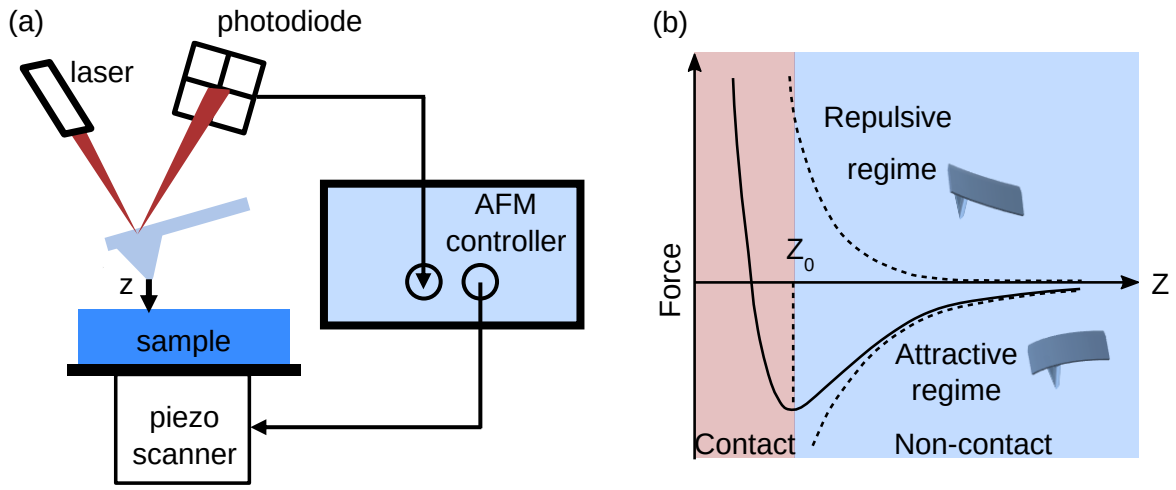

Figure 12: (a) Schematic illustration of the AFM set-up. (b) Interaction landscape as a function of the tip-sample distance. Van der Waals attractive force felt by the cantilever as the tip approaches the surface; the lever deflects downwards, then it comes in physical contact with the surface (Z_0) and deflects upwards. In liquids the presence of charges can make electrostatic force to dominate over van der Waals forces and short-range repulsive force can also be observed.

2.2.2 AFM topography scanning modes

The topography of the sample can be obtained by operating the AFM in different modes. The optimal mode to select depends mostly on the probe we are using and the sample to be imaged.

We recall that the Van-der-Waals force is attractive, but repulsive forces of a different origin appear when the tip gets in close contact to the sample surface (Figure 12 (b)). According to which part of the force is sensed in the AFM experiment, different operation modes were developed.

AFM images obtained operating in the close contact repulsive region are acquired in Contact mode, whereas, when working in both repulsive and attractive region (or intermittent contact region), one refers to Dynamic or Amplitude Modulation mode.

In contact mode, the deflection of the cantilever is kept constant by a feedback loop, that adjusts the piezo movements in response to changes of a magnitude dictated by the user (set-point). This value can be chosen to be higher or lower, depending on how much pressure do we want to exert on the sample. Ideally one would like to work at set-point close to 0, avoiding that way any damage of the sample. The topography is displayed as z piezo displacement, as the probe scans the surface.

In Dynamic mode instead, the cantilever is mechanically excited to oscillate at its mechanical resonance frequency. The amplitude of the oscillation is precisely detected by measuring the oscillation of the photodiode signal with a lock-in amplifier, which selects the signal, in this case the amplitude, only at the resonance frequency. The measured oscillation amplitude is finally used to drive the feedback that keeps the distance between tip and sample constant. Therefore, one defines a set-point for the amplitude smaller than the oscillation amplitude out of contact (free oscillation amplitude), that is maintained during the scan by the feedback control-circuit.

Apart from the amplitude that is used to measure the sample topography, the lock-in also acquires the phase shift of the cantilever oscillation with respect to the excitation signal for every image point. This phase image gives access to additional material properties like the

stiffness of the sample or the local adhesion. These properties allow the detection of changes in the material composition, which cannot be discriminated from the topography.

Usually, suitable cantilevers for Dynamic mode have slightly higher spring constant (k~1 N/m or more) than the ones used for Contact mode, and higher resonance frequency (f_{res}>10 kHz). This parameter is especially important when it comes to liquid measurements where the resonance frequency drops by about 50% due to hydrodynamic drag.

However, Dynamic mode is particularly suitable for the measurement of soft biological samples like bio-membranes since the interaction can be tuned to be much softer. Furthermore, there is no lateral force present during scanning, which could lead to modifications of the sample as in the case of contact mode.

To further lower the interaction with the sample, one option is to use the non-contact or Frequency Modulation mode, which is similar to Dynamic mode, but with the tip never contacting the sample and being maintained in the attractive regime of the van der Waals force. Another difference, stands in the fact that changes of the resonance frequency are measured, usually using a Phase lock loop amplifier (PLL). The resonance frequency changes slightly as the tip is very proximal to the sample surface (in attractive regime) and at that point the piezo elongates or retracts to maintain the cantilever at its resonant frequency. However, because the frequency of oscillation of the cantilever can both increase or decrease as we approach the sample (depending on if we are in attractive or repulsive regime), sometimes this mode is very difficult to operate when the objects are heterogeneously high (as in the case of cells), because the tip can crash easily.

In all modes, the minimum detectable force is limited by the thermal motion of the cantilever. These modes are parametric, in the sense that observables like amplitude, phase or frequency shift, recorded at every position on the surface, are later related to mechanical properties by some analytical theory [159].

Finally, it is worth to mention the Force Spectroscopy imaging mode, in which one tip-sample approach curve per pixel is acquired, giving access to the topographical information and mechanical properties of the sample simultaneously.

Once the contact point (CP) in each curve is identified, topography is obtained. The mechanical properties are instead extracted from the approach or the retraction curves, depending on which is the physical magnitude of interest. The most common fitting model is the Hertz model [162], to extract local Young's Modulus of the sample from approach curves, while adhesion maps are generated by displaying the adhesion force from the retraction curve [163].

Force spectroscopy is widely used for studying supported biomembranes [164, 165, 166, 167, 168]. Force-distance based modes have been also extended to molecular recognition [169] and composition mapping [156, 157, 159]. Force spectroscopy is nowadays improved in speed, i.e. images can be acquired in less than a minute, thanks to faster scanners and close loop systems. Consequently, drifting problems are reduced, and the mode can be even applied to materials that encounter some sort of degradation over time. Furthermore, as the images can be acquired faster, the number of pixels can be increased giving access to smaller heterogeneities of the sample. Recently, given also the massive improvements of computer processors and in data storage, the so-called Force Volume modes are rising. They are multi-dimensional modes that allow to acquire a wide range of physicochemical properties at the same time while sweeping the z distance [159].

Given these advantages and the fact that force-distance based modes are very suitable for imaging high, heterogeneously shaped objects, they are widely applied for imaging tissues [170] and intact cells [171, 172, 173, 174, 175]. Additionally, the force resolution achieved can be excellent (in the piconewton range). However, sometimes the lack of reliable methods to identify the contact point in the case of soft materials and the lack of accurate analytical expression to

describe the contact mechanics quantitatively, makes the technique difficult to apply to the study of such systems.

2.2.3 High-speed AFM

Biological processes happening on the membranes like protein-protein recognition and lipid domains formation and rearrangements are fast (on the millisecond scale). No AFM could follow them until the development of the high-speed AFMs, among which highlights the setup by Toshio Ando [176].

But what does the technology developed to achieve such high imaging rates consists of? A first, easy thing to guess, refers to fast scanners. Consequently, very high resonant frequency tips (in the MHz order) were required since it is always necessary to record few cantilever oscillations cycles per pixel, to allow the lock-in to work properly. Commercially available cantilevers were far away from such resonance frequencies, and thus the idea of scaling them down until they could reach that range. Fast ultrashort cantilever with resonance frequencies in air of ~2 MHz and k=0.2 N/m are now available.

Optical beam deflection (OBDs) systems were adapted consequently. Fast amplitude and phase detectors have been developed, capable of detecting the amplitude and phase signal every oscillation cycle of the cantilever, that for high-speed cantilevers can be less than a μs.

Fast PID controller were also incorporated, together with active dumping techniques for the z scanner, to remove effects due to hydrodynamic pressure and unwanted vibrations.

The final response time is actually controlled by the limited response speed of all the devices abovementioned, which are contained in the feedback loop, and by the time delay due to a parachuting effect. This effect is due to the fact that when a piezo-actuator is driven for a long time, its temperature increases and the free oscillation amplitude decreases. Thus, the

feedback system misinterprets the situation and withdraws the stage from the cantilever tip. The delay is due to the time taken to reapproach the sample.

The high-speed set-up presents overall an increased feedback bandwidth due to the development of these fast response devices, which allows to acquire tens of images per second.

2.3 Scanning Dielectric Probe Microscopies

After the invention of SPM in the 80s, several SPM-based electrical techniques have been developed to achieve dielectrical characterization of biological samples at the nanoscale, simultaneously to their structural properties. This task was extremely challenging since the local signal to detect is very weak in comparison to non-local contributions (Figure 13) as well as topographical artifacts [177].

However, new instrumentation among which wide-bandwidth low-noise current amplifier and lock-in detection, and new measurement approaches to resolve local capacitance finally allowed these methods to rise. In particular, the measurement of the local signal was achieved by considering not the capacitance itself, but its variation (ΔC) or the derivative (dC/dz).

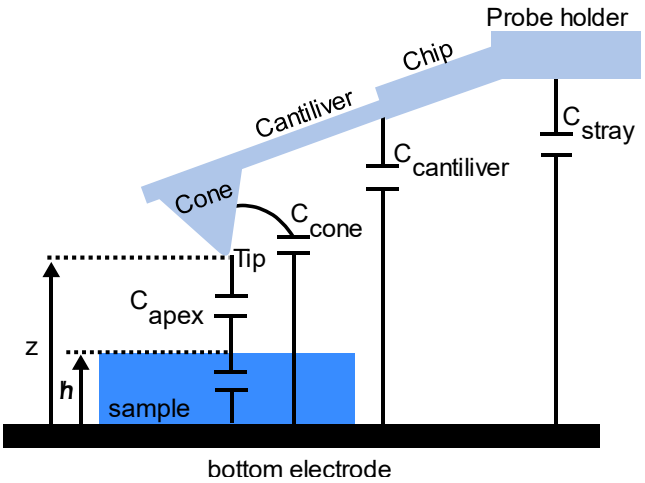

Figure 13: Capacitive contributions arising from different parts of the probe. The total capacitance is given by $C = C_{apex}+C_{cone}+C_{cantilever}+C_{stray}$.

Scanning Dielectric Probe Microscopies complement the electrical measurements with theoretical methods and calibration procedures for their accurate quantification.

2.3.1 Current and Force-sensing techniques

Scanning Dielectric Probe Microscopies can be divided into two categories: current-sensing and force-sensing techniques. In currents-sensing dielectric techniques, the measured quantities are alternating currents, which flows from the substrate to the tip and carry information about the electrical properties of interest. The AFM probe, which has to be conductive, is used here as a nanoelectrode displaced with nanometric precision, either in contact with the surface or not (which is possible for ac currents), and which can be vertically controlled by using a force feedback. Among the current sensing techniques we find ac current sensing Atomic Force Microscopy (AC-AFM) [16, 20, 178], Scanning Capacitance Microscopy (SCM) [179, 180], Nanoscale Impedance Microscopy (NIM) [181] and Scanning Microwave Microscopy (SMM) [17, 23, 182, 183].

In comparison to current-sensing, force-detection is easier to implement, since it does not require low-noise wide bandwidth current detectors or microwave network analyzers, and thanks to the high sensitivity of the cantilever to force variations, it can achieve much higher spatial resolution.

In force-sensing techniques the physical magnitude measured by the probe is an electric force. This force correlates with different electric properties of the sample, depending on the mode of operation. Generally, force-sensing techniques are based on the application of a voltage of the form $V(t)=V_{DC}+V_{AC}\cos(\omega_{el}t)$ between a conductive AFM probe and the sample's conductive substrate. When such potential is applied, the probe feels an electrostatic force that can be expressed as:

$$F_{el}(t) = \frac{1}{2}\frac{dC(z)}{dz}(V(t)-V_{CP})^2 \quad (5)$$

where V_{CP} is the contact potential (due to difference in the work function between tip and sample or/and trapped charges) and dC(z)/dz is the derivative of the capacitance or capacitance gradient. The expression above can be expanded obtaining the following three components:

$$F_{el,DC} = \frac{1}{2}\frac{dC(z)}{dz}\left[(V_{DC}-V_{CP})^2+\frac{V_{AC}^2}{2}\right] \quad (6)$$

$$F_{el,\omega}(t) = \frac{dC(z)}{dz}(V_{DC}-V_{CP})V_{AC}\cos(\omega_{el}t) \quad (7)$$

$$F_{el,2\omega}(t) = \frac{1}{4}\frac{dC(z)}{dz}V_{AC}^2\cos(2\omega_{el}t) \quad (8)$$

The first term corresponds to a “static” DC bending, and two more harmonics are obtained at frequencies ω_{el} and $2\omega_{el}$ respectively. The electrostatic force of the $2\omega_{el}$ component is often referred to as the capacitive force.

Depending on the component recorded, different electric force modes have been developed, such as Kelvin Probe Force Microscopy (KPFM) [18, 184], Scanning Polarization Force Microscopy (SPFM) [185] and Scanning Dielectric Microscopy (SDM). Sometimes these modes are referred generically as Electrostatic Force Microscopy (EFM).

In the following section, SDM will be described in detail since this technique was chosen to carry out the present work of thesis.

2.3.2 Scanning Dielectric Microscopy (SDM) in air

Scanning Dielectric Microscopy is based on the detection of the attractive electric force that arises between a conductive probe and the sample under the application of a voltage or the ac current flowing through it, as described before, with the purpose to characterize the

dielectric properties of materials. Scanning Dielectric Microscopy in force-sensing [12, 15, 19, 186, 187, 188, 189] was largely preferred over its operation in current-sensing [13, 14, 20], because of increased electrical and lateral resolution of the technique. Force-detection SDM can be further divided into DC-SDM or AC-SDM, depending on whether the static or oscillatory contribution is measured.

DC-SDM is performed by applying a dc voltage [19] and recording the static deflection of the cantilever, which provides a lower electrical resolution as compared to dynamic modes. Furthermore, in addition to dielectric properties, it is sensitive to surface potential changes (see Eq. (6)) that should be carefully taken into account, and to thermal drift and instabilities and it is therefore more difficult to implement. In the AC-SDM mode, an ac voltage is applied and ac forces down to the piconewton can be detected, corresponding to few zeptoFarads in capacitance. Among the two harmonics generated by the application of the probe/sample ac voltage, the second harmonic is chosen, because it only contains contributions from the derivative of the capacitance, which contains information about the dielectric properties, and not the contact potential term. It is important to underline that the electrical oscillation frequency has to be selected far below the mechanical resonance frequency of the cantilever, to avoid convolution of the response with unwanted contributions coming from the mechanical response of the cantilever.

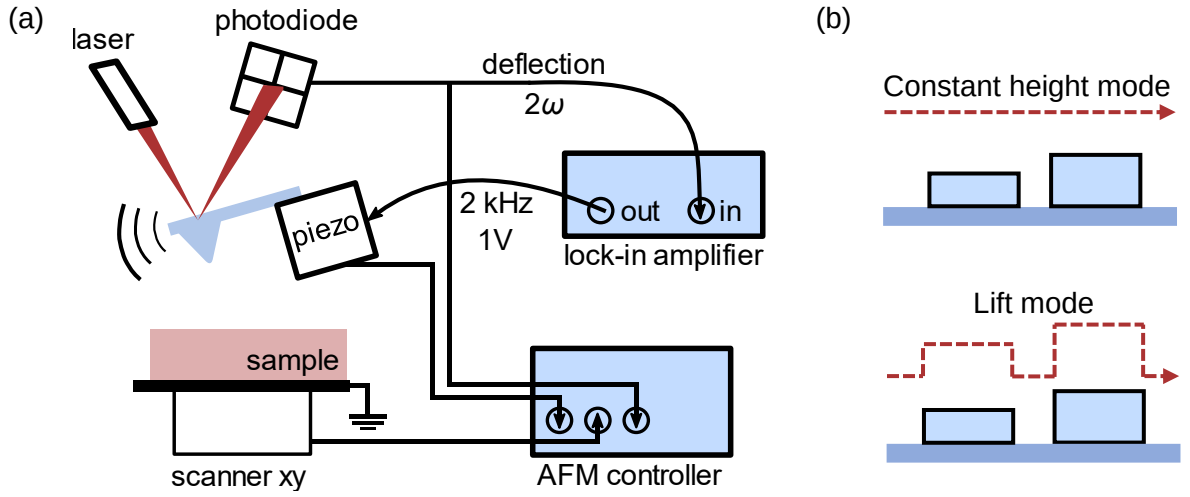

Figure 14: (a) SDM setup for air environment. (b) Modalities of the electrical pass: constant height and lift mode.

SDM is most often a two-pass mode technique which is generally operated line by line. A first topographic line is acquired most often in intermittent contact mode, without electric field applied to the tip. Afterwards, the same line is retraced with the tip lifted and scanned at a certain distance from the substrate, with no mechanical oscillation, but with the ac potential applied. This second pass can be performed in lift mode, re-tracing the topography of the sample, or constant height (off-feedback mode) (Figure 14). In the first case, the tip keeps varying its distance with respect to the conductive substrate, generating different and non-local contributions from the probe. This introduces topographic cross-talk effects [190] that must be carefully taken into account. For this reason, constant height mode is normally preferred. The z-scanning height of the second pass is measured from the sample surface at the beginning of each line. This justifies why topographical and electrical scans are alternated line by line, to reduce the error introduced by thermal drift.

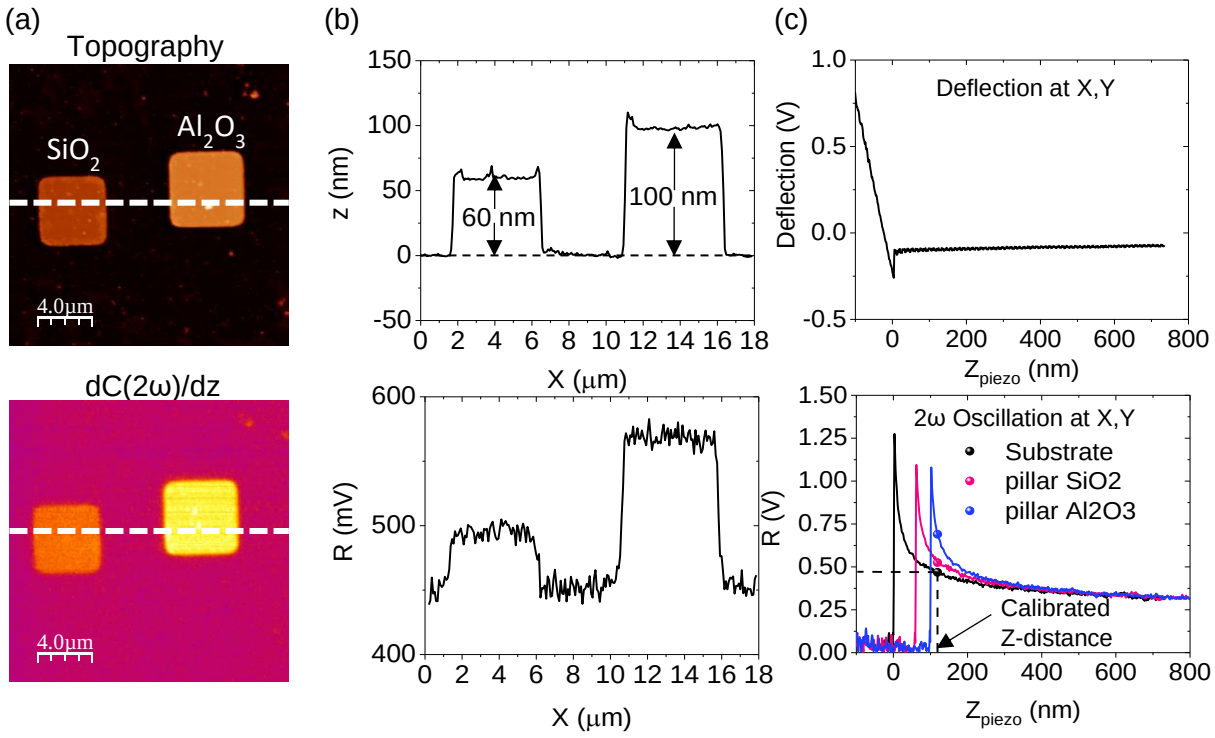

Figure 15: (a) Examples of topography and electric image of a test sample consisting of a SiO_2 and an Al_2O_3 pillar on silicon doped substrate (courtesy of Shubham Tanwar, PhD in the Nanoscale Bioelectrical Characterization group at IBEC, Barcelona). (b) Profiles of the images along the dashed lines; both pillars display a positive dielectric contrast with respect to the metallic substrate. This feature is typical of SDM images in air. Example of a mechanical approach curve (top) and electrical approach curves (bottom) on the substrate and each of the pillars are shown in (c).

During the second pass, the oscillation amplitude of the cantilever at two times the frequency of the applied voltage is recorded by the lock-in and displayed as an image (for raw data in Volts, commonly referred as R) (Figure 15 (a), bottom image). The electrostatic force detected, and thus the capacitance, depends on X, Y, Z-distance and correlates with the dielectric properties of the sample (ε_r).

In an SDM experiment, the acquisition of the electric images is complemented by approach curves on the conductive substrate, recorded before and after imaging. As the tip approaches the surface, with the ac voltage applied, the distance-normal deflection of the cantilever is recorded in parallel to the 2ω electrostatic force component. These electrical curves are needed for calibrating the probe geometry and to exclude possible potential losses or modifications of the tip geometry along the measurements. Besides, the curves are used to accurately determine the z-scan height, which can slightly differ from the nominal value. Electrical approach curves can also be directly acquired on the specimen of interest, or, in the case of highly heterogeneous samples, they can be reconstructed by using a set of dielectric images recorded at different z-scanning distances (Figure 15 (c), bottom graph) [191].

SDM images and curves only give qualitative information about the dielectric properties of the material. Quantification and mapping of the dielectric constant at the nanoscale is only achieved when calibration procedures and theoretical methods complement the SDM measurements [177]. In this case the technique exploits its full potential, and it is properly termed Scanning Dielectric Microscopy (SDM).

From the measurements, as the raw data (2ω tip oscillation) comes out of the experimental setup in Volts, the derivative of the capacitance in Farad/meter can be directly obtained through the formula:

$$\frac{\partial C(\omega)}{\partial z} = \frac{2\sqrt{2}}{v_{ac}^2} \times k \times \frac{\left(A_{2\omega} - A_{2\omega,offset}\right)}{m \times G} \quad (9)$$

where k is the cantilever equivalent spring constant, m is the sensitivity (V/nm), G is the lock-in gain and v_{ac} the RMS amplitude value of the voltage applied to the tip.

To proceed with the determination of the nanoscale dielectric properties of the sample, an accurate theoretical model of the probe-sample capacitance is needed. However, the simple parallel plate model normally used for macroscopic measurements is not accurate for a tip-sample geometry and no analytical expressions are available, other than the ones to describe a probe interacting with a plane metallic surface [192], or with ultrathin to thin (<10-50 nm) wide dielectric layers [187]. For this second model, the exact values of applicability always depend on the probe size and geometry, but as a rule of thumb, for the formula to be applicable, the film thickness should not be larger than the tip radius, and the width two/three times more than that. Only in this case the film can be approximated to be laterally infinite and the capacitive contributions (apex, cone, cantilever), are reminiscent of the expressions valid for metallic substrates introduced by Hudlet et al. [192].

Outside these simple cases, numerical modelling, although it is time consuming, is required to precisely describe the probe sample electrostatic interaction [12] (Figure 16). To obtain a capacitance model of the probe-sample system, the corresponding electrostatic problem must be solved. The total electrostatic force acting on the probe can be obtained by integrating the Maxwell stress tensor on the probe surface. The capacitance first derivative is then given by the relationship (with a factor 2 if DC simulations are done, 4 for AC and 8 for modulated AC):

$$\frac{dC}{dz} = \frac{2F_{probe,z}}{V^2} \tag{10}$$

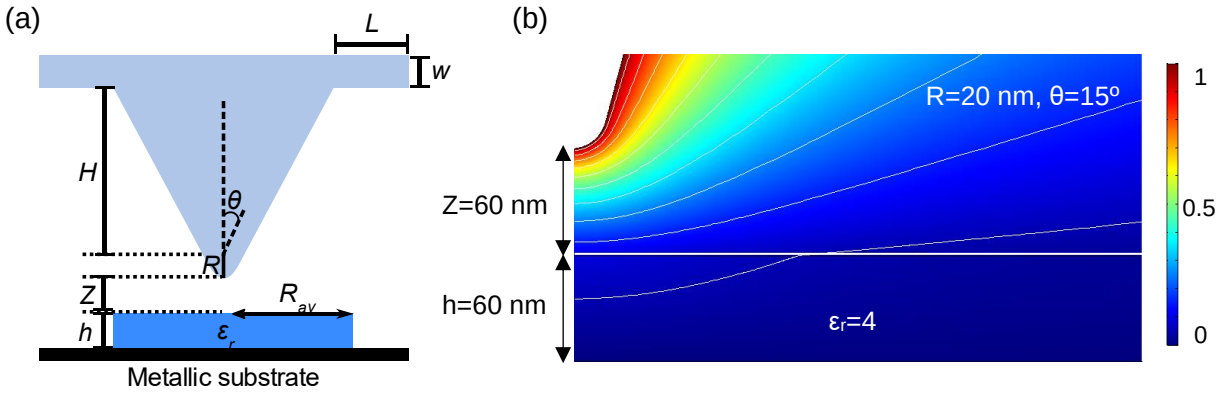

Figure 16: (a) Schematic of the tip/sample model and relevant parameters: Macroscopical parameters of the cantilever (L, W, H), tip radius (R), half cone angle (θ), geometrical parameters of the sample (h, R_{av}) and scanning distance with respect to the sample surface (Z). (b) Potential distribution calculated with the model in (a). Parameters of the simulation: R=20 nm, θ=15º, h=60 nm, R_{av} =2000 nm, $\varepsilon_{r,sample}$=4, Z=60 nm. The geometrical parameters and permittivity simulated coincide with the values for a SiO_2 pillar like the one reported in Figure 15.

Each part of the probe has a different impact on the total electrostatic force depending on the tip-surface distance, Z; close to the surface, the tip radius will dominate, while at far distances (~100 nm), the cone and the cantilever geometry will give the greater contribution. It is important to note that the impact of the cantilever on the derivative of the capacitance is usually a constant offset (C'_{offset}) [15]. This explains the preference of working with dC/dz [177].

To start the quantification, at first, the actual tip geometry needs to be calibrated (in situ before and after the measurements), since the probe-sample electrostatic interaction strongly depends on it. Calibration is achieved by fitting tip-sample approach curves on the clean, conductive substrate to a set of curves generated with the theoretical model for different combinations of R and θ, in order to identify the one optimizing the fitting [13, 193] (Figure 17 (a)). The macroscopic parameters of the cantilever are fixed to their nominal values (H=12.5 μm, W=3 μm, and L=3 μm).

Besides, the electrostatic interaction also depends on the sample topography, which can be rather complex [188]. A realistic geometrical model of the sample has to be built up in the finite-element simulator. Relatively simple models can be used for planar samples like oxide thin films [187] (as the ones reported in Figure 15), polymer blends [194, 195] and lipid bilayers [20], or non-planar samples with simple geometries, such as, macromolecular protein complexes [27, 22], liquid droplets [185], nanoparticles [12], whole bacterial cells [24], viruses [196]. However, for more complex shapes, the actual measured topography can be directly imported to the theoretical model [26].

By using the appropriate model, a table of theoretical curves can be generated for the tip geometrical parameters previously obtained and different values of the dielectric constant (Figure 17 (b)). The experimental curves acquired on the sample are thus compared to such set of curves, now with ε_r as the only fitting parameter.

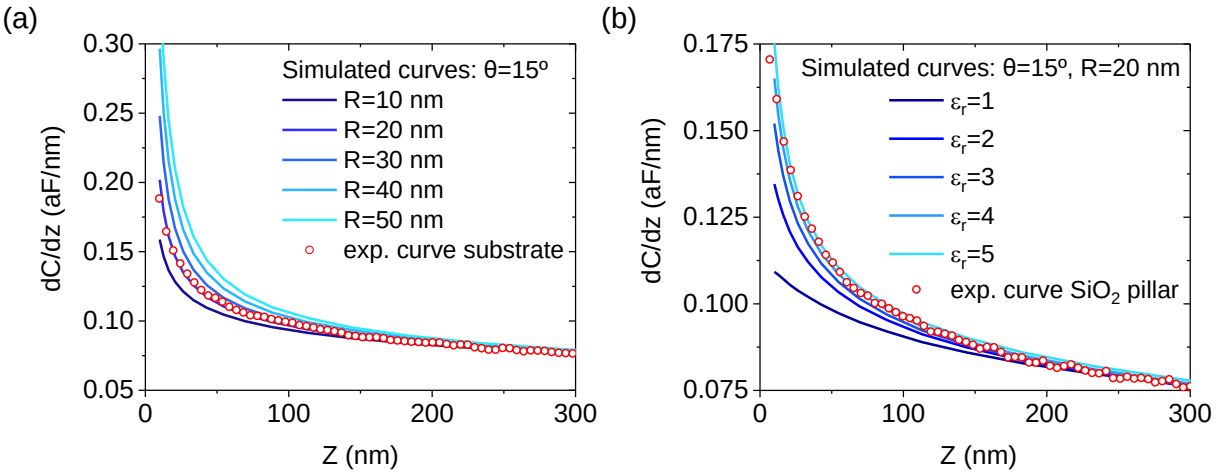

Figure 17: Fitting procedure of experimental data to theoretical curves for the example reported in Figure 15 (SiO_2 pillar). (a) The experimental electrical approach curve on the substrate (empty symbols) is compared to a table of calculated curves (continuous lines); for clarity, only curves simulated for θ=15º and R=10-50 nm is displayed. (b) A set of curves calculated with R and θ obtained by the fitting in (a) for different ε_r of the sample (continuous blue lines). The experimental curve acquired on the sample (empty symbols) is compared to the simulated table; ε_r~4 is obtained for silicon oxide, in agreement with literature.

By extension of this mode of operation, SDM force-distance curves can be recorded in an area of the sample (matrix of pixels), providing a spectroscopic imaging mode called Force-Volume SDM.

When the sample under analysis is high and topographically complex and its electric properties are nanometrically heterogeneous, as it is the case of intact cells, electrostatic force-volume modes can constitute a formidable advantage as compared to the ordinary way of performing experiments, based on few curves and constant height images. Scanning dielectric force microscopy in force-volume mode (SDFVM) was recently implemented [26], and the first ever permittivity maps of a sample containing silicon oxide pillars, bacterial flagella and bacterial cells were obtained. The bacterial cell interestingly displayed three characteristic equivalent dielectric constant values, ($\varepsilon_{r,bac1}$ = 2.6 ± 0.2, $\varepsilon_{r,bac2}$ = 3.6 ± 0.4 and $\varepsilon_{r,bac3}$ = 4.9 ± 0.5), representative of the cell wall and its heterogeneities, as well as of the cytoplasmatic region.

Although some aspects of the technique are still to be improved, like its spatial and temporal resolution, this mode of operation has the further advantage of allowing statistical studies, which lead to a more precise determination of the geometrical parameters of the probe. Besides, SDM in force-volume mode can probe dielectric properties up to certain depths, although nano-tomographic reconstruction methods, currently not available for general systems, would be required to obtain depth information.

In conclusions, SDM in air is a very effective technique, able to provide nanoscale information on the local dielectric properties of materials and among them biomembranes. The dielectric constant of DOPC lipid patches, purple membrane patches and cholesterol crystals, which are some of the main membrane components, were precisely quantified at the nanoscale in air, providing the values 1.9±0.2, 3.3±0.3 and 2.3±0.1 respectively [19, 20, 21].

The technique has the advantage of being label-free and non-invasive (because the images can be recorded far from the surface); furthermore, information on the composition can be obtained through the dielectric constant, used as physicochemical reporter.

However, the study of bio-membranes, and in general of biological samples, becomes meaningful when such systems are immersed in liquid environment, which allows them to retain their fully functional form and biological activity. Note that biological processes occur not just in water, several other molecules are needed for biological entities to perform their activities (salts, buffers, ligands, etc…).

A lot of effort has been made in the last years to push forward electrical characterization techniques, and among them Scanning Dielectric Microscopy, to liquid operation in physiological conditions.

Most of the difficulties encountered are due to the presence of ions in the solution, that under the application of a voltage, lead to the formation of the electric double layer (EDL) which completely screens the electrical signal, provokes surface stress effects on the cantilever and can promote electrochemical reactions producing large parasitic electrical currents [197].

The approaches currently available to perform electrical SPM measurements in solution are Scanning Electrochemical Microscopy (SECM) [198], Scanning Ion Conductance microscopy (SICM) [199] and in-liquid Scanning Dielectric Microscopy (SDM) [28, 50], which was successfully implemented to work in liquid environment. Each of these techniques addresses different properties.

3. In-liquid Scanning Dielectric Microscopy (SDM)

3.1 Introduction

Assessing the nanoscale dielectric properties of biomembranes in electrolyte solutions is fundamental to understand a broad variety of electric phenomena associated with them, as we have seen in the previous section.

Among the techniques used to characterize the dielectric properties of membranes at the nanoscale and in liquid environment, we find spin paramagnetic resonance (SPR) [5, 6] and functional fluorescence microscopy [7, 8, 9]. The latter is probably the most used for membranes studies. Several environmentally sensitive probes have been synthesized to obtain, at least qualitatively, information on lipids permittivity in liquid [10, 11]. Yet, effective quantification of the dielectric constant is not possible or reliable, because the polarization is affected in a complex way by many parameters and comprehensive theoretical treatments are lacking. Fluorescence microscopy and SPR are not label-free, as they make use of endogenous labels that could affect the structure and the properties of the membranes.

In parallel to these experimental measurements, estimation of the dielectric properties of biological systems has also been attempted using computer simulations, where the effective electrical permittivity is calculated from molecular dynamics simulations [200, 201]. Nevertheless, these studies must be complemented by experimental evidence.

Scanning probe microscopy approaches based on double layer interaction forces have been used to characterize membrane surface charges and membrane dipole potentials at the nanoscale and in liquid [202, 203, 204]. The information is contained in a very small distance range, where other forces can come into play, e.g. Van der Waals [205]. The static nature of these measurements makes a precise quantification of the membrane dielectric constant difficult

because both, charges and membrane dielectric polarization, influence the electrostatic forces measured.

Dielectric properties of membranes were also probed by nanoscale dielectrophoretic force microscopy and spectroscopy (DEPFM) [206]; however, it was not possible to estimate the dielectric constant with sufficient accuracy because dielectric contributions were convoluted with topographic effects.

SECM [198] and SICM [199] were applied to map local electrochemical potential and surface charges respectively, but none of the two is informative about the dielectric constant of the specimen under analysis.

In conclusion, no technique has succeeded in quantifying the dielectric constant of biomembranes with nanoscale spatial resolution and electrolyte solutions, without ambiguities in data interpretation, other than in-liquid Scanning Dielectric Microscopy [29].

The resolution of the technique allowed the in liquid characterization of features down to ~50 nm in diameter [30]. Studies on DPPC lipid patches [29], in agreement with macroscale measurements [10, 11, 140, 141], evidenced how the dielectric constant obtained for the DPPC bilayer ($\varepsilon_{r,DPPC}$ ~ 3.2) was larger than the value usually quoted for the hydrophobic part of lipid bilayers (ε_r ~2) [29]. The results suggested that the interfacial polar headgroups contributed significantly to the measured dielectric response [207], and importantly, that membranes permittivity also determines their interface with water [208].

Interfacial water has been demonstrated to exhibit smaller polarizability as compared to bulk one ($\varepsilon \approx 80$) because the rotational freedom of water dipoles decreases near surfaces [33]. This structuring of water layers near surfaces is of extreme importance in biology [209, 210, 211, 212, 213, 214] and it determines the strength of water-mediated intermolecular forces, which in turn affects phenomena such as surface hydration, ion solvation, molecular transport through nanopores,

chemical reactions, lipid bilayer fusion [141] or in the correct insertion and folding of membrane proteins [215] and macromolecular assembly [216, 217, 218].

The properties of lipids that can affect the hydration of the membranes are not only their chemical identity or the presence of net charges on their group heads, but also their phase behavior, which reflects in different packing properties and it is temperature dependent.

The possibility of using the dielectric constant as a reporter of such properties paves way to use in-liquid SDM to achieve label-free mapping of bio-membranes, as it will be shown in Chapter 4.

3.2 In-liquid SDM

Some fundamental changes are required to operate SDM in liquid environment, as compared to its operation in air. First of all, from the point of view of the measurements, the frequency of the applied voltage needs to be above the dielectric relaxation frequency of the electrolyte solution, typically in MHz range, in order to “freeze” the dynamics of the EDL which preclude the locality of the measurement [28]. The exact critical frequency at which locality is achieved strongly depends on the ionic concentration of the medium [28, 29].

When the electric double layer is fully established, the signal results completely screened, with no electrostatic force acting on the tip apex. Most of the applied voltage drops over the interfacial capacitance of the probe, whose impedance at these frequencies is much higher than the one of the solution. The high frequencies also help in eliminating the surface stress phenomena [219, 220, 221].

We note that, in the MHz frequency range, the dielectric constant is sensitive to electronic polarization of the material and to dipolar polarization of small molecules free to follow the ac electric field applied (e.g., water molecules). Therefore, static or quasistatic effects associated to surface charges (space charge layer), pH, ionic strength of the solution (bulk electrolyte

conductivity effects[197]) or dc applied potential are not likely to affect the measurements [222]. This holds true as long as the measuring distance is far from the Debye screening length, to avoid double layer interactions [28].

At such MHz frequencies of operation, commercially available cantilevers are not able to oscillate, but they do bend statically, due to the quadratic dependence of the force on the potential applied. However, recording this static bending normally presents a poor signal to noise ratio.

The strategy adopted to increase it, relies on the modulation of the high frequency (MHz), at low frequencies (in the kHz range), so that its detection can be done much more precisely [28]. This mode of detection is called heterodyne detection.

With this trick, as the frequency is progressively elevated to the MHz range, electric contrast is recoverd in the dielectric imge. The frequency maximizing the signal depends on the tip but mostly on the ionic concentration in solution. Higher ionic concentrations requires higher frequencies of operation.

Overall, the amplitude modulated voltage takes the following form:

$$v(t) = \frac{v_0}{2}(1 + \cos(\omega_{mod} t))\cos(\omega t) \tag{11}$$

Where v_0 is the amplitude of the applied voltage. The modulation frequency, $f_{mod}=(\omega_{mod}/2\pi)$, is chosen much smaller than the resonance frequency of the cantilever, f_{res}, to ensure an almost frequency-independent mechanical amplitude response of the cantilever.

Eq. (11) is equivalent to:

$$v(t) = \frac{v_0}{2}\cos(\omega t) + \frac{v_0}{4}\cos[(\omega - \omega_{mod})t] + \frac{v_0}{4}\cos[(\omega + \omega_{mod})t] \tag{12}$$

which contains three harmonics at ω, $\omega-\omega_{mod}$ and $\omega+\omega_{mod}$.

For frequencies in the MHz range and modulation frequencies in the kHz range, the three harmonics are in the high frequency range. Therefore, only high frequency electric properties are probed.

The corresponding force generated on the probe by applying such time dependent voltage between a cantilever and the substrate is given by (at high frequencies):

$$F(t) = \frac{1}{4}\frac{dC}{dz}[v(t)]^2 \tag{13}$$

where F is the force, dC/dz is the derivative of the capacitance and v the voltage.

By substituting Eq. (11) in Eq. (13), it becomes evident that the electric force has several harmonics:

$$\begin{aligned} F(t) = \frac{1}{8}\frac{dC}{dz}v_0^2\Big\{&\frac{3}{4} + \cos(\omega_{mod}t) + \frac{1}{4}\cos(2\omega_{mod}t) + \frac{3}{4}\cos(\omega t) \\ &+ \cos[(\omega + \omega_{mod})t] + cos[(\omega - \omega_{mod})t] \\ &+ \frac{1}{4}cos[(\omega + 2\omega_{mod})t] + \frac{1}{4}cos[(\omega - 2\omega_{mod})t]\Big\} \end{aligned} \tag{14}$$

In the expression, all the force harmonics, including the low frequency ones at dc, ω_{mod} and $2\omega_{mod}$, are generated by the high frequency voltage (note that all of them are proportional to the amplitude of the high frequency potential, v_0). Five of them are located at high frequencies, well above the resonance frequency of the cantilever, and cannot be detected because strongly suppressed by the mechanical response of the cantilever. The remaining three terms are dc, ω_{mod} and $2\omega_{mod}$; they are at lower frequencies and can be detected.

The first harmonic, ω_{mod}, is selected since it provides higher signal to noise ratio and can be shown to be independent from the dc voltage [222], and only dependent from the capacitive gradient.

Experimentally, the magnitude measured is the oscillation amplitude of the cantilever at the modulation frequency, $A_{\omega,mod}/mG$, where $A_{\omega,mod}$ is the amplitude measured by the lock-in

detector (in Volts), m is the photodiode sensitivity (in Volts/nm) and G the lock-in gain (in V/V). The ac force (in N) is obtained as:

$$F_{\omega,mod} = \frac{k}{mG}(A_{\omega,mod} - A_{\omega,mod\,off}) \quad (15)$$

where *k* is the equivalent spring constant of the cantilever and $A_{\omega,mod\ off}$ represents any small offset, almost negligible, present in the lock-in detector.

Combining Eq. (15) and the term $F_{\omega,mod} = \frac{1}{8}\frac{dC}{dz}v_0^2$, coming from the harmonic expansion in Eq. (14), one obtains:

$$\frac{dC}{dz} = \alpha 8k(A_{\omega,mod} - A_{\omega,mod\,off})/\ v_0^2 mG \quad (16)$$

In order to account for uncertainties in the actual potential drop between the tip and sample, and on the remaining parameters appearing in Eq. (16), a multiplicative factor, α, determined during the system calibration has been introduced [30].

Eq. (16) is the expression used to determine the experimental capacitance gradient values. Overall, the relation between raw data and the capacitance gradient is a multiplicative factor, i.e. it is just a change in the scale of the vertical axis.

3.3 Set-up and imaging characteristics

To cope with the changes required for the implementation of SDM in liquid, the set-up needs to be modified with respect to the one used for air measurements, as shown in [28, 30].

The lock-in amplifier in this case sends its output signal (~2 kHz) as the modulation input signal to a function generator, used to send the high frequency voltage to the tip (Figure 18). The modulation of the vertical deflection of the cantilever is recorded and set as the input for the lock-in amplifier to be able to detect the first harmonic of the tip oscillation.

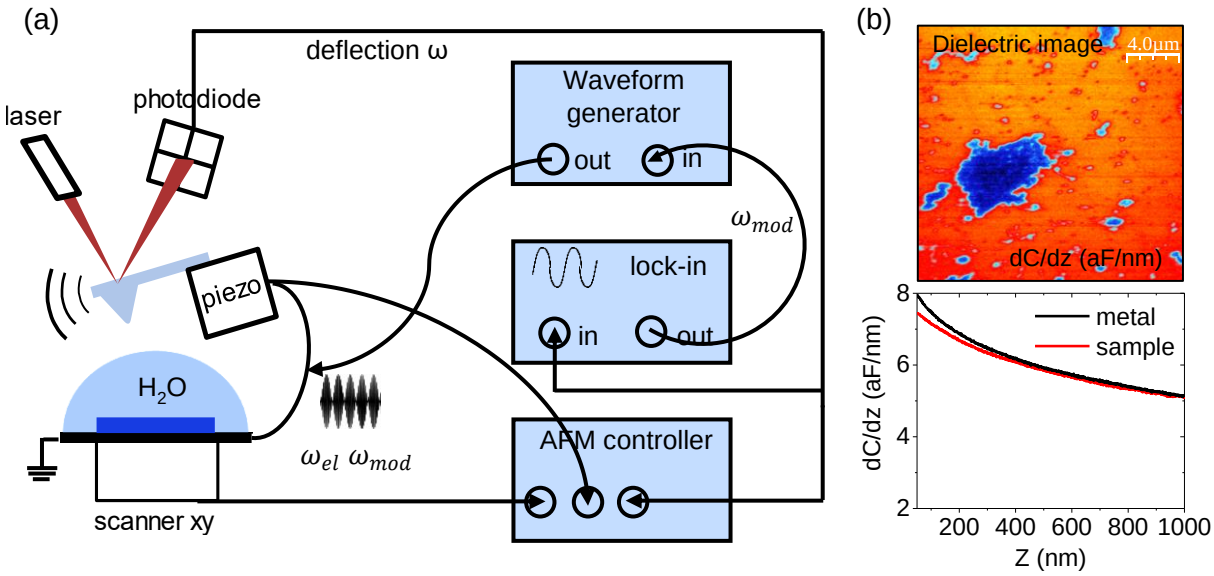

Figure 18: (a) SDM in liquid set-up. The ac voltage excitation at MHz is amplitude modulated at angular frequency in the kHz range. The high frequency is required to achieve locality, and the low frequency one to achieve a high signal to noise detection. (b) Examples of a dielectric image of DOPC lipids in liquid, showing reversed contrast as compared to the case of air, and electrical approach curves on the substrate (black) and in the centre of the lipid patch (red).

When imaging in liquid, few characteristic features differ from imaging in dry conditions. In contrast to air measurements, where the electrostaic force increases steeply and only at quite close distances from the surface (<100 nm), electrical approach curves in liquid display a more gradual increase and the force is still felt at several hundreds of nanometers or even micrometers from the substrate.

At short distances, the force depends on the sample dielectric properties at the high frequency of the voltage. The shape of the electrical curves at close separations reflects the dielectric behaviour of the material they are acquired on. Small differences in the sample properties, either thickness or dielectric constant which affect the ratio $h/\varepsilon_{r,sample}$, are magnified by the high relative dielectric constant of the solution ($\varepsilon_{r,sol}$~78). For this reason, imaging in liquid provides relatively large capacitance gradients, which are in the range of ~ 1 aF/nm, while in air they are in the order of ~0.01 aF/nm. This feature of in liquid imaging allows to operate with small voltages, as required to avoid electrochemical surface reactions.

Furthermore, the measuring frequency is chosen according to the ionic concentrations of the media [50]. Indeed, increasing the ionic concentration implies increasing the measuring frequency accordingly, in order to keep it beyond the relaxation frequency of the electrolyte [28]. In-liquid SDM measurements can be performed at frequencies below 100 MHz for concentrations up to 10-20 mM. For higher ionic concentrations, GHz frequencies become necessary [17].

SDM in liquid media also displays an inverted contrast between sample and substrate with respect to the case of air. This is basically due to the nature of water, having a relative permittivity of ~78, much higher than the one of air (ε_r~1) and normally also higher than that of the sample under analysis. Simulations predict that the contrast in liquid can be reversed when conductive systems are considered (i. e. liposomes filled with buffer).

3.4 Modelling

The quantification procedure of the dielectric permittivity goes more or less following the steps developed for the case of air measurements, where the theoretical values of the capacitance gradient have to be compared to the experimental data.

Theoretical modelling is required since the capacitance and resistance of the solution are distance dependent, and thus the exact geometry of the AFM probe (i.e. cantilever, cone, apex) has to be considered. Much of the complexity of the problem comes from the high dielectric constant of the solutions (ε_r ~ 80), for which the physics of the models used for the numerical simulation has to be modified with respect to the one used for dry environment [29]. Furthermore, the presence of water and ions in solution causes their absorption on the surfaces exposed to the electrolyte (Stern layer) and their uptake in the EDL.

These effects are considered by introducing in the modelling two capacitances, one around the tip (c_{tip}) and one on the substrate ($c_{substrate}$) [28, 29, 30, 31]. Each of these capacitances account for the presence of the compact or Stern layer capacitance, c_{Stern}, [223, 224, 225]. The c_{Stern}

determines the charge that is accumulated at the metal/electrolyte interface per unit of voltage applied. While the diffusive layer should depend only on the potential and on the electrolyte type and its concentration, as different materials can have different contact potential, the properties of the capacitive layer at the interface can be slightly affected. At the same time, the interfacial (Stern/Helmholtz) capacitance does not only depend on the material properties, but also on its roughness.

For convenience in the force evaluation, the interfacial capacitance on the tip is modelled by a thin insulating layer of thickness d_{ins} and relative dielectric constant ε_{ins}, equivalent to an interfacial capacitance $c_{tip} = \varepsilon_0\varepsilon_{ins}/d_{ins}$ [30]. The interfacial capacitance on the substrate is modelled, instead, by a distributed capacitance boundary condition [28, 30]. The specific capacitances forming at the probe-liquid and substrate-liquid interfaces have a strong impact on the shape of the dC/dz vs Z-distance curves, as reported in [30].

Specifically, when the tip and sample capacitances are smaller, the system capacitance gradient (force) at short tip-sample distance gets reduced and the curves tend to bend downwards. The opposite happens if we consider, for both c_{tip} and c_{sample}, large capacitances (>100 μFcm^{-2}) that make their contribution negligible. This feature easily allows to get an idea about the magnitude of the interfacial capacitances in the measurements. At long tip–sample distances the capacitance gradient is not sensitive to these capacitances anymore, demonstrating the locality of the measurements.

The sensitivity to c_{tip} is smaller than that to c_{sample} due to the tip-plane geometry, however its effect cannot be neglected when c_{sample} becomes comparable or higher than c_{tip} [30].

The formation of these two capacitances on the probe and sample surface cannot be avoided by applying a high frequency field and their presence highly increase the complexity of the quantification. Evaluating the Stern layer capacitances in reality is a tricky issue, due to their complicated dependence on the surface chemistry, solution properties and frequency.

The use of numerical simulations of realistic tip/sample models is necessary to precisely model the frequency, tip-sample distance and ionic concentration dependence of the electric force and determine the appropriate operation range to access local information of the sample.

The theoretical data are numerically calculated by integration of the electrostatic part of the Maxwell stress tensor in the frequency domain on the surface of the insulating layer coating the tip, for both dielectric and conductive material [30]. Cantilever parts are not included in the calculations, but their contributions are considered as a phenomenological capacitance gradient offset, C'_{offset}.

In the simulations a pure ac sinusoidal voltage of frequency ω and amplitude $v_{0,sim}$ is used, and the force at the ω harmonic, $F_{\omega,sim}$ is calculated. The relation between this force amplitude and the capacitance gradient can be shown to be:

$$\frac{dC}{dz} = \frac{4}{v_{0,sim}^2} F_{\omega,sim} \tag{17}$$

Eq. (17) is the expression used to calculate the theoretical capacitance gradient values.

The model can be schematized as follows in (Figure 19 (a)), where the two capacitances at tip-liquid and sample-liquid interfaces are introduced.

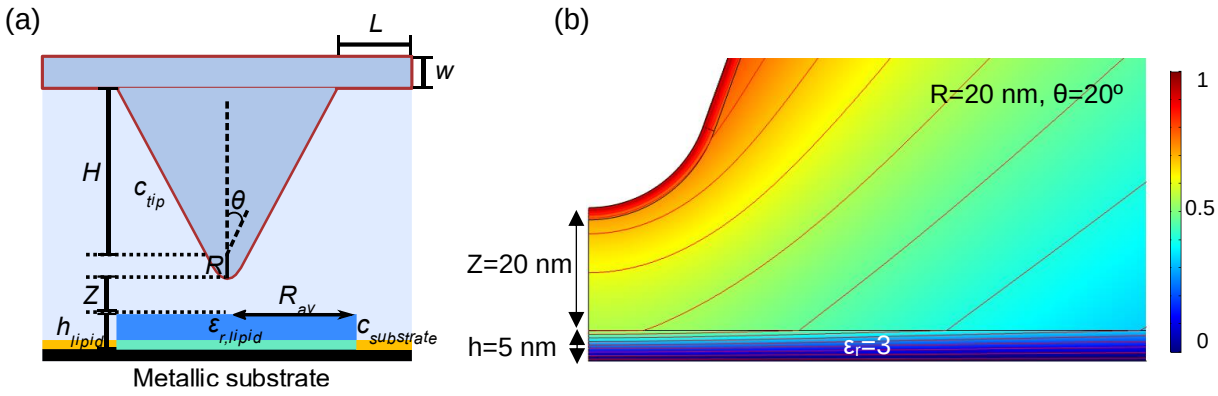

Figure 19: Modelling in liquid. (a) Schematic of the tip/sample model. The number of parameters has increased as compared to the case of air. Besides R and θ, also c_{tip} and $c_{substrate}$ must be determined. The sample here is assumed to be a lipid patch with height (h), lateral extension ($2R_{av}$) and permittivity (ε_{lipid}). (b) Voltage potential distribution generated in liquid conditions for a layer of h=5 nm R_{av}=2500 nm and ε_r=3. Other parameters of the simulation: R=20 nm, θ=20º, Z=20 nm, c_{tip} =1.8 μF/cm^2 and $c_{substrate}$ = 4.5 μF/cm^2.

The voltage potential distribution highlights that, although the overall signal in water is much higher as compared to air, and thus measurements in liquid are greatly favoured, this comes at the cost of a reduced lateral resolution of the measurements (Figure 19 (b)). In liquid, the electrical field lines extend quite far from the tip, which probes areas that are several times wider than its radius. In air, instead, they are much more focused around the tip region and guarantee a higher spatial resolution. This finite size effect, which is prominent in liquid, is a pure electrostatic effect due to the high permittivity of water [30, 31]. This effect does compromise somehow the achievable spatial resolution, which still can be below ~100 nm. The reason why such high spatial resolution can be obtained is related to the use of the force detection mode, which is sensitive to the probe–sample capacitance gradient, rather than to the capacitance.

3.5 Quantification procedure

The quantification procedure was adapted from the case of air [13, 19, 20] as reported in recent works [29, 30, 31] . The capacitance gradient curve over the substrate is used to fit theoretical curves in order to obtain the parameters R, θ, C'_{offset} and this time also c_{tip}, $c_{substrate}$. At first sight,

the fitting might look highly multiparametric, however, some assumptions can be made to restrict the possible combinations. The half cone angle in fact can be actually fixed to the nominal value, because there is normally not much error as compared to the value reported by the manufacturer. The curve gets multiplied for the normalization factor α, that serves to achieve a good fitting given the angle nominal value.

The value of c_{tip} can be determined by fitting approach curves made with gold coated tips on a clean gold substrate imposing $c_{tip} = c_{gold}$ [30]. The range of values obtained for the gold coated tips normally used within this thesis work is around 2-3 μFcm^{-2}. The same holds true then for $c_{substrate}$, when the sample is directly supported on metal. With these assumptions, the tip radius and the offset C'_{offset}, are the only parameters really left to determine. However, when the sample is not directly extended on a conductive substrate, $c_{substrate}$ must be also determined in addition. This is the case for lipid bilayers supported on SAMs, for which electrical characterization has been carried out [30]; the window of values provided depends on the length of the molecule and its polarization properties ($c_{SAM} = \varepsilon_0 \varepsilon_{SAM}/d_{SAM}$) [30].

Once the tip geometry is calibrated and the capacitance of the interfaces are extracted, the dielectric constant of the sample can be obtained by fitting to the experimental curve (or curve reconstructed by planes) the simulated ones, with its dielectric constant as the only fitting parameter. The results provided through this quantification procedure are robust, as shown by [31, 32].

4. In-liquid SDM of sub-100 nm Heterogeneous Lipid Bilayers Patch samples

After having introduced the properties of biomembranes, the need to address their nanoscale dielectric properties, the techniques available and some examples of application to monocomponent samples, we have extended the application of in-liquid SDM to the case of lipid bilayer mixtures with a heterogeneous composition. To this end, we have considered a system made of DOPC and DOPC 1:1 and addressed the dielectric properties of each component, demonstrating that cholesterol reduces the specific capacitance of the biomembrane.

This chapter reproduces almost literally the article: Cholesterol Effect on the Specific Capacitance of Submicrometric DOPC Bilayer Patches Measured by in-Liquid Scanning Dielectric Microscopy. Langmuir ***36****, 12963–12972 (2020), by Di Muzio, M., Millan-Solsona, R., Borrell, J. H., Fumagalli, L. and Gomila, G.* [31]*.*

My contribution to this work consisted in performing the experimental measurements (from sample preparation to image acquisition) and data analysis using a custom-written Matlab code written by R. Millan-Solsona and earlier members of the group. The manuscript was written in collaboration with my supervisor G. Gomila and the other authors.

4.1 Introduction

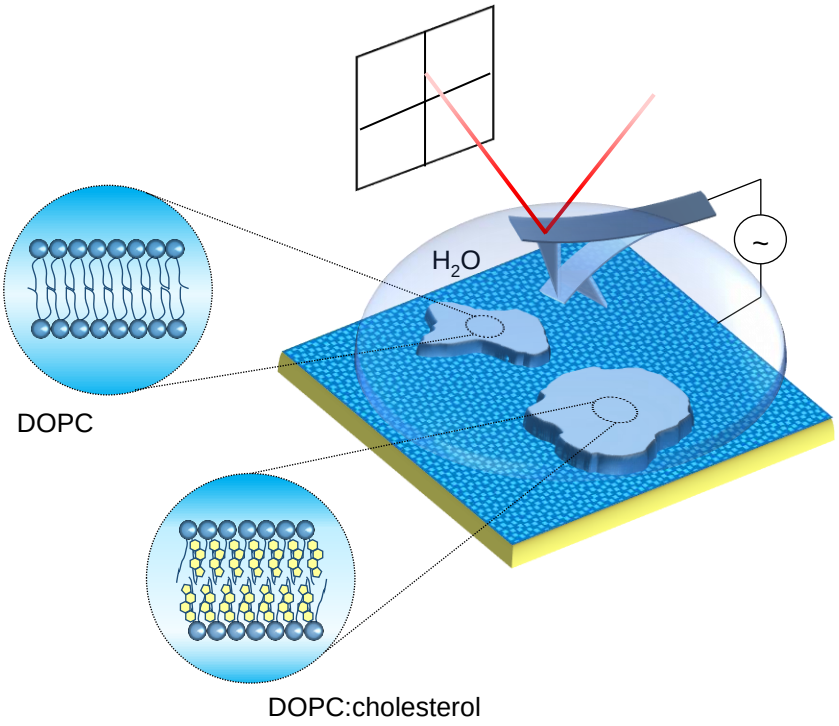

Figure 20: Schematic representation of the in-liquid SDM setup in force detection mode [28, 29] applied to supported lipid bilayer patches of different composition (DOPC and DOPC:cholesterol), adsorbed on a functionalized metallic substrate.

The specific capacitance of biological membranes determines the charge per unit of area that accumulates on their sides in response to a membrane voltage difference [226]. As we have mentioned earlier, it constitutes a key physical parameter in bioelectricity, since it determines the ions and charged molecules partitioning into the cell membrane and the very low membrane ionic conductivity [44], the charging time and propagation velocity of action potentials [226], the voltage thresholds for cell membrane electroporation [127] or the level of screening in the electrostatic interaction of biomolecules with cell membranes [227]. It also determines the cell response to external electric fields relevant in bioimpedance measurements [228] and in electrokinetic techniques such as dielectrophoresis [229] or electrorotation [230].

We recall that the specific capacitance of membranes depends on their thickness, d_m, and electric polarization properties (i.e. its relative dielectric constant, ε_m), through the relationship $c_m=\varepsilon_0\varepsilon_m/d_m$, where ε_0 is the vacuum permittivity. Any factor affecting any one of these two parameters (thickness and/or dielectric constant) influences the value of the membrane specific capacitance. Examples include the membrane composition [231, 232, 233], phase state [234, 235, 236] , temperature [236] or solution pH [237], among others. The specific capacitance is then, as stated previously, a powerful physicochemical membrane reporter, with the main advantage with respect to environmental sensitive fluorescence probes [10, 238] or spin paramagnetic resonance probes [6, 239, 240], of being determined by intrinsic properties, and, hence, not requiring exogenous probes.

Cholesterol is known to modulate the physicochemical properties of biomembranes, but its effect on the specific capacitance of biomembranes has not been fully established yet. Cholesterol (chol) is the main sterol biosynthesized by animal cells and its presence is essential for many membrane's associated processes since it can modulate membrane properties such as lipid diffusivity, stiffness or dipole moment [241] . Cholesterol has been reported to increase [231, 242, 243, 244] or decrease [245, 246, 247] the specific capacitance of biomembranes, and in some cases an increase or decrease depending on the cholesterol concentration [248]. These discrepancies have been attributed, most often, to sample preparation methods (e.g. presence of solvent on the bilayers), but, also, to a limited accuracy and reproducibility of existing measuring techniques [249].

We have mentioned that a variety of electrical techniques and methods have been developed over the years to measure the specific capacitance of biomembranes. Expanding on what said earlier, for natural cell membranes, one finds electrorotation measurements on single suspended cells [250] and current/voltage time varying measurements with micropipette electrodes attached to cells [251, 252] or to cell detached membrane patches [253]. For synthetic membranes (such as model lipid bilayers), measurements have been mostly performed by current/voltage time varying techniques on membranes suspended on small apertures (e.g.

black lipid bilayers) [254] or supported on planar solid electrodes [140, 255] (see Ref. [249] for a review). Efforts have been devoted to reduce uncertainties related to poor estimations of surface area in cells with complex geometries [253] or with membrane corrugations [252], to better control the area of suspended model membranes [256] and to reduce the presence of defects in supported membranes [247]. We have also highlighted in the introduction that some efforts have also been devoted to increase the spatial resolution of the measuring techniques by resorting to scanning probe microscopic techniques [257], and that among them, Scanning Dielectric Microscopy (SDM) played a main role. We recall that SDM is a scanning probe technique that combines either current-sensing Atomic Force Microscopy [20] or Electrostatic Force Microscopy [12] with analytical or numerical theoretical models [12, 14, 187] to extract the capacitance at the nanoscale. This technique, in force detection mode, has also been demonstrated in the liquid environment (in-liquid SDM) [28], and has been previously applied it to the study of thin dielectric films [28] and monocomponent supported lipid bilayers patches [29] in electrolyte solutions.

Here, we exploit the full potential of in-liquid SDM to study the effect of cholesterol on the specific capacitance of supported lipid bilayers patches. With its high spatial resolution, in-liquid SDM has the unique capability to be able to compare *in-situ* the dielectric properties of heterogeneous samples containing bilayer patches with different cholesterol content. To demonstrate it we considered 1,2-dioleoyl-sn-glycero-3-phosphocholine (DOPC) bilayer patches with and without cholesterol. DOPC is a double unsaturated homoacid phospholipid and is one of the main components of eukaryotic cell membranes. This lipid is in a liquid disordered phase (Ld) at room temperature (T_{DOPC}=−20ºC) and is responsible for the fluid nature of cell membranes, a ubiquitous property in signal transduction, transport and cell adaptation.

4.2 Materials and methods

4.2.1 Sample preparation

Metallic substrates. We used flat gold substrates produced by the mica replica method (MicroFab Space, IBEC), functionalized with self-assembled monolayers (SAMs) made of 2-Mercaptoethanol 99.0% (Sigma-Aldrich). The SAMs were prepared by incubation of the gold substrates in a 1 mM solution of the thiols overnight at 2-8 ºC, protecting the vial from light, and from oxidation by a nitrogen flow. Gold was selected for its excellent conductive properties, while the alcoholic moiety terminating the thiol molecules was selected to make the surface more hydrophilic, promoting the interaction with the lipid polar heads and the formation of intact bilayers from liposomes.

Lipid bilayer patches samples. DOPC (1,2-dioleoyl-sn-glycero-3-phosphocholine) and DOPC:cholesterol (50% concentration) bilayer patches were formed on the gold functionalized substrates by the liposome fusion method. For the preparation of the liposomes chloroform and methanol, HPLC grade, were purchased from Sigma Aldrich; high purity water (18.2 MU cm) was obtained with a Milli-Q water purification system (Millipore); DOPC specified as R99% pure, was obtained in powder form (Avanti Polar Lipids, Merk) and used without further purification. The DOPC liposomes were prepared as follows: DOPC was first dissolved in chloroform/methanol (3:1) (v/v) solution to a final lipid concentration of 10 mM. Then the solvent was evaporated under a nitrogen stream with constant rotation of the vial. The vial was kept in vacuum for 6-8 hours to ensure the absence of organic solvent traces. The dry lipid was then resuspended in distilled water at ~60ºC to its final concentration of 0.1 mM. The liposomes were spontaneously formed under these conditions and stored at 2ºC-8ºC, always protected from light, and used within 1–2 days. The DOPC:cholesterol liposomes were prepared in a similar way. Cholesterol was dissolved in chloroform at a concentration of 10 mM. 5 µL of DOPC stock solution and 5 µL of chol stock solution, both 10 mM, were then mixed in a vial

and sonicated in ice for 5-10 minutes to ensure disintegration of possible cholesterol aggregates, homogenization of the components and inclusion of cholesterol in the lipid bilayer (chol is expected to completely dissolve in fluid-like liquid disordered (Ld) lipid bilayers like DOPC ones). The solvent was evaporated as previously detailed and the 'lipid film-cake' was rehydrated with 1 mL of Milli-Q at about 60 ºC, to a final lipid concentration of 0.1 mM. The liposomes formed were stored at 2-8 ºC, protected from light and used within 1-2 days. For the monocomponent DOPC sample, a drop of 80 µL of the DOPC liposome suspension was added to the gold substrate at room temperature (25 ºC) and incubated for 30 min at 60 ºC. The concentration, temperature and deposition time were selected to ensure the formation of lipid bilayers only partially covering the surface (bilayer patches). Afterwards, the substrate was rinsed several times with water to remove the excess of vesicles in suspension. For the mixture sample containing DOPC and DOPC:cholesterol bilayer patches, first 40 µL of pure DOPC liposome solution and then 40 µL of DOPC:cholesterol 1:1 liposome solution were subsequently added to the substrate with an intermediate rinsing step to remove any non-adhered DOPC liposome. This sample preparation procedure was used to prevent mixing/fusion of liposomes of different types. The reduced lipid mobility on the functionalized gold substrate and the selected deposition conditions lead to the formation of isolated lipid bilayer patches of the two components (otherwise a homogeneous DOPC:cholesterol bilayer would be formed). Four different samples have been analysed in the present study containing respectively DOPC patches, DOPC:cholesterol patches (data not shown), DOPC and DOPC:cholesterol patches (1/1) and DOPC and DOPC:cholesterol patches (3/1).

4.2.2 In-liquid SDM measurements

In-liquid SDM measurements were done by following the methodology described in Ref. [28], and described in the previous chapter. Specifically, we used an amplitude modulated ac voltage $v(t) = v_0/2\left(1+\cos\left(\omega_{\mathrm{mod}}t\right)\right)\cos\left(\omega t\right)$ applied between a conductive AFM cantilever probe and the gold substrate in liquid in a Cervantes commercial AFM system (Nanotec Electronica S.L.).

The applied voltage had amplitude 0.75 V, electrical frequency 5 MHz and modulation frequency 6 kHz, and was applied with an external waveform generator (model No. 33250A, Agilent Technologies) combined with an external lock-in (LockIn 204/2, Anfatec Instruments). The low frequency value (~6 kHz) was chosen to be well below the resonance frequency of the probes in liquid (~35 kHz). The high frequency value (~5 MHz) was chosen to be larger than the dielectric relaxation frequency of the electrolyte in the drop used to perform the experiments (estimated to be in the hundreds kHz's) and to provide the best signal to noise ratio (in the MHz range the frequency response of the external electrical circuit can affect the signal reaching the tip-sample gap). The oscillation amplitude at the ω_{mod} frequency, $A_{\omega mod}$, was measured with the lock-in amplifier. The measured oscillation amplitude was converted to capacitance gradient values trough the relationship [30] $dC/dz = \alpha 8k\left(A_{\omega_{\mathrm{mod}}} - A_{\omega_{\mathrm{mod}},off}\right)\Big/ v_0^2 m$ where $A_{\omega_{\mathrm{mod}},off}$ is the lock-in offset, *k* the spring constant, *m* the photodiode sensitivity and α is a renormalization factor close to 1, which accounts for the potential losses in the electric circuitry due to the use of frequencies in the MHz range and to inaccuracies in the determination of the photodiode sensitivity and spring constant [30]. Raw data corresponding to the *dC/dz* curves reported in this chapter are shown in the Supplementary Information (Figure 31). We used HQ:NSC19/Cr-Au gold coated AFM probes (MikroMash) with a spring constant in the range 0.05 - 2.3 N/m, calibrated using Sader's method. Topographic and *dC/dz* images were acquired in the two-pass mode line by line, with the topography being recorded in conventional intermittent contact mode (with no potential applied) and the *dC/dz* image in constant height mode in off-feedback with the potential applied and with no mechanical oscillation applied. The tip-substrate distance in the electrical images was set larger than ~100 nm to ensure non-contact with the sample and to be safely larger than both the Debye screening length and the range of the van der Waals interaction, which were estimated to be at most ~20 nm from the approach curves. The image acquisition settings (set point, scan speed and gains) were chosen to optimize the electrical images rather than the topographic images, which in some cases produced topographic images with underestimated thicknesses.

As in previous works [12, 15, 20, 28, 29] approach curves (*N*=10) were measured on selected positions of the sample (typically on the bare substrate and on the centre of large membranes patches) to calibrate the tip geometry, determine the SDM imaging distances, the lipid bilayer specific capacitances and the substrate and tip interfacial capacitances. The approach speed of the approach curves was typically ~300 nm/sec. For each sample a large area image was first acquired, followed by one or two successive zoom-ins until the desired areas were identified. In these areas, electrical images at three different tip-substrate distances were acquired. Further imaging was prevented by tip contamination, probably enhanced by the applied electric potential.

4.2.3 Finite element numerical calculations

Finite element numerical calculations. We quantitatively analysed the *dC/dz* curves following the methodology applied in Refs. [12, 29], and earlier works, by solving the currents model implemented in the AC/DC Electrostatic module of COMSOL Multiphysics (Comsol Inc.). For frequencies beyond the dielectric relaxation frequency of the electrolyte, this model is equivalent to a quasi-static dielectric model (Poisson's model), and it correctly describes in-liquid SDM measurements [30, 197]. The probe was modelled as in previous works [12, 15], with the difference that an interfacial capacitance that takes into account ion adsorption, the reduced dielectric constant of water near a surface [33] and other interfacial effects was added to it as schematically shown in the inset of Figure 22 (d) [30]. Briefly, the tip consists of a conical tip of height *H* and half cone angle *θ* ended with a tangent sphere of radius R. The indirect cantilever contribution was included by adding a disc of thickness W and radius H tan(θ)+L, sitting on top of the cone as discussed in Ref. [189]. The interfacial capacitance around the tip was modelled by a physical dielectric layer of thickness d_{tip} and dielectric constant ε_{tip} ($c_{tip}=\varepsilon_0\varepsilon_{tip}/d_{tip}$). The use of a physical dielectric layer for the tip, rather than a distributed capacitance [28, 29], facilitates the integration of the Maxwell stress tensor to calculated the force, as discussed elsewhere [30]. In most calculations we kept fixed d_{tip}=2 nm and only varied ε_{tip}. The lipid bilayer patches were

modelled as a dielectric disc of radius R_m, thickness d_m and dielectric constant ε_m (corresponding to a specific capacitance $c_m=\varepsilon_0\varepsilon_m/d_m$). To represent the functionalized electrode interface, a distributed capacitance, $c_{sub,}$ was assumed on the substrate [29]. For the thicknesses of the lipid bilayers, the electric force acting on the tip only depends on their specific capacitance (as we see from the simulations reported in Figure 21).

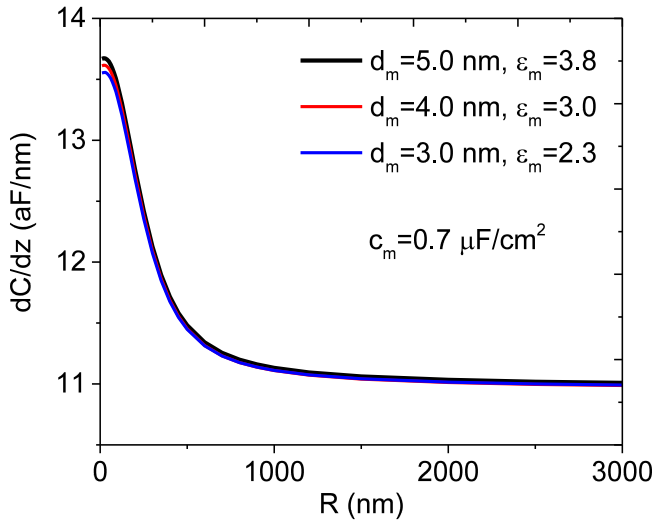

Figure 21: Dependence of the capacitance gradient as a function of the radius of the membrane patch for different values of the membrane thickness d_m and dielectric constant ε_m that correspond to the same value of the membrane specific capacitance c_m. For the range of thickness considered, the capacitance gradient is only dependent on the value of the membrane specific capacitance. The parameters of the simulations are the ones later extracted from the quantification of our experiments and reported in Table 1. Tip-sample distance, Z=101 nm.

The electric force acting on the probe was determined by integration of the Maxwell stress tensor over the conical part of the tip (integration on the cantilever was avoided to reduce the numerical noise). Direct cantilever effects were modelled phenomenologically through a constant offset, C'_{offset} [30]. Capacitance gradient approach curves were calculated by varying the tip-bilayer patch distance in the geometrical model, while capacitance gradient lateral membrane size dependent curves were obtained by keeping the distance fixed and varying the radius of the lipid bilayer patch.

Extraction of the specific capacitance of the lipid bilayer patches. To extract the specific capacitance of the lipid bilayer patches we followed a similar approach to the one detailed in Ref. [29], with the modifications discussed elsewhere [30] and introduced in the previous chapter. We calibrated the tip geometry using dC/dz curves on the metallic substrate, as in previous works [12, 15, 189]. Here, the fittings were done by keeping the half cone angle, cone height and cantilever thickness fixed to manufacturer values (H=12.5 μm, W=3 μm, θ=21º) and fixing the tip interfacial capacitance within the range c_{tip}~2-4 μF/cm^2. [30] The voltage reduction factor, α, was fixed from the long-range part of the dC/dz curve to give the set half cone angle [30]. Their values were very close to one (α=1-1.02). The cantilever length was kept to L=3 μm, which is a reasonable value to include indirect effects with a disc cantilever model [189]. The result of the fitting process provided the tip radius, R, the substrate interfacial capacitance, c_{sub} and the capacitance gradient offset, C'_{offset}. With the obtained parameters, we calculated capacitance gradient approach curves on the lipid bilayer patch with radius, R_m, and thickness, d_m, and fitted them to the experimental approach curve measured on the centre of the lipid bilayer patches, with the dielectric constant of the membrane, ε_m, as the single fitting parameter. As mentioned above, for the lipid bilayer thicknesses (< 10 nm) the fittings were sensitive to only the lipid bilayer specific capacitance, c_m, which is the value we reported. The analysis was done with a custom-made software written in Matlab (Mathworks inc.) linked to the COMSOL Multiphysics software.

4.3 Results: specific capacitance of sub-100 nm lipid bilayer patches

Figure 22 (a) shows an Atomic Force Microscopy (AFM) topographic image of DOPC bilayer patches supported on a flat gold substrate functionalized with 2-Mercaptoethanol in Milli-Q water.

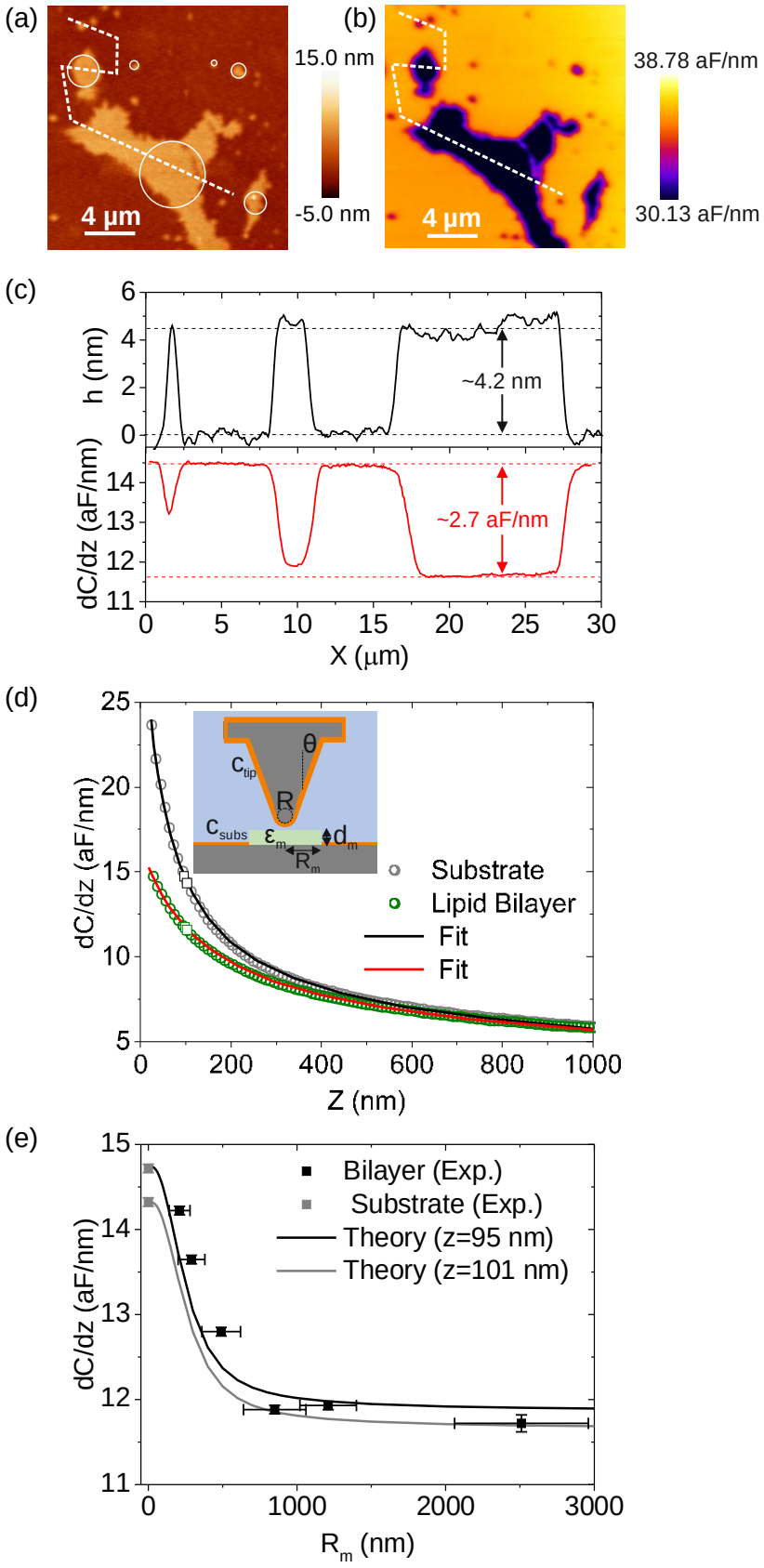

Figure 22: (a) AFM topographic and (b) in-liquid SDM dielectric images, respectively, of DOPC bilayer patches on a functionalized planar gold substrate in Milli-Q water. In-liquid SDM experimental parameters: equivalent spring constant 0.45 N/m, applied voltage amplitude 0.75 V, frequency 5 MHz,

modulation frequency 6 kHz, tip-sample distance Z=101 nm. (c) Height (black line) and capacitance gradient (red line) profiles along the dashed lines in (a) and (b), respectively. (d) Capacitance gradient approach curves measured on the bare substrate (grey circles) and on the centre of the largest DOPC patch (olive circles). Continuous lines represent a least square fitting of theoretical curves calculated with the model shown in the inset to the experimental data. The extracted parameters are listed in Table 1. The black and olive square symbols correspond to the capacitance gradient values on the substrate and centre of the largest DOPC bilayer patch in (b), respectively, from where the tip sample distance is obtained. (e) (black symbols) Capacitance gradient values measured on the centre of the DOPC bilayer patches in (a) as a function of the effective patch radius (defined from the circles in (a)). The grey symbols represent representative values on the substrate. (continuous lines) Theoretical dependence of the capacitance gradient as a function of the radius of the DOPC bilayer patch obtained with the model in the inset in (d). The parameters used in the calculations are those obtained from (d) and listed in Table 1 for DOPC.

The DOPC bilayer patches have been formed from the deposition of the respective DOPC liposomes (see Materials and Methods). A height profile measured along the dashed line in Figure 22 (a) is shown in Figure 22 (c) (black line). The membrane patches along the profile are ~4.2 nm thick (see also histogram analysis in Figure 23).

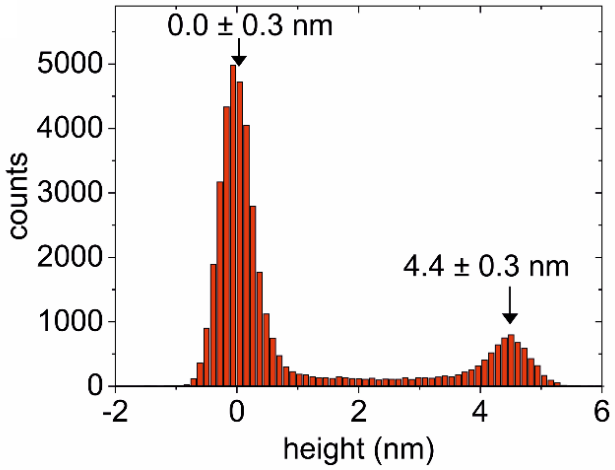

Figure 23: Histogram analysis corresponding to the topographic image in Figure 22 (a). Note that the imaging acquisition settings have been selected to optimize the electrical imaging, not the topography.

This value is in agreement with thickness values reported for solid supported DOPC patches by AFM [258] (~4.2 nm) and quantitative Differential Interference Contrast Microscopy (qDIC) [259] (~4.1 nm), and slightly smaller than the steric thickness measured on unilamellar vesicles by

Small Angle Neutron Scattering (SANS) or Small Angle X-Ray Scattering (SAXS) [260, 261] (~5 nm). The lateral sizes of the patches range from few micrometres down to ~200 nm.

Figure 22 (b) shows an in-liquid SDM image of this sample obtained at 5 MHz in constant height mode at a height *Z*=101 nm (see Materials and Methods for details and the Additional Information section for images at different tip-substrate distances). It shows variations of the electric force, represented here through the capacitance gradient, dC/dz (see above, Refs. [12, 28] and Materials and Methods). The in-liquid SDM image reveals the presence of the DOPC bilayer patches down to lateral sizes ~200 nm. The contrast in the SDM image shows an excellent signal-to-noise ratio (up to ~2.7 aF/nm signal for a noise floor of ~0.05 aF/nm, see capacitance gradient cross section profile in Figure 22 (c), red line). This excellent contrast has been achieved by enlarging on purpose the tip radius by scratching the tip on a bare clean substrate prior to its use. The contrast in the SDM image is negative indicating that the dielectric constant of the bilayer patches is smaller than that of the electrolyte solution surrounding them, similarly to what observed earlier for DPPC bilayer patches on highly doped silicon substrates [29].

The quantitative extraction of the specific capacitance of the bilayer patches has been done by measuring capacitance gradient, dC/dz, versus distance curves on the bare substrate and on the centre of the largest membrane patch (grey and olive circles in Figure 22 (d), respectively), and by fitting to them theoretical capacitance gradient approach curves numerically calculated with the model in the inset of Figure 22 (d), following procedures developed in previous works (see Materials and Methods). Here, in the model we included an interfacial capacitance to the tip, c_{tip}, necessary when dealing with metallic substrates to account for the adsorption of ions, the reduced dielectric constant of interfacial water [33] and other interfacial effects (see Materials and Methods for further details). The fitted curves are shown by continuous lines in Figure 22 (d), and the parameters extracted are summarized in Table 1 for two characteristic values of the tip interfacial capacitance, namely, c_{tip}=2 μF/cm^2 and 4 μF/cm^2 . [30] The fittings have been made down to distances ~20 nm. Below this distance

other interactions due to van der Waals forces or the presence of diffusive space charge layers may enter into play, which are not included in the theoretical model. The agreement between the theoretical and the experimental curves is excellent. The specific capacitance of the DOPC bilayer patch obtained is c_{DOPC}~0.7-0.8 μF/cm^2, which is in reasonable agreement with values reported for similar lipid bilayers measured free from solvent contributions by means of macroscopic techniques [249]. We remark that while the interfacial capacitance of the substrate depends strongly on the chosen tip interfacial capacitance [30], the specific capacitance of the lipid bilayer is almost insensitive to it.

Table 1: Specific capacitance of the lipid bilayer patches obtained from the analysis of the experimental data in Figure 22 (d) and Figure 25 (d). The parameters of the tip geometry and substrate obtained from the same analysis are also shown. The parameters without errors are fixed.

c_{tip} μF/cm^2	c_{DOPC} μF/cm^2	$c_{DOPC:chol}$ μF/cm^2	$c_{substrate}$ μF/cm^2	R nm	C'_{offset} aF/nm	θ deg
DOPC						
2	0.8+0.1	-	3.1+0.1	370±25	0.78±0.05	21
4	0.7+0.1	-	1.9+0.1	351±25	0.71±0.05	21
DOPC and DOPC:cholesterol						
2	1.0+0.1	0.7+0.1	2.1+0.1	310±25	1.10±0.05	21
4	0.9+0.1	0.6+0.1	1.5+0.1	287±25	1.06±0.05	21

We note a feature that was also observed in Ref. [30], namely, that the capacitance gradient (force) contrast in Figure 22 (b) shows a remarkable dependence on the lateral size of the membrane patches (see also cross-section profile in Figure 22 (c), red line). This dependence is illustrated in Figure 22 (e), where we plot the capacitance gradient values on the centre of each DOPC bilayer patch as a function of the patch equivalent radius, R_m (symbols). The

equivalent radius has been estimated from circles centred on the patches as shown in Figure 22 (a). The uncertainty in the radii is displayed in the figure below (Figure 24).

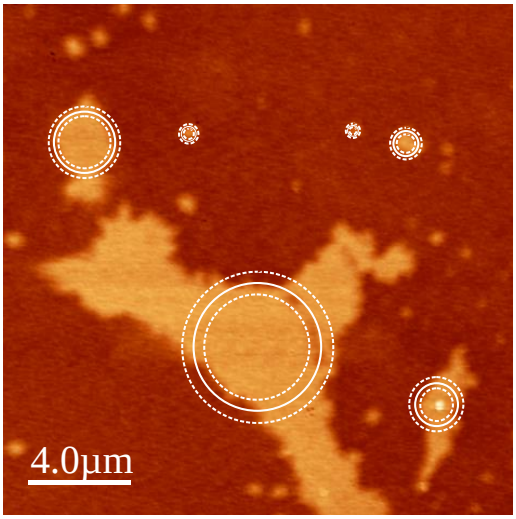

Figure 24: Radii estimation (continuous circles) and uncertainty (dashed circles) for the patches analysed in Figure 22 (e).

For reference, we also display in Figure 22 (e) characteristic values of the capacitance gradient on the substrate (grey symbols). There are two factors that can induce a dependence of the capacitance gradient on the lateral size of the patches, namely a finite-size electrostatic effect related to the relative size of the patch with respect to the scanning probe tip and a variation of the specific capacitance of the patches with their width. To answer this question, we have calculated the theoretical expected variation of the capacitance gradient as a function of the radius of the DOPC bilayer patch by using the model shown in the inset of Figure 22 (d). In the simulations, we used the parameters derived from the quantitative analysis performed on the largest patch (Table 1), with no further free parameter. The results are shown in Figure 22 (e) (continuous lines) for two tip-substrate distances compatible with the measurements, Z=95 nm and Z=101 nm (the different distances account for the slight tilting of the image and the fact that the static bending of the cantilever when the tip is on top of the largest patch is smaller than when on the smaller patches or the substrate). The numerical calculations nicely follow the experimental trend, within the uncertainty of the experiments. We therefore conclude

that down to the smallest patches detected (~200 nm), the specific capacitance of DOPC bilayer patches does not depend on its lateral size, although the measured capacitance gradient strongly depends on it. For DOPC bilayer patches larger than a few micrometres the force becomes independent from the lateral size of the patches (see Figure 22 (e)), and it can be directly correlated to the membrane specific capacitance (a larger force directly indicates a smaller specific capacitance). Otherwise, lateral finite size effects, which originates in the tip-sample electrostatic interaction, should be considered. Remarkably, lateral finite-size effects in in-liquid SDM [30] are much larger (micrometres) than those found in air [187] due to the stronger contribution of the cone part of the tip.

We analyse now the effect of cholesterol on the specific capacitance of the supported DOPC bilayer patches. We prepared a sample containing both DOPC and DOPC:chol bilayer patches by successive depositions of the corresponding liposomes (see Materials and Methods).

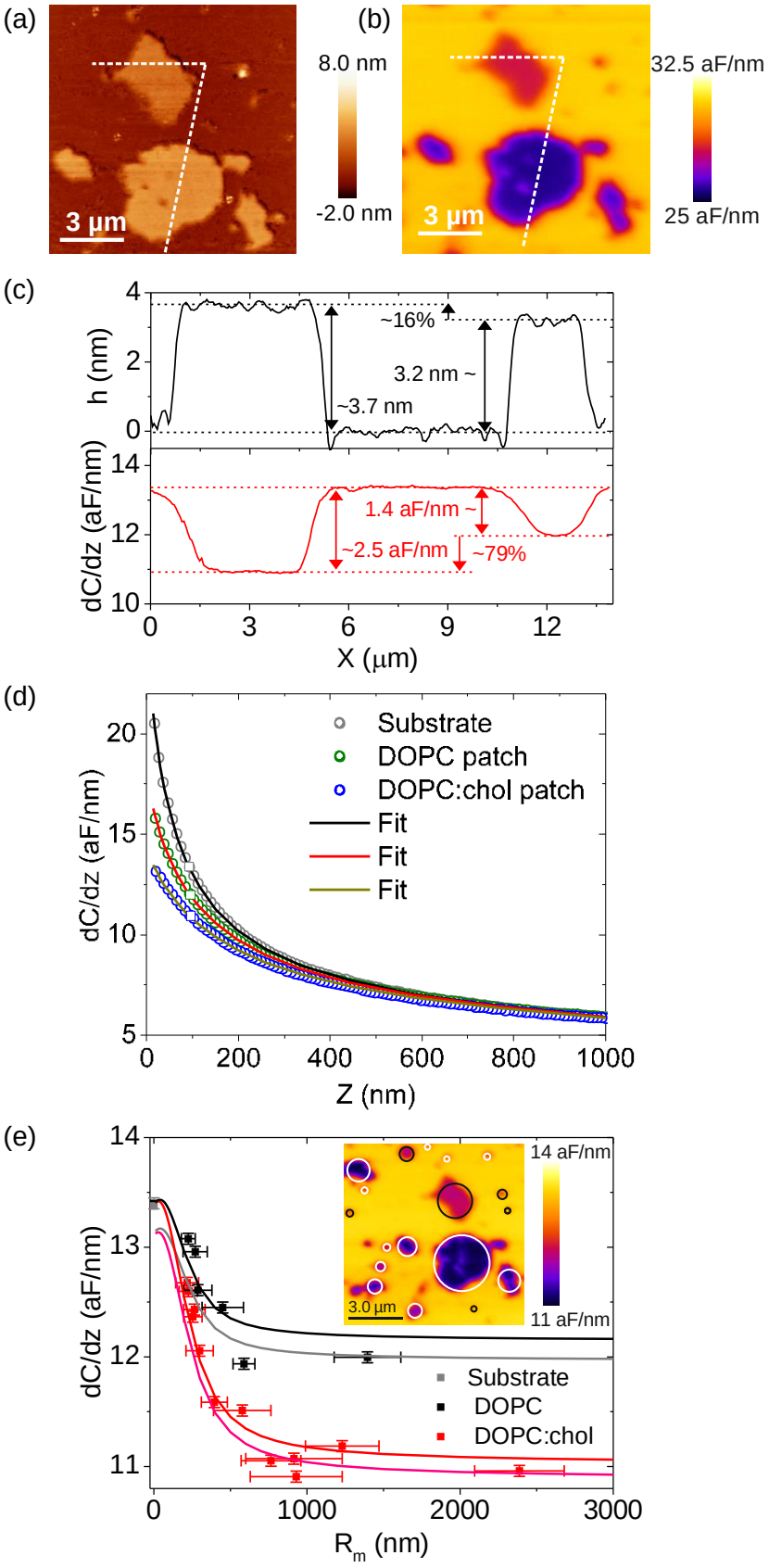

Figure 25: (a) AFM topographic and (b) SDM images of a sample containing DOPC and DOPC:cholesterol bilayer patches in a 1 to 1 proportion supported on a functionalized planar gold substrate in Milli-Q water. SDM experimental parameters: equivalent spring constant 0.45 N/m, applied

voltage 0.75 V, frequency 5 MHz, modulation frequency 6 kHz, tip-sample distance Z=93 nm. (c) Thickness (black line) and capacitance gradient (red line) profiles along the dashed lines in (a) and (b), respectively. (d) Capacitance gradient approach curves measured on the bare substrate (grey symbols) and on the two largest patches in (b) (olive and blue symbols, respectively). Continuous lines represent least square fitting of theoretical data generated with the model in the inset in Figure (d). Extracted parameters are shown in Table 1. The grey, olive and blue square symbols correspond to the values of the capacitance gradient on the substrate and the two largest membrane patches of the SDM image in (b), from where the tip sample distance is obtained. (e) (symbols) Capacitance gradient values on the centre of the DOPC bilayer patches highlighted in the large area in-liquid SDM image in the inset as a function of the effective radius of the patches. Symbols of the same colour correspond to patches with similar thickness. (continuous lines) Theoretical dependence of the capacitance gradient as a function of the radius of the DOPC bilayer patch obtained from the model in the inset in Figure (d). The parameters used in the calculations are those obtained in (d) and listed in Table 1 (DOPC and DOPC:cholesterol). The black and red lines correspond to tip sample distances Z=91 nm, while the grey and pink lines to Z=95 nm, compatible with the measurements.

Figure 25 (a) shows a topographic AFM image of the sample. A height profile measured along the dashed line in Figure 25 (a) is shown in Figure 25 (c) (black line). In it, two groups of membrane patches with slightly different thicknesses, ~3.2 nm and ~3.7 nm, are observed (as we also see in the histogram analysis below (Figure 26).

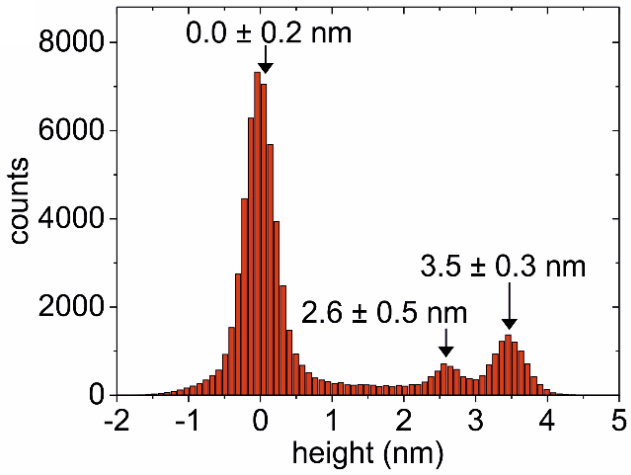

Figure26: Histogram analysis corresponding to the topographic image in Figure 25 (a). Once again, the imaging acquisition settings have been selected to optimize the respective electrical images, not the topographic images. Therefore, the actual thickness values can be affected by them.

The presence of patches with two different thicknesses agrees with the sample being prepared from liposomes with and without cholesterol, and with the fact that cholesterol is known to thicken DOPC bilayers [260, 261, 262, 263, 264] . Here, we observe a thickening of around ~16% (Figure 25 (c), black line), which is in reasonable agreement with the thickening predicted for DOPC bilayers at 40%-50% cholesterol content (~13%-19%) [260, 261, 264] . The thicker membrane patches are, then, expected to be composed of DOPC:cholesterol (see further confirmation below). We note that the absolute value of the thickness of the DOPC patches in Figure 25 is somewhat smaller (~1 nm) than the one reported in Figure 22. We attribute it to the fact that the imaging acquisition settings for mixed samples were different from those of pure samples and that they have been selected to optimize the electrical images. Therefore, the height values in these images could be somewhat underestimated, although the relative height difference between DOPC and DOPC:cholesterol patches seems to be correct. The widths of both types of patches span again a range from ~200 nm up to few micrometres. An additional and even larger area image of the sample was also acquired, and it is displayed here below (Figure 27), together with the estimation of the uncertainties in the determination of the respective equivalent radii.

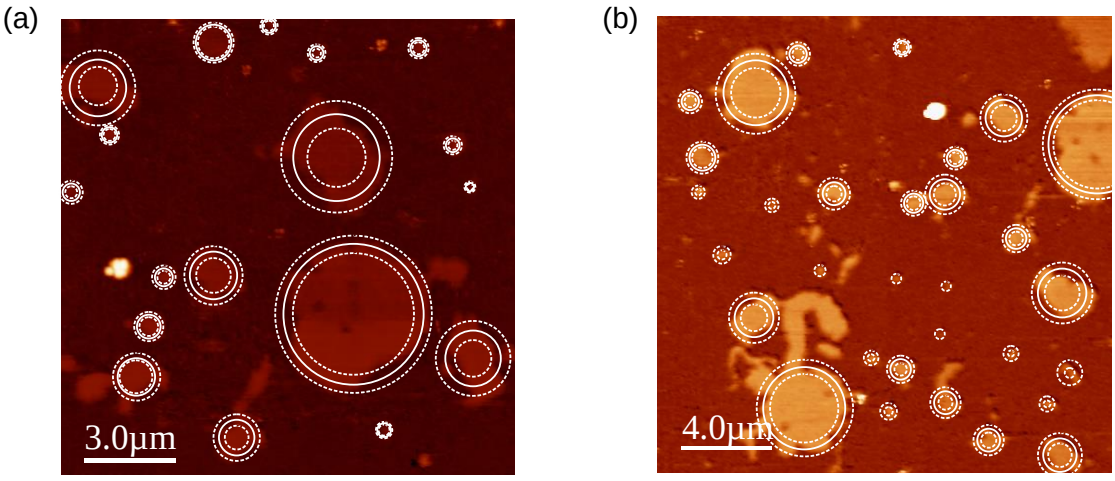

Figure 27: (a) Radii estimation (continuous circles) and uncertainty (dashed circles) for the patches analysed in [Figure 25 (e)], and in an additional and even larger area image (b).

Figure 25 (b) shows a constant height in-liquid SDM image of the sample in Figure 25 (a) acquired at 5 MHz and *Z*=93 nm (see Additional Information section for images at different tip-substrate distances). The dielectric contrast is again negative for all patches, and patches down to ~200 nm can be electrically detected. The more relevant feature displayed in Figure 25 (b) is the large difference (~79 %) in the dielectric contrast observed between the two largest patches in the image (see capacitance gradient profile in Figure 25 (c), red line). This large contrast variation should be compared with the small relative variation in thickness (~16%, Figure 25 (c), black line). Therefore, it cannot be fully attributed to the thickening effect. It cannot be attributed neither to a difference in the lateral size of the patches, since both patches are few-micrometre large and, hence, their capacitive signals are independent from the lateral size of the patches, as discussed above. Therefore, the large difference in the dielectric contrast must reflect a variation in the dielectric properties of the DOPC lipid bilayer due to the presence of cholesterol.

To investigate this effect, we have quantified the specific capacitances of the two largest lipid bilayer patches in Figure 25 (a) by acquiring capacitance gradient approach curves on their centres and on the bare substrate by proceeding as described above (Figure 25 (d)). The parameters obtained from this analysis are shown in Table 1. The relative difference between the specific capacitance of the DOPC bilayer patches without and with cholesterol (c_{DOPC}~0.9 μF/cm^2 and $c_{DOPC:chol}$~0.6 μF/cm^2, respectively) is ~35%, much larger than the observed thickness variation (~16%), thus confirming that cholesterol reduces the dielectric response of the DOPC bilayer patches (see discussion section).

The conclusions reached for the two largest patches in Figure 25 (a) are confirmed for the sub-micrometric lipid bilayer patches present in the sample.

Figure 25 (e) shows the capacitance gradient measured at the centre of patches in the figure in the inset of Figure 25 (e), which is a zoom out of Figure 25 (b).

Patches ranging from ~200 nm up to several micrometres are considered. The thinner patches (DOPC) are represented by the black symbols and surrounded with a white circle in

the inset of Figure 25 (e), while the thicker ones (DOPC:cholesterol) are represented by the red symbols and surrounded by a black circle. Two distinct dependencies are clearly observed for the two groups of patches. Finite element numerical calculations (continuous lines in Figure 25 (e)) show that each group of patches can be described by a single specific capacitance, corresponding to the values reported in Table 1. These results confirm that down to ~200 nm the lateral size does not affect the value of the specific capacitance of the DOPC:cholesterol bilayer patches, like we showed above and here again for DOPC bilayer patches, and that the thicker patches (DOCP/cholesterol) show a much lower specific capacitance than thinner ones (DOPC). A similar analysis for the SDM image of the larger area in Figure 27 (b), combined with the one of the previous (Figure 25 (e), inset) is provided in Figure 28.

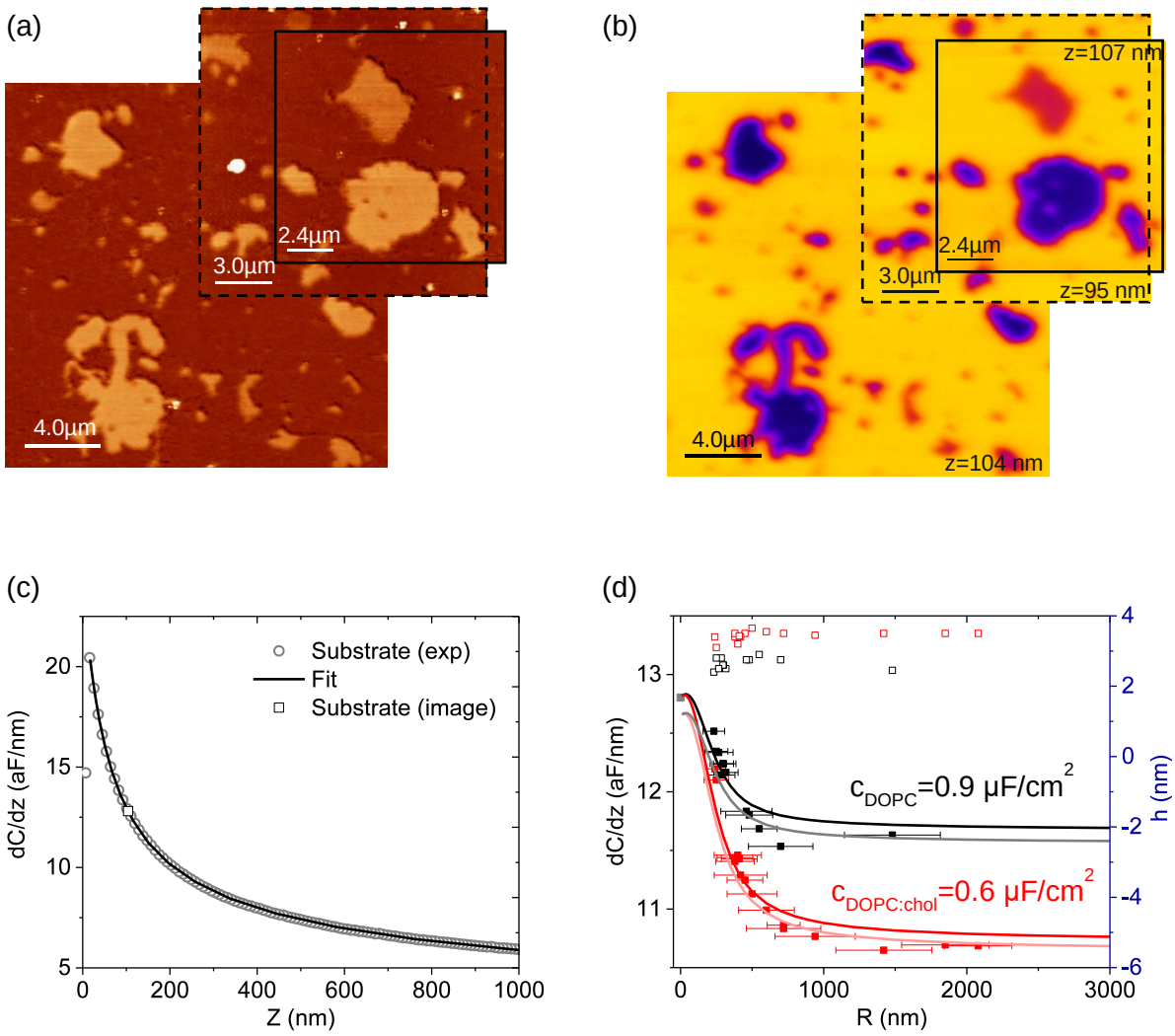

Figure28: (a) Composed AFM topographic image of three regions of the DOPC and DOPC:cholesterol mixture sample. The region bound by a continuous line is the one shown in Figure 25 (a) and the region bound by a dashed line is the one analysed in Figure 25 (e). The rest of the composed image is analysed in (d). (b) Composed in-liquid SDM images corresponding to the composed image in (a). Each image has been acquired at the same nominal distance (Z~100 nm). The actual distance of each image has been more precisely determined from the capacitance gradient approach curves acquired on the bare substrate of each image (Figure 25 (d) grey symbols and curve in (c), giving slight differences with the nominal distance (~±5 nm). Continuous and dashed frames have the same meaning as in (a). (c) (grey circles) Capacitance gradient approach curve taken on a bare part of the substrate of the non-framed image in (a). (continuous line) Theoretical fit of the experimental curve. The extracted parameters are: R=277±20 nm, θ=21°, c_{tip}= 4 µF/cm², $c_{substrate}$=1.6 µF/cm², C'_{offset}=1.00 ±0.05 aF/nm, α=1.067. (d) (Left axis, solid symbols) Capacitance gradient at the centre of the patches surrounded by circles in Figure 27(b) as a function of the equivalent radius of the membrane patches. Black and red symbols represent the thin (DOPC) and thick (DOPC:cholesterol) patches, respectively. (Left axis, continuous lines). Theoretical dependence of the capacitance gradient as a function of the membrane patch radius. The calculations have been done with the parameters obtained from (c) and the specific capacitance values

of the bilayers reported in Table 1. Two tip sample distances have been considered Z=104 nm (black and red lines) and Z=108 nm (grey and pink lines). (Right axis, empty symbols). Height of the patches analysed. As before black and red symbols represent the thin (DOPC) and thick (DOPC:cholesterol) patches, respectively.

To further confirm that thicker bilayer patches correspond to those containing cholesterol, we have considered an additional sample prepared by reducing by a factor of three the concentration of DOPC:cholesterol liposomes in the solution (so that we expect DOPC:cholesterol bilayer patches to be much less abundant than DOPC ones). Figure 29 (a) and (b) show, respectively, large area AFM topographic and in-liquid SDM images obtained on this sample.

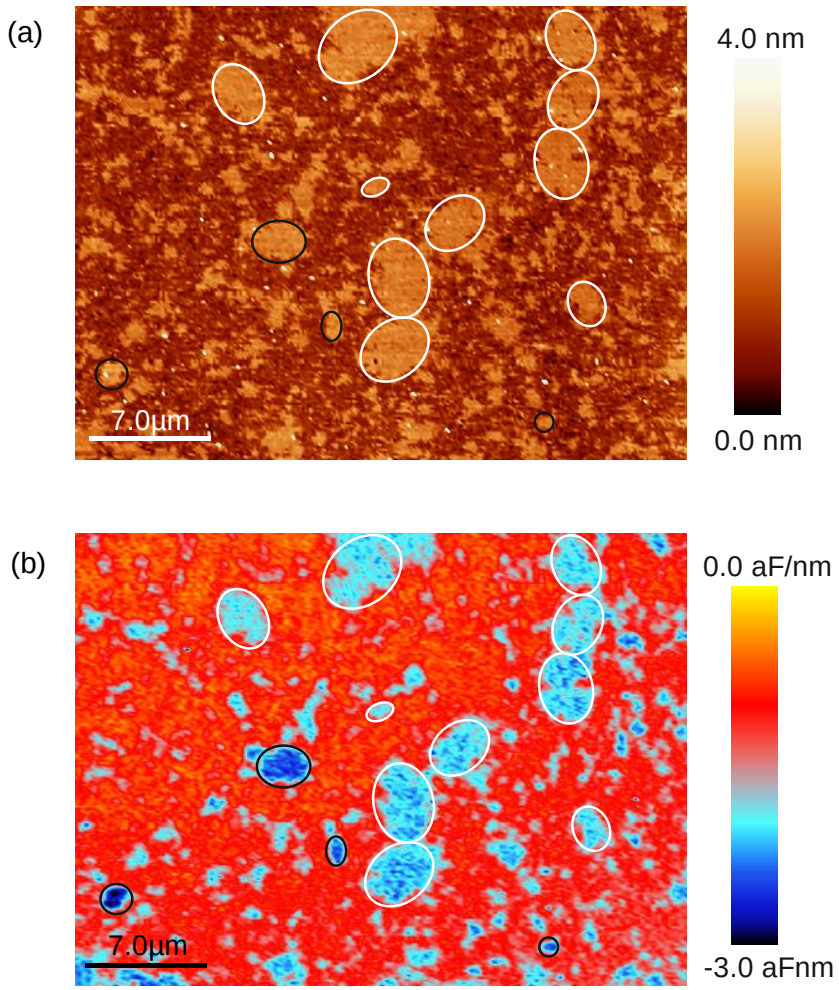

Figure 29: (a) AFM topographic and (b) in-liquid SDM dielectric images of a sample containing DOPC and DOPC:cholesterol membrane patches in a 3:1 proportion on a functionalized planar gold substrate in Milli-Q water. SDM experimental parameters: equivalent spring constant 0.76 N/m, applied voltage

0.75 V, frequency 5 MHz, modulation frequency 6 kHz and tip-sample distance Z=11 nm. In (a) and (b) black and white circles identify thicker and thinner patches with supra-micrometric sizes (>1 μm), respectively. The colour scale is different from that of Figure 22 and Figure 25 and it has been chosen to highlight the difference in contrast between the two type of patches for this sample.

As before, in the topographic image (Figure 29 (a)) two groups of patches with different thicknesses can be identified from a careful analysis (see also histogram analysis in the figure below (Figure 30)).

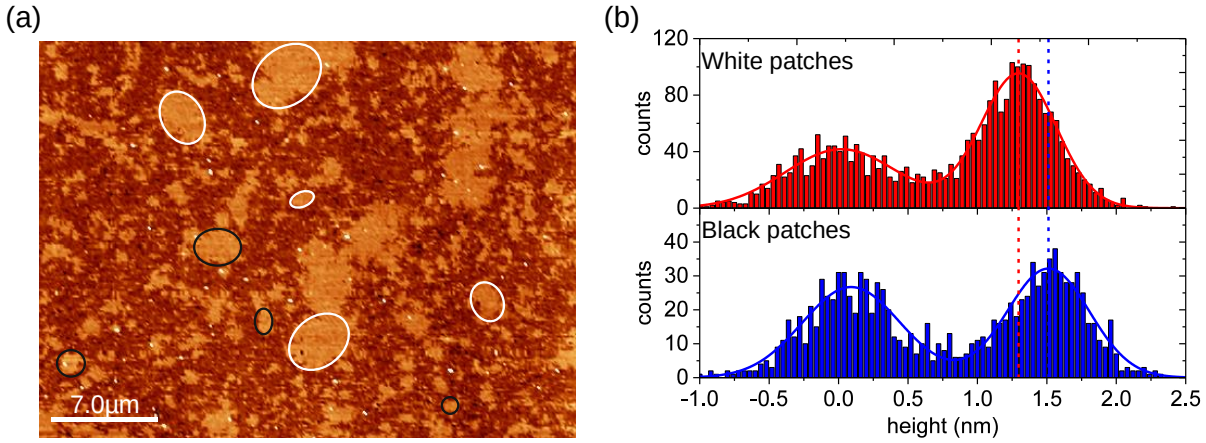

Figure 30: (a) Topography, same as Figure 29 (a), with some selected patches giving different dielectric contrast: white circled patches give low contrast and black ones, high contrast. (b) Histogram analysis of the heights of the selected patches. The peaks at around 0 nm correspond to the substrate regions. The black circled patches systematically give larger thicknesses. The absolute values of the thicknesses are not accurate since for this large area scan the imaging settings required to obtain a good electrical image imposed a too high set point for the topographic image.

We marked with white and black circles the thin and thick patches, respectively (only supra-micrometric patches have been analyzed). Thicker patches are clearly much less abundant, what by taking into account the sample composition, confirms that they correspond to DOCP:cholesterol composition.

The in-liquid SDM image (Figure 29 (b)) shows also two distinct contrasts for the patches analyzed. The thicker patches (black circles corresponding to DOCP:cholesterol) show larger contrasts, indicating that they have a smaller specific capacitance (remember that for large

patches the SDM contrast can be correlated directly to the specific capacitance of the patch). These results then unambiguously confirm that DOPC:cholesterol bilayer patches show a strong reduction of the specific capacitance as compared to pure DOPC bilayer patches.

4.4 Discussion

We have found that cholesterol at a 50% concentration largely reduces (by an amount ~35%) the specific capacitance of DOPC bilayer patches. This reduction cannot be attributed to the slight increase in the bilayer thickness (~16%). According to the simple expression for the specific capacitance, $c_m=\varepsilon_0\varepsilon_m/d_m$, the relative variation in specific capacitance due to both thickness and dielectric constant variations is given by $\Delta c_m/c_m=\Delta\varepsilon_r/\varepsilon_r-\Delta h/h$. Since the thickness variation amounts to only $\Delta h/h$ ~16%, the remaining variation should correspond to a decrease of the dielectric constant of the lipid bilayer caused by the presence of cholesterol, $\Delta\varepsilon_r/\varepsilon_r$ ~ -20%. A possible explanation of the reduction in the dielectric constant observed can be attributed to a reduction of the hydration level of the DOPC bilayers containing cholesterol. To support this statement we calculate the dielectric constants of the DOPC and DOPC:cholesterol patches and compare them with the corresponding values obtained earlier in air environment by using the same technique [21]. By taking the measured bilayer thickness from Figure 25 (d_{DOPC} ~3.2 nm) and the measured specific capacitance (c_{DOPC}~0.9 μF/cm^2), the dielectric constant of pure DOPC bilayers in Milli-Q water is $\varepsilon_{DOCP,liq}$~3.2 (a similar value is also obtained from the measurement in Figure 22, in which the thickness was ~4.5 nm and the specific capacitance ~0.7 μF/cm^2). This value matches the one we obtained earlier with the same technique on DPPC bilayer patches in liquid, $\varepsilon_{DPPC,liq}$~3.2 [29], and is larger than the value $\varepsilon_{DOCP,dry}$~2 measured in dry air conditions [21]. The larger dielectric constant observed in liquid environment was attributed to the hydration of the polar head groups of the lipid bilayers [29]. For the DOPC:cholesterol patches, instead, by using a thickness $d_{DOPC:chol}$ ~3.7 nm and a specific capacitance $c_{DOPC:chol}$~0.6 μF/cm^2, the dielectric constant obtained in liquid is $\varepsilon_{DPPC:chol,liq}$ ~2.5. This value is similar to the values obtained for DOPC bilayer patches and cholesterol

crystals in dry conditions ($\varepsilon_{DOCP,dry}$~2 and $\varepsilon_{chol,dry}$~2.3) [21]. This result suggests that at 50% chol content DOPC:cholesterol patches are hardly hydrated, contrary to what happens with pure DOPC patches. The reorganization of the head groups in the presence of cholesterol necessary to achieve a non-hydrated configuration is the same than the one assumed in the so-called umbrella model, used to explain the solubility of cholesterol in lipid bilayers [265] and other properties [241].

On the other hand, we note that the specific capacitances of DOPC bilayer patches reported here, and their variation with cholesterol, are in striking agreement with recent results reported for supported DMPC+DMTAP bilayers with and without cholesterol and obtained from macroscopic electrochemical impedance spectroscopy [247] with strict control of bilayer quality (e.g. absence of bilayer defects and of solvent).

The use of in-liquid SDM in force detection mode has shown relevant advantages in the present study as compared to current/voltage time varying macroscopic techniques [243]. First, in-liquid SDM displays a high spatial resolution [30], what enables studying isolated lipid bilayer patches, with no need to consider extended defect-free lipid bilayers, required for macroscopic measurements. Second, it enables comparing directly the specific capacitances of different bilayer patches with different composition *in situ* and under the same experimental conditions, reducing uncertainties related to successive independent measurements. In-liquid SDM also provides direct access to the bilayer thickness, thus enabling identifying whether a specific capacitance variation is associated with either a thickness or a dielectric constant variation. Finally, in-liquid SDM measurements are performed at high frequencies in the MHz range (beyond the dielectric relaxation frequency of the electrolyte solution). In this frequency range, the capacitance contribution associated to ionic diffusive space charges can be neglected [30], what simplifies the quantitative analysis. For measurements performed at lower frequencies (e.g. below kHz, as in the case of most existing macroscopic techniques [249]), the diffusive space charge capacitance needs to be accounted for and subtracted from the measurements,

which is not always simple and can introduce some inaccuracy and variability in the values thus obtained, depending on the assumptions made.

Concerning the accuracy of the specific capacitance values obtained for supported lipid bilayers by in-liquid SDM some considerations are in order. The electric force measured by the in-liquid SDM probe depends on the whole system capacitance gradient, which includes contributions from the tip-electrolyte interface, the electrolyte, the electrolyte-membrane-substrate interface, and the electrolyte-substrate interface. The bulk electrolyte contribution is accounted for by solving the Poisson's equation for the tip-sample system with realistic and calibrated tip and sample geometries. The tip-electrolyte interfacial contribution at the frequencies of the measurements (MHz) is expected to include only effects from the so-called compact or Stern layer, $c_{tip}=c_{int,tip}$ [30]. The substrate-electrolyte interface, instead, includes contributions from both the functionalization self-assembled monolayer, c_{SAM}, and its interface with the electrolyte, $c_{int,SAM}$, i.e. $c_{substrate}=(c_{SAM}^{-1}+c_{int,SAM}^{-1})^{-1}$. Finally, the electrolyte-membrane-substrate interface includes contributions from the self-assembled monolayer on the substrate, c_{SAM}, the lipid bilayer itself, c^*_m, and the interfacial lipid bilayer-electrolyte compact layer, $c_{int,m}$, i.e. $c_m=(c_{SAM}^{-1}+c_{int,m}^{-1}+c^{*}_{m}{}^{-1})^{-1}$. Since the functionalization SAM used here is very short (two carbons) and the compact layer is usually also very short (a few water layers) we expect that their respective specific capacitances will be much larger than the specific capacitance of the lipid bilayer, so that the measured values, c_m, are expected to be good estimations of the lipid bilayer specific capacitance, c_m^* ($c_m \sim c_m^*$). Finally, we note that the uncertainty in the value of the tip interfacial capacitance, c_{tip}, (c_{tip}=2-4 μF/cm^2) [30], introduces a minor uncertainty on the specific capacitance values of the lipid bilayer patches, c_m, as it can be seen in Table 1. The uncertainty is larger for the value of $c_{substrate}$ since it is of the same order of magnitude than c_{tip}, as discussed elsewhere [30]. Other substrate effects such roughness (rms~0.2-0.3 nm in the present study) or a reduction of the lipid lateral mobility (which involve diffusion times much longer than the period of the ac voltage) are not expected to affect the extracted values of the bilayer specific capacitances.

In the present work we have compared the specific capacitance of mixed samples containing pure DOPC and DOPC:cholesterol bilayer patches at a fairly large cholesterol concentration (50%), close to the cholesterol solubility limit. The relative variation measured (~35%) is expected to be close to the maximal relative variation that can be found with solubilized cholesterol. For smaller cholesterol concentrations a smaller relative variation of the specific capacitance is expected according to the monotonous trend with cholesterol concentration shown by other physical properties (e.g. thickness, bending rigidity or area per lipid) in DOPC bilayers [261, 264]. Preparing mixed samples containing patches with several intermediate cholesterol concentration by the successive liposome deposition method used here has been found challenging, and further research to find alternative sample preparation methods becomes necessary to explore simultaneously several intermediate cholesterol concentrations by SDM.

The results presented in this work open interesting applications in the analysis of natural membranes, which are highly heterogeneous composition and structure [55, 266], as well as, to address the electrical properties of small scale biomembrane structures such as exosomes [267], outer membrane vesicles [268] or membrane nano-extensions, some of which show especial electric properties [269].

4.5 Conclusions

We have shown by means of in-liquid Scanning Dielectric Microscopy in force detection mode that cholesterol at 50% concentration strongly reduces the specific capacitance of supported DOPC bilayer patches. The reduction observed (~35%) is partially due to a small increase in the membrane thickness (~16%), but, overall, to a significant reduction in the dielectric constant of the lipid bilayer itself (~20%). The reduction of the dielectric constant of the DOPC:cholesterol bilayer patches could be associated to the dehydration of the polar head groups caused by the presence of cholesterol molecules. This conclusion has been observed to hold for lipid bilayer patches down to, at least, ~200 nm in lateral size. The results presented

here have confirmed the potential of in-liquid SDM to measure the specific capacitance of artificial and natural biomembranes at high spatial resolution with important implications in biology, biochemistry or biosensor characterization.

4.6 Supplementary Information

Raw data for the capacitance gradient approach curves in Figure 22 and Figure 25.

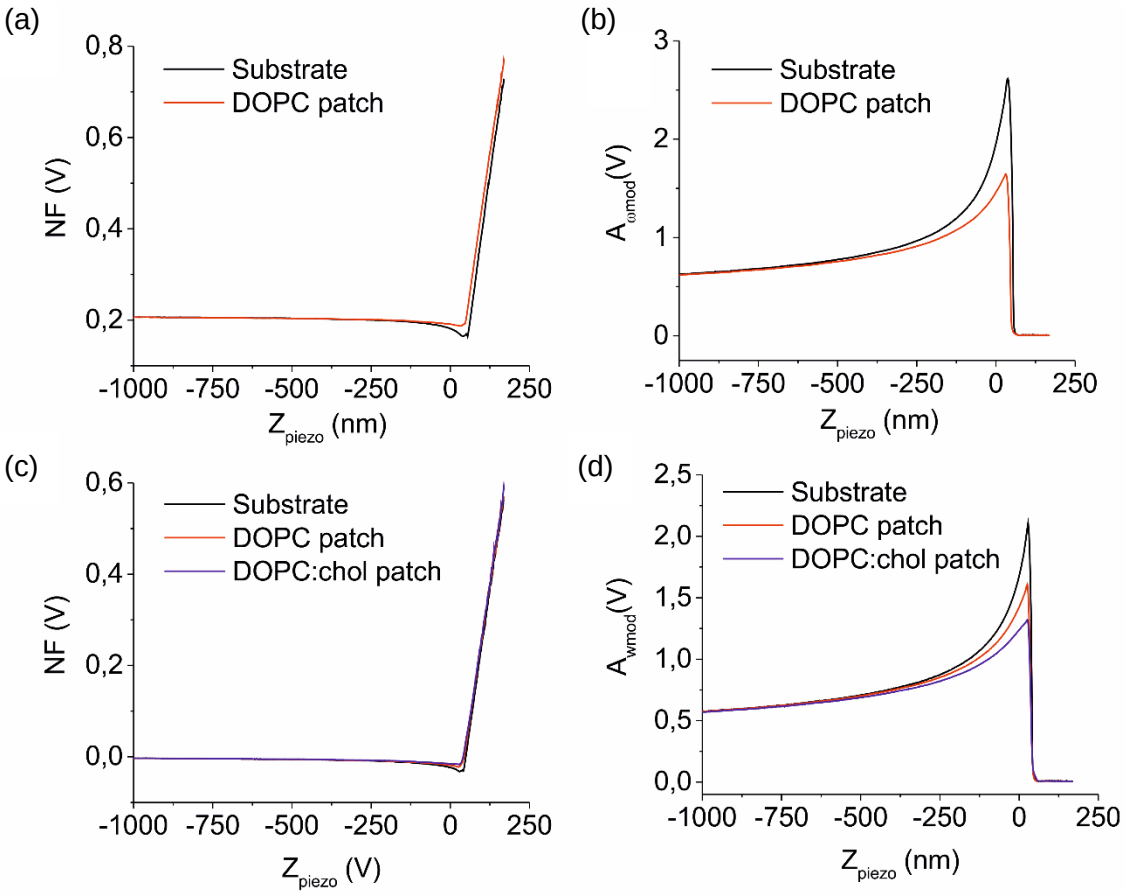

Figure 31: Raw data for the normal deflection and oscillation amplitude at the ω_{mod} harmonic approach corresponding to the capacitance gradient approach curves shown in Figure 22 (d) [(a) and (b)] and Figure 25 (d) [(c) and (d)].

Additional SDM images for Figure 22 and Figure 25 at different tip sample distances.

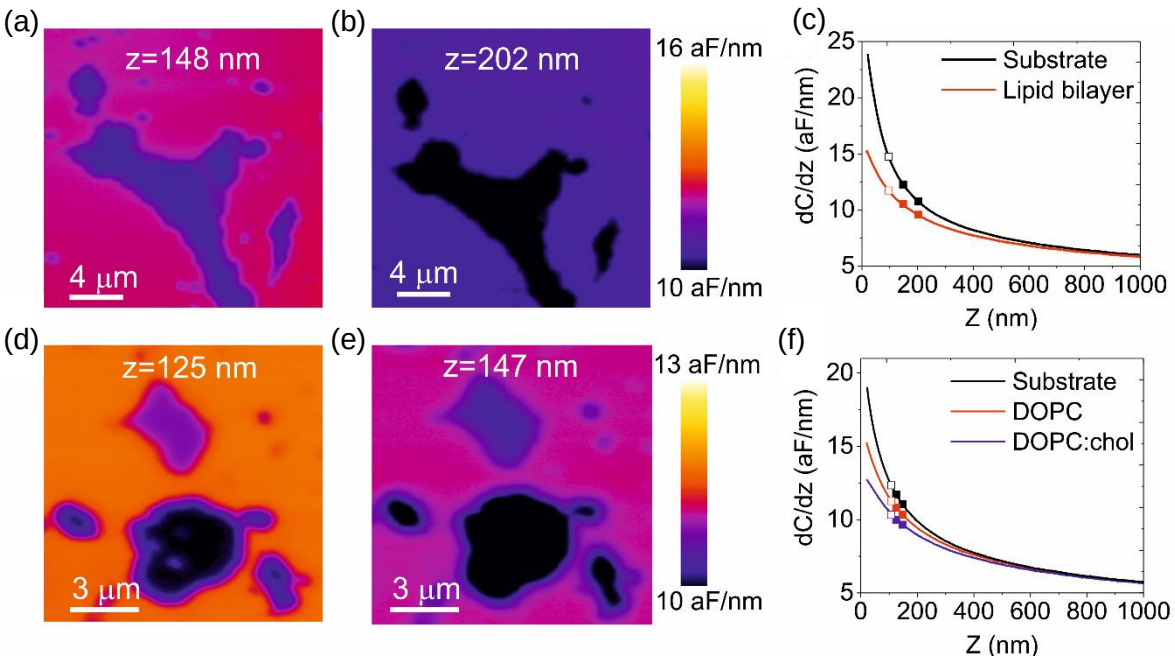

Figure 32: (a) and (b) SDM images of the sample in Figure 22 containing DOPC patches supported on a functionalized planar gold substrate in Milli-Q water at tip-substrate distances Z=148 nm and Z=202 nm, respectively. Experimental parameters: same as in Figure 22 (c). Values of the capacitance gradient on the bare substrate (black solid symbols) and on the centre of the largest patch bilayer (red solid symbols) plotted on top of the capacitance gradient approach curves measured at that positions (same data as in Figure 22 (d)). The empty symbols represent the values obtained from the SDM image in Figure 22 (b) acquired at Z=101 nm. (d)-(f) Idem but for the sample in Figure 25, containing DOPC and DOPC:cholesterol patches supported on a functionalized planar gold substrate in Milli-Q water at tip-substrate distances Z=125 nm and Z=147 nm.

4.7 Appendix: Probing viscosity with the fluorogenic dye BODIPY

4.7.1 Introduction

Variations in the viscosity of the DOPC and DOPC:cholesterol compositions could be related to the hydration of the layers, which we suspect linked to the different specific capacitances previously extracted. For this reason, we decided to probe the viscosity of the

sample as a complementary study to support the results obtained. To this end we used functional fluorescence microscopy.

Fluorescence microscopy can be used to address properties of lipid membranes like polarity, viscosity of different phases, hydration, as well as molecular order, environment relaxation, and electrostatic potentials. A whole set of environment-sensitive probes has been synthesized with this purpose [10, 238, 270]. Environment-sensitive probes respond to a change in their microenvironment by changing their fluorescence intensity (fluorogenic dyes [271]) or colour (e.g., solvatochromic dyes [272, 273, 274, 275]).

Fluorogenic probes usually exploit intramolecular rotation as a design concept, with molecular rotors being the main representatives. These probes are particularly efficient for imaging viscosity and lipid order in biomembranes, of which hydration is often a consequence. BODIPY (4,4-difluoro-4-bora-3a,4a-diaza-s-indacene) is one of the major representatives of this category. It is an intrinsically lipophilic molecule, that can be conjugated to phospholipids themselves or also to cholesterol. BODIPY fluorescence quantum yield it is pretty high, together with its photostability and absorptivity.

The immediate consequence of the viscosity-dependent intramolecular rotation is the sharp increase in both the fluorescence quantum yield (φ_f) and the fluorescence lifetime (τ_f) as a function of the increasing viscosity (η) [276].

The main problem in using the quantum yield of molecular rotors is the inability to distinguish between viscosity and other factors which might affect the fluorescence intensity, such as the local dye concentration. However, ratiometric approaches can be used to remove the uncertainties in the probe concentration. Alternatively, as we did, it is possible to exploit the dependence of fluorescence lifetime of molecular rotors on viscosity:

$$\tau = z\, k_r^{-1} \eta^{\alpha} \qquad (18)$$

where k_r is a radiative decay constant and z and α are constants.

Fluorescence lifetime imaging (FLIM) is an imaging technique which uses the detection of fluorescence lifetime instead of fluorescence intensities to obtain informations on the micro-environment of the fluorophore. One of the applications of FLIM is the study of the interaction distance of molecules labelled with a donor-acceptor pair via FRET (Förster resonance energy transfer).

When a fluorophore is excited by a photon, it can return back to the ground state through a number of different decay pathways, radiative and non-radiative; each of them with a different probability based on the decay rates. To observe fluorescence, one of those pathways must be followed by spontaneous emission of a photon. The fluorescence will decay with time according to:

$$I(t) = I_0 e^{-t/\tau} \tag{19}$$

where $1/\tau = \sum_i k_i$, where ki are the rates for each decay pathway.

The main advantage of fluorescence lifetime is that this technique is independent from the fluorophore concentration, in the absence of self-quenching and/or aggregation. Thus, FLIM experiments can be used to obtain information about viscosity in heterogeneous environments.

Fluorogenic probes were claimed to enable quantitative analysis of the viscosity when combined with advanced microscopy, such as FLIM [277, 278, 279]. However, it has to be emphasized that viscosity in highly anisotropic systems, such as membranes and especially if supported on a substrate, it is not trivial to interpret, because for example different viscosities in the membrane plane (η) and in contact with the outer liquid (η') are experienced [280]. Thus, the viscosity of the system is model dependent and probe sensitive. Furthermore, the position of the fluorophore in the layer is important and not always well controlled. For these reasons, our approach to the analysis of the viscosity in SLBs has been only qualitative.

We decided to make use of a fluorogenic probe, the derivative BODIPY PC, to investigate the same lipid mixture selected for the previous study, i.e. DOPC and DOPC:cholesterol 1:1 on glass.

Some works done on GUVs have already reported an increase in the lifetime of different BODIPY derivatives upon addition of cholesterol to DOPC [271, 281]. It was concluded that the viscosity is higher when cholesterol is present. We tried to verify these results by performing FLIM measurements on our specific lipid mixture.

These experiments have been carried out at CBS Monpellier, during a scheduled secondment in the framework of the SPM2.0 Marie Slodowska-Curie Initial Training Network, under the guidance and supervision of Dr. Milhiet and Dr. Costa.

4.7.2 Materials and methods

Sample preparation

The fluorescent probe selected for the FLIM experiments is the 2-(4,4-difluoro-5,7-dimethyl-4-bora-3a,4a-diaza-s-indacene-3-dodecanoyl)-1-hexadecanoyl-sn-glycero-3-phosphocholine, shortened as β-BODIPY™ FL C12-HPC (D3792, Thermo Fisher Scientific), a phospholipid molecule to which the fluorophore BODIPY is connected. This BODIPY probe is excited at 488 nm (blue) and emits in the green (500-565 nm). 18 µL of DOPC 10 mM (dissolved in $CHCl_3$/MeOH 2:1), together with 2 µL, 1 mM of the fluorophore, have been introduced in a glass tube, preventively cleaned with $CHCl_3$/MeOH.

The lipids and the fluorophore were purchased from Thermofisher; chloroform and methanol from Sigma-Aldrich. The final concentration of BODIPY in the mixture was about 0.1%; at higher ratios the dye can aggregate, and this would have brought to a lengthening in the observation times.

The tube was vortexed for 2 minutes to ensure homogenization of the dye in the mixture. Afterwards, the sample was dried under argon flux for about 2 h at 30 °C. The film was finally rehydrated with 1 mM buffer at 60 °C (Tris 20 mM, NaCl 150 mM) and the tube was vortexed again to promote the formation of the liposomes in suspension.

For the cholesterol containing sample, the same procedure was used, but 9 µL of DOPC 10 mM and 9 µL cholesterol 10 mM have been initially introduced in the glass tube, together with the 2 µL of BODIPY solution. This time the mixture has been sonicated in ice for 10 minutes to ensure cholesterol insertion; later, the film was dried and rehydrated as before.

The glass coverslips for liposomes incubation were cleaned by sonication in KOH 1M for 15 minutes, 20 times washing with Milli-Q, further sonication in Milli-Q for 15 minutes and plasma treatment.

80 µL of the DOPC and DOPC:cholesterol liposomes suspension prepared with the BODIPY derivative were separately incubated on different glass coverslips for 30 minutes. The buffer was then exchanged several times to remove material in excess and the sample was mounted on the AFM JPK sample holder equipped with the fluorescence setup (Figure 33)).

Fluorescence lifetime imaging microscopy by time domain FLIM

We performed measurements in the time domain (TD FLIM), which are single point measurements combined with a scanning method provided by a confocal laser scanning microscope. TD FLIM yields high sensitivity and good time resolution [282].

Fluorescence lifetime images were acquired using a custom-made confocal microscope (based on a Zeiss inverted optical microscope) coupled to an AFM Nanowizard 4 (JPK Instruments, Bruker), equipped with a Tip Assisted Optics (TAO) module and a Vortis-SPM control unit. The setup is shown in Figure 33. A supercontinuum laser (Leukos) is used as light source operating at 20 MHz (50 ns pulses of width <100 ps). An excitation filter later selects the frequency of excitation, in agreement with the one of the fluorophore. Before being sent to the sample, the laser light passes through a pinhole, which allows to restrict the illuminated area near to the diffraction limit [283]. The light pulses are delivered to the sample though a path of lenses and mirrors, while the JPK TAO sample scanner moves the sample. Lifetime measurements can be carried out simultaneously and correlated with AFM characterization. The fluorescence emitted by the sample was collected for every pixel; each of them carries the

contribution of several fluorescent molecules. A dichroic mirror was used to select the fluorescence and filters out the laser light. The fluorescence is finally directed through another pinhole which cuts out the photons that does not belong to the focal point.

When simultaneous AFM/FLIM images were acquired (see for example Figure 33), the AFM tip and confocal spot positions were fixed by co-aligning them. Any mismatch during imaging was adjusted by correcting the tip position. Keeping the confocal spot and AFM tip aligned during data acquisition has the advantage to maintain constant all spurious effects resulting from synchronous operation [284].

The acquisition of the fluorescent lifetime was performed using an excitation filter at 488/10 nm and an emission filter at 535/40 nm, with a laser excitation power of 1 μW. The measurements were performed at room temperature and under liquid conditions in Tris 20 mM, NaCl 150 mM buffer.

After a short excitation, the time-dependent intensity profile is detected. Following the excitation, the precise time of detection of the emitted photon is recorded, being the reference for the timing the excitation pulse.

Since it is physically impossible to detect the required amount of photons from one single excitation-emission cycle, periodic excitation is used and a many single photons are recorded by a time-correlated single photon counter (TCSPC) [285, 286].

The single-photons arrival times are collected and grouped in “bins”, and the histogram of their distribution is built up. By adjusting laser power and repetition rate the probability of recording more than one photon is kept low to avoid the pile up effect. The result is a TCSPC histogram with an exponential drop of counts at increasing times; we fitted a single decay function for every pixel, extracting the fluorescence lifetime and amplitude for every pixel.

The analysis was carried out through the software SPCImage (Becker & Hickl) using a single exponential decay and spatial binning of 2.

The fit parameter, τ_m, is given by the weighted average of the different lifetime components in each pixel (t_m).

$$\tau_m = \sum_{i=1}^{N} a_i \tau_i \Big/ \sum_{i=1}^{N} a_i \tag{20}$$

The software minimizes the chi-square value between the data and the model function during the fit process. The result is a set of parameters (e.g. lifetimes) for each individual pixel of the image. An image is generated by the intensity information from the number of photons in each pixel while the lifetime image derives from the information of the fit parameter extracted from every pixel.

4.7.3 Results and Discussion

After absorption of light, a fluorophore remains in its excited state for a certain amount of time (usually nanoseconds) before returning to the ground state either emitting a photon or by non-radiative energy transfer. The transition from excited to ground state is a statistical process and therefore the emission of fluorescence follows an exponential decay law. The average time between the excitation and emission for several cycles is called fluorescence lifetime of a given fluorescent molecule. Lifetime is not an intrinsic property because it is based on the stability of the molecule's excited state, which depends on the local environment. For this reason, the lifetime can be used to characterize a fluorophore in a well-defined medium, detecting changes in the immediate surrounding or conformational movements or interactions with other molecules such as FRET.

Figure 33 shows a first test measurement of a DOPC:cholesterol, BODIPY PC 0.1% sample. In the measurement, as expected, we always observed simple mono-exponential decays of the form:

$$I(t) = I_0 e^{-t/\tau} \tag{21}$$

This justifies and confirms the fact that the system under analysis is composed by only one (Ld) phase, in agreement to literature [164] and previous studies.

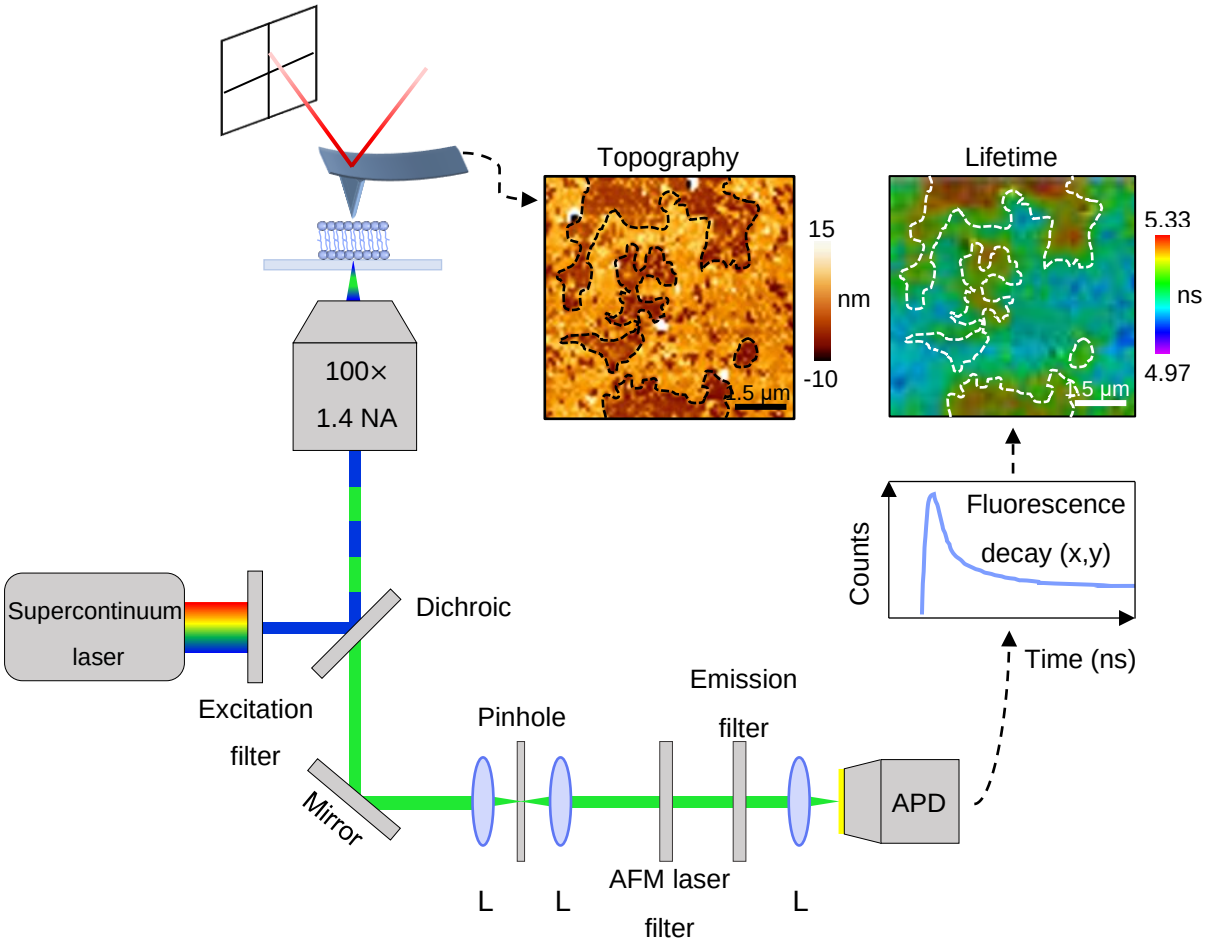

Figure 33: (a) Correlative AFM and confocal microscopy setup adapted from Ref. [284]. The topography in QI mode is acquired simultaneously to fluorescence lifetime decays at every pixel, for a sample made of DOPC:cholesterol 1:1 (0.1% BODIPY PC) and supported on a glass coverslip, in buffer Tris 20 mM, NaCl 150 mM. Cantilever used for AFM: MLCT-BIO-DC / C, Bruker (k=0.014 N/m). The correlation between the two images is highlighted by the lines drawn on the contours of the topography and reported on the lifetime image.

By looking at the images displayed in Figure 33, we immediately notice that, even pixels corresponding to the bare substrate, display a red colour in the lifetime image, which is informative for high lifetimes. This feature is however not physically significant, because the photons collected in bare areas are very few; thus, although the software keeps fitting any function, practically the data in those points are meaningless.

If we have a look especially at the borders, highlighted by dashed lines, we observe that the correlation of the lifetime with the AFM topography is not perfect. This is due to the resolution of the technique, the optical diffraction limit [283]. Indeed, we need to consider that the illuminated area is about 500 nm and thus, when the pixel measured contains only in part information from the membrane, the lifetime obtained is not reliable. This, in the image displayed, does not happen only at the border, but also in correspondence of small holes in the bilayer. Any defect of the layer smaller than the size of the illuminated area will contribute to a pixel and be responsible for an increase in the fluorescence lifetime displayed. The AFM topography image in Figure 33 shows that there are several holes in the bilayer, some of them very little, which surely generate quite some variability in the observed lifetime. The presence of small un-extended vesicles can also affect the obtained lifetime.

It is thus evident that, for a proper comparison of the fluorescence lifetimes between experiments, it is important to dispose of intact and extended bilayers, as the ones in Figure 34.

Besides, we highlight that other factors could in principle affect the observed lifetimes and lead to contradictive results, like for instance a different interaction of the bilayers with the substrate [287]. This normally depends on the material used as a substrate, but it is not to exclude that it can also be experiment dependent. For example, interaction of the lipids to glass coverslips might vary depending on different conditions of the plasma treatment.

Another factor to carefully consider is the fluorophore concentration. Although FLIM experiments should be independent from it, excessive concentrations can cause dye aggregation and alteration of the lifetime response. When this is the case, a bi-exponential decay can arise [288].

A further parameter that can affect the observed lifetime is the depth and tilt [287, 289] of the probe in the membrane, which is often difficult to control. In this regard, we underline that the molecule BODIPY, for its chemical structure, might like to stack to the cholesterol molecules,

which are present in very high concentrations in our model systems. Such interaction could infer a tilt of the fluorophore in the layer, which would in turn affect the lifetime.

Figure 34 shows the intensity and fluorescence lifetime of BODIPY PC in extended layers of DOPC and DOPC:cholesterol 1:1 respectively.

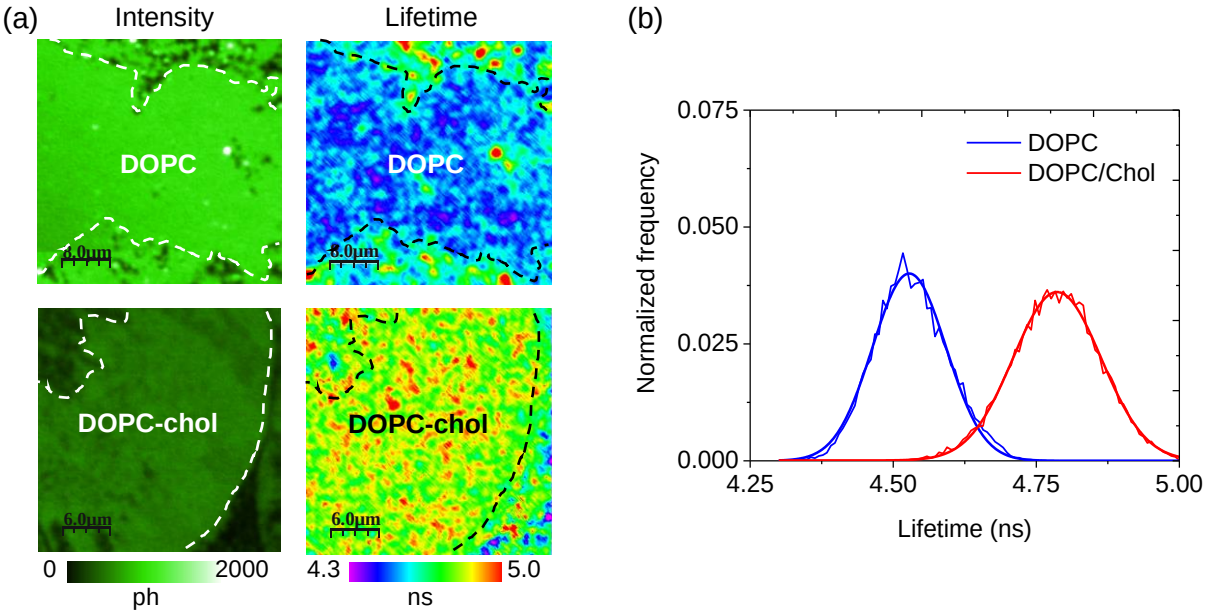

Figure 34: (a) Intensity (photons) and FLIM image of DOPC and DOPC:cholesterol lipid layers supported on glass coverslips (128×128 pixels). (c) Histograms of the lifetimes for the two compositions, highlighting that, when cholesterol is present, the fluorescence lifetime of BODIPY PC in the layer increases of ~0.25 ns.

The two samples display a good coverage of the substrate and not many defects are visible, at least at this scale, from the intensity image. From these measurements, as expected, we obtain that the lifetime of the DOPC:cholesterol composition is higher than the one of the pure DOPC component. This would indicate that the environment of the probe, when cholesterol is present, is more viscous. Nevertheless, additional measurements are necessary to arrive to a final conclusion.

4.7.4 Conclusions

Fluorescence approaches for evaluating layer properties like packing and hydration, although reported in several works, are sometimes difficult to use, even just qualitatively, given the high number of variables that could affect the measurements. In this case, the non-homogeneous extension of the layers was often providing misleading results. Nevertheless, our results seem to support the fact that, in presence of cholesterol, the viscosity of the DOPC system increases. These findings go in the same direction of what was extrapolated from our dielectric characterization, i.e. that cholesterol might, by increasing the lipid packing, allow less hydration of the layer.

5. In-Liquid SDM of Single Liposomes

After addressing the properties of planar supported lipid bilayers, our attention was drawn to more complex and physiological 3D biomembranes configurations, such as DOPC liposomes. We characterized not only the dielectric properties of their membranes, which is in good agreement with the results of the previous chapter, but also their internal structure, i.e. number of lamellae.

This chapter is based on the article in preparation: 'Electrical Properties and Lamellarity of Single Liposomes Measured by In-Liquid Scanning Dielectric Microscopy'. My contribution to this work consists of the experimental measurements (from sample preparation to image acquisition) and data analysis using a custom-written Matlab code written by R. Millan-Solsona and earlier members of the group. The manuscript was written in collaboration with my supervisor G. Gomila and the rest of the authors.

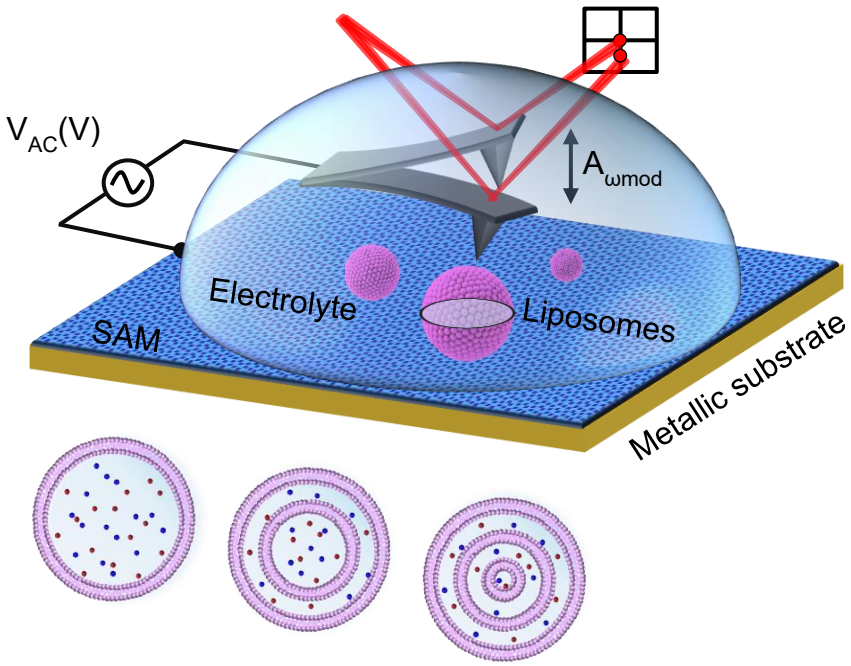

Figure 35: Schematic representation of the in-liquid SDM setup in force detection mode [28, 29] applied to liposomes adsorbed on a functionalized metallic substrate.

5.1 Introduction

As we have mentioned in the Introduction, liposomes consist of single or multiple concentric lipid bilayers encapsulating an aqueous compartment. Their sizes range from tens of nanometres to tens of micrometres [290]. Liposomes are widely used as drug delivery nanocarriers [291, 292, 293] , as well as cell model systems to study cell membrane properties [290, 294] , transmembrane processes [81] and intracellular biochemistry [81].

A bunch of techniques already exist to probe the structural, physical and chemical properties of liposomes [295, 296, 297]. Among the structural properties, lamellarity, i.e. the number of concentric lipid bilayers present in a liposome, is among the most relevant ones. Lamellarity, determines the stability of liposome preparations [298], the amount of lipophilic drugs that can be encapsulated, the kinetics of its release [293] and the fate of liposomes when interacting with cells [295]. Moreover, it also determines the overall mechanical [299] and dielectric [300] properties of the liposomes, which are relevant in their interaction with cells [301, 302] or in their electrokinetic manipulation [303]. Finally, in the use of liposomes as cell model systems, strict control of the lamellarity is required [81].

Lamellarity can be determined at the population level by using techniques such as Nuclear Magnetic Resonance, X-Ray Small Angle Scattering and Fluorescence Spectroscopy [304, 305]. These techniques provide the average lamellarity of the liposome population. Lamellarity can also be determined at the single liposome level by considering imaging techniques such as cryo-Electron Microscopy, Freeze-fracture Electron Microscopy and Light Microscopy [306, 307]. Lamellarity on single liposomes can also be determined by means of mechanical techniques such as micropipette aspiration and deformation [308, 309], and more recently, by means of force spectroscopy measurements with the Atomic Force Microscope (AFM) [299]. Despite their success, single liposome lamellarity techniques still present some drawbacks. The most relevant one is that none of them is at the same time non-invasive and label-free, i.e. the methods are either destructive and invasive or require of exogenous labels or staining agents. Developing a non-invasive and label-free single liposome lamellarity technique would be

desirable, for instance, for applications involving the monitoring of processes occurring in a single liposome along time.

The response of single liposomes to external ac electric fields offers a possible route to develop such techniques. The response depends on the size and electrical properties of the liposomes (e.g. conductivity, lipid bilayer capacitance), but also, on their internal structure. An example of it can be found in the use of electrorotation to determine the lamellarity of single liposomes [300, 310]. In electrorotation, the revolution velocity of a vesicle suspended in a rotating electric field cage is determined as a function of the frequency of the external ac potential, from where the lamellarity can be inferred thanks to the long-range nature of the electric interaction, which probes the liposomes' interior [300, 310]. However, downscaling this type of techniques based on fixed microelectrode set-ups to probe sub-micrometric liposomes is very challenging and has not been achieved yet. An alternative approach consists in the use of nanoelectrodes in electric Scanning Probe Microscopy (SPM) set-ups. Measuring the ac electric forces acting on a conductive SPM probe in response to an applied ac voltage has been shown, theoretically [34, 36, 311] and experimentally [33, 35, 37, 38, 39, 312, 313, 314, 315, 316], to provide access to the subsurface properties of nanocomposite materials with nanoscale spatial resolution. Examples include the detection of carbon nanotubes (and other nanoscale objects) buried within polymer nanocomposites [35, 37, 38, 39, 312, 313, 314], the imaging of sub-surface chemical transformation in molecular materials [315, 316] and the measurement of the dielectric properties of water confined in buried nanochannels [33].

In the present work we extend the subsurface capabilities of Electric Force SPM techniques to the liquid environment to probe the interior of sub-micrometric single liposomes and to determine their lamellarity in a non-invasive and label-free way. To this end we use in-liquid Scanning Dielectric Microscopy (in-liquid SDM) in the force detection mode [28], which recently has shown a high potential for nanoscale electrical characterization in electrolyte solutions (e.g. measurement of the local specific capacitance of thin dielectric films and solid supported lipid bilayer patches [29, 31], nanopatterned self-assembled monolayers [30] and of the local

conductivity and interfacial capacitance of electrolyte gated field effect transistors [41]). Here, we demonstrate that with this technique one can access the sub-surface properties of sub-micrometric liposomes and probe the liposomes' interior structure. The proposed approach, in addition, provides a method to accurately determine the specific capacitance of the lipid bilayers forming the liposomes, which constitutes a key parameter in Bioelectricity [317].

5.2 Materials and methods

5.2.1 Liposomes preparation and absorption on functionalized metallic substrates

DOPC multi-lamellar (1,2-dioleoyl-sn-glycero-3-phosphocholine) liposomes were obtained by hydration method, without a further step of extrusion, in a salt-reach buffer composed of Tris 20 mM, KCl 100 mM. For the preparation of the liposomes, chloroform and methanol, HPLC grade, were purchased from Sigma Aldrich; high purity water (18.2 MU cm) was obtained with a Milli-Q water purification system (Millipore, Billerica, MA); DOPC specified as R99% pure, was obtained in powder form (Avanti Polar Lipids (Merk)) and used without further purification. The liposomes were prepared as follows: DOPC was first dissolved in chloroform/methanol (3:1) (v/v) solution to a final lipid concentration of 10 mM. Then the solvent was evaporated under a nitrogen stream with constant rotation of the vial. The vial was kept in vacuum for 6-8 hours to ensure the absence of organic solvent traces. The dry lipid film was then resuspended in Tris 20 mM, KCl 100 mM to a final concentration of 0.1 mM. The liposomes were spontaneously formed under these conditions and stored at 2ºC -8ºC, always protected from light, and used within 1–2 days. A drop of 60 µL of DOPC liposomes suspension was added to a flat functionalized gold substrate at room temperature (25ºC) and incubated for 10 min. The salt-reach buffer and the short incubation time at 20 ºC withhold the rupture of most liposomes onto the surface. The multi-lamellar nature also contributes to that. Afterwards, the substrate was rinsed several times with Milli-Q water to remove the excess of vesicles in suspension and change the imaging media (low salt concentration is necessary for SDM

imaging). The flat gold substrates were produced by mica replica (MicroFab Space, IBEC, Spain), functionalized with self-assembled monolayers (SAMs) made of 2-Mercaptoethanol 99.0% (Sigma-Aldrich). The SAMs were prepared by incubating the gold substrates in a 2 mM solution of the thiols overnight at 2-8 ºC, protecting the vial from light and from oxidation by filling it with nitrogen before storage. Gold was selected for its excellent conductive properties, while the alcoholic moiety terminating the thiol molecules was chosen to make the surface more hydrophilic, promoting the interaction with the lipid polar heads and the anchoring of the liposomes.

5.2.2 In-liquid SDM measurements

In-liquid SDM measurements were carried out as explained in Chapter 4, by following the methodology described in Ref. [31]. The parameters of operation have been set to the same values, i.e. we applied an electrical frequency at f_{el}=5 MHz, a modulation frequency f_{mod}=6 kHz, and a voltage amplitude v_0=0.7 V. The same HQ:NSC19/Cr-Au gold coated AFM probes have been used for imaging. Topographic and electrical images have been acquired as before, but this time, rather than performing approach curves on the sample, we acquired several constant height images at different Z-distances from the substrate. These electrical images have been later used to reconstruct electrical curves per points on every liposome. The measured oscillation amplitude, $A_{\omega_{mod}}$, was converted to capacitive gradient, *dC/dz*, through the relation reported in Chapter 4. Once again, as described before and in previous works [12, 15, 20, 28, 29], approach curves on the substrate were acquired to later calibrate the tip geometry, determine the SDM imaging distances, and the substrate and tip interfacial capacitances.

5.2.3 Finite element numerical calculations and extraction of the equivalent homogeneous dielectric constant of the liposomes

We quantitatively analysed the SDM images following the methodology applied in Ref. [12] adapted to the liquid environment [29, 30], and reported in Chapter 4. We calculated the *dC/dz* values by solving the currents model implemented in the AC/DC Electrostatic module of COMSOL Multiphysics (Comsol Inc.). The Maxwell stress tensor was integrated over the conical part of the tip, with the cantilever effects modelled through a constant offset, C'_{offset} [30]. We did not include ionic diffusive effects, since they can be neglected at the frequencies of the SDM measurements [30, 197]. The modelling of the tip geometry, the interfacial capacitance around the tip (c_{tip}) and on substrate ($c_{substrate}$) has been already described in Chapter 4. The probe was modelled as in [12, 15], including the presence of c_{tip} according to [30], and $c_{substrate}$, as introduced in [29, 31].

The liposomes have been modelled as caps of height *h* and width *D* and geometry described by the revolution of the function $Z(X)=h-a\,|X-X_0|^b$, where X_0 is the centre of the liposome (position of the maximum), $a=h/(D/2)^b$ and $b=\ln(2)/\ln(D/FWHM)$, with FWHM being the full width at half maximum. By substituting a and b into the function Z(X), we obtain that the geometry is described by:

$$Z(x) = h\left(1-\left(\frac{2\,|X-X_0|}{D}\right)^{\frac{\log(2)}{\log\left(\frac{D}{FWHM}\right)}}\right) \tag{22}$$

This geometry is determined from three parameters of the topographic image, the height, h, the diameter, D, and the full width at half maximum FWHM. A spherical cap geometry also provides a good description of the measured topography, although, since it is determined from only two parameters from the topography (the height, h, and the diameter, D) it is slightly less accurate. Explicitly, the spherical cap geometry is given by:

$$Z_{sph}(x) = h - R_c + \sqrt{R_c^2 - (X-X_0)^2} \tag{23}$$

where h is the height and R_c the radius of curvature, which for a spherical cap is given by:

$$R_c = \frac{(\frac{D}{2})^2 + h^2}{2h} \tag{24}$$

In Figure 36, we compare the predictions of the two geometrical models with the measured topography of four adsorbed liposomes spanning the full range of sizes considered. In general, both models describe correctly the measured topography, but the phenomenological model adjusts better the profiles for larger liposomes.

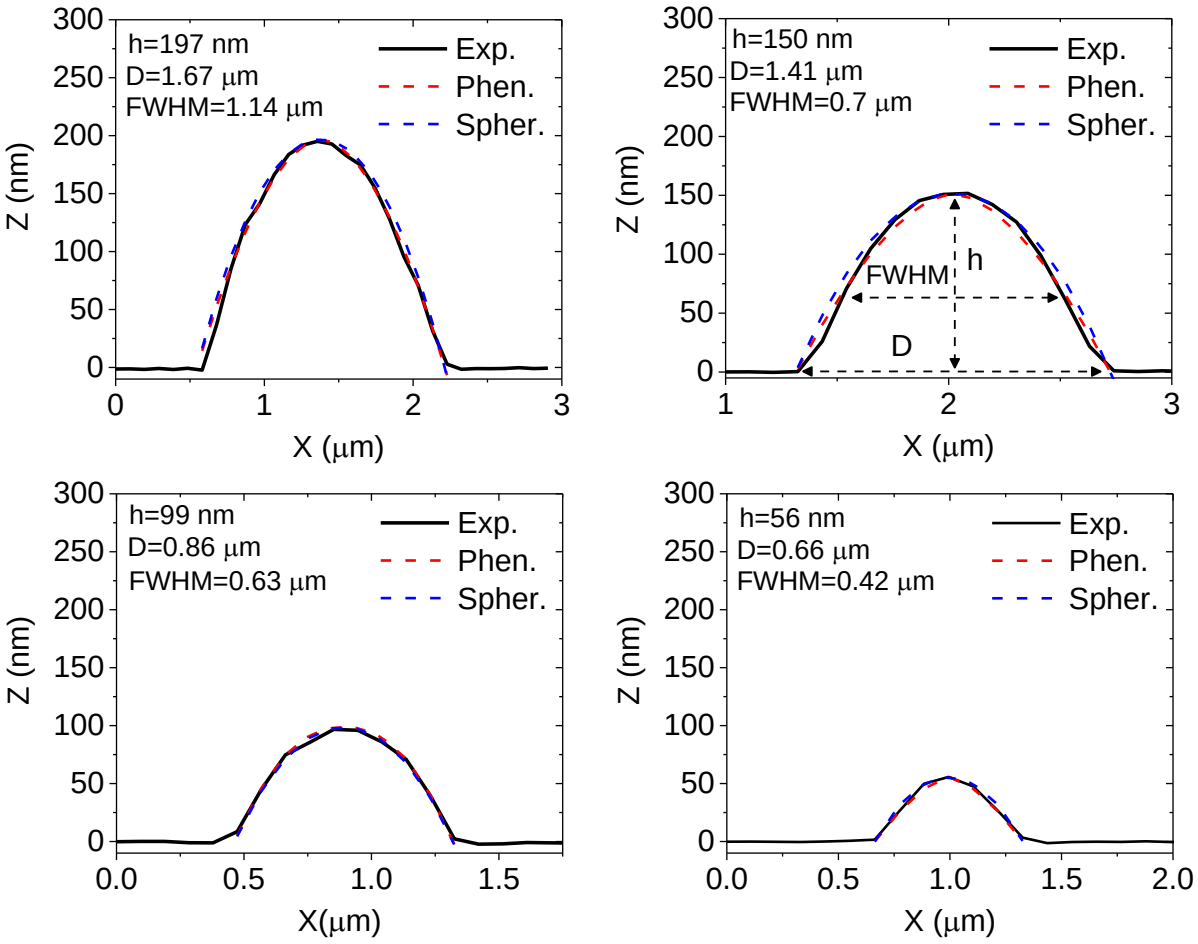

Figure 36: Comparison between the measured topography of four adsorbed liposomes (continuous black lines) and the modelled geometries according to the phenomenological function in Eq (22) (red dashed lines) and the spherical cap function in Eq (23) (blue dashed lines).

For the DOPC liposomes adsorbed on the substrate that we analysed, we find the following linear relationships between the parameters h, FWHM and D:

$$h(nm) = -39.9 + 0.14D(nm) \quad (25)$$

$$FWHM(nm) = -99.8 + 0.75D(nm) \quad (26)$$

These relationships together with Eq (22) allows generating liposome geometries of any size compatible with the shape of the adsorbed liposomes. We used this fact, for instance, to generate generic theoretical predictions, as those reported later in the text (Figure 38 (a) or Figure 42).

To determine the equivalent homogeneous dielectric constant, ε_{eq}, we considered the geometrical model shown in Figure 37 (a), in which the whole liposome is assumed to have a uniform dielectric constant, ε_{eq}, and the shape and size being given from the topographic image. To describe the properties of uni-lamellar liposomes we considered the model in Figure 37 (b). In the model, a membrane of thickness, d_m, and dielectric constant, ε_m, surrounds a core with dielectric constant ε_{lip} and conductivity σ_{lip}. For small membrane thicknesses, the dielectric response only depends on the membrane specific capacitance $c_m=\varepsilon_0\varepsilon_m/d_m$.

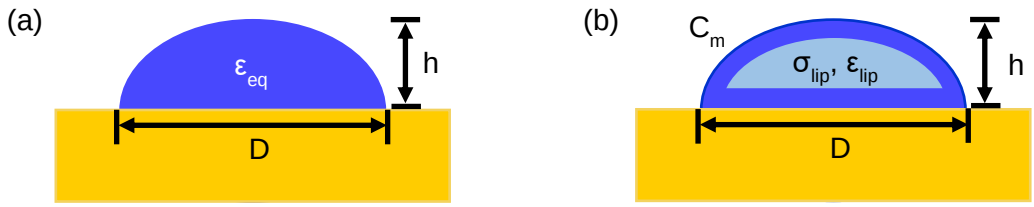

Figure 37: Schematic of two models for liposomes analysis. (a) Homogeneous model of a supported liposome of height (h) and diameter (D) considered to extract the equivalent permittivity (ε_{eq}) of the vesicles, and (b) model considered to describe uni-lamellar liposomes.

To describe bi-lamellar liposomes, we considered instead the model in the inset of Figure 38 (a), which adds a concentric internal lamella to the uni-lamellar model at a distance, d, from the external membrane.

Extraction of the equivalent homogeneous dielectric constant of the liposomes. To extract the equivalent homogeneous dielectric constant of the liposomes we have considered the model in Figure 37 (a) and followed a similar approach to the one detailed in Ref. [12], with the adaptations to the liquid environment discussed elsewhere [29, 30]. As mentioned before, we calibrated the tip geometry and substrate interfacial capacitance by using dC/dz curves on the metallic substrate, as in previous works [12, 15, 189]. The parameters L, H, W, θ were kept fixed to the same values reported in Chapter 4. The tip interfacial capacitance was in this case fixed to c_{tip}=2.7 μF/cm^2. The voltage reduction factor in the present work was α=1.24. With the parameters obtained as a result of the fitting process (R, $c_{substrate}$, C'_{offset} (Figure 41)), we calculated capacitance gradient values, dC/dz, for the tip located on top of the liposomes at its centre at a distance Z from the substrate and fitted them to the experimental values with the equivalent dielectric constant of the liposome, ε_{eq}, as the single fitting parameter. The analysis was done with a custom-made software written in Matlab (Mathworks inc.) linked to the COMSOL Multiphysics software.

5.3 Results: dielectric constant and lamellarity of single liposomes

To measure the response of a single liposome to an external ac electric field we followed an approach similar to the one used to analyse the dielectric properties of single dielectric nanoparticles and virus particles in air environment [12, 22] , property adapted to work in an electrolyte solution [28]. A schematic representation of the in-liquid SDM set-up used in the present work and applied to a liposome sample is shown in Figure 35.

The tip-liposome capacitance gradient, dC/dz, is a function of the structural and electrical properties of the liposome. Explicitly, the capacitance gradient, dC/dz, depends on the tip-substrate distance, Z, the frequency of the applied voltage, f_{el}, the tip geometry (tip radius, R, and half cone angle θ), the liposome geometry and size (height, h, and diameter, D), the specific capacitance of the lipid bilayer ($c_m = \varepsilon_0 \varepsilon_m / t_m$, where t_m and ε_m are the thickness and dielectric constant of the lipid bilayer and ε_0 the vacuum permittivity), the electrical properties

of the internal and external solutions (conductivities, σ_{lip} and σ_{sol}, and dielectric constants, ε_{lip} and ε_{sol}, respectively), and, more importantly, the liposome internal structure (number of lamellae, n, and separation between them, d) (see Figure 38 (a)).

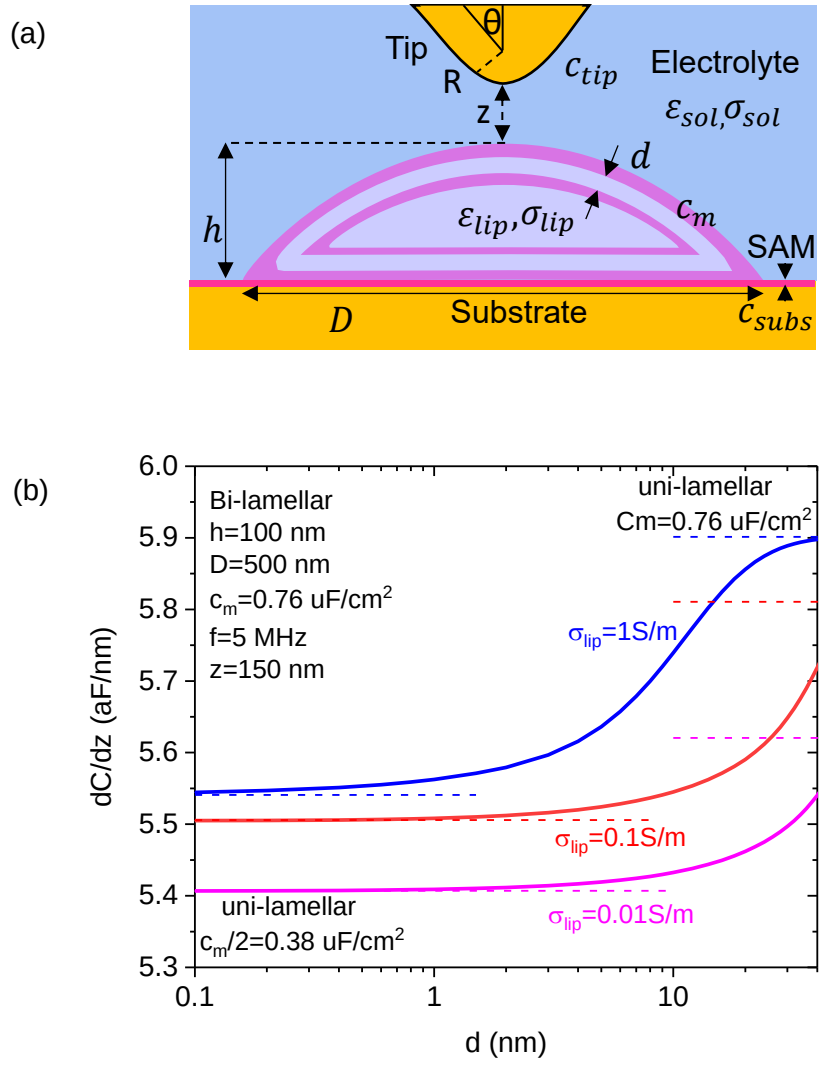

Figure 38: (a) Schematic representation of the theoretical model used to compute the tip-liposome capacitance gradient, dC/dz, *for the case of a bi-lamellar adsorbed liposome. (b) Numerically calculated dependence of the tip-liposome capacitance gradient,* dC/dz, *for a bi-lamellar liposome as a function of the separation between the lamellae,* d, *for three different conductivities of the internal solution, σ_{lip}=0.01 S/m, 0.1 S/m, 1 S/m (continuous lines). The dashed and dot-dashed lines correspond to the capacitance gradient values,* dC/dz, *for a uni-lamellar model with membrane capacitance c_m=0.76 mF/cm^2 and c_m/2= 0.38 mF/cm^2, respectively. Parameters of the calculations: tip radius, R=30 nm, half cone angle, θ=20º, cone height, H=12.5 mm, cantilever disc radius, L=3 μm, cantilever disc thickness, W=3 mm, tip-substrate distance, Z=150 nm, spherical liposome shape, liposome height, h=100 nm, liposome diameter, D=500 nm, internal and external solution dielectric constants, ε_{sol}=ε_{lip}=78, external solution conductivity, σ_{sol}=0.2 mS/m, tip interfacial capacitance, c_{tip}=2.7 mF/cm^2, substrate interfacial capacitance, $c_{substrate}$=0.65 mF/cm^2 , frequency of the applied voltage, f_{el}=5 MHz.*

Due to the non-trivial tip-liposome geometry we cannot use analytical expressions to determine the system capacitance gradient, dC/dz, and we must resort to numerical calculations to evaluate it. Figure 38 (b) shows the numerically calculated tip-liposome capacitance gradient, dC/dz, as a function of the inter-lamellar separation for a bi-lamellar liposome of diameter D=500 nm and height h=100 nm, with lipid bilayer specific capacitance c_m~0.76 mF/cm^2 (in the range of the usual values for lipid bilayers, c_m~0.5-1 mF/cm^2). The external aqueous solution has been assumed to be of low conductivity (σ_{sol}=0.2 mS/m, ε_{sol}=78), adequate for in-liquid SDM measurements [50], while the internal one has been assumed to cover the physiological relevant range σ_{lip}=0.01 S/m - 1 S/m (ε_{lip}=78). The tip radius, half cone angle and tip-substrate distance are R=30 nm, θ=20º and Z=150 nm, respectively, while the excitation frequency is f_{el}=5 MHz, above the dielectric relaxation frequency of the external electrolyte solution, as required for in-liquid SDM measurements [50]. For comparison we plotted also the dC/dz values corresponding to uni-lamellar liposomes of the same size with membrane specific capacitances c_m=0.76 mF/cm^2 (dashed lines) and c_m/2=0.38 mF/cm^2 (dotted-dashed lines). The tip-liposome capacitance gradient, dC/dz, (continuous lines in Figure 38 (b)) clearly depends on the interlamellar separation, d, evolving from the value that would correspond to a uni-lamellar liposome with half the membrane specific capacitance, c_m/2 (for small interlamellar separations), to that of a uni-lamellar liposome with the given membrane specific capacitance, c_m (for large interlamellar separations). The latter limit is reached only for the largest internal conductivities. This behaviour is consistent with the fact that for small inter-lamellar separations the liposome is like a uni-lamellar liposome with double membrane thickness and, hence, half specific capacitance. On the other hand, for large inter-lamellar separations, the liposome behaves as uni-lamellar (with the given membrane specific capacitance), since the internal lamella contributes little to the signal due to its very small surface area.

For liposomes with larger number of lamellae (n>2) a similar behaviour is expected: for small inter-lamellar separations, the capacitance gradient (dC/dz) will show values corresponding to a uni-lamellar liposome with membrane specific capacitances $c_m/3$, $c_m/4$, etc. for tri-, tetra-, etc; while for large separations, instead, the signal recorded will tend to that of a uni-lamellar liposome with specific capacitance c_m. These results demonstrate that by measuring the tip-liposome capacitance gradient, dC/dz, the lamellarity of single liposomes can be determined, as well as the separation between lamellae and the specific capacitance of the lipid bilayer membrane.

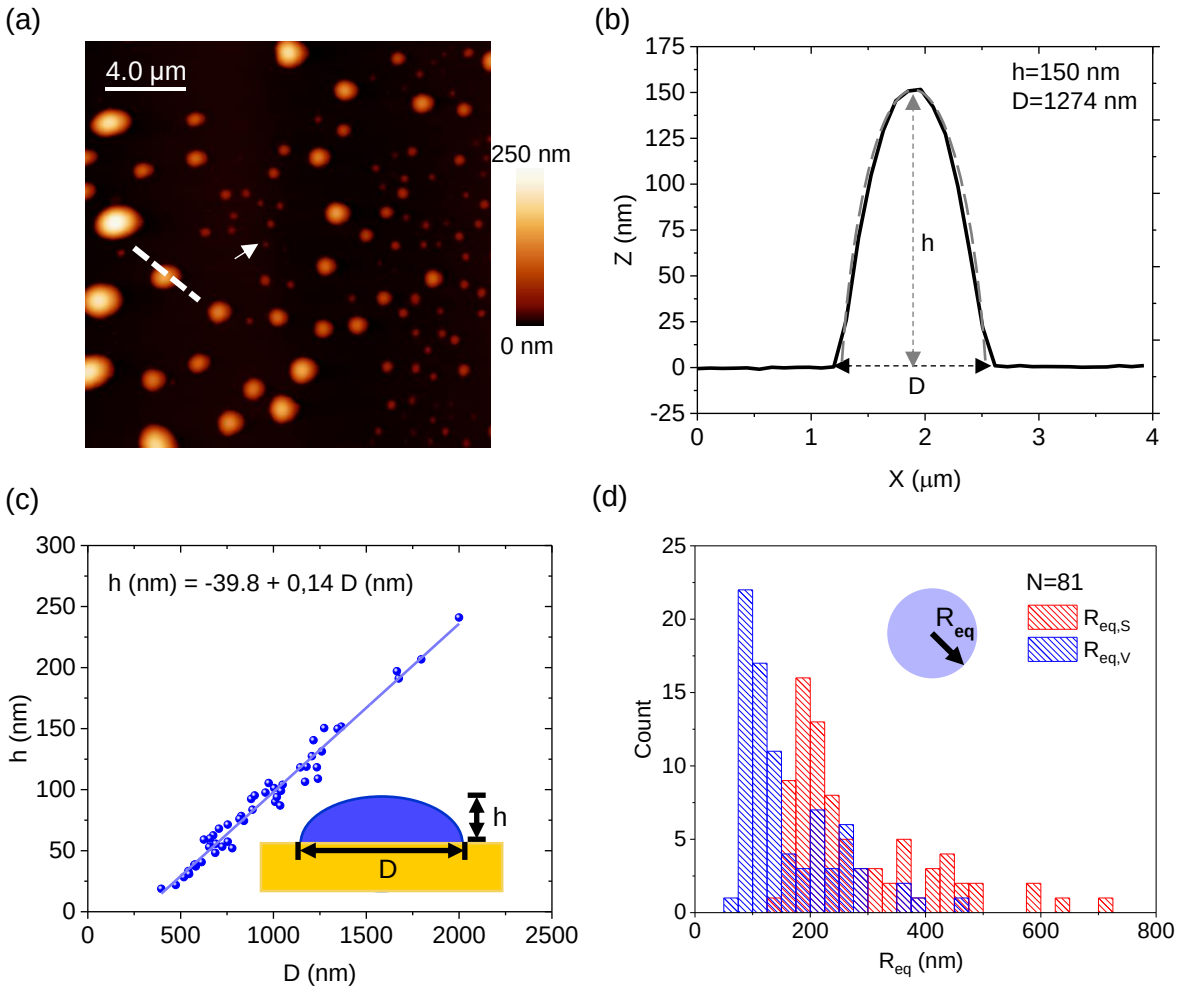

Figure 39: (a) AFM topographic image of DOPC liposomes adsorbed on a functionalized planar gold substrate. (b) Cross-section topographic (black line) profile along the dashed line in (a). The grey dashed line represents the adjustment of profile to the function $Z=h-a\,(X-X_0)^b$*. (c) Height versus width (D) of the liposomes in (a) (symbols). The continuous line is a linear fit to the data. (d) Distribution of equivalent spherical radii of the liposomes in (a) assuming a constant surface or volume area during the adsorption (red and blue bars respectively).*

Figure 39 (a) shows a topographic AFM image of non-extruded DOPC liposomes prepared by the hydration method and adsorbed on a flat gold substrate functionalized with a Mercaptoethanol self-assembled monolayer, as described above. The liposomes have been prepared in a solution with moderate conductivity (σ_{lip}=0.8 S/m) and imaged in a low conductivity solution (σ_{sol}=0.2 mS/m) to facilitate in-liquid SDM operation. The liposomes show an approximately spherical cap geometry (see topographic and spherical cap cross-section profiles, continuous black and dashed grey lines in Figure 39 (b)). The heights of the adsorbed liposomes range from ~25 nm to ~250 nm, and the diameters from ~250 nm to ~2 μm (see Figure 39 (c)). A linear relationship is found between the height and the diameter of the liposomes with a slope (aspect ratio) ~0.14. The relatively low aspect ratio implies a strong flattening of the adsorbed liposomes, which is consistent with their very soft nature, since DOPC is in the liquid phase at the temperature of the experiments [318]. From the measured heights and diameters, we have determined the distribution of equivalent spherical radii, R_{eq}. The comparison of the distribution of equivalent radii obtained by assuming constant the surface area or the volume, for the liposomes in (a), is shown in Figure 39 (d) (in red and blue respectively). By assuming the surface area to be constant, the equivalent radii distribution spans the range ~100 nm-800 nm. If one assumes the volume to remain constant, instead, the range of equivalent spherical radii is ~50 nm-500 nm.

The equivalent radii calculated by considering the surface area and volume of a spherical cap, are given respectively by:

$$S_{cap} = \pi \left[\left(\frac{D}{2} \right)^2 + h^2 \right] + \pi \left(\frac{D}{2} \right)^2 \tag{27}$$

$$V_{cap} = \frac{1}{6} \pi h \left[3 \left(\frac{D}{2} \right)^2 + h^2 \right] \tag{28}$$

From which the radii will follow:

$$R_{eq,S} = \frac{1}{2}\sqrt{(2\left(\frac{D}{2}\right)^2 + h^2)} \tag{29}$$

$$R_{eq,V} = \frac{1}{2}\sqrt[3]{h\left[3\left(\frac{D}{2}\right)^2 + h^2\right]} \tag{30}$$

Figure (a) shows a set of four constant height in-liquid SDM images acquired at f_{el}=5 MHz. The first image measured high enough to avoid touching any of the liposomes is the one at a tip-substrate distance of 270 nm. The images show a negative contrast for all the liposomes in the sample (see in Figure 40 (b) the capacitance gradient cross-section profiles along the dashed lines in (a), corresponding to the liposome topography in Figure 39 (b)). This fact implies that the equivalent homogeneous dielectric constant of the liposomes should be smaller than that of the surrounding solution (ε_{sol}=78) (see below). The smallest liposome electrically detected in the SDM image has dimensions h=23 nm and D=402 nm, corresponding to an equivalent radius of ~143 nm (indicated with a white arrow in Figure 39 (a)).

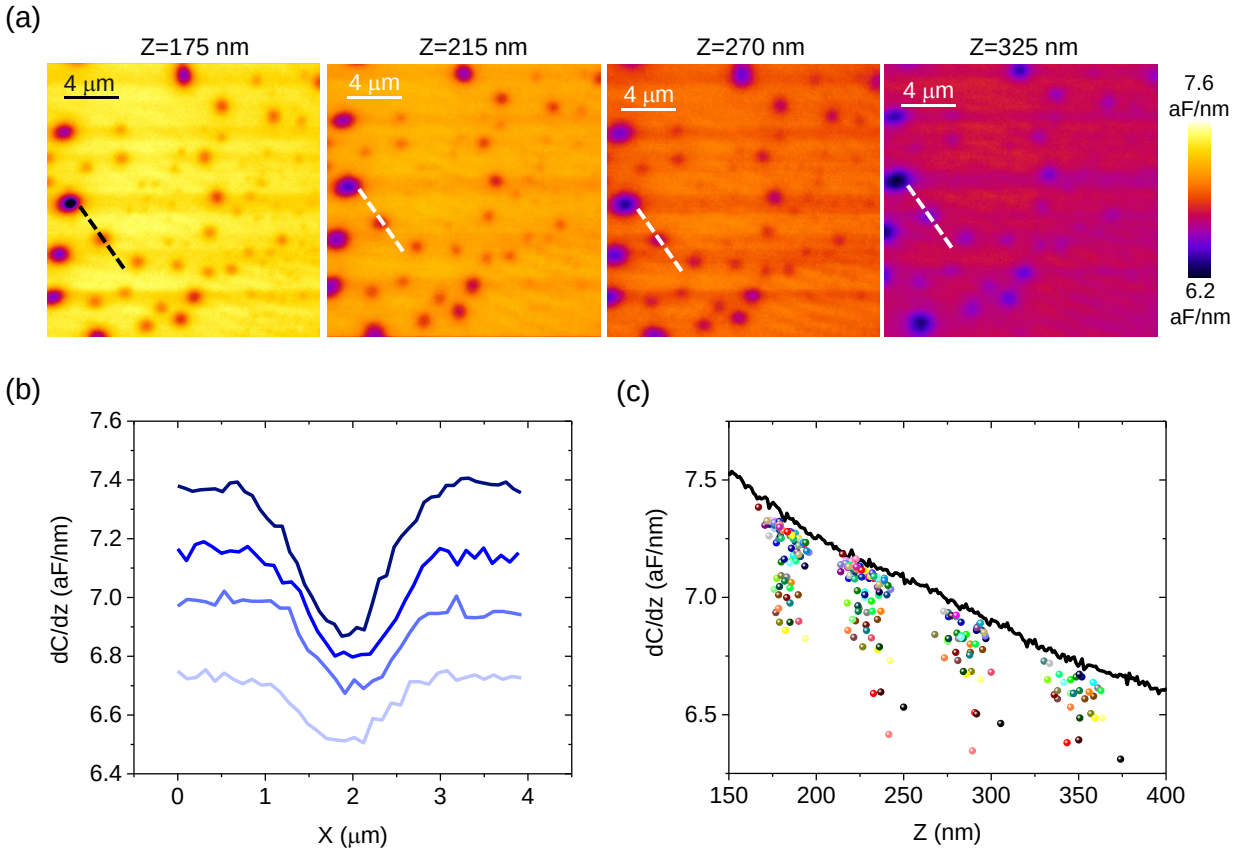

Figure 40: (a) Constant height in-liquid SDM images of the liposomes sample in Figure 39 (a) acquired at four increasing distances from the substrate; Z=175 nm, 215 nm, 270 nm and 325 nm. (b) dC/dz profiles of the liposome indicated by the dashed lines in (a) for the four planes recorded. (c) Capacitance gradient at the centre of each detected liposome in the SDM images measured at four tip-substrate distances. For the largest liposomes (h>200 nm,) data for Z=175 nm are not available. Experimental parameters: σ_{sol}=0.2 mF/m, σ_{lip}=0.8 S/m, f_{mod}=6 kHz, v_{ac}=0.7 V, k~0.43 N/m, f_0=70 kHz (in air).

The value of the capacitance gradient (dC/dz) is determined at the centre of each electrically detected liposome (N=81) from the four SDM images. These values are plotted against the respective distance of acquisition from the substrate (see Figure 40 (c), where the reconstructed electrical approach curves (dotted, coloured data) are compared with the curve acquired on the substrate (black continuous line).

For the largest liposomes no values at the closest distance are obtained. In all cases, the signal on the liposomes is smaller than on the substrate at the same height, from where the negative contrast in the dC/dz images. As expected, the capacitance gradient, dC/dz,

decreases by increasing the imaging distance. For a given imaging distance the values of dC/dz span a range that includes variations ~0.5-0.9 aF/nm much larger than the measuring noise (~0.03 aF/nm). This fact implies that different liposomes show different polarization properties due to their different sizes, but also, due to their different internal structures, as will be shown below.

To show that indeed the SDM measurements are sensitive to the internal structure of the liposomes, we have determined the equivalent homogeneous dielectric constant, ε_{eq}, for each liposome. ε_{eq} is the dielectric constant a homogeneous liposome of a given size would have to give the same capacitance gradient values, dC/dz, as the measured one. If liposomes were homogeneous, ε_{eq} would be independent from its size and shape. Instead, if some internal structure is present ε_{eq} will depend on the size and shape of the liposome.

To determine ε_{eq} we followed the methods of SDM [12], i.e. we calculated theoretical dC/dz vs distance curves for a homogeneous dielectric liposome model (Figure 37 (a) and bottom inset in Figure 42 (a)) and fitted them to the experimental dC/dz vs distance values reported in Figure 40 (c). Before that, the tip geometry and interfacial capacitances were calibrated from an approach curve acquired on a bare part of the metallic substrate [12, 28, 30] (the experimental curve and relative fitting is reported in Figure 41).

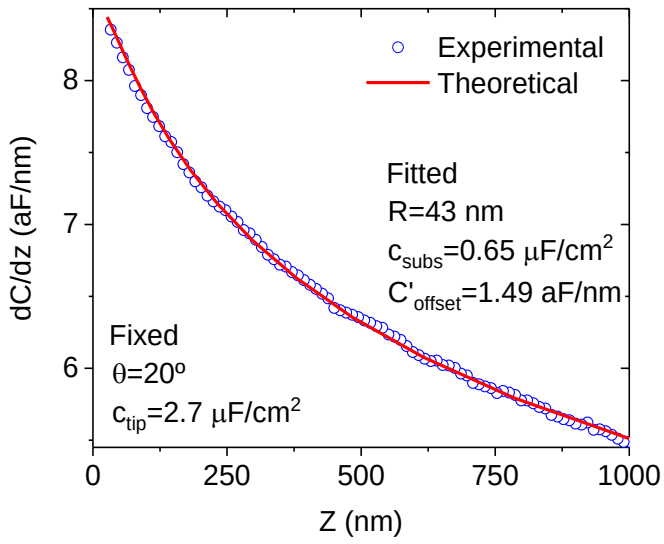

Figure 41: (Symbols) Capacitance gradient approach curve acquired on a bare part of the functionalized metallic substrate. (continuous line) Fitted theoretical curve obtained from a tip/substrate model. The

parameters fitted are the tip radius, R=43 nm, the substrate interfacial capacitance, $c_{substrate}$=0.65 μF/cm^2 and the capacitance gradient offset C'_{offset}=1.49 aF/nm. The tip parameters that have been kept fixed are: half cone angle, θ=20º, tip interfacial capacitance, c_{tip}=2.7 μF/cm^2, cone height, H=12.5 mm, cantilever thickness, W=3 μm and cantilever length, L=3 μm. A global renormalization factor α=1.24 has been applied to account for potential losses and uncertainties in the photodiode sensitivity. The renormalization factor does not affect the specific capacitance values.

The shape and size of each liposome are obtained from the topographic image, and once the tip geometry and interfacial capacitances are calibrated, ε_{eq} can be extracted, being the single fitting parameter. For the conductivity and dielectric constant of the external solution we took σ_{sol}=0.2 mS/m and ε_{sol}=78, respectively, although the actual conductivity value does not play any role since the frequency is above the relaxation frequency of the electrolyte.

Figure 42 (a) (symbols) show the obtained values for the equivalent homogeneous dielectric constants for the N=81 liposomes electrically detected as a function of the height of each liposome. The values of ε_{eq} show a clear dependence on the size of the liposomes, what is an unambiguous indication that the liposomes present some internal dielectric heterogeneity. As it is well known, the internal electrical heterogeneity of the liposomes comes from the existence of one (or several) lipid bilayers with electric properties much different from those of the enclosed solution. We also note that the equivalent homogeneous dielectric constant values, ε_{eq}, span a range from ~4 to ~48. In all cases, these values are smaller than the dielectric constant of the external solution (ε_{sol}=78), from where the negative contrast observed in the in-liquid SDM images (Figure 40 (a)), as anticipated before.

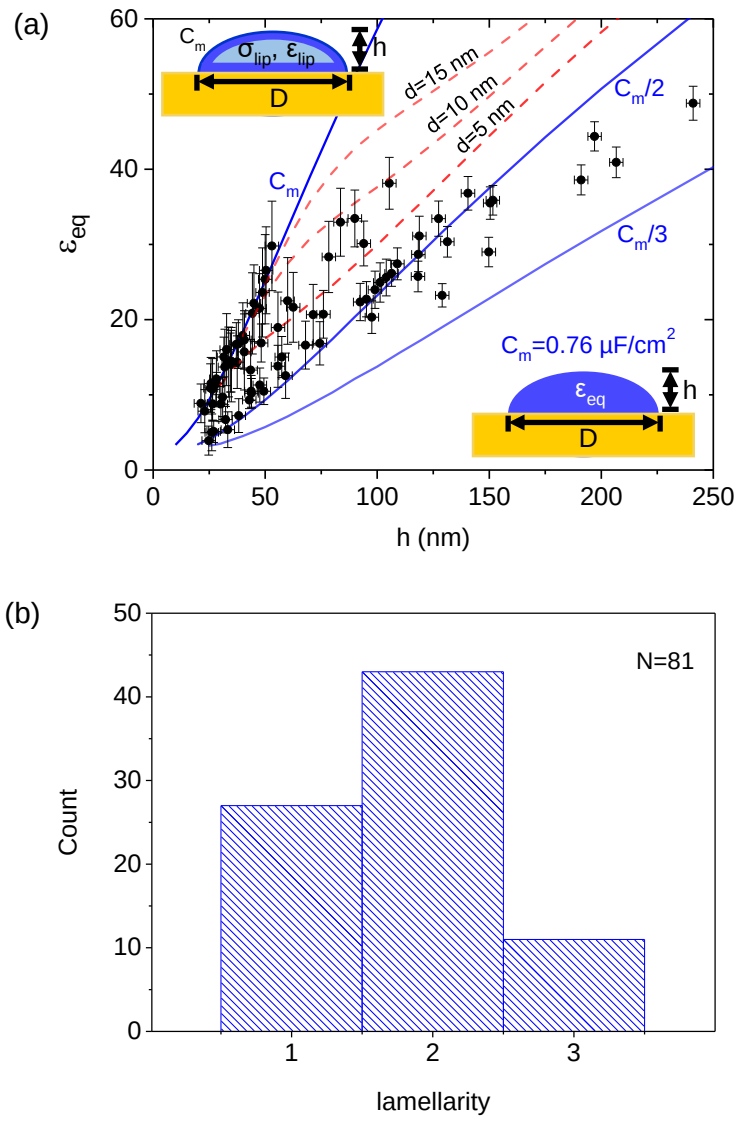

Figure 42: (a) (symbols) Equivalent homogeneous dielectric constant, ε_{eq}, of the liposomes as a function of its height for the liposomes electrically detected in Figure 40 (a). The vertical error bars correspond to the fitting error, while the horizontal one to the uncertainty of the height determination. The model used in the calculations is shown in the bottom inset. The height and width (and shape) have been determined from the topographic image in Figure 39 (a). The tip geometry has been determined from a calibration dC/dz *approach curve acquired on a bare part of the substrate (Figure 41), giving* R*=43 nm,* θ*=20º,* C'_{offset}*=1.5 aF/nm and* $c_{substrate}$*=0.6 μF/cm². The remaining parameters of the tip and solution are the same as in Figure 38 (b). Blue continuous lines: theoretical values for* ε_{eq} *predicted from the uni-lamellar liposome model shown in the top inset, with membrane specific capacitances* c_m*=0.78 μF/cm², *c_m*/2 and* c_m*/3. For the internal solution we took* σ_{lip}*=0.8 S/m,* ε_{sol}*=78, corresponding to the solution used to prepare the liposomes. Red dashed lines: theoretical values for* ε_{eq} *predicted for a bi-lamellar model with* c_m*=0.78 μF/cm² and interlamellar separations d=5 nm, 10 nm and 15 nm. (b) Distribution of lamellarity corresponding to the liposomes electrically detected in Figure 40 (a).*

To obtain more information on the internal structure of the liposomes, we have considered a uni-lamellar liposome model (Figure 37 (b) and top inset in Figure 42 (a)) with membrane specific capacitances c_m, $c_m/2$ and $c_m/3$. This model predicts the behaviour expected for uni-, bi- and tri-lamellar liposomes for small interlamellar separations, as we have shown before. For the internal solution conductivity and dielectric constant, we took the values corresponding to the solution used to prepare the liposomes, σ_{lip}=0.8 S/m and ε_{lip}=78, respectively. For the specific capacitance of the lipid bilayer, we have taken the value that makes that no value of ε_{eq} lies on the left of the curve for the uni-lamellar liposome with specific capacitance, c_m. With this condition we obtain c_m=0.78 μF/cm^2. Remarkably, this value is within the range of values obtained with the same technique for the membrane specific capacitance of solid supported DOPC planar lipid bilayers (c_{DOPC}=0.7-0.8 μF/cm^2) [31] studied in the precedent chapter. The dependence of the equivalent homogeneous dielectric constant, ε_{eq}, as a function of the height of the liposomes predicted by this model is shown by the continuous blue lines in Figure 42 (a). The theoretical curves nicely predict the trend of the experimental equivalent homogeneous dielectric constant values with the height of the liposomes. Most experimental ε_{eq} values fall on the curves corresponding to c_m and $c_m/2$, while a few of them fall in between the curves for $c_m/2$ and $c_m/3$ and between the curves for c_m and $c_m/2$. According to the analysis presented above (Figure 38), the liposomes whose ε_{eq} values fall on the curves for c_m and $c_m/2$ correspond to uni- and bi-lamellar liposomes, with the lamellae close packed in the latter case. Moreover, those liposomes whose ε_{eq} values fall between the curves for c_m and $c_m/2$ (res. $c_m/2$ and $c_m/3$) correspond to bi-lamellar (res. tri-lamellar) liposomes with the lamellae being some distance apart. The separation between the lamellae can be estimated by considering multilamellar models. For instance, by considering the bi-lamellar liposome model in the insert of Figure 38 (a) we can determine the theoretical dependence of ε_{eq} as a function of the liposome height for different interlamellar separations, d. The result of these calculations is represented by the red dashed lines in Figure 42 (a). According to this analysis, we can conclude that the separation between lamellae for the bi-lamellar liposomes is below ~10 nm.

The above analysis shows that the lamellarity of each individual liposome can be determined from in-liquid SDM measurements, and that the inter-lamella separation can be estimated, especially in the case of low lamellarity liposomes (n=2). The distribution of lamellarity corresponding to the sample in Figure 40 (a) is shown in Figure 42 (b). Bi-lamellar liposomes are the more abundant ones (~53%), followed by uni-lamellar liposomes (~33%) and tri-lamellar liposomes (~14%).

5.4 Discussion

We have measured the dielectric properties of sub-micrometric liposomes adsorbed on planar electrodes by means of in-liquid scanning dielectric microscopy in force detection mode (in-liquid SDM). For each liposome we have measured the equivalent homogeneous dielectric constant, ε_{eq}, and demonstrated that from this parameter one can obtain information on the lamellarity of the liposomes (number of lamellae), the separation between the lamellae, d, and the specific capacitance of the lipid bilayer, c_m. For the DOPC liposomes analysed here, we have detected liposomes containing up to 3 lamellae, with the bi-lamellar liposomes being the more abundant ones (Figure 42 (b)). Concerning the separation between lamellae, we have found it to be small in the case of bi-lamellar liposomes (d<10 nm), indicating that the internal lamella is closed packed with the external one. As lamellarity increases (n>2), the sensitivity to lamellarity, and even more, to interlamellar separation, decreases, so that information on the interlamellar separation cannot be unambiguously determined.

With the present approach the lamellarity of the liposomes has been determined in a non-invasive and label-free way, what constitutes an advantage with respect to other existing techniques to determine the lamellarity of single liposomes, such as electron or fluorescence microscopies or mechanical probing [306, 307]. For instance, with respect to cryo-Transmission Electron Microscopy or Freeze-Fracture Electron Microscopy, it offers the advantage of being non-destructive, in the sense that it enables determining the lamellarity and performing further functional analyses to be carried on a given liposome (e.g. to determine other biophysical

properties or investigate biochemical reactions and time dependent processes). With respect to fluorescence microscopy, it offers the advantage of being label-free and to provide information on the lipid bilayer capacitance, complementary to the functional information obtained by using environmental sensitive probes [10, 270, 238]. Finally, with respect to mechanical techniques such as micropipette aspiration and deformation [308, 309] and force spectroscopy AFM [299], the present approach offers the advantage of being a non-contact technique, and hence less invasive, and applicable to both gel and liquid phase liposomes. For liquid phase liposomes the detection of deformations or multiple rupture events can be problematic due to their very soft nature (stiffness ~mN/m) [318]. Besides this, the present approach offers electrical information on the liposome (e.g. specific lipid bilayer capacitance) complementary to the mechanical information obtained from mechanical techniques.

With the proposed approach one has access to both the lamellarity of the liposomes and its size and shape. Therefore, it constitutes a unique technique to investigate whether there is any relation between the lamellarity of the liposomes and their size and shape once adsorbed. Lamellarity has been shown to (slightly) affect the stiffness of liposomes adsorbed on solid supports [299], and the stiffness has been shown to correlate with the liposome shape (contact angle) once absorbed [318], so that it is reasonable to expect that some relation can exists between the shape of adsorbed liposomes and its lamellarity. To investigate it we have characterized the size of the liposomes by the equivalent spherical radius, R_{eq}, and the shape by the ratio h/R_c, where R_c is the radius of curvature of the liposomes, which if assumed spherical, is given by $R_c=[(D/2)^2+h^2]/2h$. The parameter h/R_c contains the same information than the contact angle, α, for flattened liposomes, since $h/R_c=1-\cos(\alpha)$ for $\alpha<90$. These parameters have been used earlier in the analysis of the stiffness [318] and lamellarity of adsorbed liposomes [299].

Figure 43 shows the dependence of the ratio h/R_c with the equivalent spherical radius R_{eq} for the liposomes analysed in the present work. Symbols have been coloured according to the

number of lamellae of the corresponding liposome as determined from the electrical measurements (Figure 42).

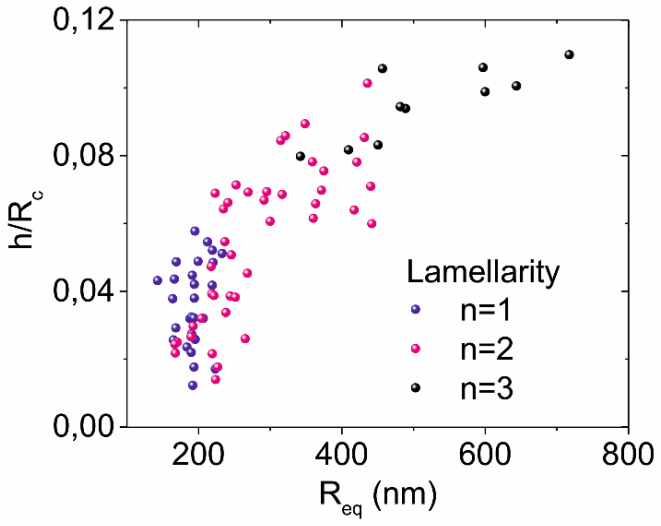

Figure 43: Geometrical shape ratio h/R_c *as a function of the liposome equivalent spherical radius,* R_{eq}*, for the liposomes electrically analysed in Figure 42. Symbols have been coloured according to the number of lamellae of the corresponding liposome as identified from Figure 42.*

According to Figure 43, a correlation between lamellarity and size exists, in agreement with usual liposome classifications [295]. In the present case, large liposomes (500 nm<R_{eq}<800 nm) are found to be mainly tri-lamellar; intermediate sized liposomes (250 nm<R_{eq}<500 nm) are found to be mostly bi-lamellar; finally, small liposomes (R_{eq} <250 nm) are found to be either uni- or bi-lamellar. Interestingly, large uni-lamellar liposomes (with R_{eq} >250 nm) are not found in this sample. On the other hand, the liposome shape, represented by the parameter h/R_c, does not seem to provide additional information on lamellarity, besides that given already by the size, at least for the case of DOCP liposomes. The lack of an eventual relationship between lamellarity and shape can be specific of liquid phase liposomes, like DOPC liposomes, for which a relation between shape and stiffness was also difficult to establish [318], and for which lamellarity analysis by mechanical methods, such as force spectroscopy AFM measurements, can find difficulties due their very soft nature [299]. The fact that in-liquid SDM can provide the lamellarity in the case of both liquid and gel phase liposomes (because is a non-contact technique) constitutes a clear added value of the proposed methodology.

The in-liquid SDM measurements have shown to be sensitive to the inter-lamellar separation, especially for bi-lamellar liposomes, what constitutes a remarkable result of the present work. Figure 44 (a) shows the sensitivity of the capacitance gradient to the interlamellar separation, $\partial/\partial d\left(dC/dz\right)$, as a function of the interlamellar separation for a bi-lamellar liposome for three different conductivities of the internal solution (the curves are just the derivatives of the curves shown in Figure 38 (b)). As a reference instrumental value, we have drawn the sensitivity corresponding to a 5 nm variation of the interlamellar separation with a typical noise of the measuring instrument of ~0.05 aF/nm, $\partial/\partial d\left(dC/dz\right)_{ref} = 0.01\,\mathrm{aF/nm^2}$ (dashed line in Figure 44 (a)). It is seen that in-liquid SDM is sensitive to the interlamellar separation for relatively large conductivities (here for σ_{lip} >0.1 S/m). In addition, the range of interlamellar distances accessible is also dependent on the conductivity of the internal solution. For instance, for the data in Figure 44, it is predicted that the measurements would not be sensitive to the interlamellar separation for the smallest internal conductivities (σ_{lip}=0.01 S/m and 0.1 S/m), while for σ_{lip}=1 S/m (close to the experimental value of σ_{lip}~0.8 S/m) they are sensitive to interlamellar separation smaller than ~20 nm only. These simulations confirm what we concluded from the analysis of Figure 42 (a).

In order to improve the access to the interlamellar separation one could vary the frequency of the applied voltage, f_{el}. Figure 44 (b) shows the dependence of the sensitivity of dC/dz to the interlamellar separation, $\partial/\partial d\left(dC/dz\right)$, as a function of the interlamellar separation for a bi-lamellar liposome with internal conductivity σ_{lip}=1 S/m, for four different frequencies of the applied potential f_{el}=1 MHz, 5 MHz, 10 MHz and 100 MHz (5 MHz is the one used in the measurements reported in the present work). The rest of parameters are the same as those in Figure 38 (b). As a rule, by increasing the frequency of the applied potential the sensitivity to the interlamellar separation decreases and at the same time broadens. Therefore, a trade-off between sensitivity and available range of interlamellar distances should be met. The frequency of 5 MHz (green line in Figure 44 (b)) used in the present work satisfies precisely

this trade-off for liposomes with an internal conductivity in the range σ_{lip}~0.8 S/m like the ones analysed here.

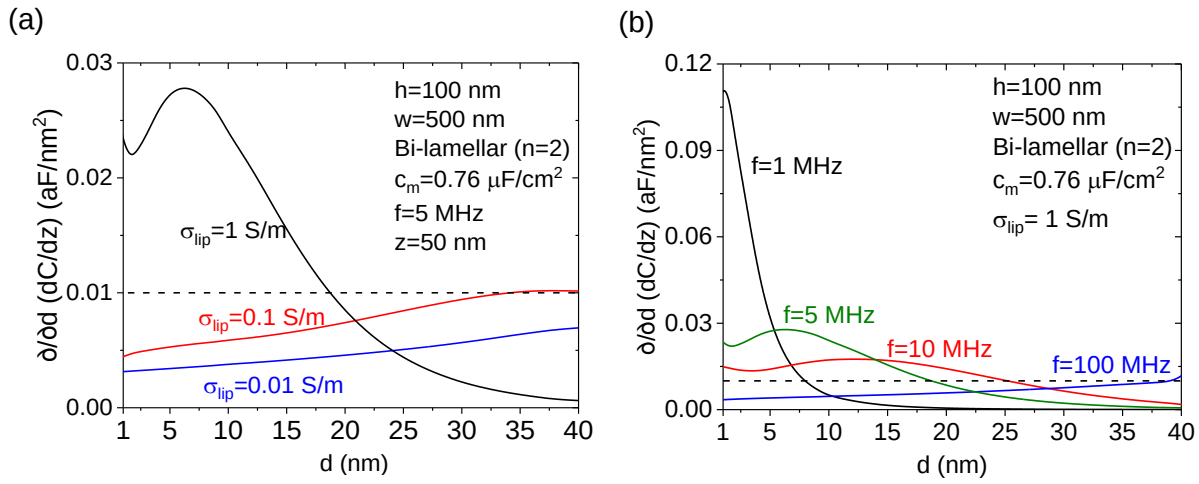

Figure 44: Sensitivity of dC/dz *to the interlamellar separation,* d*, as a function of the interlamellar separation for a bi-lamellar liposome for (a) three internal conductivities, σ_{lip}=0.01 S/m, 0.1 S/m and 1 S/m and (b) four different frequencies of the applied electric potential, f_{el}=1 MHz, 5 MHz, 10 MHz and 100 MHz. The dashed line represents the sensitivity required to detect an interlamellar distance variation of 5 nm for an instrumental noise of 0.05 aF/nm. The rest of the parameters are the same as those in Figure 38 (b).*

From the analysis of the lamellarity by means of in-liquid SDM we derived also the value of the lipid bilayer specific capacitance, c_m. The value obtained in the present study, c_m~0.75 µF/cm^2, is in remarkable agreement with the value found recently on solid supported DOPC planar lipid bilayer patches by using the same technique (c_m~0.70-0.8 µF/cm^2) [31]. This result demonstrates that the lipid bilayer specific capacitance can be measured on adsorbed liposomes by means of in-liquid SDM. In the case that the specific capacitance was the magnitude of interest, it would be more convenient to prepare uni-lamellar liposome samples, by using any of the existing methods for that purpose (e.g extrusion or the inverted emulsion method). The tip-liposome capacitance gradient, dC/dz, for uni-lamellar liposomes depends roughly logarithmically with the membrane specific capacitance in the range of values of interest 0.1-1 µF/cm^2 (as we see in Figure 45).

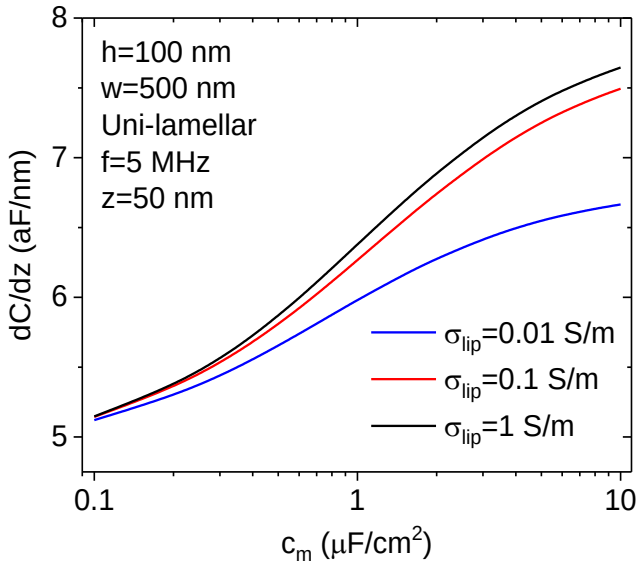

Figure 45: Numerically calculated dependence of the tip-liposome capacitance gradient with the specific capacitance of the lipid bilayer for a uni-lamellar liposome. The dependence is roughly logarithmic. The parameters used are the same as in Figure 38 (b).

This dependence is strong enough in relation to the sensitivity of the measuring instrument to enable extracting this parameter with good accuracy. We show it explicitly in Figure 46, where we plot the sensitivity of dC/dz to the membrane specific capacitance $\partial/\partial c_m\,(dC/dz)$, as a function of the specific capacitance for a uni-lamellar liposome with internal conductivities in the range σ_{lip}=0.001 S/m-1 S/m (the rest of parameters are the same as in Figure 38 (b)). For comparison we plot the sensitivity corresponding to a variation of the specific capacitance of 0.1 μF/cm^2 for an instrument with noise 0.05 aF/nm, $\partial/\partial c_m\left(dC/dz\right)_{ref} = 0.5\,10^2\,nm$ (dashed line in Figure 46). For the range of c_m=0.1-1 μF/cm^2 the instrument can access to variations of the c_m. In this respect, it is worth to note that despite the relatively large height of the adsorbed liposomes as compared to that of a planar lipid bilayer, the sensitivity of the capacitance gradient dC/dz to the specific lipid bilayer capacitance, c_m, is similar in both systems. This is demonstrated in Figure 46, where we compare the sensitivity of the capacitance gradient to the specific capacitance as a function of the specific capacitance, c_m, for measurements performed on a solid supported bilayer patch 5 nm thick and 500 nm wide (dashed red line)

and on a uni-lamellar liposome 100 nm high and 500 nm wide with internal conductivities spanning the range 0.001 S/m-1 S/m. The sensitivities for both systems are comparable. This result is a consequence of the fact that the ac voltage drop across the lipid bilayer in a liposome is much larger than the voltage-drop in the core of the liposome, even for low internal conductivities, because the dielectric constant and conductivity of the lipid bilayer (ε_m~2-3, σ_m~0) is much lower than that of the solution inside the liposome (ε_{lip}~78, σ_{lip}~0.01-1 S/m). This fact makes the size of the liposomes to play a relatively small role.

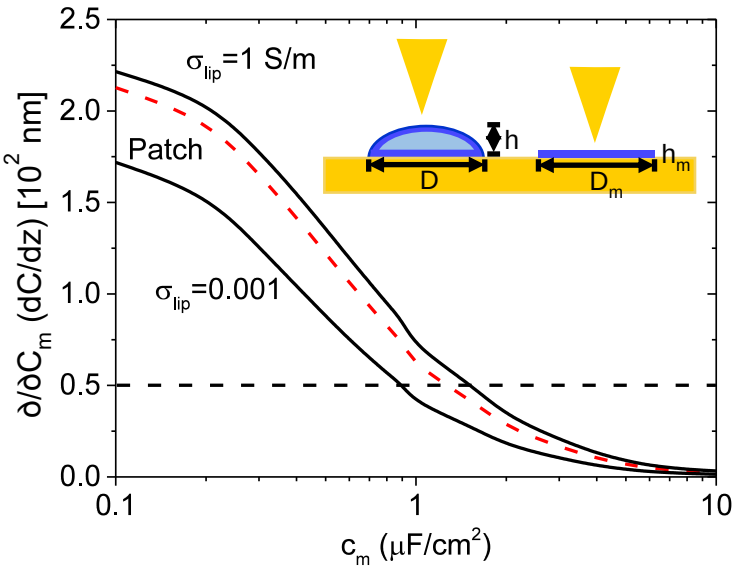

Figure 46: Sensitivity of the capacitance gradient to the specific capacitance of the lipid bilayer membrane as a function of the specific capacitance for measurements performed on a supported lipid bilayer patch (red dashed line) and on a uni-lamellar liposome with internal conductivity spanning the range s_{lip}=0.001 S/m-1 S/m (black continuous lines). Parameters of the calculations: w_{patch}=500 nm, h_{patch}=5 nm, w_{lip}=500 nm, h_{lip}=100 nm, σ_{sol}=0.2 S/m, ε_{sol}=ε_{lip}=78, R=30 nm, θ=20º, f_{el}=5 MHz, Z=50 nm. Inset: schematic representation of the two systems.

Finally, we comment that in the present work measurements have been done in a low conductivity external solution (nominally σ_{sol}~0.2 mS/m, although in practice probably higher due to salt contamination). In-liquid SDM measurements can be performed also in solutions of higher conductivity, as reported earlier [28]. In this case higher measuring frequencies become necessary. Typically, for solutions up to 10 mM ion concentration measurements can be performed for frequencies lower than 100 MHz, following the methods described here. For

higher concentrations, frequencies in the GHz rage would be required, which require of some specific adaptations of the measuring set-ups.

5.5 Conclusions

We have shown that the lamellarity of single liposomes can be measured in a non-invasive and label-free way by means of in-liquid Scanning Dielectric Microscopy. In addition, information on the interlamellar separation can also be obtained in low lamellarity liposomes, and on the specific capacitance of the lipid bilayer membrane. For non-extruded DOPC liposomes with equivalent spherical radius in the range ~100 nm - 800 nm we have found that for sizes larger than ~400 nm only tri-lamellar liposomes are identified, for sizes between ~250 and 400 nm only bi-lamellar ones have been found, while for sizes below ~250 both uni- and bi-lamellar liposomes are equally found. No large uni-lamellar liposomes have been detected. In the case of bi-lamellar liposomes, we have found that the interlamellar separation was below ~10 nm. Concerning the lipid bilayer specific capacitance value obtained, it agrees with that obtained on planar lipid bilayers. We have shown that the accuracy with which this parameter can be determined in the liposomes is similar to that on planar lipid bilayers. One relevant advantage of the proposed approach is that it can be equally applied to liquid and gel phase liposomes since it is essentially a non-contact technique. Present results open interesting routes for the analysis and characterization of single liposomes and of nanovesicles in general.

5.6 Supplementary information

In the present work, all the theoretical analyses have been done by means of finite element numerical calculations. While numerical calculations are necessary in order to obtain an accurate quantitative description of the tip-liposome interaction, it would be convenient to have at a disposal qualitative analytical models to analyse the complex phenomenology of the system.

Based on previous analysis of the tip-nanoparticle electrical interaction in air environment [12], it has been found that the values of the tip-liposome capacitance gradient can be described qualitatively by the colloidal theory of multi-shell particles [32], according to the phenomenological relation:

$$\frac{dC}{dz} \approx \alpha + \beta \log\left(\left|\varepsilon_{eq}^{*}\right|\right) \tag{31}$$

where ε_{eq}^{*} is the equivalent homogeneous complex permittivity of the liposomes in a uniform external electric field [319, 320], and a and b two phenomenological parameters that depend on the size of the liposome and of the tip, and on the tip-sample distance, among other factors. Figure 47 shows the comparison of the numerically calculated data in Figure 38 (b) with the prediction of Eq. (31) adjusting a=3.53 aF/nm and b=1.7 aF/nm and using the expression for ε_{eq}^{*} corresponding to a spheroidal bi-lamellar liposome in a uniform electric field (Ref. [32]).

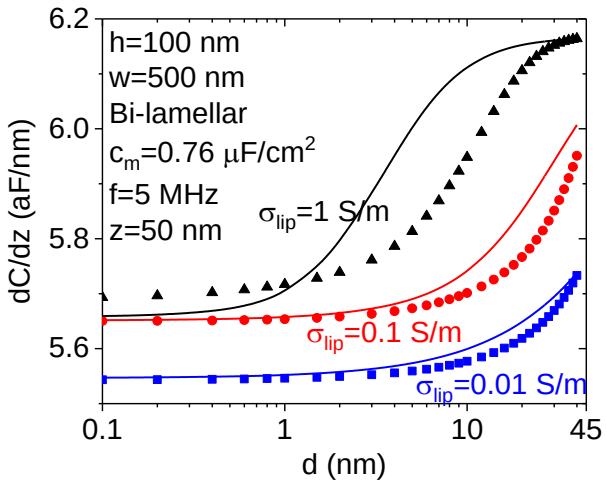

Figure 47: (continuous lines) Capacitance gradient as a function of the interlamellar separation obtained from Eq. (31) with ε_{eq}^{*} given by the expression corresponding to a spheroidal bi-lamellar liposome in an external uniform electric field (detailed in Ref. [32]) of height h=100 nm, diameter D=500 nm, bilayer thickness t_m=3.5 nm, and bilayer dielectric constant ε_m=3 (corresponding to a specific membrane capacitance c_m=0.76 mF/cm²). The internal and external solutions are assumed to have the same dielectric constant, ε_{lip}= ε_{sol}=78. The external conductivity is σ_{sol}=0.2 μS/m (same parameters as in Figure 38 (b)). The phenomenological parameters in eq. (31) have been set to a=3.53 aF/nm and b=1.7 aF/nm in order to reproduce qualitatively the capacitance gradient values numerically calculated for an adsorbed bi-lamellar liposome (symbols, same data as in Figure 38 (b)).

The agreement is quite reasonable given the crude approximations made. It shows that this simple model also captures pseudo-quantitatively the dependence of the capacitance gradient on other parameters such as the bilayer specific capacitance or the frequency of the external applied voltage, as shown below.

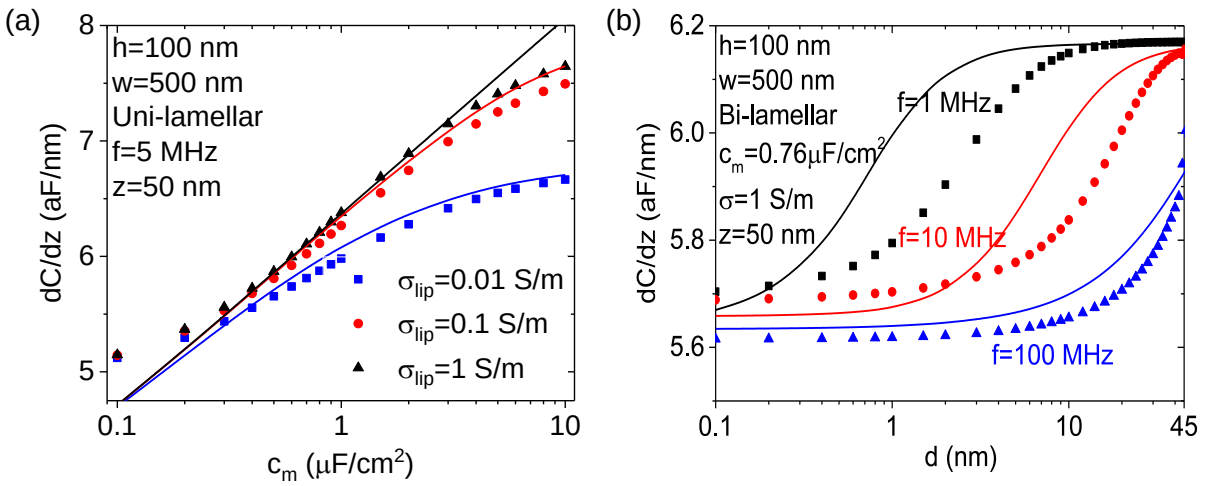

Figure 48: (a) (continuous lines) Capacitance gradient as a function of the specific capacitance of the lipid bilayer for a uni-lamellar liposome of height h=100 nm, width w=500 nm, bilayer thickness t_m=3.5 nm, and an aqueous internal solution (ε_{lip}=78) with three different conductivities σ_{lip}=0.01 S/m, 0.1 S/m, 1 S/m, predicted by Eq. (31) with the equivalent complex permittivity calculated with for a frequency of 5 MHz. The phenomenological parameters appearing in Eq. (31) have been set to a=3.53 aF/nm and b=1.7 aF/nm. The symbols represent the results of the finite element numerical calculations made on an adsorbed liposome of the same width and height. Remember that the geometry of the adsorbed liposome corresponds approximately, although not exactly, to a spherical cap, while the geometry used to derive the equation for ε^*_{eq} corresponds to a full spheroid (detailed in [32]). (b) (continuous lines) Idem for capacitance gradient of a bi-lamellar liposome as a function of the inter-lamellar separation and fixed lipid bilayer specific capacitance, c_m=0.76 μF/cm² and conductivity s_{lip}=1 S/m (continuous lines) for three different frequencies f=1 MHz, 10 MHz and 100 MHz. The symbols represent the finite element numerically calculated values for a bi-lamellar adsorbed liposome.

6. Towards natural samples: In-liquid SDM of Purple Membrane Patches

In this chapter we take one step forward, reporting in-liquid SDM experiments performed on natural purified purple membrane (PM) patches. The challenges of moving towards the analysis of natural systems are presented. We observe that supported PMs can manifest a curvature of the membrane surface, which can possibly arise due to environmental conditions (e.g. light and pH) or lipid content. We highlight that for the quantification of the dielectric constant of PMs by in-liquid SDM, we rely on identifying unambiguously the topography of these structures, that can also be affected by electrostatic contributions given by the tip and sample EDLs interaction in low ionic concentrated media. Aware of this problematic, we performed a preliminary analysis of the SDM data, exploring ways to circumvent this issue and evaluating which conclusions could be drawn. However, further investigations are required to provide a reliable method of analysis and definitive answers about the dielectric properties of PM patches in water.

6.1 Introduction

The lipid bilayer forming the "skeleton" of bio-membranes presents a unique two-dimensional hydrophobic environment for membrane proteins. The study of membrane proteins in their functional environment is preferred over, for instance, crystallized proteins (which are suitable for X-ray diffraction experiments), also due to the technical difficulties for their crystallization [321, 322].

Several protocols have been developed to produce or purify and later introduce a wide variety of proteins in model lipid systems; this is mostly done to simplify their study in a less complex environment. However, it is far more appealing to characterize the proteins in their native environment; this can be attempted by directly isolating the membranes from cells

sources (bacteria, eukaryotic). These procedures are not always easy, and in general provide a unique array of technical challenges, but it also creates research opportunities.

One of the membranes which isolation and purification is quite established, and thus constitutes a popular test sample, is the Purple Membrane (PM) [323, 324]. PM patches are derived from the plasma membrane of Halobacterium Salinarum. They are composed of one single type of protein: bacteriorhodopsin (BR), a light-driven proton pump composed of seven transmembrane helices. BR has extraordinary functionality and several high-tech applications based on it have been suggested, for instance high capacity data storage [325].

Upon light exposure, the protein experiences a spectral change that depends on the illumination time and reflects the photobleaching process of PM [326]. This leads to structural changes [327] among which a transient “wedge-like” geometrical change of the protein, due to a tilt in one of the seven R-helical domains of BR (helix F). This process is accompanied by release or uptake of protons [328] from the cytoplasm to the extracellular space.

In the membrane, BR proteins form a two-dimensional array: Protein trimers are arranged in a hexagonal lattice, surrounded by lipids in a stoichiometric ratio of 10:1 between lipids and BR. The stiffness of the BR crystal is consistently higher as compared to the lipid bilayer [329].

The proteins in the lattice are all oriented in the same way, therefore the patches exhibit two different sides, intracellular or cytoplasmic (CP) and extracellular (EC) with distinct characteristics (Figure 49). The EC side is very resistant to pH or salt concentration changes of the surrounding buffer and maintains the well-known stability of PM. The CP leaflet, instead, contains very mobile intertrimer phospholipids largely affected by salt and pH changes [330].

Charged residues are present on both sides of the membrane [331]; glutamates on the EC and aspartic acids on the CP. These residues are included in protein’s loops that protrude above the lipid surface [326]. Among them in particular, a negatively charged C-terminus loop ($4<pH<9$) extends toward the CP side. This C terminus is very dynamic and, in addition to the

net charge, it also contains many other polar residues. The charge density of PM patches was determined in several works [332, 333, 334] and on different substrates (mica in [335], alumina in [336]).

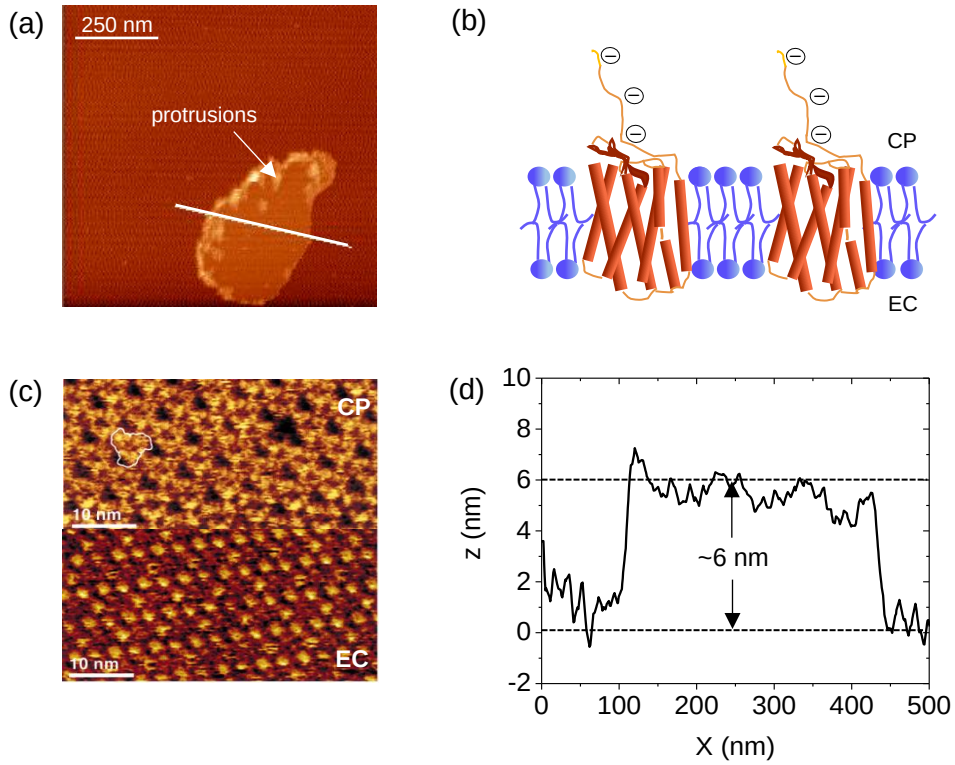

Figure 49: (a) PM patch in 20 mM Tris, 300 mM KCl pH8 on mica. The patch displays several protrusions all around its borders. (b) Schematic of BR proteins in a layer. (c) High resolution images of the BR crystal lattice, cytoplasmic (CP) side and extracellular (EC) side, images adapted from [326]. (d) Profile taken along the white line drawn on the patch in (a); the thickness measured is ~6 nm, quite in agreement with literature data.

The thickness of such protein crystal measured by AFM in strong ionic conditions was reported to be ~6.4 nm (6.2 nm according to x-ray and electron crystallography studies [337]) (see Figure 49). Purified patches can sometimes present a 'corolla' around the more structured protein lattice, mostly composed of lipids (about 2.8 nm). It is also reported that, when the membrane is only 1 nm thinner than the crystal, it is probably non-assembled, i.e. composed of lipids plus proteins but not in a crystal arrangement [330]. This happens at high pH>10, at which the assembly can become more difficult.

Dielectric studies on PM in dry were extensively carried out by our research group in current [20] and force-sensing [19] (at kHz frequencies).

In dry environment (<5% humidity), a constant dielectric permittivity of ~3 was extracted at all frequencies, in agreement with previous studies of BR in dry [21]; although other works reported a value of ~2 [19, 20]. Ensemble measurements at the lowest possible hydration (21%) provided a value of $\varepsilon_r \sim 3.3$ at 1 MHz [338].

The dielectric constant at MHz frequencies (1 to 10 MHz at least), which is our range of operation, was also found to be ~3 in humidity >30%; while another ensemble study (at 60% humidity) reports the double of this value [339].

Even if BR remains functional despite being dried (in humid air [18]), water plays an essential role for dipole fluctuations in the protein as well as for the stacking of proteins into layers [17]. Furthermore, several other proteins are only functional in liquid environment, stating the importance of in-liquid SDM. In the present chapter we take advantage of the implementation of in-liquid SDM to carry out dielectric measurements on PM patches in liquid environment, opening the way for the study of many more natural biomembranes and their transmembrane proteins.

Yet, the complexity of the quantification of the results is increased, and further research will be needed to complete it.

6.2 Indentation vs electrostatic interaction

As mentioned, solid supported PM patches can display a curved topography due to the strong coupling between the BR units in the crystalline lattice, depending on pH and illumination conditions [340, 341, 342]. In nature, only low light levels occur and the total number of BRs in the "wedge-shaped" state is supposed to be negligible [343]. However, in AFM experiments, performed in a drop of few tens of microliters and especially when it is not possible to work in buffer (as for in-liquid SDM measurements), the pH of the solution is a

difficult parameter to control. Furthermore, the curvature of PMs can be regulated by lipid content [343]. All these factors may result in a “dome-like” shaped BR patch. In addition, depending on the substrate of choice and the type of interaction established, BR patches can even ‘re-close’ their own extremities forming vesicles, or stack on top of each other.

In general, the topographical characterization of soft systems like natural membranes is not trivial to carry out by AFM. When approach curves are performed, depending on the “cohesion” of the membrane, the parameters of the lever (spring constant and geometry of the tip apex and its radius) and the approach speed, contact events are not even detected, or the object is indented before a deflection of the cantilever is visualized.

Besides being dependent on real topographical features, the height of biomolecules measured with the AFM in solution also depends on electrostatic interactions [344]. Indeed, when a charge of the same sign is present on both the sample surface and tip, in solutions with low ionic strenght, the length of the double layers established at the solid-liquid interfaces can be relatively high; their overlap occurs at further distances, and a repulsive force is felt by the tip as it approaches the sample, in agreement with the DLVO model. This interaction has been reported for PM in several works [335, 344, 336] and adds a contribution to the height measured of the PM surface, which it is not of structural origin. In this case, what might look like deflection of the cantilever due to contact with the surface, can instead just be the result of a long-range electrostatic interaction. This effect only vanishes in concentrated buffer solutions (e.g. Tris 20 mM and KCl 300 mM is normally used to achieve high resolution of the BR crystal lattice) [345].

In diluted solutions, depending on which side the patch is deposited on the substrate (CP or EC side), AFM-topographical images can display a “dome-like” profile. A curved topography was observed by Zhong et al. when the CP side of the membrane was facing up [335]. This topographical feature was only apparent, due to the interaction of the tip with charges on the surface and the protein-loop extending towards the outside.

We carried out similar experiments. The data presented in this chapter were acquired using a Nanowizard 4 AFM system (JPK), in collaboration with Oscar Saavedra, PhD student within

the SPM2.0 ITN network. The AFM images were acquired in QI force volume mode, while the force curves displayed were recorded using the “force map” option of the instrument. Only few curves are displayed for clarity.

Our measurements seem to support previous findings. In Milli-Q water, some PM patches display a high topography (patch A Figure 50 (a)), which vanishes upon buffer addition (Figure 50 (b)). Other patches are instead displayed flat even in water (Patch B in Figure 50 (a), h~12-14 nm).

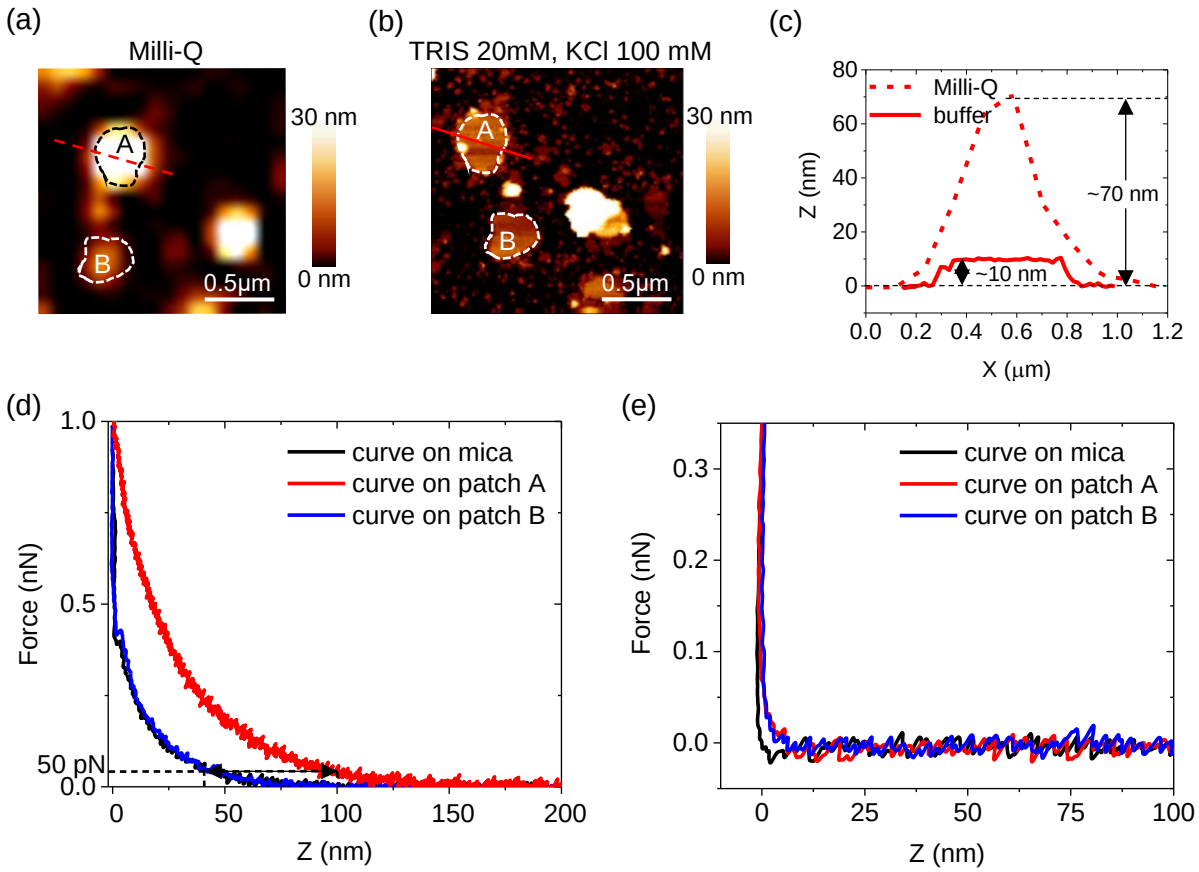

Figure 50: PM patches on mica. Topography in QI mode with set point 50 pN in Milli-Q (18×18 pixels) (a), and after exchange with Tris 20 mM, KCl 100 mM (128×128 pixels) (b). Profiles of patch A along the red lines in (a) and (b). Curves acquired on the substrate and in the centre of patch A and B in Milli-Q water (d) and buffer (e). Tip: MLCT - bio – DC/ cantilever C (material: silicon nitride); k: 0.014 N/m. The “dome-like” structure (patch A), visualized in Milli-Q, spontaneously flattened upon addition of salt in the media, highlights the electrostatic nature of its topography. This is also visible in the force distance approach curves.

The force required to overcome the electrostatic repulsion depends on several parameters intrinsic to the AFM experiment such as the electrolyte type and its concentration, the pH of the buffer solution, the radius and surface charge of the AFM tip and the side (CP or EC) of the PM [344, 345, 346].

Nevertheless, in some other cases, the measured topography is not only the result of an electrostatic contribution, since not all the patches flatten after buffer exchange; even if the layer thickness often decreases with increasing ionic strength of the medium (Figure 51).

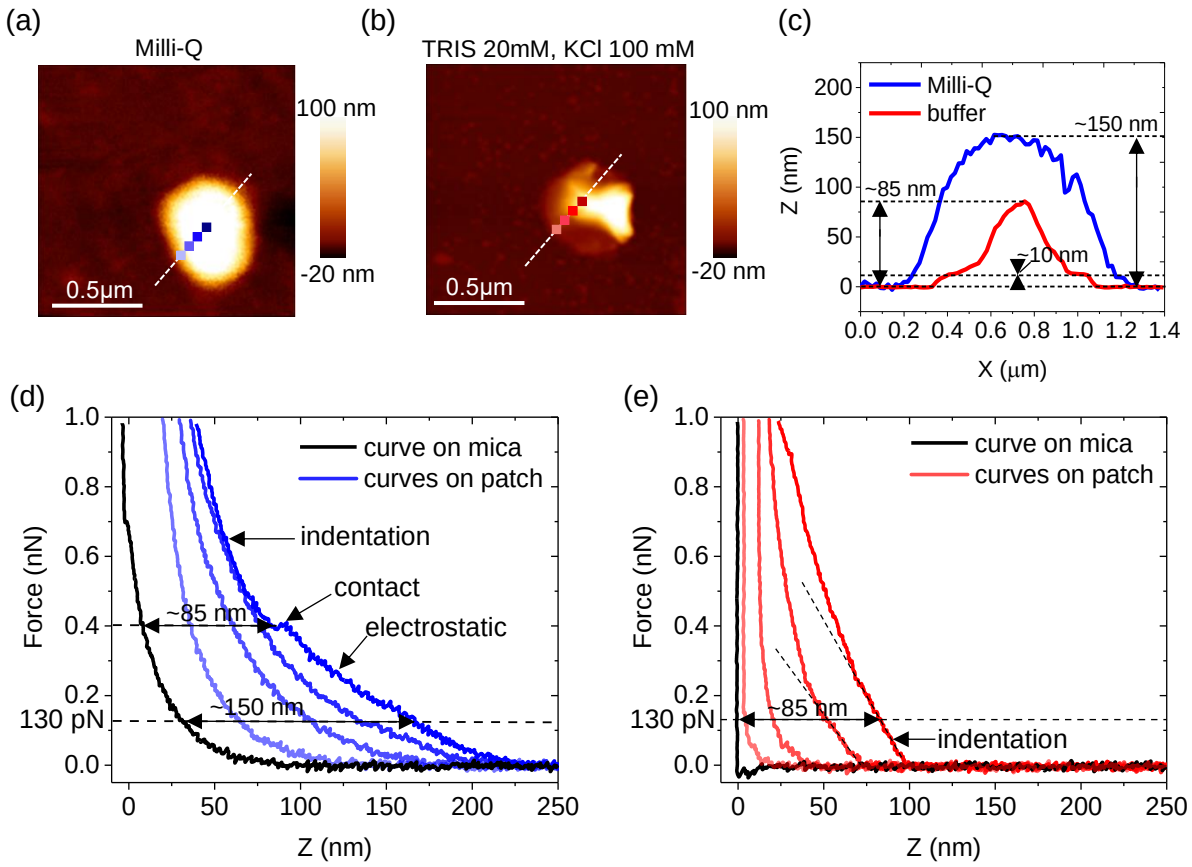

Figure 51: PM patches on mica. Topography of a "dome-like" PM patch acquired in QI mode (128×128 pixels, set point 130 pN) in Milli-Q water (a) and after exchange with Tris 20 mM, KCl 100 mM buffer (b). (c) Profiles of the two topographies along the dashed lines in (a) and (b). (d) Force curves in Milli-Q on the substrate (black) and in the positions indicated by the blue pixels in (a). (e) Force curves on the substrate (black) and in the positions indicated by the red pixels in (b), after buffer addition.

In Figure 51 we again attribute the difference between the topography in water and buffer to long range electrostatic interactions, disappearing upon buffer addition. Yet, in this case,

even if the extremities of the patch re-approach the thickness of a single BR layer, the centre still displays a height of ~ 85 nm (by applying a force of 130 pN), which we identify this time with a real topographical feature.

These observations would confirm that both effects of curvature and charge can be present when imaging PM in Milli-Q. Whether the topography observed is real (curved membranes) or an effect of charges on the surface (apparent “dome-like” topographies), the amplitude of oscillation and the set-point value greatly affect the profiles obtained. Important topographical variations of PM can be observed, as reported, depending on the buffer concentration [344] and the applied force [347] [344], in line with our experiments (Figure 50, Figure 51).

In AFM, it can be difficult to discriminate between pure electrostatic interaction and actual indentation. One way to attempt it, is to fit the force-distance curves with different models; Hertz for indentation (which can be also modified to consider the bottom effect [348, 172]) and DLVO for the electrostatic regime. However, even if a variety of models has been developed for the interpretation of AFM data on biological samples, difficulties in discriminating artefacts in topographies are still present.

The two effects of actual curvature and fictitious topography due to electrostatic interaction further complicate the determination of the contact point, which remains a challenge for soft samples like natural membranes and intact cells. Imaging a surface under different salt concentration provides a route to distinguish electrostatic from purely topographic interactions.

The complexities associated to the imaging of PM patches are representative of the complexities expected when dealing with natural samples. For this reason, we considered PM to be a good test sample to investigate the capabilities of in-liquid SDM to address the dielectric properties of natural biomembranes. In what follows, we describe the results obtained from a preliminary study and the conclusions drawn from it, which, even if not fully satisfactory, could be of interest for further dielectric investigations on natural membranes.

6.3 Materials and methods

6.3.1 Sample preparation for in-liquid SDM measurements

PM patches suspended in 20 mM Tris, 100 mM KCl buffer have been provided by Dr. Milhiet at CBS, Montpellier (purified from Dr. Levy, Institut Curie, Paris, France). 60 µL, 2 µM PM suspension in 20 mM Tris, 100 mM KCl, pH 8 were incubated over freshly cleaved HOPG, for 15 minutes and at room temperature. Afterwards, the buffer was gently exchanged with Milli-Q water, with the scope of removing weakly attached membrane patches and providing the low ionic conditions to carry out SDM imaging. High purity water (18.2 MU cm) was obtained with a Milli-Q water purification system (Millipore). We underline that the pH of a 60 µL drop, where we perform our SDM experiments, cannot be accurately controlled in absence of buffer [349], and pH mis-regulation in the sample is a real possibility.

6.3.2 In-liquid SDM measurements

In-liquid SDM measurements were performed in liquid according to the reported methodology [28], in a commercial Cypher-S AFM system (Oxford Instruments), using HQ:NSC10/Cr Au gold coated probes. The applied voltage had an amplitude 0.75 V, electrical frequency 10 MHz and modulation frequency 2 kHz. The oscillation amplitude measured at the ω_{mod} was converted to capacitance gradient values as in previous works [30] and as reported in Chapter 4.

Topographic and *dC/dz* images in constant height have been acquired in parallel as described earlier in this work. In some cases, at close Z-distances, features start to appear in the phase of the electrical pass, possibly indicating mechanical contact with the surface. Indeed, we normally use this image to monitor the contact with the sample. However, we are not sure whether the phase of the electrical pass can display some other effect, due for

example to conductivity, that might have to be considered when imaging membrane proteins (channels or pumps).

The image acquisition settings (set point, scan speed and gains) were always chosen to optimize the electrical images. In some cases, the thickness of the patches is consistent with literature data; in some others, “dome-like” features are revealed upon slight changes of set-point. Even when the patches topography in the images is displayed as flat, the layers adhesion to the substrate is not guaranteed, since it is setpoint dependent. In our case, this happens especially because the spring constant of the tip used for the electric measurements is quite high (~0.5 N/m) as compared to the ones used for imaging biological samples, and the set-point is not always kept minimum. Force distance curves have been recorded on the substrate and normally in the centre of each patch. The mechanical approach curves can be used to further investigate the real topography of the sample. The fact that an electric field is applied while acquiring the mechanical approach curves might be another factor to consider, although possible effects on the material and its topography still have to be verified.

The electric curves on the substrate, as always, serve for calibration of the tip geometry, determination of the SDM imaging distances, and the substrate and tip interfacial capacitances as reported in previous works [20, 12, 28, 29, 15] and Chapter 4, 5. In several cases, most of the images in constant height are acquired at distances where the cantilever starts to display some deflection in the force-distance curve. Thus, we are not sure whether the system is being indented or the deflection is due to space charge layers. For this reason, the images are not used for quantification, but only help us doing some qualitative considerations. By the same token, the electric curves acquired on the patches are solely considered for fitting from far Z-distances, where we can be sure of avoiding mechanical interactions, van der Waals forces or the presence of diffusive space charge layers.

6.3.3 Finite-element numerical calculations and extraction of the specific capacitance

We quantitatively analysed the SDM images following the methodology applied in Ref. [12] adapted to the liquid environment [29, 30], as described in Chapters 4.

We calibrated the tip geometry and substrate interfacial capacitance by using dC/dz curves on the metallic substrate, as in previous works [12, 15, 189]. The parameters L, H, W were kept fixed to the same values reported in Chapter 4. The half cone angle, θ, was fixed to 20º. The remaining parameters R, c_{tip} and $c_{substrate}$ were obtained from the fitting (they are reported in the caption of Figure 54). The voltage reduction factor was α=1.15.

To extract the dielectric constant of the PM, given the uncertainties in the topography of the patches, which can vary from flat to dome-like of several tents of nanometers, we carried out the quantification considering different possible geometries.

When the patch is considered flat, the system is modelled as a dielectric disc of radius R_m, thickness d_m and dielectric constant ε_m (corresponding to a specific capacitance $c_m=\varepsilon_0\varepsilon_m/d_m$), as in previous works [30, 31].

When the patch is considered dome-like instead, its geometry is defined by the function $Z = h - ax^b$, where $a = \frac{h}{L^b}$, $b = \frac{ln(2)}{ln\left(L_2/L\right)}$. A shell of thickness, d_m, and dielectric constant, ε_m, surrounds a core with dielectric constant and conductivity of water, ε_{water}~80 and σ_{water} ~ 188 uS/m respectively.

In this model, the distributed capacitance, $c_{substrate}$, obtained at the substrate/liquid interface outside the object, it is also assigned to the interface inside the structure.

The electric force acting on the probe depends on the specific capacitance of the membrane, as clarified in Ref. [31], but also, in the case of “dome-like” patches, on the properties of the media that they enclose, as shown in Chapter 5 (and of course the proximity of the

surface to the tip). Capacitance gradient approach curves were calculated with both flat and inflated patch model by varying the tip-patch distance, Z, in the geometrical model.

After calibration of the tip geometry [20, 12, 28, 29, 15], the permittivity of the PM (ε_m) in the case of a flat patch was obtained by fitting the experimental curve on the membrane patch with a table of curves calculated for different permittivities [29, 30].

In the case of an inflated patch, the permittivity was instead determined by varying progressively the height of the simulated dome and fitting the experimental curve to the calculated curves for different permittivities of the layer. Here the experimental curve was progressively shifted by the simulated topography for each case, as the reference for the simulations is the Z tip-sample distance.

We have to consider that the permittivity of the membrane obtained is only meaningful when the simulated model coincides with the real geometry of the membrane patch.

6.4 Results and discussion

Figure displays an SDM experiment performed on PMs patches in Milli-Q water.

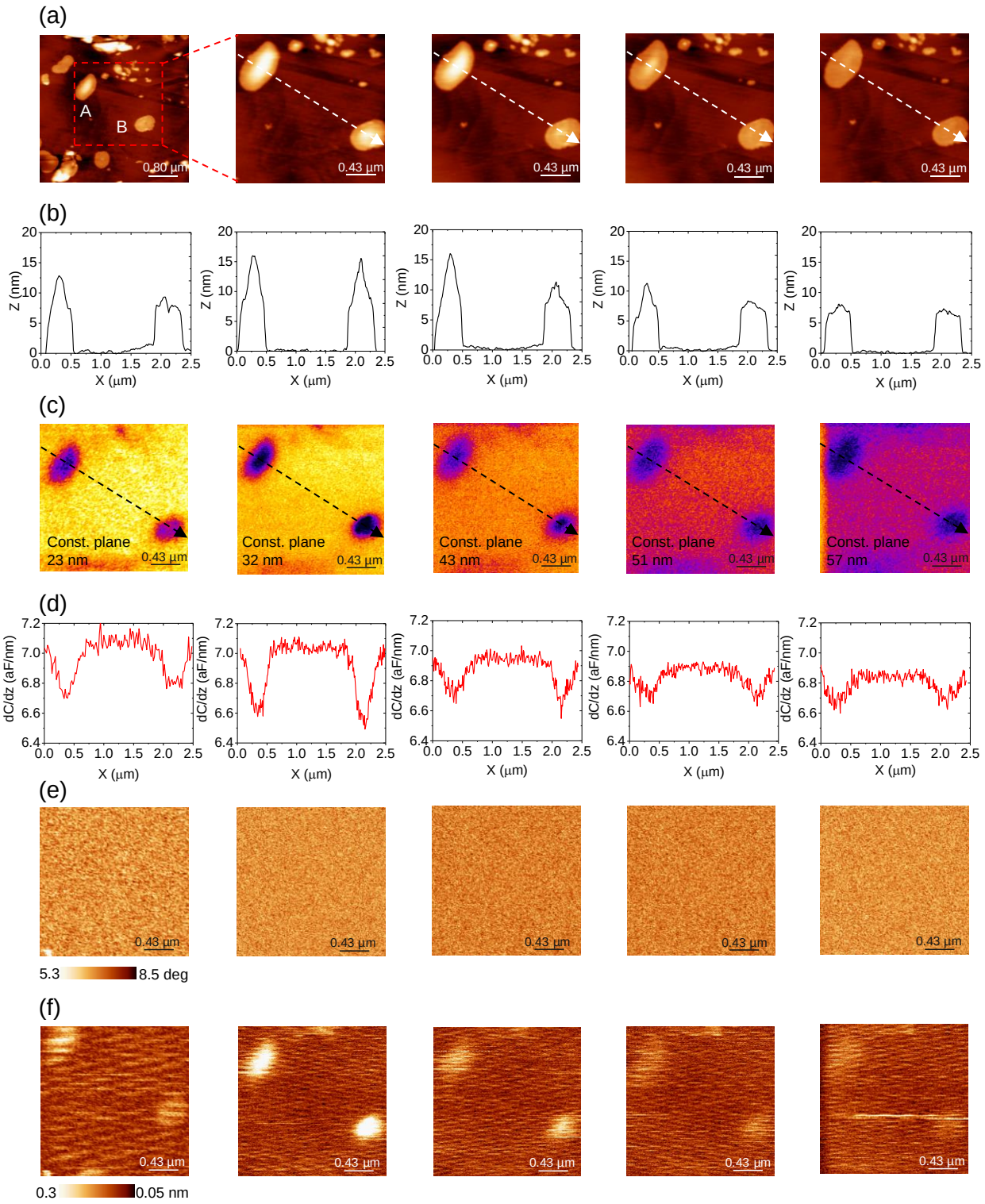

Figure 52: SDM measurements of PM patches on HOPG, in Milli-Q. (a)Topographic images acquired in tapping mode. The first image to the left is a zoom-out of the area later selected (red dashed frame),

which is further scanned changing the set-point. The profiles of the two patches, A and B, traced along the white dashed lines in the topographies are reported in (b). (c) Electric images in constant height at increasing distances from the substrate. The profiles traced along these images are displayed in (d). (e) and (f) are the phase and deflection image of the electrical pass, respectively.

After a first scan over a larger area which contains several PMs (left image in Figure 52 (a)), we focused on patches A and B, enclosed in the dashed red frame drawn on the image. Four topographical images have been acquired starting from lower to higher force, until the thickness of the BR layers is recovered (see also the respective profiles in Figure 52 (b)). We can observe that when a lower force is applied, both patches display a “dome-like” topography with a maximum of ~16 nm. However, we do not know whether this topographical feature is apparent, i.e. due to electrostatic repulsion, or real, i.e. the patches are inflated and full of water, with only the borders adhered to the surface. The topography observed could also be the result of a combination of these two effects, as discussed before. Besides, even excluding the presence of an electrostatic component, we cannot ensure whether the measured profiles correspond to the real height of the patches, or if the hard tapping is affecting their shape consistently.

In parallel to topography, dielectric images in constant height at increasing Z-distances, phase and deflection images are acquired in the electrical pass (Figure 52 (c), (e) and (f) respectively). As the phase images do not display any feature, we presume that the surface of the layers is not being touched during the acquisition of the electric images, not even when the closest scan to the surface is performed. However, the tip, although very minimal (maximum ~0.3 nm), does display some deflection while passing over the patches.

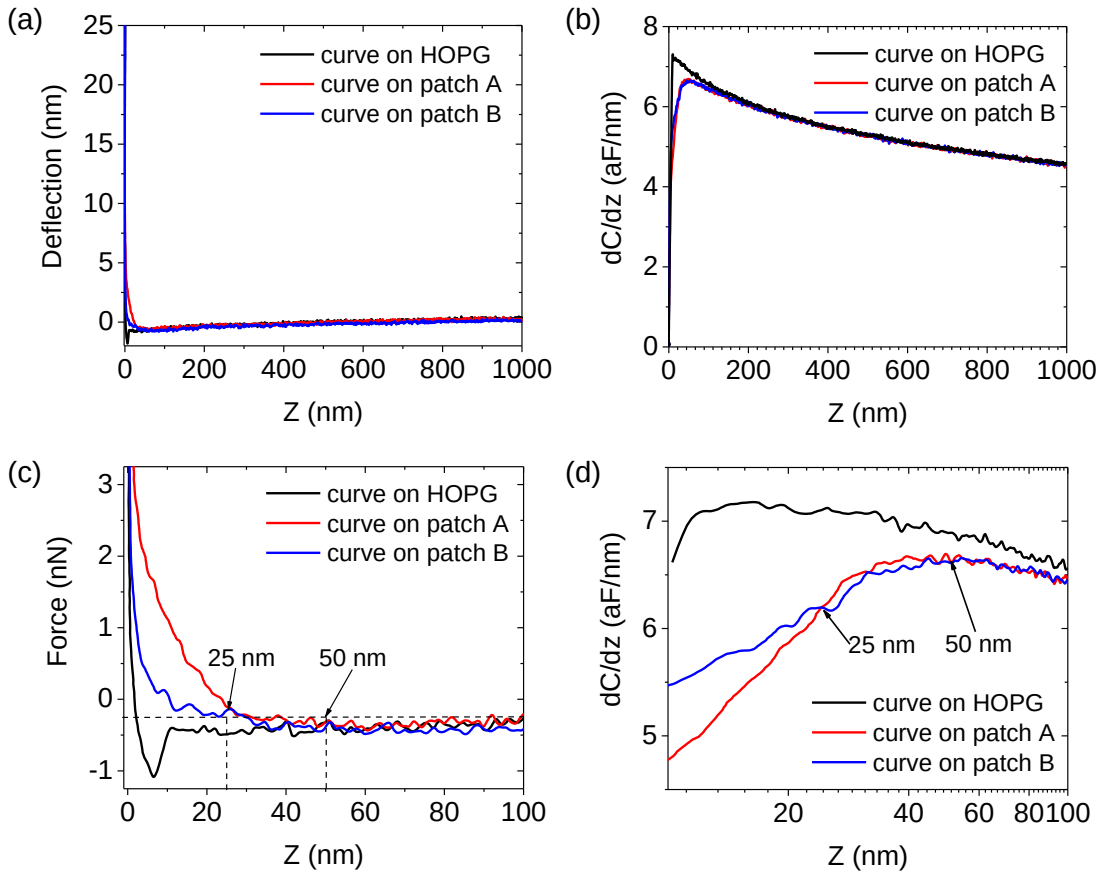

Figure 53: (a) Mechanical approach curves over the substrate and the centre of each patch (a). A zoom-in of these curves at short distances is displayed in (c). The tip starts to deflect slightly at ~50 nm from the surface. (b) Electrical approach curves measured in parallel to the mechanical ones. The curves are also represented in log scale to better evidence the difference at short distances (d).

In addition to images, force curves have been acquired on the substrate and at the centre of patch A and B (see Figure 53).

The electrical force curves acquired on the patches (red and blue, Figure 53 (d)), intersecting at ~25 nm from the substrate surface, explain why the images dielectric contrast between patch A and B reverses as we scan from the closest (Z=23 nm), to the second plane acquired (Z=32 nm) (see dielectric profiles in Figure 52 (d)).

From the zoom-in at short Z-distances of the mechanical approach curves (Figure 53 (c)), a slight deflection of the tip on the patches is already displayed at ~50 nm. At the same

distance, the electrical approach curves on the two patches start to diverge (Figure 53 (d)), while at larger distances they are indistinguishable.

This initial deflection, starting at ~50 nm for both patches and increasing very smoothly, could possibly be due to electrostatic repulsion. The curve on patch A seems to display a second regime, starting at ~25-30 nm, which could maybe mark the beginning of the indentation of the layer.

Although the previous speculations are not unreasonable, we cannot rely on them until we confirm the nature of the interactions observed and precisely identify the contact with the PM surface. For this reason, in the attempt of exploiting in-liquid SDM to gain information about the dielectric properties of the PM, we decided to model the layers topography with a set of different possible geometries.

As previously mentioned, in order to be sure of not dealing with indentation or space charge layers effects, that are not considered by the models, the fitting of the experimental curves on the PMs with the calculated data is only performed considering the far part of the electrical curves, where the mechanical counterpart is not displaying any deflection of the tip.

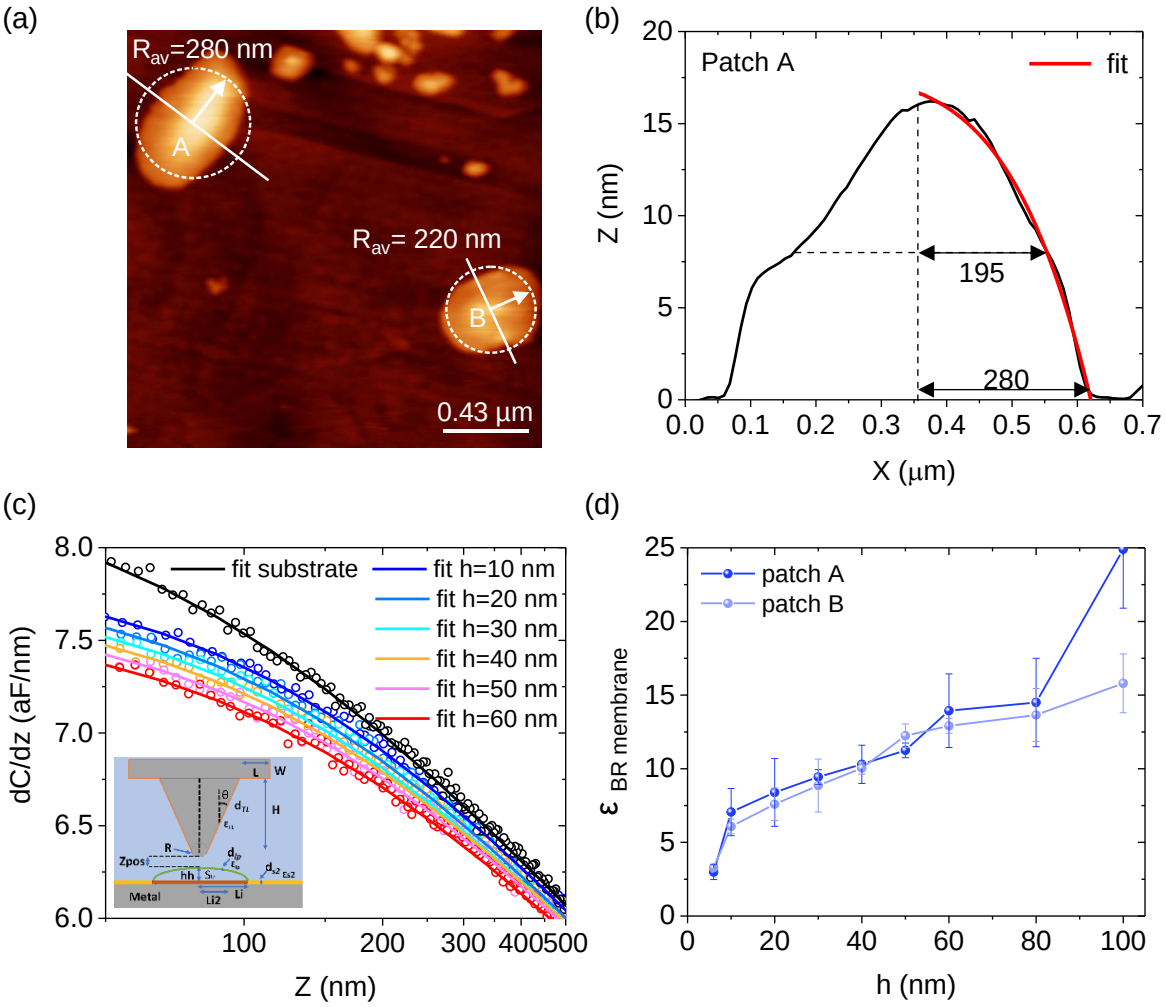

Figure 54: (a) Topography of the patches A and B measured at the lowest set-point. An average radius is defined from the dashed circles enclosing the layers, respectively of 280 nm for A and 220 nm for B. (b) The fitting of the profile of A to the function $Z = h - ax^b$, used to simulate the geometry for curved patches, is reported as an example. (c) Experimental curve on the substrate (black, empty circles) and best fit achieved by simulations. Parameters obtained: α=1.15, R=25 nm, θ=20°, c_{tip}=1.8 µF/cm², $c_{substrate}$=0.89 µF/cm². Experimental curves on patch A (coloured empty circles); they are always the same data but progressively shifted to the left depending on the simulated height of the patch. The model of the 'floating patch' used to calculate the theoretical curves is shown in the inset. The permittivity and conductivity of the solution enclosed inside the dome-like structure were assumed to match the ones of water (outer medium: 78 and 188 uS/m respectively). The thickness of the membrane was set to be 6 nm, the width at half maximum of the structure is kept constant (L2=195 nm) since it changes only very slightly as the height changes. The height of the dome-like structure is progressively increased (10-100 nm), and the experimental data are fitted to simulated tables of curves. The best fitting for each curve is represented by a continuous line of the respective colour in (c). (d) Permittivity of the membrane obtained for each case. The analysis was also carried out with the model of the flat patch (first point of the trend in (d)). The same quantification was repeated for patch B.

From this analysis (Figure 54) we obtain that, when the patch is assumed to be curved and the dome model is used, the permittivity of the membrane is always higher than 5 and progressively increases as the simulated structure is higher. Instead, when the PM patches are considered flat, i.e. as if the topography displayed was not real but an effect of charges, we obtain $\varepsilon_{patch\ A} = 3.2 \pm 0.5$ and $\varepsilon_{patch\ B} = 3.3 \pm 0.5$.

We collected additional data for other patches (Figure 55 and Figure 56) within the same experiment and carried out the analysis in the same way.

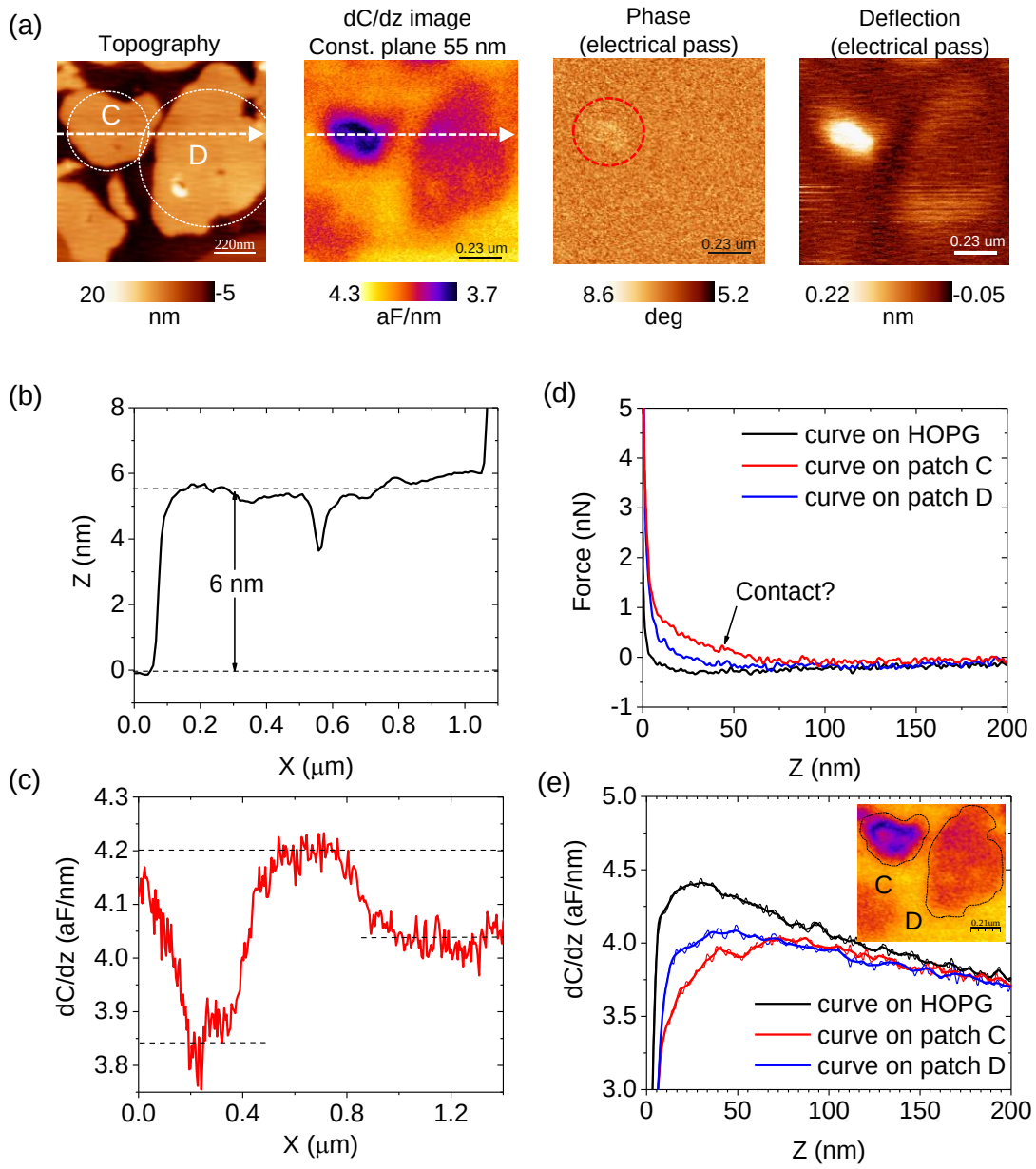

Figure 55: PM patches on HOPG in Milli-Q. (a) Topography in tapping mode, electric image in constant height at 55 nm, phase and deflection in the electrical pass. The profile of the topography and electric

image along the white dashed arrows are displayed in (b) and (c) respectively. Mechanical approach curves on the substrate and the centre of each patch are displayed in (d), electrical ones recorded in parallel in (e). The inset of (e) shows an additional SDM image in constant height at about the same Z-distance, 56 nm, which shows interesting features, as the smaller patch, C, displays a clearer central area surrounded by a darker border.

Figure 55 shows two patches with the same thickness (C and D). Patch C, while smaller, exhibits a much larger electric contrast than patch D. This does not agree with the lateral size effect discussed for flat patches in Chapter 4. Higher topographies were not revealed in this case. However, this observation does not discard the possibility of having features like the ones of the previous experiment, since the AFM parameters have been optimized for electrical imaging. As in the previous case, the electrical approach curves on the patches display deflection at several tens of nanometers away from the surface. In particular, we also observe a small kink in the red curve (patch C) at ~50 nm. This feature is even more evident in the respective electrical curve and represents a possible point of interaction with the layer's surface. The electrical pass phase, at 55 nm, shows some subtle features (see dashed red circle on the image in Figure 55). This could be a further confirmation that patch C is curved and full of water, with a topography of ~50-55 nm. The deflection image recorded in the electrical pass also shows a higher deflection on the smaller PM layer. Nevertheless, once again, it is hard to identify with precision the contact points with the patches' surfaces.

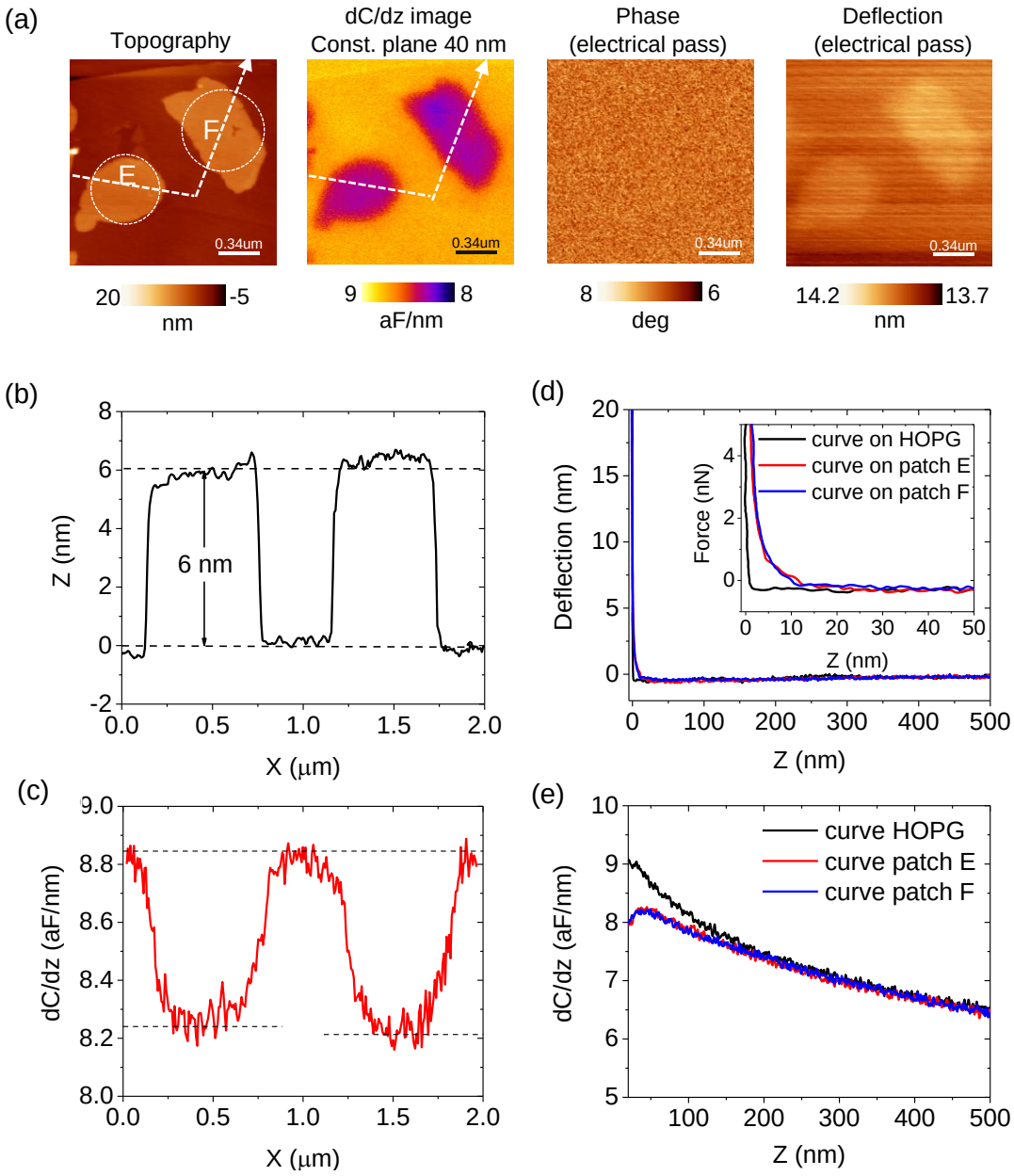

Figure 56: PM patches on HOPG in Milli-Q water. (a) Topography in tapping mode, electric image in constant height at 40 nm, phase and deflection in the electrical pass. Profile along the dashed arrow traced in the topography (b) and along the capacitance gradient image (c). (d) Tip-sample distance curves on HOPG and on the centre of each of the patches. A zoom-in of the curves is displayed in the inset of the figure; the y-axes was transformed into force (nN). (e) Electrical approach curves recorded in parallel with the mechanical ones.

An additional measurement is shown in Figure 56; this time the two patches display the same contrast at all distances and the tip only starts to deflect importantly at ~12 nm. However, as before, we are not sure whether the force felt by the tip on the PMs is of electrostatic nature,

due to indentation of a higher structure, or a combination of both as we suspect in the case of patch C.

For these additional measurements, we extracted the dielectric permittivity of the PM patches C, D and E (F gives results similar to E) as before, by simulating different possible topographies, from flat patches to “domes” of different height. The results are reported below (Figure 57).

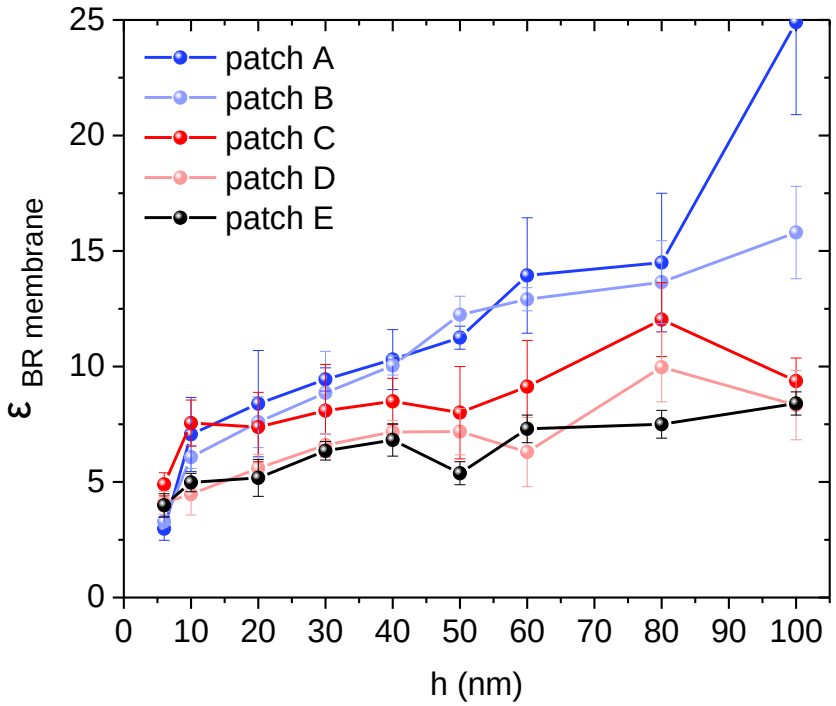

Figure 57: Dielectric constants extracted for every patch by simulating progressively higher topographies. The permittivity of the membranes obtained when the patches are assumed flat are: $\varepsilon_{patch\ A}$ = 3.2 ±0.5, $\varepsilon_{patch\ B}$=3.3 ±0.5, $\varepsilon_{patch\ C}$ =4.9± 0.5, $\varepsilon_{patch\ D}$ = 4.1 ± 0.5, $\varepsilon_{patch\ E}$ = 4.0 ± 0.5.

The permittivity of the different patches, when considered flat, ranges from ~3 to ~5. These experiments have been all performed with the same tip; very similar parameters for its geometry and interfacial capacitances are extracted and used for quantification. Under- or overestimation of the lateral dimension of the layers is possible, although it does not seem to account for the differences encountered between the dielectric constants. Indeed, for instance, the patches C and D are found in a crowded area, and possibly their average radius is being

underestimated; however, when larger radii are considered, the permittivity obtained is even higher.

Thus, if all the patches are in reality flat, the difference found between the dielectric constants of the PM could depend on composition or on some conductivity effect, that the flat patch model does not account for. In particular, one would expect a difference in permittivity between the patches C and D, given the different contrast they display in the dielectric images. However, when calculated trough the dC/dz curves, the permittivity of patch C (4.9 ± 0.5) is obtained higher than the one for patch D (4.1 ± 0.5), while, because of the contrast shown, it should be the opposite. This fact might lead us to think that, instead, the layers have different topographies, and thus the flat patch model does not provide truthful results in some cases.

Increasing trends of the permittivity of the layers are obtained with the inflated patch model, with different steepness, depending on the patch. The trends of A and B are superimposable and rise more rapidly with the height simulated. Patch D of the second experiment (Figure 55) and patch F of the third (Figure 56) also display the same behaviour, while the trend of patch C is approximately in the middle.

It is important to underline once more that the permittivity of the layer is the correct one only when the real geometry is simulated, i.e. in one single point of each trend in Figure 57.

Given these results and from the discussion above, one might propose that patches D and E are really flattened on the surface and possess a permittivity of ~4, while the other three patches, in addition to a possible contribution of an electrostatic component, are in reality curved. However, the uncertainty in the real topography, for the moment, does not allow us to precisely extract the permittivity of the layers, which nevertheless seems to be higher than 5.

Further analysis will be carried out to untangle the problem and identify the true topography of these PM patches, which will give us access to ε_{PM} for each case.

6.4 Conclusions

We have measured the dielectric properties of PM patches in Milli-Q water. We exposed the difficulties in the determination of the real topography of the patches, since PM can form curved, dome-like structures, but also electrostatic contributions to topography can increase the complexity of the case. This problematic is actually very relevant for the study of many other biological systems in water, such as cells. The presented experiments can offer a simplified case of study and maybe the possibility to better understand how to overcome this difficulty. For the moment, we carried out a preliminary quantification of the measurements for several possible cases. Although we can speculate on the position of the contact point, further analysis will be needed to ensure the truthfulness of our evaluations.

Conclusions

In this work of thesis, we achieved nanoscale dielectrical characterization in liquid of lipid membranes with heterogeneous composition, i.e. DOPC and DOPC:cholesterol, of DOPC liposomes presenting a 3D geometry, and of PM patches as a representative example of natural membranes. The technique selected to carry out the present study was in-liquid Scanning Dielectric Microscopy.

The specific capacitances of the two components, DOPC and DOPC:cholesterol, have been found to be $c_{s,DOPC}$ = 0.9-1 μF/cm^2 and $c_{s,DOPC:chol}$ = 0.6-0.7 μF/cm^2 respectively. Therefore, we concluded that cholesterol at 50% concentration strongly reduces the specific capacitance of supported DOPC bilayer patches. The reduction of the dielectric constant of the DOPC:cholesterol bilayer patches can be associated to the dehydration of the polar head groups caused by the presence of cholesterol molecules.

Indeed, we underline that, although the differences are subtle, while the value of permittivity obtained for pure DOPC is of ~3-3.5, in agreement with preliminary studies in liquid [29], the dielectric constant extracted when high percentage of cholesterol is present, is more similar to the value obtained for bilayers in dry conditions (~2) [21]. Very different electric contrast was observed for the two components; this constituted a first proof-of-concept of the possibility of achieving non-invasive, label-free mapping, with in-liquid SDM.

On the technical side, when imaging planar membranes in liquid conditions, we have found a more pronounced lateral size electrostatic effect, as compared to the case of air measurements. Thus, the modelling was adapted to account for the finite lateral dimension of the lipid patches [30], and the dielectric properties extracted with good precision. Although the dielectric contrast in the image greatly reduces as the lateral extension of the bilayers diminishes, we demonstrated that the specific capacitance of the layers does not depend on it. This holds true for patches down to, at least, ~200 nm in lateral size.

Afterwards, we have analysed the dielectric properties of a population of multilamellar DOPC liposomes. In this case, we have shown how the signal depends on the dielectric properties of the shell and on the conductivity of the core, but also on the number of lamellae and their separation, that was determined for liposomes down to ~100 nm spherical radius in a non-invasive way. The bilayer specific capacitance was found once again in agreement with previous results (0.76 μF/cm^2), demonstrating the reliability of the technique. The accuracy of determining the specific capacitance for liposomes is similar to the accuracy obtained with planar lipid bilayers. Liposomes up to three lamellae have been identified in the batch, the smaller ones being for the most part uni-lamellar and the bigger ones being mainly tri-lamellar. Bi-lamellar liposomes were the most abundant, with intra-lamellar separations up to 10 nm. The number of lamellae cannot be extracted accurately from a geometrical analysis of the liposomes, and force spectroscopy measurements are much more invasive. Thus, this study opened interesting possibilities for the characterization of natural vesicles of very soft nature, since the technique is essentially non-contact.

Once concluded the study of model membrane systems, we focused on extending the methods to natural membranes, where increased complexities were expected. To this end, we studied the dielectric properties of a very popular natural purified membrane sample, PM patches. We have performed a preliminary analysis by imaging the patches in QI mode, with a soft tip, in Milli-Q water and after exchange with Tris 20 mM, KCl 100 mM buffer. When in Milli-Q water, we highlighted the possible coexistence of a curvature of the membrane together with a contribution to topography given by pure electrostatic interactions.

Since the two effects are not trivial to distinguish, and in general, it is often problematic to determine the contact point with very soft samples like membranes, the true topography of these patches remains uncertain. The quantification of the permittivity of the layer was thus carried out for several possible cases, i.e. assuming the patch being from flat to dome-like, with a progressively higher height. We remark that the dielectric constant obtained is only meaningful when the model reflects the real geometry of the system. We are currently looking

for strategies to discriminate the topography with the sufficient accuracy to obtain meaningful values of the permittivity of PMs. If successful, interesting conclusions could be drawn regarding the electric properties of this first natural sample with high protein content measured by SDM in liquid conditions.

Future Perspectives

The present work of thesis leads the way to interesting future perspectives, some of which have already been examined during the development of this thesis. The first case refers to the study of the nanoscale dielectric properties of living cells. Characterizing for the first time the dielectric properties of the membrane of a cell in activity could reveal very interesting features, from the presence of nanoscale compositional heterogeneities never spotted in vivo before, to manifested bioelectrical phenomena related to the action of ion channels and pumps. Initial investigations with living Neuroblastoma cells have been carried out by using SDM in force-volume mode [26]. This project was developed in collaboration with Maria Elena Piersimoni, a PhD student in the framework of the SPM2.0 Marie Curie network.

For imaging, several buffers with low ionic molarity have been screened to compromise between the possibility of operating in-liquid SDM and obtaining good electrical curves, and the wealth of the cells, which are quite delicate systems and whose functioning depends on temperature, nutrients, pH, etc. A solution of 20 mM MOPS buffer was selected for imaging by SDFVM (Figure 58).

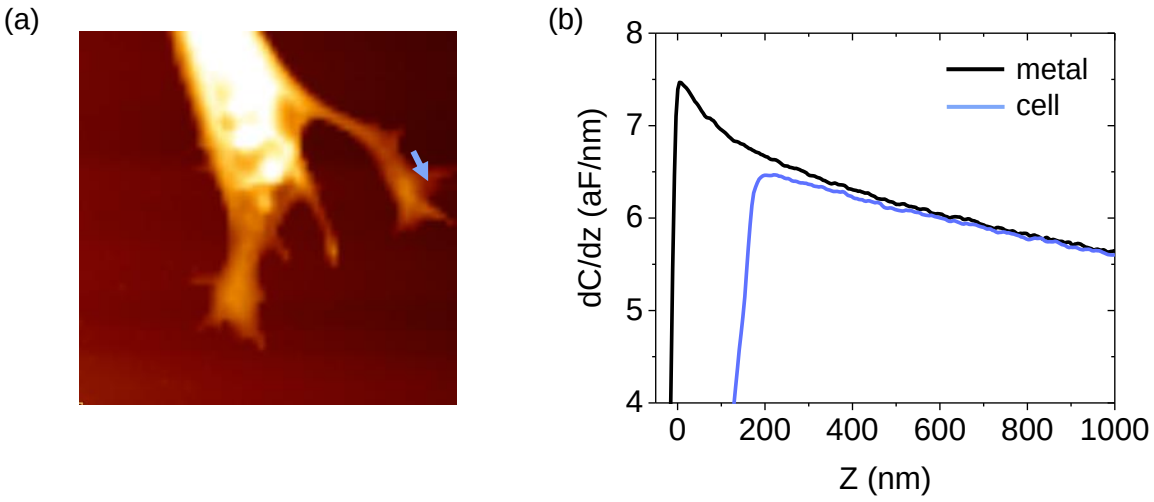

Figure 58: (a) Topography of a neuroblastoma cell in 20 mM MOPS, well adhered and stretched on a gold substrate, acquired in QI mode with a Nanowizard 4 AFM system (JPK). (b) Examples of two electrical force curves, out of the whole data cube acquired by SDFVM, on the metallic substrate (black) and on the cell (position indicated by the light blue arrow in (a). Parameters of the in-liquid SDM

measurement: amplitude of the applied voltage, 1 V, electrical frequency 2 MHz and modulation frequency 2 kHz.; Probe: PPP-CONTSCPt from Nanosensors (k=0.1 N/m).

Applying in-liquid SDM to living cells can pose some challenges, because the sensitivity of the method decreases quickly as the thickness of the sample increases. In addition, cells can be very hydrated, to the point that their electric properties are maybe not so different from their environment. Furthermore, as already discussed for the purple membranes case, the determination of the “true” topography of such soft samples is a crucial point to address.

The examination of the results, currently ongoing, is now being led by Ruben Millan-Solsona. The group is also collaborating with experts in the field, trying to implement new algorithms for the analysis of these cubes of data generated by SDFVM.

Besides its application to biological samples, in-liquid SDM offers important applications in other fields of research where electrical characterization in liquid is necessary. One example is represented by the case of electrolyte-gated organic field effect transistors, EGOFETs, which in recent years have been used to carry out bioelectronic recording of excitable cells [128, 350, 351] and very much investigated as biosensors [42, 352, 353, 354, 355, 356].

Unlike the classical Organic Field Effect Transistor (OFET), where a solid dielectric is used for operating the transistor in air, EGOFETs have instead the organic semiconducting film in contact with an electrolyte solution.

In this framework, I used my expertise with in-liquid SDM to contribute to the nanoscale electrical characterization of an EGOFET under operation (Figure 59).

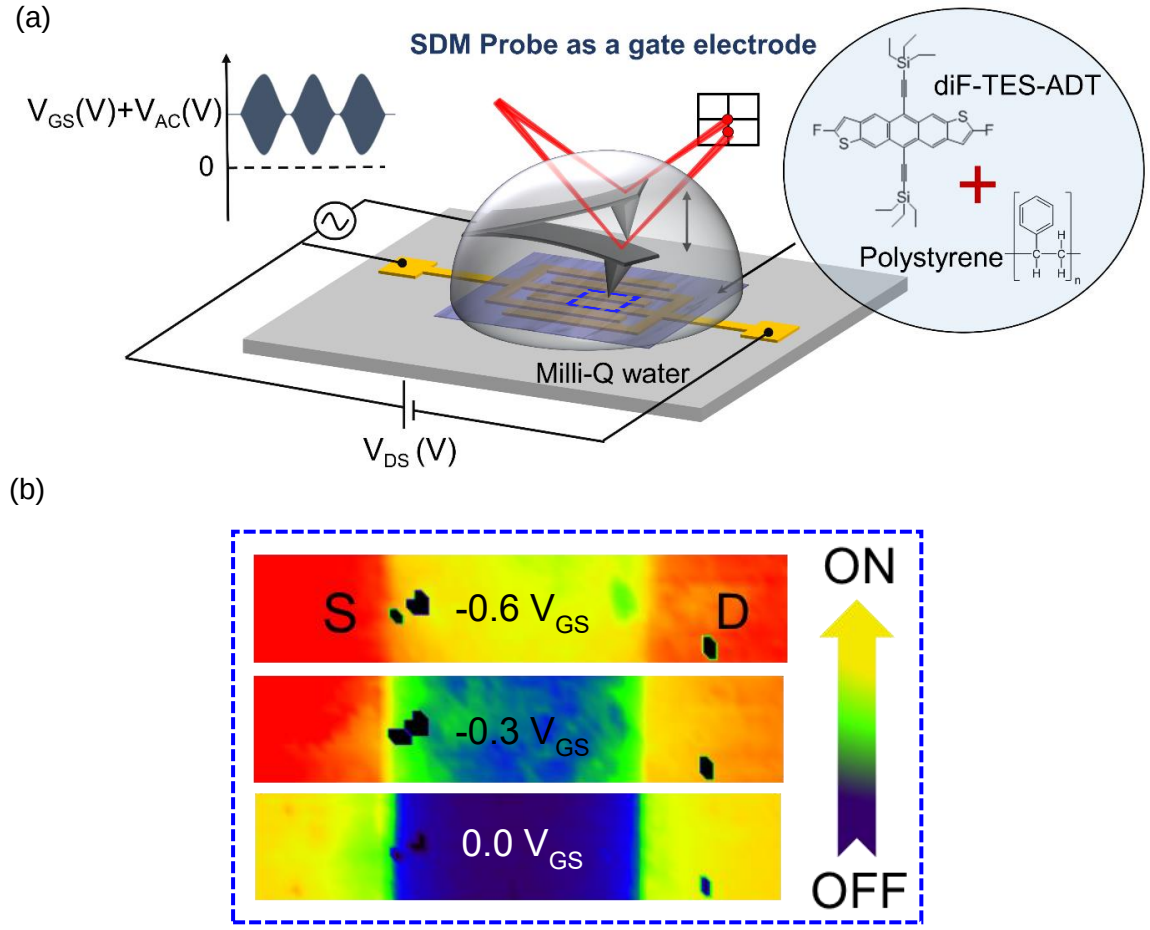

Figure 59: (a) In-liquid SDM setup for the nanoscale electrical characterization of a functional EGOFET. The organic film is a blend of the semiconducting material 2,8-difluoro-5,11-bis(triethylsilylethynyl)anthradithiophene (diF-TES- ADT) with the insulating polymer polystyrene (PS). EGOFETs are normally non-permeable to ions, charges are injected in the organic material with the help of a gate voltage and can be driven along the device by applying a source/drain voltage. In order to incorporate the in-liquid SDM technique presented in Chapter 3 to the functional EGOFET; we have used the SDM probe as both gate electrode and force sensor. An amplitude-modulated ac potential with frequency ω_{el} > 1 MHz and modulation frequency ω_{mod} of about 2 kHz is applied between the source of the transistor and the conductive probe in the electrolyte solution. An additional dc voltage offset is applied as a gate voltage V_{GS}. A potential V_{DS} is applied between the source and the drain, and the I_{DS} current is recorded by a current–voltage source meter (not shown in the figure). In this way local electrostatic force versus gate voltage transfer characteristics were obtained on the device in parallel to the global current–voltage transfer characteristics of the EGOFET. (b) Constant height dielectric images reconstructed from the electric force–voltage transfer characteristics curves for three gate voltages V_{GS}, as the transistor goes from the off to the on state.

When the transistor passes from the off state to the on state, dielectric images of the semiconductor surface acquired at different gate voltages evidenced sub-micrometric heterogeneities in the polymeric layer due to vertical phase separation of diF-TES-ADT and PS (Figure 59). Such features are sometimes not displayed in topography, as they can measure only ~1 nm in thickness (see Ref. [41] for additional images).

The contrast in the electric images is instead very evident and enables to directly identify which parts of the surface are covered by PS and which parts are not. These heterogeneities are given by interfacial capacitances and conductivity effects, which were mapped in liquid for the first time and quantified with the help of numerical calculations. The analysis of the data was carried out by other members of the group. Such findings would offer the possibility to optimize the device performance and open fascinating possibilities to study the transduction mechanisms at the organic semiconductor/electrolyte interface relevant for bioelectronic applications.

Resumen

La estructura y propiedades fisicoquímicas de las biomembranas son fundamentales para el funcionamiento de las células, y muchas patologías (cáncer, neurodegeneraciones, obesidad, etc.) [1, 2] se han asociado a su alteración . Por este motivo, las biomembranas han sido objeto de intensas investigaciones. Sin embargo, todavía existe un conocimiento limitado de las biomembranas, que muestran una estructura heterogénea a la nanoescala, que en realidad son las que están presentes de forma natural en las células y determinan muchos de los fenómenos que ocurren a través de ellas a nivel molecular [3, 4].

Las propiedades eléctricas, debido a su papel destacado en la electrofisiología, se encuentran entre las propiedades físicas más relevantes de las biomembranas. La mayoría de las veces se presta atención a las propiedades de conducción de las biomembranas y al papel que juegan en ellas los canales iónicos. Sin embargo, las propiedades dieléctricas de la biomembrana también son de interés central en los fenómenos bioeléctricos y, también, pueden considerarse como un poderoso indicador de la composición de la biomembrana, que puede aprovecharse para desarrollar métodos de mapeo sin marcadores. Sin embargo, la mayoría de las técnicas disponibles han abordado las propiedades de la membrana dieléctrica en la macroescala y al nivel de células individuales (micrómetros), por lo que carecen de resolución espacial. En otros casos, hacen uso de etiquetas exógenas, como en el caso de la resonancia paramagnética de espín [5, 6] y la microscopía de fluorescencia [7, 8, 9, 10, 11].

En los últimos años, el grupo de Caracterización Bioeléctrica en la Nanoescala del IBEC, así como otros grupos, ha desarrollado técnicas basadas en Microscopias de Sonda de Barrido (SPM) para la caracterización dieléctrica en la nanoescala [12, 13, 14, 15, 16] y aplicarlas a biomembranas [17, 18, 19, 20, 21] y otros biosistemas [12, 22, 23, 24, 25, 26, 27]. Inicialmente, estas técnicas se implementaron para ser operadas en aire o ambiente seco, pero en los últimos años se han ido extendiendo también al ambiente líquido [28, 29]. La implementación de la microscopía dieléctrica de barrido (SDM) en líquido allanó el camino para la precisa caracterización

dieléctrica de las biomembranas en la nanoescala, en condiciones fisiológicas y sin marcadores [28, 29].

El SDM en líquido se basa en medir la fuerza electrostática que actúa sobre una sonda nanométrica bajo la aplicación de un voltaje modulado entre la punta y un sustrato conductor, sobre el cual se asienta la muestra. En comparación con la técnica de SDM en aire, el funcionamiento en un entorno líquido requiere varias modificaciones. En términos de configuración, es necesario aplicar frecuencias por encima de la frecuencia de relajación dieléctrica del electrolito. También son necesarios cambios significativos para la parte del modelado [30].

Este trabajo de tesis aprovecha los últimos desarrollos de SDM en líquido para caracterizar las propiedades dieléctricas de sistemas de membranas de modelo heterogéneo y membranas naturales purificadas en líquido. En este trabajo, se han obtenido nuevos conocimientos sobre la técnica de SDM en líquido, como por ejemplo sobre el prominente efecto electrostático de tamaño finito. También se han probado y optimizado diferentes modelos para el análisis de las medidas.

Primero, me concentré en caracterizar mezclas de bicapa lipídicas soportadas mono y bicomponente que contienen colesterol, proporcionando una primera prueba de concepto de las capacidades de mapeo sin etiqueta de la técnica en líquido, ampliando el trabajo realizado anteriormente en aire sobre nanopartículas [12]. Este estudio permitió obtener información sobre la composición de dominios de membrana submicrométricos en su entorno natural [31] y proporcionó valores fiables de las propiedades dieléctricas intrínsecas de las composiciones de DOPC y DOPC / colesterol, sobre las cuales hubo cierto debate en la literatura. Los bajos valores obtenidos son responsables de la baja permeabilidad de las membranas a los iones, en concordancia con estudios previos sobre biomembranas monocomponentes [29]. Nuestros resultados permiten especular sobre propiedades fundamentales de las bicapas lipídicas como la viscosidad e hidratación de las capas que contienen colesterol.

Posteriormente, ampliamos los métodos para tratar con estructuras 3D de biomembranas más complejas, como los liposomas [32]. Mediante SDM en liquído, se han obtenido imágenes de liposomas de unas pocas docenas de nanómetros de altura, mostrando una sensibilidad comparable a la de las biomembranas planas, de solo unos pocos nanómetros de espesor. Una vez más, se extrajeron con precisión las propiedades dieléctricas de la biomembrana de los liposomas, esta vez en una configuración más natural de la biomembrana. Este estudio también destacó las capacidades subsuperficiales de la técnica en líquido, demostradas anteriormente solo en medidas de aire [33, 34, 35, 36, 37, 38, 39]. Esta técnica permitió obtener de forma 'label-free' la lamelaridad de los liposomas, un parámetro crucial en esta tecnología. La metodología desarrollada tiene el potencial de usarse para diferenciar una gran cantidad de diferentes composiciones de liposomas (capa y núcleo), ya que se demostró que el SDM en líquido no solo es sensible a las propiedades dieléctricas de la membrana, sino también a la conductividad del medio en el interior de los liposomas. Este logro fue fundamental para evaluar su futura aplicación a las células vivas y constituye uno de los principales logros de esta tesis.

Durante la tesis también se hizo la caracterización dieléctrica de membranas naturales purificadas en líquido. Como muestra de prueba, nos centramos en el caso de la membrana púrpura (PM), que previamente había sido estudiada en aire [19, 20, 40]. Las PMs están constituidas por la proteína bacteriorodopsina (BR), dispuesta en una red cristalina, y de lípidos en una relación 10: 1 lípidos:proteínas. Sin embargo, una incertidumbre no resuelta en la determinación de la topografía real de los parches de PM soportados en líquido, que también puede mostrar una superficie cóncava, hizo que la cuantificación dieléctrica fuera problemática. Más experimentos serán necesarias para proporcionar valores fiables de la permitividad de estas capas en líquido.

En resumen, el objetivo e hilo conductor que conecta todos los capítulos de esta tesis ha sido implementar y demostrar las capacidades del SDM en líquido en la caracterización

dieléctrica de biomembranas, modelos y sistemas naturales, en condiciones líquidas, con resolución espacial nanométrica.

Creo que este trabajo sentó las bases para dilucidar la estructura y las propiedades dieléctricas de sistemas de membranas más complejos y sus fenómenos eléctricos asociados, como por ejemplo la conducción. Se llevaron a cabo estudios preliminares de la membrana celular directamente en células de neuroblastoma vivas, en solución tampón MOPS en baja concentración, en colaboración con Maria Elena Piersimoni, estudiante de doctorado en el Imperial College de Londres. El grupo ahora está colaborando con expertos en el campo y tratando de desarrollar nuevos algoritmos, fundamentales para extender la técnica de SDM en líquido a las células vivas.

Además del objetivo principal de mi proyecto de tesis, también participé en un proyecto paralelo sobre la caracterización SDM en líquido de un transistor EGOFET [41] operativo, crucial para optimizar dichos dispositivos y comprender mejor el mecanismo de transducción con entidades biológicas. De hecho, una de las fronteras más recientes de dicha tecnología es el uso de bicapa lipídicas soportadas con fines de biodetección [42].

Appendix: List of publications and congress presentations

Publications

Di Muzio, M., Millan-Solsona, R., Borrell, J. H., Fumagalli, L. and Gomila, G., Cholesterol Effect on the Specific Capacitance of Submicrometric DOPC Bilayer Patches Measured by in-Liquid Scanning Dielectric Microscopy. *Langmuir* **36**, 12963–12972 (2020).

Di Muzio, M., Millán, R., Borrell, J. H., Fumagalli, L. and Gomila, G., Electrical Properties and Lamellarity of Single Liposomes Measured by In-Liquid Scanning Dielectric Microscopy. *[in Preparation].*

Kyndiah, A., Checa, M., Leonardi, F., Millan-Solsona, R., **Di Muzio, M.**, Tanwar, S., Fumagalli, L., Mas-Torrent, M. and Gomila, G., Nanoscale Mapping of the Conductivity and Interfacial Capacitance of an Electrolyte-Gated Organic Field-Effect Transistor under Operation. *Adv. Funct. Mater.* 2008032, 1–8 (2020).

Oral communications

Di Muzio, M., Millán, R., and Gomila, G., Nanoscale dielectric imaging of supported lipid membranes by in-liquid Electrostatic Force Microscopy, EBSA Biophysics Course on Membrane and Lipid-Protein Interactions, La Grande Motte, France, 10^{th}-15^{th} June 2018.

Di Muzio, M., Millán, R., and Gomila, G., Nanoscale dielectric imaging of supported lipid membranes by in-liquid electrostatic force microscopy, XXI Annual Linz Winter Workshop, Linz, Austria, 1^{st}-4^{th} February 2019.

Di Muzio, M., Composition mapping of biomembranes by in liquid Scanning Dielectric Microscopy, Workshop on Advanced Scanning Probe Microscopies, Barcelona, Spain (Virtual meeting), 10^{th}-11^{th} December 2020.

Poster presentations

Di Muzio, M., Millán, R., and Gomila, G., Nanoscale composition mapping with electrostatic force microscopy, 4th International conference on Scanning Probe Microscopy on Soft and Polymeric Materials, SPMonSPM 2018, Leuven, Belgium, 20th-24th August 2018.

Di Muzio, M., Millán, R., and Gomila, G., Nanoscale dielectric imaging of supported lipid membranes by in-liquid Electrostatic Force Microscopy, 11th IBEC Symposium: Bioengineering for Regenerative Therapies, Barcelona, Spain, 2nd October 2018.

Di Muzio, M., Millán, R., and Gomila, G., Nanoscale composition mapping by in-liquid Electrostatic Force Microscopy, 12th IBEC Symposium: Bioengineering for Active ageing, Barcelona, Spain, 17th July 2019.

Di Muzio, M., Millan-Solsona, R., Borrell, J. H., Fumagalli, L. and Gomila, G., Lamellarity and electrical properties of single liposomes measured by in-liquid scanning dielectric microscopy, 13th IBEC Symposium: Bioengineering for Future & Precision Medicine, Barcelona, Spain, 27th-28th October 2020.

List of acronyms and abbreviations

ac Alternating Current

AFM Atomic Force Microscopy

BODIPY 2-(4,4-difluoro-5,7-dimethyl-4-bora-3a,4a-diaza-s-indacene-3-dodecanoyl)-1-hexadecanoyl-sn-glycero-3-phosphocholine,

BR BacterioRhodopsin

C-AFM Conductive Atomic Force Microscopy

CP Cytoplasmic

CP Contact Point

dc Direct Current

diF-TES-ADT 2,8-dif luoro-5,11-bis(triethylsilylethynyl)anthradithiophene

DLVO Derjaguin, Landau, Verwey, Overbeek theory

DOPC 1,2-dioleoyl-sn-glycero-3-phosphocholine

DPN Dip-pen Nanolitography

DPPC 1,2-dipalmitoylphosphatidylcholine

EC Exoplasmic

EDL Electric Double Layer

EFM Electrostatic Force Microscopy

EGOFET Electrolyte Gated Organic Field Effect Transistor

FLIM Fluorescence lifetime Imaging Microscopy

FRET Föster Resonance Energy Transfer

GM Ganglioside

GUV Giant Unilamellar Vesicle

HF High Frequency

HOPG Highly Oriented Pyrolytic Graphite

IR Infrared

IS Impedance Spectroscopy

KCl Potassium Chloride

KPFM Kelvin Probe Force Microscopy

LUV Large Unilamellar Vesicle

MLV Multi Lamellar Vesicles

MOPS 3-(N-Morpholino)propanesulfonic acid, 4-Morpholinepropanesulfonic acid

NIM Nanoscale Impedance Microscopy

OBD Optical Beam Detector

OFET Organic Field Effect Transistor

PA Phosphatidic Acid

PC Phosphatidylcholine

PE Phosphatidylethanolamine

PI Phosphatidylinositol

PIP Phosphatidylinositol Phosphate

PM Purple Membrane

PS Polystyrene

PD Phosphatidylserine

SALB Solvent Assisted Lipid Bilayer

SAM Self Assembled Monolayer

SCM Scanning Capacitance Microscopy

SDM Scanning Dielectric Microscopy

SECM Scanning Electrochemical Microscopy

SICM Scanning Ion Conductance Microscopy

SM Sphingomyelin

SMM Scanning Microwave Microscopy

SLB Supported Lipid Bilayer

SPFM Scanning Polarization Force Microscopy

SPM Scanning Probe Microscopy

SPR Spin Paramagnetic Resonance

SUV Small Unilamellar Vesicles

SDFVM Scanning Dielectric Force Volume Microscopy

TCSPC Time-Correlated Single Photon Counting

TD Time Domain

Tris Tris(hydroxymethyl)aminomethane

UV Ultraviolet

VDS Voltage Drain Source

VGS Voltage Gate Source

Acknowledgements

I want to thank Dr Gabriel Gomila for being a great mentor, apart from an excellent scientist. Thank you for this incredible opportunity you have given me.

I would also like to acknowledge the ‘Nanobioelec’ group and the IBEC community, who gave me plenty of support and help at every moment. A special thanks to Ruben, with whom I share all the achievements of this PhD, and Adrica, that has always been the model I look up to. Thanks to Hari, Helena, Martí, Ricardo, René, Shubham, Larissa and Annalisa for being a great team to laugh and to grow with.

Thanks to the CBS members, Dr Pierre-Emmanuel Milhiet and Dr. Luca Costa for being so available and dedicated to science. I would like to thank all the members of the SPM2.0 network for the interesting discussions and friendship.

Finally, to all the people who shared this journey with me and made it worthwhile.

References

(1) Lauwers, E.; Goodchild, R.; Verstreken, P. Membrane Lipids in Presynaptic Function and Disease. *Neuron* **2016**, *90* (1), 11–25. https://doi.org/10.1016/j.neuron.2016.02.033.

(2) Ashrafuzzaman, M., Tuszynski, J. *Membrane-Related Diseases*, Springer-V.; Springer-Verlag Berlin Heidelberg 2012, 2012.

(3) Mueller, P.; Rudin, D. O. Resting and Action Potentials in Experimental Bimolecular Lipid Membranes. *J. Theor. Biol.* **1968**, *18* (2), 222–258. https://doi.org/10.1016/0022-5193(68)90163-x.

(4) Hodgkin, A. L.; Huxley, A. F. A Quantitative Description of Membrane Current and Its Application to Conduction and Excitation in Nerve. *J Physiol.* **1952**, *117*, 500–544. https://doi.org/10.1109/ICCCT2.2017.7972284.

(5) Kurad, D.; Jeschke, G.; Marsh, D. Lipid Membrane Polarity Profiles by High-Field EPR. *Biophys. J.* **2003**, *85* (2), 1025–1033. https://doi.org/10.1016/S0006-3495(03)74541-X.

(6) Marsh, D. Polarity and Permeation Profiles in Lipid Membranes. *Proc. Natl. Acad. Sci. U. S. A.* **2001**, *98* (14), 7777–7782. https://doi.org/10.1073/pnas.131023798.

(7) Huang, H.; McIntosh, A. L.; Atshaves, B. P.; Ohno-Iwashita, Y.; Kier, A. B.; Schroeder, F. Use of Dansyl-Cholestanol as a Probe of Cholesterol Behavior in Membranes of Living Cells. *J. Lipid Res.* **2010**, *51* (5), 1157–1172. https://doi.org/10.1194/jlr.M003244.

(8) Parasassi, T.; De Stasio, G.; Ravagnan, G.; Rusch, R. M.; Gratton, E. Quantitation of Lipid Phases in Phospholipid Vesicles by the Generalized Polarization of Laurdan Fluorescence. *Biophys. J.* **1991**, *60* (1), 179–189. https://doi.org/10.1016/S0006-3495(91)82041-0.

(9) Signore G., Abbonato G., Storti B., Stöckl M., Subramaniam V., B. R. Imaging the Static Dielectric Constant in Vitro and in Living Cells by a Bioconjugable GFP Chromophore Analog. *ChemComm* **2013**, *49* (1723). https://doi.org/10.1039/b000000x.

(10) Demchenko, A. P.; Mély, Y.; Duportail, G.; Klymchenko, A. S. Monitoring Biophysical Properties of Lipid Membranes by Environment-Sensitive Fluorescent Probes. *Biophys. J.* **2009**, *96* (9), 3461–3470. https://doi.org/10.1016/j.bpj.2009.02.012.

(11) Epand, R. M.; Kraayenhof, R. Fluorescent Probes Used to Monitor Membrane Interfacial Polarity. *Chem. Phys. Lipids* **1999**, *101* (1), 57–64. https://doi.org/10.1016/S0009-3084(99)00055-9.

(12) Fumagalli, L.; Esteban-Ferrer, D.; Cuervo, A.; Carrascosa, J. L.; Gomila, G. Label-Free Identification of Single Dielectric Nanoparticles and Viruses with Ultraweak Polarization Forces. *Nat. Mater.* **2012**, *11* (9), 808–816. https://doi.org/10.1038/nmat3369.

(13) Fumagalli, L.; Ferrari, G.; Sampietro, M.; Gomila, G. Dielectric-Constant Measurement of Thin Insulating Films at Low Frequency by Nanoscale Capacitance Microscopy. *Appl. Phys. Lett.* **2007**, *91* (24), 15–18. https://doi.org/10.1063/1.2821119.

(14) Gomila, G.; Toset, J.; Fumagalli, L. Nanoscale Capacitance Microscopy of Thin Dielectric Films. *J. Appl. Phys.* **2008**, *104* (2). https://doi.org/10.1063/1.2957069.

(15) Fumagalli, L.; Gramse, G.; Esteban-Ferrer, D.; Edwards, M. A.; Gomila, G. Quantifying

the Dielectric Constant of Thick Insulators Using Electrostatic Force Microscopy. *Appl. Phys. Lett.* **2010**, *96* (18), 88–91. https://doi.org/10.1063/1.3427362.

(16) Fumagalli, L.; Ferrari, G.; Sampietro, M.; Casuso, I.; Martínez, E.; Samitier, J.; Gomila, G. Nanoscale Capacitance Imaging with Attofarad Resolution Using Ac Current Sensing Atomic Force Microscopy. *Nanotechnology* **2006**, *17* (18), 4581–4587. https://doi.org/10.1088/0957-4484/17/18/009.

(17) Gramse, G.; Schönhals, A.; Kienberger, F. Nanoscale Dipole Dynamics of Protein Membranes Studied by Broadband Dielectric Microscopy. *Nanoscale* **2019**, *11* (10), 4303–4309. https://doi.org/10.1039/c8nr05880f.

(18) Knapp, H. F.; Mesquida, P.; Stemmer, A. Imaging the Surface Potential of Active Purple Membrane. *Surf. Interface Anal.* **2002**, *33*, 108–112. https://doi.org/10.1002/sia.1172.

(19) Gramse, G.; Casuso, I.; Toset, J.; Fumagalli, L.; Gomila, G. Quantitative Dielectric Constant Measurement of Thin Films by DC Electrostatic Force Microscopy. *Nanotechnology* **2009**, *20* (39). https://doi.org/10.1088/0957-4484/20/39/395702.

(20) Fumagalli, L.; Ferrari, G.; Sampietro, M.; Gomila, G. Quantitative Nanoscale Dielectric Microscopy of Single-Layer Supported Biomembranes. *Nano Lett.* **2009**, *9* (4), 1604–1608. https://doi.org/10.1021/nl803851u.

(21) Dols-Perez, A.; Gramse, G.; Caló, A.; Gomila, G.; Fumagalli, L. Nanoscale Electric Polarizability of Ultrathin Biolayers on Insulating Substrates by Electrostatic Force Microscopy. *Nanoscale* **2015**, *7*, 18327–18336. https://doi.org/10.1039/x0xx00000x.

(22) Cuervo, A.; Dans, P. D.; Carrascosa, J. L.; Orozco, M.; Gomila, G.; Fumagalli, L. Direct Measurement of the Dielectric Polarization Properties of DNA. *Proc. Natl. Acad. Sci. U. S. A.* **2014**, *111* (35). https://doi.org/10.1073/pnas.1405702111.

(23) Biagi, M. C.; Fabregas, R.; Gramse, G.; Van Der Hofstadt, M.; Juárez, A.; Kienberger, F.; Fumagalli, L.; Gomila, G. Nanoscale Electric Permittivity of Single Bacterial Cells at Gigahertz Frequencies by Scanning Microwave Microscopy. *ACS Nano* **2016**, *10* (1), 280–288. https://doi.org/10.1021/acsnano.5b04279.

(24) Esteban-Ferrer, D.; Edwards, M. A.; Fumagalli, L.; Juárez, A.; Gomila, G. Electric Polarization Properties of Single Bacteria Measured with Electrostatic Force Microscopy. *ACS Nano* **2014**, *8* (10), 9843–9849. https://doi.org/10.1021/nn5041476.

(25) Van Der Hofstadt, M.; Fabregas, R.; Millan-Solsona, R.; Juarez, A.; Fumagalli, L.; Gomila, G. Internal Hydration Properties of Single Bacterial Endospores Probed by Electrostatic Force Microscopy. *ACS Nano* **2016**, *10* (12), 11327–11336. https://doi.org/10.1021/acsnano.6b06578.

(26) Checa, M.; Millan-Solsona, R.; Blanco, N.; Torrents, E.; Fabregas, R.; Gomila, G. Mapping the Dielectric Constant of a Single Bacterial Cell at the Nanoscale with Scanning Dielectric Force Volume Microscopy. *Nanoscale* **2019**, *11* (43), 20809–20819. https://doi.org/10.1039/c9nr07659j.

(27) Lozano, H.; Fabregas, R.; Blanco-Cabra, N.; Millán-Solsona, R.; Torrents, E.; Fumagalli, L.; Gomila, G. Dielectric Constant of Flagellin Proteins Measured by Scanning Dielectric Microscopy. *Nanoscale* **2018**, *10* (40), 19188–19194. https://doi.org/10.1039/c8nr06190d.

(28) Gramse, G.; Edwards, M. A.; Fumagalli, L.; Gomila, G. Dynamic Electrostatic Force Microscopy in Liquid Media. *Appl. Phys. Lett.* **2012**, *101* (21). https://doi.org/10.1063/1.4768164.

(29) Gramse, G.; Dols-Perez, A.; Edwards, M. A.; Fumagalli, L.; Gomila, G. Nanoscale Measurement of the Dielectric Constant of Supported Lipid Bilayers in Aqueous

Solutions with Electrostatic Force Microscopy. *Biophys. J.* **2013**, *104* (6), 1257–1262. https://doi.org/10.1016/j.bpj.2013.02.011.

(30) Millán, R.; Checa, M.; Fumagalli, L.; Gomila, G. Mapping the Capacitance of Self-Assembled Monolayers at Metal/Electrolyte Interfaces at the Nanoscale by In-Liquid Scanning Dielectric Microscopy. *Nanoscale* **2020**, *12* (40), 20658–20668. https://doi.org/10.1039/d0nr05723a.

(31) Di Muzio, M.; Millan-Solsona, R.; Borrell, J. H.; Fumagalli, L.; Gomila, G. Cholesterol Effect on the Specific Capacitance of Submicrometric DOPC Bilayer Patches Measured by In-Liquid Scanning Dielectric Microscopy. *Langmuir* **2020**, *36* (43), 12963–12972. https://doi.org/10.1021/acs.langmuir.0c02251.

(32) Di Muzio, M.; Millán, R.; Gomila, G. Electrical Properties and Lamellarity of Single Liposomes Measured by In-Liquid SDM. *[in Preparation].*

(33) Fumagalli, L.; Esfandiar, A.; Fabregas, R.; Hu, S.; Ares, P.; Janardanan, A.; Yang, Q.; Radha, B.; Taniguchi, T.; Watanabe, K.; et al. Anomalously Low Dielectric Constant of Confined Water. *Science* **2018**, *360* (6395), 1339–1342. https://doi.org/10.1126/science.aat4191.

(34) Fabregas, R.; Gomila, G. Dielectric Nanotomography Based on Electrostatic Force Microscopy: A Numerical Analysis. *J. Appl. Phys.* **2020**, *127* (2). https://doi.org/10.1063/1.5122984.

(35) Castañeda-Uribe, O. A.; Reifenberger, R.; Raman, A.; Avila, A. Depth-Sensitive Subsurface Imaging of Polymer Nanocomposites Using Second Harmonic Kelvin Probe Force Microscopy. *ACS Nano* **2015**, *9* (3), 2938–2947. https://doi.org/10.1021/nn507019c.

(36) Riedel, C.; Alegra, A.; Schwartz, G. A.; Arinero, R.; Colmenero, J.; Senz, J. J. On the Use of Electrostatic Force Microscopy as a Quantitative Subsurface Characterization Technique: A Numerical Study. *Appl. Phys. Lett.* **2011**, *99* (2), 99–101. https://doi.org/10.1063/1.3608161.

(37) Zhao, M.; Gu, X.; Lowther, S. E.; Park, C.; Jean, Y. C.; Nguyen, T. Subsurface Characterization of Carbon Nanotubes in Polymer Composites via Quantitative Electric Force Microscopy. *Nanotechnology* **2010**, *21* (22). https://doi.org/10.1088/0957-4484/21/22/225702.

(38) Cadena, M. J.; Misiego, R.; Smith, K. C.; Avila, A.; Pipes, B.; Reifenberger, R.; Raman, A. Sub-Surface Imaging of Carbon Nanotube-Polymer Composites Using Dynamic AFM Methods. *Nanotechnology* **2013**, *24* (13). https://doi.org/10.1088/0957-4484/24/13/135706.

(39) Alekseev, A.; Chen, D.; Tkalya, E. E.; Ghislandi, M. G.; Syurik, Y.; Ageev, O.; Loos, J.; De With, G. Local Organization of Graphene Network inside Graphene/Polymer Composites. *Adv. Funct. Mater.* **2012**, *22* (6), 1311–1318. https://doi.org/10.1002/adfm.201101796.

(40) Casuso, I.; Fumagalli, L.; Gomila, G.; Padrós, E. Nondestructive Thickness Measurement of Biological Layers at the Nanoscale by Simultaneous Topography and Capacitance Imaging. *Appl. Phys. Lett.* **2007**, *91* (6), 063111–063113. https://doi.org/10.1063/1.2767979.

(41) Kyndiah, A.; Checa, M.; Leonardi, F.; Millan-Solsona, R.; Di Muzio, M.; Tanwar, S.; Fumagalli, L.; Mas-Torrent, M.; Gomila, G. Nanoscale Mapping of the Conductivity and Interfacial Capacitance of an Electrolyte-Gated Organic Field-Effect Transistor under Operation. *Adv. Funct. Mater.* **2020**, *2008032*, 1–8. https://doi.org/10.1002/adfm.202008032.

(42) Lubrano, C.; Matrone, G. M.; Iaconis, G.; Santoro, F. New Frontiers for Selective

Biosensing with Biomembrane-Based Organic Transistors. *ACS Nano* **2020**, *14* (10), 12271–12280. https://doi.org/10.1021/acsnano.0c07053.

(43) Guest, W. C.; Cashman, N. R.; Plotkin, S. S. A Theory for the Anisotropic and Inhomogeneous Dielectric Properties of Proteins. *Phys. Chem. Chem. Phys.* **2011**, *13* (13), 6286–6295. https://doi.org/10.1039/c0cp02061c.

(44) Dilger, J.; McLaughlin, S.; McIntosh, T.; Simon, S. The Dielectric Constant of Phospholipid Bilayers and the Permeability of Membranes to Ions. *Science* **1979**, *206*, 1196–1198.

(45) Coster, H. G. L. The Physics of Cell Membranes. *J. Biol. Phys.* **2003**, *29* (4), 363–399. https://doi.org/10.1023/A:1027362704125.

(46) Hardy, W. L. Propagation Speed in Myelinated Nerve: I. Experimental Dependence on External Na+ and on Temperature. *Biophys. J.* **1973**, *13* (10), 1054–1070. https://doi.org/10.1016/S0006-3495(73)86045-X.

(47) Hardy, W. L. Propagation Speed in Myelinated Nerve: II. Theoretical Dependence on External Na+ and on Temperature. *Biophys. J.* **1973**, *13* (10), 1071–1089. https://doi.org/10.1016/S0006-3495(73)86046-1.

(48) Tasaki, I. The Electro-Saltatory Transmission of the Nerve Impulse and the Effect of Narcosis upon the Nerve Fiber. *Am. J. Psychol.* **1939**, *127* (1), 211–227.

(49) J. B. Hursh. Conduction Velocity and Diameter of Nerve Fibers. *Am. J. Physiol.* **1939**, *127* (1), 131–139.

(50) Gramse, G.; Edwards, M. A.; Fumagalli, L.; Gomila, G. Theory of Amplitude Modulated Electrostatic Force Microscopy for Dielectric Measurements in Liquids at MHz Frequencies. *Nanotechnology* **2013**, *24* (41). https://doi.org/10.1088/0957-4484/24/41/415709.

(51) Lim, C. T.; Zhou, E. H.; Quek, S. T. Mechanical Models for Living Cells - A Review. *J. Biomech.* **2006**, *39* (2), 195–216. https://doi.org/10.1016/j.jbiomech.2004.12.008.

(52) Domínguez-Bajo, A.; González-Mayorga, A.; Guerrero, C. R.; Palomares, F. J.; García, R.; López-Dolado, E.; Serrano, M. C. Myelinated Axons and Functional Blood Vessels Populate Mechanically Compliant RGO Foams in Chronic Cervical Hemisected Rats. *Biomaterials* **2019**, *192*, 461–474. https://doi.org/10.1016/j.biomaterials.2018.11.024.

(53) Escribá, P. V.; González-Ros, J. M.; Goñi, F. M.; Kinnunen, P. K. J.; Vigh, L.; Sánchez-Magraner, L.; Fernández, A. M.; Busquets, X.; Horváth, I.; Barceló-Coblijn, G. Membranes: A Meeting Point for Lipids, Proteins and Therapies: Translational Medicine. *J. Cell. Mol. Med.* **2008**, *12* (3), 829–875. https://doi.org/10.1111/j.1582-4934.2008.00281.x.

(54) Lombard, J. Once upon a Time the Cell Membranes: 175 Years of Cell Boundary Research. *Biol. Direct* **2014**, *9* (1), 1–35. https://doi.org/10.1186/s13062-014-0032-7.

(55) Sezgin, E.; Levental, I.; Mayor, S.; Eggeling, C. The Mystery of Membrane Organization : Composition , Regulation and Roles of Lipid Rafts. *Nat. Rev. Mol. Cell. Biol.* **2017**, *18* (6), 361–374. https://doi.org/10.1038/nrm.2017.16.

(56) Desai, A. J.; Miller, L. J. Changes in the Plasma Membrane in Metabolic Disease: Impact of the Membrane Environment on G Protein-Coupled Receptor Structure and Function. *Br. J. Pharmacol.* **2018**, *175* (21), 4009–4025. https://doi.org/10.1111/bph.13943.

(57) Casares, D.; Escribá, P. V.; Rosselló, C. A. Membrane Lipid Composition: Effect on Membrane and Organelle Structure, Function and Compartmentalization and Therapeutic Avenues. *Int. J. Mol. Sci.* **2019**, *20* (9).

https://doi.org/10.3390/ijms20092167.

(58) Escribá, P. V.; Busquets, X.; Inokuchi, J. I.; Balogh, G.; Török, Z.; Horváth, I.; Harwood, J. L.; Vígh, L. Membrane Lipid Therapy: Modulation of the Cell Membrane Composition and Structure as a Molecular Base for Drug Discovery and New Disease Treatment. *Prog. Lipid Res.* **2015**, *59*, 38–53. https://doi.org/10.1016/j.plipres.2015.04.003.

(59) Escribá, P. V. Membrane-Lipid Therapy: A Historical Perspective of Membrane-Targeted Therapies — From Lipid Bilayer Structure to the Pathophysiological Regulation of Cells. *Biochim. Biophys. Acta - Biomembr.* **2017**, *1859* (9), 1493–1506. https://doi.org/10.1016/j.bbamem.2017.05.017.

(60) E, O. *The Probable Origin and Physiological Significance of Cellular Osmotic Properties. In Papers on Biological Membrane Structure*; Branton D, P. R. B., Ed.; Little, Brown and Company, 1968.

(61) Gorter, E.; Grendel, F. On Bimolecular Layers of Lipoids on the Chromocytes of the Blood. *J. Exp. Med.* **1925**, *41* (4), 439–444. https://doi.org/10.1084/jem.41.4.439.

(62) CHAPMAN, G. B.; KROLL, A. J. Electron Microscopy of Ultrathin Sections of Spirillum Serpens. *J. Bacteriol.* **1957**, *73* (1), 63–71. https://doi.org/10.1128/jb.73.1.63-71.1957.

(63) HILLIER, J.; HOFFMAN, J. F. On the Ultrastructure of the Plasma Membrane as Determined by the Electron Microscope. *J. Cell. Comp. Physiol.* **1953**, *42* (2), 203–247. https://doi.org/10.1002/jcp.1030420205.

(64) Murray, R. G. E. Direct Evidence for a Cytoplasmic Membrane in Sectioned Bacteria. *Can J. Microbiol* **1957**, *3*, 3–6.

(65) Singer, S. J.; Nicolson, G. L. The Fluid Mosaic Model of the Structure of Cell Membranes. *Science (80-.).* **1972**, *175*, 720–731.

(66) Edidin, M. Lipid Microdomains in Cell Surface Membranes. *Curr. Opin. Struct. Biol.* **1997**, *7* (4), 528–532. https://doi.org/10.1016/S0959-440X(97)80117-0.

(67) Edidin, M. The State of Lipid Rafts: From Model Membranes to Cells. *Annu. Rev. Biophys. Biomol. Struct.* **2003**, *32*, 257–283. https://doi.org/10.1146/annurev.biophys.32.110601.142439.

(68) Van Meer, G.; Voelker, D. R.; Feigenson, G. W. Membrane Lipids: Where They Are and How They Behave. *Nat. Rev. Mol. Cell Biol.* **2008**, *9* (2), 112–124. https://doi.org/10.1038/nrm2330.

(69) Mouritsen, O. G.; Zuckermann, M. J. Mouritsen_Zuckermann_2004. **2004**, *39* (11), 1101–1113.

(70) Hannich, J. T.; Umebayashi, K.; Riezman, H. Distribution and Functions of Sterols and Sphingolipids. *Cold Spring Harb. Perspect. Biol.* **2011**, *3* (5), 1–14. https://doi.org/10.1101/cshperspect.a004762.

(71) Yamashita, A.; Hayashi, Y.; Nemoto-Sasaki, Y.; Ito, M.; Oka, S.; Tanikawa, T.; Waku, K.; Sugiura, T. Acyltransferases and Transacylases That Determine the Fatty Acid Composition of Glycerolipids and the Metabolism of Bioactive Lipid Mediators in Mammalian Cells and Model Organisms. *Prog. Lipid Res.* **2014**, *53* (1), 18–81. https://doi.org/10.1016/j.plipres.2013.10.001.

(72) Harayama, T.; Riezman, H. Understanding the Diversity of Membrane Lipid Composition. *Nat. Rev. Mol. Cell Biol.* **2018**, *19* (5), 281–296. https://doi.org/10.1038/nrm.2017.138.

(73) PL., Y. *The Structure of Biological Membranes*, 2nd ed.; Boca Raton, New York: CRC Press, 2005.

(74) Ingólfsson, H. I.; Melo, M. N.; Van Eerden, F. J.; Arnarez, C.; Lopez, C. A.; Wassenaar, T. A.; Periole, X.; De Vries, A. H.; Tieleman, D. P.; Marrink, S. J. Lipid Organization of the Plasma Membrane. *J. Am. Chem. Soc.* **2014**, *136* (41), 14554–14559. https://doi.org/10.1021/ja507832e.

(75) Philip L. Yeagle. *The Structure of Biological Membranes*, second edi.; CRC PRESS, 2005.

(76) Simons, K.; Ikonen, E. Functional Rafts in Cell Membranes. *Nature* **1997**, *387* (6633), 569–572. https://doi.org/10.1038/42408.

(77) Patil, Y. P.; Jadhav, S. Novel Methods for Liposome Preparation. *Chem. Phys. Lipids* **2014**, *177*, 8–18. https://doi.org/10.1016/j.chemphyslip.2013.10.011.

(78) Chiba, M.; Miyazaki, M.; Ishiwata, S. Quantitative Analysis of the Lamellarity of Giant Liposomes Prepared by the Inverted Emulsion Method. *Biophys. J.* **2014**, *107* (2), 346–354. https://doi.org/10.1016/j.bpj.2014.05.039.

(79) El-Hammadi, M. M.; Arias, J. L. An Update on Liposomes in Drug Delivery: A Patent Review (2014-2018). *Expert Opin. Ther. Pat.* **2019**, *29* (11), 891–907. https://doi.org/10.1080/13543776.2019.1679767.

(80) Karlsson, A.; Sott, K.; Markström, M.; Davidson, M.; Konkoli, Z.; Orwar, O. Controlled Initiation of Enzymatic Reactions in Micrometer-Sized Biomimetic Compartments. *J. Phys. Chem. B* **2005**, *109* (4), 1609–1617. https://doi.org/10.1021/jp0459716.

(81) Pick, H.; Alves, A. C.; Vogel, H. Single-Vesicle Assays Using Liposomes and Cell-Derived Vesicles: From Modeling Complex Membrane Processes to Synthetic Biology and Biomedical Applications. *Chem. Rev.* **2018**, *118* (18), 8598–8654. https://doi.org/10.1021/acs.chemrev.7b00777.

(82) Ries, R. S.; Choi, H.; Blunck, R.; Bezanilla, F.; Heath, J. R. Black Lipid Membranes: Visualizing the Structure, Dynamics, and Substrate Dependence of Membranes. *J. Phys. Chem. B* **2004**, *108* (41), 16040–16049. https://doi.org/10.1021/jp048098h.

(83) Frey, C. M.; Barth, H.; Kranz, C.; Mizaikoff, B. Horizontal Black Lipid Bilayer Membranes for Studying Pore-Forming Toxins. *Anal. Methods* **2018**, *10* (26), 3153–3161. https://doi.org/10.1039/c8ay01122b.

(84) Mueller, P.; Rudin, D. O.; Ti Tien, H.; Wescott, W. C. Reconstitution of Cell Membrane Structure in Vitro and Its Transformation into an Excitable System. *Nat. Int. J. Sci.* **1962**, *194*, 979–980. https://doi.org/https://doi.org/10.1038/1961048b0.

(85) Tsemperouli, M.; Amstad, E.; Sakai, N.; Matile, S.; Sugihara, K. Black Lipid Membranes: Challenges in Simultaneous Quantitative Characterization by Electrophysiology and Fluorescence Microscopy. *Langmuir* **2019**, *35* (26), 8718–8757. https://doi.org/10.1021/acs.langmuir.9b00673.

(86) Blodgett, K. B. Films Built by Depositing Successive Monomolecular Layers on a Solid Surface. *J. Am. Chem. Soc.* **1935**, *57* (6), 1007–1022. https://doi.org/10.1021/ja01309a011.

(87) Richter, R. P.; Brisson, A. R. Following the Formation of Supported Lipid Bilayers on Mica: A Study Combining AFM, QCM-D, and Ellipsometry. *Biophys. J.* **2005**, *88* (5), 3422–3433. https://doi.org/10.1529/biophysj.104.053728.

(88) Richter, R. P.; Bérat, R.; Brisson, A. R. Formation of Solid-Supported Lipid Bilayers: An Integrated View. *Langmuir* **2006**, *22* (8), 3497–3505. https://doi.org/10.1021/la052687c.

(89) Yee, C. K.; Amweg, M. L.; Parikh, A. N. Membrane Photolithography: Direct Micropatterning and Manipulation of Fluid Phospholipid Membranes in the Aqueous Phase Using Deep-UV Light. *Adv. Mater.* **2004**, *16* (14), 1184–1189.

https://doi.org/10.1002/adma.200306498.

(90) Levy, D.; Milhiet, P. Imaging of Transmembrane Proteins Directly Incorporated Within Supported Lipid Bilayers Using Atomic Force Microscopy. In *Sousa A., Kruhlak M. (eds) Nanoimaging. Methods in Molecular Biology (Methods and Protocols)*; Humana Press, Totowa, NJ., 2013; Vol. 950, pp 343–357. https://doi.org/10.1007/978-1-62703-137-0.

(91) Milhiet, P. E.; Gubellini, F.; Berquand, A.; Dosset, P.; Rigaud, J. L.; Le Grimellec, C.; Lévy, D. High-Resolution AFM of Membrane Proteins Directly Incorporated at High Density in Planar Lipid Bilayer. *Biophys. J.* **2006**, *91* (9), 3268–3275. https://doi.org/10.1529/biophysj.106.087791.

(92) Sumino, A.; Yamamoto, D.; Iwamoto, M.; Dewa, T.; Oiki, S. Gating-Associated Clustering-Dispersion Dynamics of the KcsA Potassium Channel in a Lipid Membrane. *J. Phys. Chem. Lett.* **2014**, *5* (3), 578–584. https://doi.org/10.1021/jz402491t.

(93) Goennenwein, S.; Tanaka, M.; Hu, B.; Moroder, L.; Sackmann, E. Functional Incorporation of Integrins into Solid Supported Membranes on Ultrathin Films of Cellulose: Impact on Adhesion. *Biophys. J.* **2003**, *85* (1), 646–655. https://doi.org/10.1016/S0006-3495(03)74508-1.

(94) Tanaka, M.; Kaufmann, S.; Kaufmann, S.; Nissen, J.; Hochrein, M. Orientation Selective Immobilization of Human Erythrocyte Membranes on Ultrathin Cellulose Films. *Phys. Chem. Chem. Phys.* **2001**, *3* (18), 4091–4095. https://doi.org/10.1039/b105007a.

(95) Tanaka, M.; Wong, A. P.; Rehfeldt, F.; Tutus, M.; Kaufmann, S. Selective Deposition of Native Cell Membranes on Biocompatible Micropatterns. *J. Am. Chem. Soc.* **2004**, *126* (10), 3257–3260. https://doi.org/10.1021/ja038981d.

(96) Nissen, J.; Gritsch, S.; Wiegand, G.; Rädler, J. O. Wetting of Phospholipid Membranes on Hydrophilic Surfaces - Concepts towards Self-Healing Membranes. *Eur. Phys. J. B* **1999**, *10* (2), 335–344. https://doi.org/10.1007/s100510050862.

(97) Tanaka, M.; Rehfeldt, F.; Schneider, M. F.; Mathe, G.; Albersdörfer, A.; Neumaier, K. R.; Purrucker, O.; Sackmann, E. Wetting and Dewetting of Extracellular Matrix and Glycocalix Models. *J. Phys. Condens. Matter* **2005**, *17* (9). https://doi.org/10.1088/0953-8984/17/9/022.

(98) Schaub, M.; Wenz, G.; Wegner, G.; Stein, A.; Klemm, D. Ultrathin Films of Cellulose on Silicon Wafers. *Adv. Mater.* **1993**, *5* (12), 919–922. https://doi.org/10.1002/adma.19930051209.

(99) Sackmann, E. Supported Membranes: Scientific and Practical Applications. *Science* **1996**, *271* (5245), 43–48. https://doi.org/10.1126/science.271.5245.43.

(100) Knoll, W.; Frank, C. W.; Heibel, C.; Naumann, R.; Offenhäusser, A.; Rühe, J.; Schmidt, E. K.; Shen, W. W.; Sinner, A. Functional Tethered Lipid Bilayers. *Rev. Mol. Biotechnol.* **2000**, *74* (3), 137–158. https://doi.org/10.1016/s1389-0352(00)00012-x.

(101) Sackmann, E.; Tanaka, M. Supported Membranes on Soft Polymer Cushions: Fabrication, Characterization and Applications. *Trends Biotechnol.* **2000**, *18* (2), 58–64. https://doi.org/10.1016/S0167-7799(99)01412-2.

(102) Elender, G.; Sackmann, E. Wetting and Dewetting of Si/SiO 2 -Wafers by Free and Lipidmonolayer Covered Aqueous Solutions under Controlled Humidity . *J. Phys. II* **1994**, *4* (3), 455–479. https://doi.org/10.1051/jp2:1994107.

(103) Tanaka, M.; Sackmann, E. Polymer-Supported Membranes as Models of the Cell Surface. *Nature* **2005**, *437* (7059), 656–663. https://doi.org/10.1038/nature04164.

(104) Dietrich, C.; Schmitrr, L.; Tampe, R. Molecular Organization of Histidine-Tagged

Biomolecules at Self-Assembled Lipid Interfaces Using a Novel Class of Chelator Lipids (Membranes/Protein Engineering/Fluorescence Microscopy/Film Balance/Supramolecular Assemblies). *Proc. Nat. Acad. Sci. USA* **1995**, *92* (September), 9014–9018.

(105) Heyse, S.; Vogel, H.; Sänger, M.; Sigrist, H. Covalent Attachment of Functionalized Lipid Bilayers to Planar Waveguides for Measuring Protein Binding to Biomimetic Membranes. *Protein Sci.* **1995**, *4* (12), 2532–2544. https://doi.org/10.1002/pro.5560041210.

(106) Cho, N. J.; Cho, S. J.; Kwang, H. C.; Glenn, J. S.; Frank, C. W. Employing an Amphipathic Viral Peptide to Create a Lipid Bilayer on Au and TiO2. *J. Am. Chem. Soc.* **2007**, *129* (33), 10050–10051. https://doi.org/10.1021/ja0701412.

(107) Reimhult, E.; Höök, F.; Kasemo, B. Intact Vesicle Adsorption and Supported Biomembrane Formation from Vesicles in Solution: Influence of Surface Chemistry, Vesicle Size, Temperature, and Osmotic Pressure. *Langmuir* **2003**, *19* (5), 1681–1691. https://doi.org/10.1021/la0263920.

(108) Tabaei, S. R.; Choi, J. H.; Haw Zan, G.; Zhdanov, V. P.; Cho, N. J. Solvent-Assisted Lipid Bilayer Formation on Silicon Dioxide and Gold. *Langmuir* **2014**, *30* (34), 10363–10373. https://doi.org/10.1021/la501534f.

(109) Ferhan, A. R.; Yoon, B. K.; Park, S.; Sut, T. N.; Chin, H.; Park, J. H.; Jackman, J. A.; Cho, N. J. Solvent-Assisted Preparation of Supported Lipid Bilayers. *Nat. Protoc.* **2019**, *14* (7), 2091–2118. https://doi.org/10.1038/s41596-019-0174-2.

(110) Sekula, S.; Fuchs, J.; Weg-Remers, S.; Nagel, P.; Schuppler, S.; Fragala, J.; Theilacker, N.; Franzreb, M.; Wingren, C.; Ellmark, P.; et al. Multiplexed Lipid Dip-Pen Nanolithography on Subcellular Scales for the Templating of Functional Proteins and Cell Culture. *Small* **2008**, *4* (10), 1785–1793. https://doi.org/10.1002/smll.200800949.

(111) Steven, L.; Mirkin, C. A.; Fuchs, H. In Situ Lipid Dip-Pen Nanolithography under Water. *Scanning* **2010**, *32* (1), 15–23. https://doi.org/10.1002/sca.20166.

(112) Zhong, J.; Sun, G.; He, D. Classic, Liquid, and Matrix-Assisted Dip-Pen Nanolithography for Materials Research. *Nanoscale* **2014**, *6* (21), 12217–12228. https://doi.org/10.1039/c4nr04296d.

(113) Naumann, R.; Schiller, S. M.; Giess, F.; Grohe, B.; Hartman, K. B.; Kärcher, I.; Köper, I.; Lübben, J.; Vasilev, K.; Knoll, W. Tethered Lipid Bilayers on Ultraflat Gold Surfaces. *Langmuir* **2003**, *19* (13), 5435–5443. https://doi.org/10.1021/la0342060.

(114) Peng, Z.; Tang, J.; Han, X.; Wang, E.; Dong, S. Formation of a Supported Hybrid Bilayer Membrane on Gold: A Sterically Enhanced Hydrophobic Effect. *Langmuir* **2002**, *18* (12), 4834–4839. https://doi.org/10.1021/la011194e.

(115) Hudalla, G. A.; Murphy, W. L. Chemically Well-Defined Self-Assembled Monolayers for Cell Culture: Toward Mimicking the Natural ECM. *Soft Matter* **2011**, *7* (20), 9561–9571. https://doi.org/10.1039/c1sm05596h.

(116) Casalini, S.; Bortolotti, C. A.; Leonardi, F.; Biscarini, F. Self-Assembled Monolayers in Organic Electronics. *Chem. Soc. Rev.* **2017**, *46* (1), 40–71. https://doi.org/10.1039/c6cs00509h.

(117) Love, J. C.; Estroff, L. A.; Kriebel, J. K.; Nuzzo, R. G.; Whitesides, G. M. Self-Assembled Monolayers of Thiolates on Metals as a Form of Nanotechnology. *Chem. Rev.* **2005**, *105*, 1103–1169. https://doi.org/10.1002/(SICI)1521-4095(199910)11:15<1285::AID-ADMA1285>3.0.CO;2-J.

(118) Morigaki, K.; Baumgart, T.; Offenhäusser, A.; Knoll, W. Patterning Solid-Supported Lipid Bilayer Mmembranes by Lithographic Polymerization of a Diacetylene Lipid.

Angew. Chem Int. Ed. **2001**, *40* (1), 172–174. https://doi.org/10.1007/s11664-015-3694-8.

(119) Hovis, J. S.; Boxer, S. G. Patterning Barriers to Lateral Diffusion in Supported Lipid Bilayer Membranes by Blotting and Stamping. *Langmuir* **2000**, *16* (3), 894–897. https://doi.org/10.1021/la991175t.

(120) Elemans, J. A. A. W.; Lei, S.; De Feyter, S. Molecular and Supramolecular Networks on Surfaces: From Two-Dimensional Crystal Engineering to Reactivity. *Angew. Chemie - Int. Ed.* **2009**, *48* (40), 7298–7332. https://doi.org/10.1002/anie.200806339.

(121) Hille, B. Ionic Channels in Excitable Membranes. Current Problems and Biophysical Approaches. *Biophys. J.* **1978**, *22* (2), 283–294. https://doi.org/10.1016/S0006-3495(78)85489-7.

(122) AlGhatrif, M.; Lindsay, J. A Brief Review: History to Understand Fundamentals of Electrocardiography. *J. Community Hosp. Intern. Med. Perspect.* **2012**, *2* (1), 14383. https://doi.org/10.3402/jchimp.v2i1.14383.

(123) Sheinerman, F. B.; Honig, B. On the Role of Electrostatic Interactions in the Design of Protein-Protein Interfaces. *J. Mol. Biol.* **2002**, *318* (1), 161–177. https://doi.org/10.1016/S0022-2836(02)00030-X.

(124) Zhou, H. X.; Pang, X. Electrostatic Interactions in Protein Structure, Folding, Binding, and Condensation. *Chem. Rev.* **2018**, *118* (4), 1691–1741. https://doi.org/10.1021/acs.chemrev.7b00305.

(125) Pohl, H. A. *Dielectrophoresis: The Behavior of Neutral Matter in Nonuniform Electric Fields*; Cambridge University Press, London, 1978.

(126) Grimnes, S.; Martinsen, O. *Bioimpedance and Bioelectricity Basics*; Academic Press, San Diego, CA., 2000.

(127) Weaver, J. C.; Chizmadzhev, Y. A. Theory of Electroporation: A Review. *Bioelectrochemistry Bioenerg.* **1996**, *41* (2), 135–160. https://doi.org/10.1016/S0302-4598(96)05062-3.

(128) Kyndiah, A.; Leonardi, F.; Tarantino, C.; Cramer, T.; Millan-Solsona, R.; Garreta, E.; Montserrat, N.; Mas-Torrent, M.; Gomila, G. Bioelectronic Recordings of Cardiomyocytes with Accumulation Mode Electrolyte Gated Organic Field Effect Transistors. *Biosens. Bioelectron.* **2020**, *150*, 111844. https://doi.org/10.1016/j.bios.2019.111844.

(129) Cramer, T.; Chelli, B.; Murgia, M.; Barbalinardo, M.; Bystrenova, E.; De Leeuw, D. M.; Biscarini, F. Organic Ultra-Thin Film Transistors with a Liquid Gate for Extracellular Stimulation and Recording of Electric Activity of Stem Cell-Derived Neuronal Networks. *Phys. Chem. Chem. Phys.* **2013**, *15* (11), 3897–3905. https://doi.org/10.1039/c3cp44251a.

(130) HODGKIN, A. L.; RUSHTON, W. A. The Electrical Constants of a Crustacean Nerve Fibre. *Proc. R. Soc. Med.* **1946**, *134* (873), 444–479. https://doi.org/10.1098/rspb.1946.0024.

(131) Waller, M. D.; Augustus, D. A Demonstration on Man of Electromotive Changes Accompanying the Heart's Beat. *J Physiol.* **1887**, *8* (5), 229–234.

(132) Fahanik-babaei, J.; Eliassi, A.; Jafari, A.; Sauve, R.; Salari, S.; Saghiri, R. Biochimica et Biophysica Acta Electro-Pharmacological Profile of a Mitochondrial Inner Membrane Big-Potassium Channel from Rat Brain. *Biochim. Biophys. Acta - Biomembr.* **2011**, *1808* (1), 454–460. https://doi.org/10.1016/j.bbamem.2010.10.005.

(133) Chen, C. C.; Cang, C.; Fenske, S.; Butz, E.; Chao, Y. K.; Biel, M.; Ren, D.; Wahl-Schott, C.; Grimm, C. Patch-Clamp Technique to Characterize Ion Channels in

Enlarged Individual Endolysosomes. *Nat. Protoc.* **2017**, *12* (8), 1639–1658. https://doi.org/10.1038/nprot.2017.036.

(134) Maki, B. A.; Cummings, K. A.; Paganelli, M. A.; Murthy, S. E.; Popescu, G. K. One-Channel Cell-Attached Patch-Clamp Recording. *J. Vis. Exp.* **2014**, No. 88, 2014. https://doi.org/10.3791/51629.

(135) Neher, E.; Sakmann, B. Single-Channel Currents Recorded from Membrane of Denervated Frog Muscle Fibres. *Nature* **1976**, *260* (5554), 799–802. https://doi.org/10.1038/260799a0.

(136) Cole, K. S.; Moore, J. W. Potassium Ion Current in the Squid Giant Axon: Dynamic Characteristic. *Biophys. J.* **1960**, *1* (1), 1–14. https://doi.org/10.1016/S0006-3495(60)86871-3.

(137) Schwan, H. P.; Kay, C. F. The Conductivity of Living Tissues. *Ann. N. Y. Acad. Sci.* **1957**, *65* (6), 1007–1013. https://doi.org/10.1111/j.1749-6632.1957.tb36701.x.

(138) Cole, K. S. *Membrane, Ions and Impulses*; of California Press, Berkeley, 1972.

(139) Goldman, D. E. Potential, Impedance and Rectification in Membranes. *J. Gen. Physiol.* **1943**, *27* (1), 37–60.

(140) Coster, H. G. L.; Chilcott, T. C.; Coster, A. C. F. Impedance Spectroscopy of Interfaces, Membranes and Ultrastructures. *Bioelectrochemistry Bioenerg.* **1996**, *40* (2), 79–98. https://doi.org/10.1016/0302-4598(96)05064-7.

(141) Ohki, S.; Arnold, K. Surface Dielectric Constant, Surface Hydrophobicity and Membrane Fusion. *J. Membr. Biol.* **1990**, *114* (3), 195–203. https://doi.org/10.1007/BF01869214.

(142) Jansen, J. C. *Encyclopedia of Membranes*; 2016. https://doi.org/10.1007/978-3-662-44324-8.

(143) Höber, R. Eine Methode, Die Elektrische Leitfahigkeit Im Innem von Zellen Zu Messen. *Arch. Ges. Physiol.* **1910**, *133*, 237–259.

(144) Overton, E. Ueber Die Allgemeinen Osmotischen Eigenschaften Der Zelle, Ihre Vermutlichen Ursachen Und Ihre Bedeutung Fur Die Physiologie. *Vjschr. Naturf. Ges. Zurich* **1899**, *44*, 88–113.

(145) Morse, H. F. and S. The Electrical Resistance and Capacity of Blood for Frequencies between 800 Hz and 4.5 MHz. *J. Gen. Physiol.* **1925**, *9*, 153–167.

(146) T. Hanai, D. A. H. and J. L. T. An Investigation by Electrical Methods of Lecithin-in-Hydrocarbon Films in Aqueous Solution. *Proc. R. Sot. London, Ser. A* **1964**, *281*, 337–391.

(147) Robertson, J. D. The Molecular Structure and Contact Relationships of Cell Membranes. *Prog. Biophys.* **1960**, *10*, 343–418.

(148) Cheung, K. C.; Berardino, M. Di; Schade-Kampmann, G.; Hebeisen, M.; Pierzchalski, A.; Bocsi, J.; Mittag, A.; Tárnok, A. Microfluidic Impedance-Based Flow Cytometry. *Cytom. Part A* **2010**, *77* (7), 648–666. https://doi.org/10.1002/cyto.a.20910.

(149) Rodriguez-Trujillo, R.; Castillo-Fernandez, O.; Garrido, M.; Arundell, M.; Valencia, A.; Gomila, G. High-Speed Particle Detection in a Micro-Coulter Counter with Two-Dimensional Adjustable Aperture. *Biosens. Bioelectron.* **2008**, *24* (2), 290–296. https://doi.org/10.1016/j.bios.2008.04.005.

(150) Castillo-Fernandez, O.; Rodriguez-Trujillo, R.; Gomila, G.; Samitier, J. High-Speed Counting and Sizing of Cells in an Impedance Flow Microcytometer with Compact Electronic Instrumentation. *Microfluid. Nanofluidics* **2014**, *16* (1–2), 91–99. https://doi.org/10.1007/s10404-013-1225-6.

(151) Spencer, D.; Morgan, H. High-Speed Single-Cell Dielectric Spectroscopy. *ACS Sensors* **2020**, *5* (2), 423–430. https://doi.org/10.1021/acssensors.9b02119.

(152) Binnig, G.; Rohrer, H. Scanning Tunneling Microscopy. *Helv. Phys.Acta* **1982**, *55*, 726–735.

(153) Binnig, G.; Quate, C. F. Atomic Force Microscope. *Phys. Rev. Lett.* **1986**, *56* (9), 930–933. https://doi.org/10.1201/9781420075250.

(154) Pürckhauer, K.; Weymouth, A. J.; Pfeffer, K.; Kullmann, L.; Mulvihill, E.; Krahn, M. P.; Müller, D. J.; Giessibl, F. J. Imaging in Biologically-Relevant Environments with AFM Using Stiff QPlus Sensors. *Sci. Rep.* **2018**, *8* (1), 1–9. https://doi.org/10.1038/s41598-018-27608-6.

(155) Leitner, M.; Seferovic, H.; Stainer, S.; Buchroithner, B.; Schwalb, Christian H. Deutschinger, Alexander Ebner, A. Atomic Force Microscopy Imaging in Turbid Liquids: A Promising Tool in Nanomedicine. *Sensors* **2020**, *20* (13), 3715.

(156) Medalsy, I.; Hensen, U.; Muller, D. J. Imaging and Quantifying Chemical and Physical Properties of Native Proteins at Molecular Resolution by Force-Volume AFM. *Angew. Chemie - Int. Ed.* **2011**, *50* (50), 12103–12108. https://doi.org/10.1002/anie.201103991.

(157) Saavedra, V. Oscar Fernandes, Thales F. D. Milhiet, Pierre-Emmanuel Costa, L. Compression, Rupture, and Puncture of Model Membranes at the Molecular Scale. *Langmuir* **2020**, *36* (21), 5709–5716.

(158) Garcia-Manyes, S.; Redondo-Morata, L.; Oncins, G.; Sanz, F. Nanomechanics of Lipid Bilayers: Heads or Tails? *J. Am. Chem. Soc.* **2010**, *132* (37), 12874–12886. https://doi.org/10.1021/ja1002185.

(159) Garcia, R. Nanomechanical Mapping of Soft Materials with the Atomic Force Microscope: Methods, Theory and Applications. *Chem. Soc. Rev.* **2020**, *49* (16), 5850–5884. https://doi.org/10.1039/d0cs00318b.

(160) Toshio Ando, Noriyuki Kodera, Eisuke Takai, Daisuke Maruyama, Kiwamu Saito, and A. T. A High-Speed Atomic Force Microscope for Studying Biological Macromolecules. *Proc. Nat. Acad. Sci. USA* **2001**, *98* (22), 12468–12472.

(161) Kodera, N.; Yamamoto, D.; Ishikawa, R.; Ando, T. Video Imaging of Walking Myosin V by High-Speed Atomic Force Microscopy. *Nature* **2010**, *468* (7320), 72–76.

(162) Hertz, H. Über Die Berührung Fester Elastischer Körper. *J. für die reine und Angew. Math.* **1881**, *92*, 156–171.

(163) Schaefer, D. M.; Gomez, J. Atomic Force Microscope Techniques for Adhesion Measurements. *J. Adhes.* **2000**, *74* (1–4), 341–359. https://doi.org/10.1080/00218460008034535.

(164) Gumí-audenis, B.; Costa, L.; Carlá, F.; Comin, F.; Sanz, F.; Giannotti, M. I. Structure and Nanomechanics of Model Membranes by Atomic Force Microscopy and Spectroscopy : Insights into the Role of Cholesterol and Sphingolipids. *Membranes (Basel).* **2016**, *6* (58). https://doi.org/10.3390/membranes6040058.

(165) Gumí-Audenis, B.; Sanz, F.; Giannotti, M. I. Impact of Galactosylceramides on the Nanomechanical Properties of Lipid Bilayer Models: An AFM-Force Spectroscopy Study. *Soft Matter* **2015**, *11* (27), 5447–5454. https://doi.org/10.1039/c5sm01252j.

(166) Gumí-Audenis, B.; Illa-Tuset, S.; Grimaldi, N.; Pasquina-Lemonche, L.; Ferrer-Tasies, L.; Sanz, F.; Veciana, J.; Ratera, I.; Faraudo, J.; Ventosa, N.; et al. Insights into the Structure and Nanomechanics of a Quatsome Membrane by Force Spectroscopy Measurements and Molecular Simulations. *Nanoscale* **2018**, *10* (48), 23001–23011. https://doi.org/10.1039/c8nr07110a.

(167) Gumí-Audenis, B.; Costa, L.; Ferrer-Tasies, L.; Ratera, I.; Ventosa, N.; Sanz, F.; Giannotti, M. I. Pulling Lipid Tubes from Supported Bilayers Unveils the Underlying Substrate Contribution to the Membrane Mechanics. *Nanoscale* **2018**, *10* (30), 14763–14770. https://doi.org/10.1039/c8nr03249a.

(168) Gumí-Audenis, B.; Giannotti, M. I. Structural and Mechanical Characterization of Supported Model Membranes by AFM. *Biomim. Lipid Membr. Fundam. Appl. Commer.* **2019**, 1–27. https://doi.org/10.1007/978-3-030-11596-8_1.

(169) Preiner, J.; Ebner, A.; Chtcheglova, L.; Zhu, R.; Hinterdorfer, P. Simultaneous Topography and Recognition Imaging: Physical Aspects and Optimal Imaging Conditions. *Nanotechnology* **2009**, *20* (21), 215103.

(170) Calò, A.; Romin, Y.; Srouji, R.; Zambirinis, C. P.; Fan, N.; Santella, A.; Feng, E.; Fujisawa, S.; Turkekul, M.; Huang, S.; et al. Spatial Mapping of the Collagen Distribution in Human and Mouse Tissues by Force Volume Atomic Force Microscopy. *Sci. Rep.* **2020**, *10* (1), 1–12. https://doi.org/10.1038/s41598-020-72564-9.

(171) Rico, F.; Roca-Cusachs, P.; Gavara, N.; Farré, R.; Rotger, M.; Navajas, D. Probing Mechanical Properties of Living Cells by Atomic Force Microscopy with Blunted Pyramidal Cantilever Tips. *Phys. Rev. E - Stat. Nonlinear, Soft Matter Phys.* **2005**, *72* (2), 1–10. https://doi.org/10.1103/PhysRevE.72.021914.

(172) Garcia, P. D.; Guerrero, C. R.; Garcia, R. Nanorheology of Living Cells Measured by AFM-Based Force–Distance Curves. *Nanoscale* **2020,** *12* (16), 9133-9143. https://doi.org/10.1039/c9nr10316c.

(173) Guerrero, C. R.; Garcia, P. D.; Garcia, R. Subsurface Imaging of Cell Organelles by Force Microscopy. *ACS Nano* **2019**, *13* (8), 9629–9637. https://doi.org/10.1021/acsnano.9b04808.

(174) Mandriota, N.; Friedsam, C.; Jones-Molina, J. A.; Tatem, K. V.; Ingber, D. E.; Sahin, O. Cellular Nanoscale Stiffness Patterns Governed by Intracellular Forces. *Nat. Mater.* **2019**, *18* (10), 1071–1077. https://doi.org/10.1038/s41563-019-0391-7.

(175) Shibata, M.; Uchihashi, T.; Ando, T.; Yasuda, R. Long-Tip High-Speed Atomic Force Microscopy for Nanometer-Scale Imaging in Live Cells. *Sci. Rep.* **2015**, *5*, 1–7. https://doi.org/10.1038/srep08724.

(176) Ando, T.; Kodera, N.; Takai, E.; Maruyama, D.; Saito, K.; Toda, A. A High-Speed Atomic Force Microscope for Studying Biological Macromolecules. *Proc. Natl. Acad. Sci. U. S. A.* **2001**, *98* (22), 12468–12472. https://doi.org/10.1073/pnas.211400898.

(177) Fumagalli, L.; Gomila, G. Probing Dielectric Constant at the Nanoscale with Scanning Probe Microscopy. In *Capacitance Spectroscopy of Semiconductors*; Li, J. V., Ferrari, G., Eds.; Pan Stanford Publishing Pte. Ltd., Standford, 2018; pp 361–390.

(178) Lee, D. T.; Pelz, J. P.; Bhushan, B. Instrumentation for Direct, Low Frequency Scanning Capacitance Microscopy, and Analysis of Position Dependent Stray Capacitance. *Rev. Sci. Instrum.* **2002**, *73* (10), 3525. https://doi.org/10.1063/1.1505655.

(179) Barrett, R. C.; Quate, C. F. Charge Storage in a Nitride-Oxide-Silicon Medium by Scanning Capacitance Microscopy. *J. Appl. Phys.* **1991**, *70* (5), 2725–2733. https://doi.org/10.1063/1.349388.

(180) Williams, C. C. Two-Dimensional Dopant Profiling by Scanning Capacitance Force Microscopy. *Annu. Rev. Mater. Sci.* **1999**, *29*, 471–504. https://doi.org/10.1016/S0169-4332(02)01486-1.

(181) Shao, R.; Kalinin, S. V.; Bonnell, D. A. Nanoimpedance Microscopy and Spectroscopy. *Mater. Res. Soc. Symp. - Proc.* **2003**, *738* (December), 163–168.

https://doi.org/10.1557/proc-738-g4.4.

(182) Gramse, G.; Kölker, A.; Lim, T.; Stock, T. J. Z.; Solanki, H.; Schofield, S. R.; Brinciotti, E.; Aeppli, G.; Kienberger, F.; Curson, N. J. Nondestructive Imaging of Atomically Thin Nanostructures Buried in Silicon. *Sci. Adv.* **2017**, *3* (6), 1–9. https://doi.org/10.1126/sciadv.1602586.

(183) Tuca, S. S.; Badino, G.; Gramse, G.; Brinciotti, E.; Kasper, M.; Oh, Y. J.; Zhu, R.; Rankl, C.; Hinterdorfer, P.; Kienberger, F. Calibrated Complex Impedance of CHO Cells and E. Coli Bacteria at GHz Frequencies Using Scanning Microwave Microscopy. *Nanotechnology* **2016**, *27* (13), 1-9. https://doi.org/10.1088/0957-4484/27/13/135702.

(184) Nonnenmacher, M.; O'Boyle, M. P.; Wickramasinghe, H. K. Kelvin Probe Force Microscopy. *Appl. Phys. Lett.* **1991**, *58* (25), 2921–2923. https://doi.org/10.1063/1.105227.

(185) Hu, J.; Xiao, X. D.; Salmeron, M. Scanning Polarization Force Microscopy: A Technique for Imaging Liquids and Weakly Adsorbed Layers. *Appl. Phys. Lett.* **1995**, *67*, 476. https://doi.org/10.1063/1.114541.

(186) Fumagalli, L.; Edwards, M. A.; Gomila, G. Quantitative Electrostatic Force Microscopy with Sharp Silicon Tips. *Nanotechnology* **2014**, *25* (49). https://doi.org/10.1088/0957-4484/25/49/495701.

(187) Gomila, G.; Gramse, G.; Fumagalli, L. Finite-Size Effects and Analytical Modeling of Electrostatic Force Microscopy Applied to Dielectric Films. *Nanotechnology* **2014**, *25* (25). https://doi.org/10.1088/0957-4484/25/25/255702.

(188) Gomila, G.; Esteban-Ferrer, D.; Fumagalli, L. Quantification of the Dielectric Constant of Single Non-Spherical Nanoparticles from Polarization Forces: Eccentricity Effects. *Nanotechnology* **2013**, *24* (50). https://doi.org/10.1088/0957-4484/24/50/505713.

(189) Gramse, G.; Gomila, G.; Fumagalli, L. Quantifying the Dielectric Constant of Thick Insulators by Electrostatic Force Microscopy: Effects of the Microscopic Parts of the Probe. *Nanotechnology* **2012**, *23* (20). https://doi.org/10.1088/0957-4484/23/20/205703.

(190) Tevaarwerk, E.; Keppel, D. G.; Rugheimer, P.; Lagally, M. G.; Eriksson, M. A. Quantitative Analysis of Electric Force Microscopy: The Role of Sample Geometry. *Rev. Sci. Instrum.* **2005**, *76* (5), 1–6. https://doi.org/10.1063/1.1898183.

(191) Capacitance Spectroscopy of Semiconductors. *Capacitance Spectroscopy of Semiconductors*. 2018. https://doi.org/10.1201/b22451.

(192) Hudlet, S.; Saint Jean, M.; Guthmann, C.; Berger, J. Evaluation of the Capacitive Force between an Atomic Force Microscopy Tip and a Metallic Surface. *Eur. Phys. J. B* **1998**, *2* (1), 5–10. https://doi.org/10.1007/s100510050219.

(193) Sacha, G. M.; Verdaguer, A.; Martínez, J.; Sáenz, J. J.; Ogletree, D. F.; Salmeron, M. Effective Tip Radius in Electrostatic Force Microscopy. *Appl. Phys. Lett.* **2005**, *86* (12), 1–3. https://doi.org/10.1063/1.1884764.

(194) Crider, P. S.; Majewski, M. R.; Zhang, J.; Oukris, H.; Israeloff, N. E. Local Dielectric Spectroscopy of Polymer Films. *Appl. Phys. Lett.* **2007**, *91* (1). https://doi.org/10.1063/1.2753539.

(195) Riedel, C.; Arinero, R.; Tordjeman, P.; Lévêque, G.; Schwartz, G. A.; Alegria, A.; Colmenero, J. Nanodielectric Mapping of a Model Polystyrene-Poly(Vinyl Acetate) Blend by Electrostatic Force Microscopy. *Phys. Rev. E - Stat. Nonlinear, Soft Matter Phys.* **2010**, *81* (1), 1–4. https://doi.org/10.1103/PhysRevE.81.010801.

(196) Dufrêne, Y. F.; Martínez-Martín, D.; Medalsy, I.; Alsteens, D.; Müller, D. J.

Multiparametric Imaging of Biological Systems by Force-Distance Curve-Based AFM. *Nat. Methods* **2013**, *10* (9), 847–854. https://doi.org/10.1038/nmeth.2602.

(197) Checa, M.; Millan-Solsona, R.; Gomila, G. Frequency-Dependent Force between Ac-Voltage-Biased Plates in Electrolyte Solutions. *Phys. Rev. E* **2019**, *100* (2), 1–19. https://doi.org/10.1103/PhysRevE.100.022604.

(198) Polcari, D.; Dauphin-Ducharme, P.; Mauzeroll, J. Scanning Electrochemical Microscopy: A Comprehensive Review of Experimental Parameters from 1989 to 2015. *Chem. Rev.* **2016**, *116* (22), 13234–13278. https://doi.org/10.1021/acs.chemrev.6b00067.

(199) Zhu, C.; Huang, K.; Siepser, N. P.; Baker, L. A. Scanning Ion Conductance Microscopy. *Chem. Rev.* **2020**. https://doi.org/10.1021/acs.chemrev.0c00962.

(200) Nymeyer, H.; Zhou, H.-X. A Method to Determine Dielectric Constants in Nonhomogeneous Systems: Application to Biological Membranes. *Biophys J.* **2008**, *94* (4), 1185–1193.

(201) Mori, T.; Miyashita, N.; Im, W.; Feig, M.; Sugita, Y. Molecular Dynamics Simulations of Biological Membranes and Membrane Proteins Using Enhanced Conformational Sampling Algorithm. *Biochim. Biophys. Acta* **2016**, *1858* (7), 1635–1651.

(202) Raiteri, R.; Grattarola, M.; Butt, H.-J. Measuring Electrostatic Double-Layer Forces at High Surface Potentials with the Atomic Force Microscope. *J. Phys. Chem* **1996**, *100* (41), 16700–16705.

(203) Yang, Y.; Mayer, K. M.; Hafner, J. H. Quantitative Membrane Electrostatics with the Atomic Force Microscope. *Biophys. J.* **2007**, *92* (6), 1966–1974. https://doi.org/10.1529/biophysj.106.093328.

(204) Yang, Y.; Mayer, K. M.; Wickremasinghe, N. S.; Hafner, J. H. Probing the Lipid Membrane Dipole Potential by Atomic Force Microscopy. *Biophys. J.* **2008**, *95* (11), 5193–5199. https://doi.org/10.1529/biophysj.108.136507.

(205) Umeda, K.; Kobayashi, K.; Oyabu, N.; Matsushige, K.; Yamada, H. Molecular-Scale Quantitative Charge Density Measurement of Biological Molecule by Frequency Modulation Atomic Force Microscopy in Aqueous Solutions. *Nanotechnology* **2015**, *26* (28), 285103. https://doi.org/10.1088/0957-4484/26/28/285103.

(206) Lynch, B. P.; Hilton, A. M.; Simpson, G. J. Nanoscale Dielectrophoretic Spectroscopy of Individual Immobilized Mammalian Blood Cells. *Biophys. J.* **2006**, *91* (7), 2678–2686. https://doi.org/10.1529/biophysj.106.082412.

(207) Fukuma, T. Water Distribution at Solid/Liquid Interfaces Visualized by Frequency Modulation Atomic Force Microscopy. *Sci. Technol. Adv. Mater.* **2010**, *11* (3), 033003. https://doi.org/10.1088/1468-6996/11/3/033003.

(208) Nymeyer, H.; Zhou, H. X. A Method to Determine Dielectric Constants in Nonhomogeneous Systems: Application to Biological Membranes. *Biophys. J.* **2008**, *94* (4), 1185–1193. https://doi.org/10.1529/biophysj.107.117770.

(209) Lee, C. Y.; McCammon, J. A.; Rossky, P. J. The Structure of Liquid Water at an Extended Hydrophobic Surface. *J. Chem. Phys.* **1984**, *80* (9), 4448–4455. https://doi.org/10.1063/1.447226.

(210) Cicero, G.; Grossman, J. C.; Schwegler, E.; Gygi, F.; Galli, G. Water Confined in Nanotubes and between Graphene Sheets : A First Principle Study. *J. Am. Chem .Soc.* **2008**, *130* (12), 1871–1878.

(211) Tocci, G.; Joly, L.; Michaelides, A. Friction of Water on Graphene and Hexagonal Boron Nitride from Ab Initio Methods: Very Different Slippage Despite Very Similar Interface Structures. **2014**. https://doi.org/10.1021/nl502837d.

(212) Israelachvili, J. N.; Pashley, R. M. Molecular Layering of Water at Surfaces and Origin of Repulsive Hydration Forces. *Nature* **1983**, *306*, 17–18.

(213) Toney, M. F.; Howard, J. N.; Richer, J.; Borges, G. L.; Gordon, J. G.; Melroy, O. R.; Wiesler, D. G.; Yee, D.; Sorensen, L. B. Voltage-Dependent Ordering of Water Molecules at an Electrode-Electrolyte Interface. *Nature* **1994**, *368*, 444–446.

(214) Wu, C. H.; Pascal, T. A.; Wan, L. F.; Guo, J.; Prendergast, D. The Structure of Interfacial Water on Gold Electrodes Studied by X-Ray Absorption. *Science* **2014**, *346* (October), 1–6.

(215) Warshel, A.; Sharma, P. K.; Kato, M.; Parson, W. W. Modeling Electrostatic Effects in Proteins. *Biochim. Biophys. Acta - Proteins Proteomics* **2006**, *1764* (11), 1647–1676. https://doi.org/10.1016/j.bbapap.2006.08.007.

(216) Israelachvili, J. N. *Intermolecular and Surface Forces*, ed. 3.; Academic Press, San Diego, CA., 2011.

(217) Leikin, S.; Parsegian, V. A.; Rau, D. C. Hydration Forces. *Annu. Rev. Phys. Chem.* **1993**, *44*, 369–395.

(218) Honig, B.; Nicholls, A. Classical Electrostatics in Biology and Chemistry. *Science* **1995**, *268*, 1144–1149.

(219) Umeda, K.; Kobayashi, K.; Matsushige, K.; Yamada, H. Direct Actuation of Cantilever in Aqueous Solutions by Electrostatic Force Using High- Frequency Electric Fields. *Appl. Phys. Lett.* **2012**, *101* (123112). https://doi.org/10.1063/1.4754289.

(220) Raiteri, R.; Butt, H.-J. Measuring Electrochemically Induced Surface Stress with an Atomic Force Microscope. *J. Phys. Chem.* **1995**, *99*, 15728–15732.

(221) Umeda, K.; Oyabu, N.; Kobayashi, K.; Hirata, Y.; Matsushige, K.; Yamada, H. High-Resolution Frequency-Modulation Atomic Force Microscopy in Liquids Using Electrostatic Excitation Method. *Appl. Phys. Express* **2010**, *3* (065205), 3–6. https://doi.org/10.1143/APEX.3.065205.

(222) Kobayashi, N.; Asakawa, H.; Fukuma, T. Nanoscale Potential Measurements in Liquid by Frequency Modulation Atomic Force Microscopy. *Rev. Sci. Instrum.* **2010**, *81* (12), 5–9. https://doi.org/10.1063/1.3514148.

(223) Grahame, D. C. The Electrical Double Layer and the Theory of Electrocapillarity. *Chem. Rev.* **1947**, *41*, 441–501. https://doi.org/10.1021/cr60130a002.

(224) Parsons, R. Electrical Double Layer : Recent Experimental and Theoretical Developments. *Chem. Rev.* **1990**, *90*, 813–826.

(225) Parsons, R. The Metal-Liquid Electrolyte Interface. *Solid State Ion.* **1997**, *94*, 91.

(226) Chiantia, S.; Ries, J.; Kahya, N.; Schwille, P. Combined AFM and Two-Focus SFCS Study of Raft-Exhibiting Model Membranes. *ChemPhysChem* **2006**, *7* (11), 2409–2418. https://doi.org/10.1002/cphc.200600464.

(227) Massimo Olivotto , Annarosa Arcangeli, M. C. and E. W. Electric Fields at the Plasma Membrane Level: A Neglected Element in the Mechanisms of Cell Signalling. *Bioessays* **1996**, *18*, 495–504.

(228) Grimnes, S.; Martinsen, O. *Bioimpedance and Bioelectricity Basics*; Academic Press: San Diego, 2000.

(229) Pohl, H. A. *Dielectrophoresis: The Behavior of Neutral Matter in Nonuniform Electric Fields*; Cambridge University Press: London, 1978.

(230) Jones, T. B. Basic Theory of Dielectrophoresis and Electrorotation. *IEEE Eng. Med. Biol.* **2003**, *22*, 33–42.

(231) Hanai, T.; Haydon, D. A.; Taylor, J. The Influence of Lipid Composition and of Some Adsorbed Proteins on the Capacitance of Black Hydrocarbon Membranes. *J Theor Biol.* **1965**, *9*, 422–432.

(232) Benz, R.; Fröhlich, O.; Läuger, P.; Montal, M. Electrical Capacity of Black Lipid Films and of Lipid Bilayers Made from Monolayers. *Biochim. Biophys. Acta* **1975**, *394*, 323–334.

(233) Naumowicz, M.; Petelska, A. D.; Figaszewski, Z. A. Impedance Analysis of Phosphatidylcholine – Cholesterol System in Bilayer Lipid Membranes. *Electrochim. Acta* **2005**, *50*, 2155–2161. https://doi.org/10.1016/j.electacta.2004.09.023.

(234) Taylor, G. J.; Heberle, F. A.; Seinfeld, J. S.; Katsaras, J.; Collier, C. P.; Sarles, S. A. Capacitive Detection of Low-Enthalpy, Higher-Order Phase Transitions in Synthetic and Natural Composition Lipid Membranes. *Langmuir* **2017**, *33*, 10016–10026. https://doi.org/10.1021/acs.langmuir.7b02022.

(235) Velikonja, A.; Kramar, P.; Miklavčič, D.; Lebar, A. M. Specific Electrical Capacitance and Voltage Breakdown as a Function of Temperature for Different Planar Lipid Bilayers. *Bioelectrochemistry* **2016**, *112*, 132–137. https://doi.org/10.1016/j.bioelechem.2016.02.009.

(236) Abraham, S.; Heckenthaler, T.; Morgenstern, Y.; Kaufman, Y. Effect of Temperature on the Structure, Electrical Resistivity, and Charge Capacitance of Supported Lipid Bilayers. *Langmuir* **2019**, *35*, 8709–8715. https://doi.org/10.1021/acs.langmuir.9b00726.

(237) Naumowicz, M.; Figaszewski, Z. A. The Effect of PH on the Electrical Capacitance of Phosphatidylcholine- Phosphatidylserine System in Bilayer Lipid Membrane. *J. Membr. Biol.* **2014**, *247* (4), 361–369. https://doi.org/10.1007/s00232-014-9644-1.

(238) Klymchenko, A. S. Solvatochromic and Fluorogenic Dyes as Environment-Sensitive Probes: Design and Biological Applications. *Acc. Chem. Res.* **2017**, *50* (2), 366–375. https://doi.org/10.1021/acs.accounts.6b00517.

(239) Erilov, D. A.; Bartucci, R.; Guzzi, R.; Shubin, A. A.; Maryasov, A. G.; Marsh, D.; Dzuba, S. A.; Sportelli, L. Water Concentration Profiles in Membranes Measured by ESEEM of Spin-Labeled Lipids. *J. Phys. Chem. B* **2005**, *109*, 12003–12013.

(240) Guzzi, R.; Bartucci, R. Electron Spin Resonance of Spin-Labeled Lipid Assemblies and Proteins. *Arch. Biochem. Biophys.* **2015**, *580*, 102–111. https://doi.org/10.1016/j.abb.2015.06.015.

(241) Botet-carreras, A.; Montero, M. T.; Domènech, Ò.; Borrell, J. H. Effect of Cholesterol on Monolayer Structure of Different Acyl Chained Phospholipids. *Colloids Surfaces B Biointerfaces* **2019**, *174*, 374–383. https://doi.org/10.1016/j.colsurfb.2018.11.040.

(242) Ohki, S. The Electrical Capacitance of Phospholipid Membranes. *Biophys. J.* **1969**, *9* (10), 1195–1205. https://doi.org/10.1016/S0006-3495(69)86445-3.

(243) Ashcroft, R. G.; Coster, H. G. L.; Laver, D. R.; Smith, J. R. The Effects of Cholesterol Inclusion on the Molecular Organisation of Bimolecular Lipid Membranes. *BBA - Biomembr.* **1983**, *730* (2), 231–238. https://doi.org/10.1016/0005-2736(83)90338-3.

(244) Naumowicz, M.; Petelska, A. D. Capacitance and Resistance of the Bilayer Lipid Membrane Formed of Phosphatidylcholine and Cholesterol. *Cell. Mol. Biol. Lett.* **2003**, *8*, 5–18.

(245) Naumowicz, M.; Figaszewski, Z. A. Impedance Analysis of Lipid Domains in Phosphatidylcholine Bilayer Membranes Containing Ergosterol. *Biophys. J.* **2005**, *89* (5), 3174–3182. https://doi.org/10.1529/biophysj.105.063446.

(246) Karolis, C.; Coster, H. G. L.; Chilcott, T. C.; Barrow, K. D. Differential Effects of

Cholesterol and Oxidised-Cholesterol in Egg Lecithin Bilayers. *Biochim. Biophys. Acta - Biomembr.* **1998**, *1368* (2), 247–255. https://doi.org/10.1016/S0005-2736(97)00180-6.

(247) Abraham, S.; Heckenthaler, T.; Bandyopadhyay, D.; Morgenstern, Y.; Kaufman, Y. Quantitative Description of the Vesicle Fusion Mechanism on Solid Surfaces and the Role of Cholesterol. *J. Phys. Chem. C* **2018**, *122*, 22985–22995. https://doi.org/10.1021/acs.jpcc.8b06566.

(248) Alobeedallah, H.; Cornell, B.; Coster, H. The Effect of Cholesterol on the Dielectric Structure of Lipid Bilayers. *J. Membr. Biol.* **2018**, *251* (1), 153–161. https://doi.org/10.1007/s00232-017-0007-6.

(249) Coster, H. G. L. Dielectric and Electrical Properties of Lipid Bilayers in Relation to Their Structure. In *Planar Lipid Bilayers (BLMs) and Their Applications; Tien, H. T., Ottova-Leitmannova, A.*; 2003, Vol. 7; 75–108.

(250) Sukhorukov, V. L.; Arnold, W. M.; Zimmermann, U. Hypotonically Induced Changes in the Plasma Membrane of Cultured Mammalian Cells. *J. Membr. Biol.* **1993**, *132*, 27–40.

(251) Asami, K.; Takahashit, Y.; Takashima, S. Frequency Domain Analysis of Membrane Capacitance of Cultured Cells (HeLa and Myeloma) Using the Micropipette Technique. *Biophys. J.* **1990**, *58*, 143–148. https://doi.org/10.1016/S0006-3495(90)82360-2.

(252) Solsona, C.; Innocenti, B.; Ferna, J. M. Regulation of Exocytotic Fusion by Cell Inflation. *Biophys. J.* **1998**, *74*, 1061–1073. https://doi.org/10.1016/S0006-3495(98)74030-5.

(253) Gentet, L. J.; Stuart, G. J.; Clements, J. D. Direct Measurement of Specific Membrane Capacitance in Neurons. *Biophys. J.* **2000**, *79* (1), 314–320. https://doi.org/10.1016/S0006-3495(00)76293-X.

(254) White, S. H. The Physical Nature of Planar Bilayer Membranes. In *Ion Channel Reconstitution*; Springer: Boston, 1986; 3–35.

(255) Kalinowski, S. Electrochemical Methods and Their Application. In *In Advances in Planar Lipid Bilayers and Liposomes; Ottova-Leitmannova, A.; vol 2*; Diego, A. P. S., Ed.; 2005; pp 1–47.

(256) Gross, L. C. M.; Heron, A. J.; Baca, S. C.; Wallace, M. I. Determining Membrane Capacitance by Dynamic Control of Droplet Interface Bilayer Area. *Langmuir* **2011**, *27*, 14335–14342.

(257) Asami, K. Dielectric Imaging of Biological Cells. *Colloid Polym Sci* **1995**, *273*, 1095–1097.

(258) Basu, A.; Karmakar, P.; Karmakar, S. Supported Planar Single and Multiple Bilayer Formation by DOPC Vesicle Rupture on Mica Substrate : A Mechanism as Revealed by Atomic Force Microscopy Study. *J. Membr. Biol.* **2020**, *253* (2010). https://doi.org/10.1007/s00232-020-00117-2.

(259) Regan, D. .; Williams, J. .; Borri, P. .; Langbein, W. Lipid Bilayer Thickness Measured by Quantitative DIC Reveals Phase Transitions and Effects of Substrate Hydrophilicity. *Langmuir* **2019**, *35*, 13805−13814.

(260) Kučerka, N.; Pencer, J.; Nieh, M.-P.; Katsaras, J. Influence of Cholesterol on the Bilayer Properties of Monounsaturated Phosphatidylcholine Unilamellar Vesicles. *Eur. Phys. J. E* **2007**, *23*, 247–254. https://doi.org/10.1140/epje/i2007-10202-8.

(261) Chakraborty, S.; Doktorova, M. .; Molugu, T. R. .; Heberle, F. A. .; Scott, H. L. .; Dzikovski, B. .; Nagao, M. .; Stingaciu, L.-R. .; Standaert, R. F. .; Barrera, F. N. .; Katsaras, J. .; et al. How Cholesterol Stiffens Unsaturated Lipid Membranes. *Proc.*

Natl. Acad. Sci. USA **2020**, *117* (36), 21896–21905. https://doi.org/10.1073/pnas.2004807117.

(262) Pan, J.; Mills, T. T.; Tristram-Nagle, S.; Nagle, J. F. Cholesterol Perturbs Lipid Bilayers Nonuniversally. *Phys. Rev. Lett.* **2008**, *100* (19), 1–4. https://doi.org/10.1103/PhysRevLett.100.198103.

(263) Dols-perez, A.; Fumagalli, L.; Gomila, G. Structural and Nanomechanical Effects of Cholesterol in Binary and Ternary Spin-Coated Single Lipid Bilayers in Dry Conditions. *Colloids Surfaces B Biointerfaces* **2014**, *116*, 295–302. https://doi.org/10.1016/j.colsurfb.2013.12.049.

(264) Hung, W. C.; Lee, M. T.; Chen, F. Y.; Huang, H. W. The Condensing Effect of Cholesterol in Lipid Bilayers. *Biophys. J.* **2007**, *92* (11), 3960–3967. https://doi.org/10.1529/biophysj.106.099234.

(265) Huang, J.; Feigenson, G. W. A Microscopic Interaction Model of Maximum Solubility of Cholesterol in Lipid Bilayers. *Biophys. J.* **1999**, *76* (4), 2142–2157. https://doi.org/10.1016/S0006-3495(99)77369-8.

(266) Engelman, D. M. Membranes Are More Mosaic than Fluid. *Nature* **2005**, *438* (7068), 578–580. https://doi.org/10.1038/nature04394.

(267) Théry, C.; Zitvogel, L.; Amigorena, S. Exosomes : Composition, Biogenesis and Function. *Rev. Immunol.* **2002**, *2* (August), 569–579. https://doi.org/10.1038/nri855.

(268) Schwechheimer, C.; Kuehn, M. J. Outer-Membrane Vesicles from Gram-Negative Bacteria: Biogenesis and Functions. *Nat. Rev. Microbiol.* **2015**, *13* (10), 605–619. https://doi.org/10.1038/nrmicro3525.

(269) Pirbadian, S.; Barchinger, S. E.; Leung, K. M.; Byun, H. S.; Jangir, Y.; Bouhenni, R. A.; Reed, S. B.; Romine, M. F.; Saffarini, D. A.; Shi, L.; et al. Shewanella Oneidensis MR-1 Nanowires Are Outer Membrane and Periplasmic Extensions of the Extracellular Electron Transport Components. *Proc. Natl. Acad. Sci. U. S. A.* **2014**, *111* (35), 12883–12888. https://doi.org/10.1073/pnas.1410551111.

(270) Yang, Z.; Cao, J.; He, Y.; Yang, J. H.; Kim, T.; Peng, X.; Kim, J. S. Macro-/Micro-Environment-Sensitive Chemosensing and Biological Imaging. *Chem. Soc. Rev.* **2014**, *43* (13), 4563–4601. https://doi.org/10.1039/c4cs00051j.

(271) Wu, Y.; Štefl, M.; Olzyńska, A.; Hof, M.; Yahioglu, G.; Yip, P.; Casey, D. R.; Ces, O.; Humpolíčková, J.; Kuimova, M. K. Molecular Rheometry: Direct Determination of Viscosity in Lo and Ld Lipid Phases via Fluorescence Lifetime Imaging. *Phys. Chem. Chem. Phys.* **2013**, *15* (36), 14986–14993. https://doi.org/10.1039/c3cp51953h.

(272) Gaus, K.; Zech, T.; Harder, T. Visualizing Membrane Microdomains by Laurdan 2-Photon Microscopy (Review). *Mol. Membr. Biol.* **2006**, *23* (1), 41–48. https://doi.org/10.1080/09687860500466857.

(273) Bondar, O. P.; Rowe, E. S. Preferential Interactions of Fluorescent Probe Prodan with Cholesterol. *Biophys. J.* **1999**, *76* (2), 956–962. https://doi.org/10.1016/S0006-3495(99)77259-0.

(274) Melcrová, A.; Pokorna, S.; Vošahlíková, M.; Sýkora, J.; Svoboda, P.; Hof, M.; Cwiklik, L.; Jurkiewicz, P. Concurrent Compression of Phospholipid Membranes by Calcium and Cholesterol. *Langmuir* **2019**, *35* (35), 11358–11368. https://doi.org/10.1021/acs.langmuir.9b00477.

(275) Disalvo, E. A.; Arroyo, J.; Bernik, D. L. Interfacial Properties of Liposomes as Measured by Fluorescence and Optical Probes. *Methods Enzymol.* **2003**, *367*, 213–233. https://doi.org/10.1016/S0076-6879(03)67014-X.

(276) Kuimova, M. K. Mapping Viscosity in Cells Using Molecular Rotors. *Phys. Chem.*

Chem. Phys. **2012**, *14* (37), 12671–12686. https://doi.org/10.1039/c2cp41674c.

(277) Hosny, N. A.; Mohamedi, G.; Rademeyer, P.; Owen, J.; Wu, Y.; Tang, M. X.; Eckersley, R. J.; Stride, E.; Kuimova, M. K. Mapping Microbubble Viscosity Using Fluorescence Lifetime Imaging of Molecular Rotors. *Proc. Natl. Acad. Sci. U. S. A.* **2013**, *110* (23), 9225–9230. https://doi.org/10.1073/pnas.1301479110.

(278) Vyšniauskas, A.; Balaz, M.; Anderson, H. L.; Kuimova, M. K. Dual Mode Quantitative Imaging of Microscopic Viscosity Using a Conjugated Porphyrin Dimer. *Phys. Chem. Chem. Phys.* **2015**, *17* (11), 7548–7554. https://doi.org/10.1039/c5cp00439j.

(279) Kashirina, A. S.; López-Duarte, I.; Kubánková, M.; Gulin, A. A.; Dudenkova, V. V.; Rodimova, S. A.; Torgomyan, H. G.; Zagaynova, E. V.; Meleshina, A. V.; Kuimova, M. K. Monitoring Membrane Viscosity in Differentiating Stem Cells Using BODIPY-Based Molecular Rotors and FLIM. *Sci. Rep.* **2020**, *10* (1), 1–12. https://doi.org/10.1038/s41598-020-70972-5.

(280) Hill, R. J.; Wang, C. Y. Diffusion in Phospholipid Bilayer Membranes: Dual-Leaflet Dynamics and the Roles of Tracer-Leaflet and Inter-Leaflet Coupling. *Proc. R. Soc. A Math. Phys. Eng. Sci.* **2014**, *470* (2167). https://doi.org/10.1098/rspa.2013.0843.

(281) Kahya, N.; Scherfeld, D.; Bacia, K.; Poolman, B.; Schwille, P. Probing Lipid Mobility of Raft-Exhibiting Model Membranes by Fluorescence Correlation Spectroscopy. *J. Biol. Chem.* **2003**, *278* (30), 28109–28115. https://doi.org/10.1074/jbc.M302969200.

(282) Ahmed, S.; Thankiah, S.; Machán, R.; Hof, M.; Clayton, A. H. A.; Wright, G.; Sibarita, J.-B.; Korte, T.; Herrmann, A. Practical Manual For Fluorescence Microscopy Techniques. *PicoQuant GmbH* **2016**.

(283) Abbe, E. Beiträge Zur Theorie Des Mikroskops Und Der Mikroskopischen Wahrnehmung. *Arch. für mikroskopische Anat.* **1873**, *9* (1), 413–418. https://doi.org/10.1007/BF02956173.

(284) Fernandes, T. F. D.; Saavedra, O.; Margeat, E.; Milhiet, P. E.; Costa, L. Synchronous, Crosstalk-Free Correlative AFM and Confocal Microscopies/Spectroscopies. *Sci. Rep.* **2020**, *10* (1), 1–12. https://doi.org/10.1038/s41598-020-62529-3.

(285) Rainer Erdmann, Jorg Enderlein, M. W. *Time Correlated Single-Photon Counting and Fluorescence Spectroscopy*; Wiley-VCH, 2005.

(286) Becker, W. The Bh TCSPC Handbook. *Scanning* **2010**, No. 800, 1–566.

(287) Burns, A. R.; Frankel, D. J.; Buranda, T. Local Mobility in Lipid Domains of Supported Bilayers Characterized by Atomic Force Microscopy and Fluorescence Correlation Spectroscopy. *Biophys. J.* **2005**, *89* (2), 1081–1093. https://doi.org/10.1529/biophysj.105.060327.

(288) Shimolina, L. E.; Izquierdo, M. A.; López-Duarte, I.; Bull, J. A.; Shirmanova, M. V.; Klapshina, L. G.; Zagaynova, E. V.; Kuimova, M. K. Imaging Tumor Microscopic Viscosity in Vivo Using Molecular Rotors. *Sci. Rep.* **2017**, *7*, 1–11. https://doi.org/10.1038/srep41097.

(289) Dewitt, B. N.; Dunn, R. C. Interaction of Cholesterol in Ternary Lipid Mixtures Investigated Using Single-Molecule Fluorescence. *Langmuir* **2015**, *31* (3), 995–1004. https://doi.org/10.1021/la503797w.

(290) Bangham, A. D.; Hill, M. W.; Miller, N. G. Preparation and Use of Liposomes as Models of Biological Membranes. In *In Methods in Membrane Biology; Korn, E. D.; Vol. 1*; Plenum: New York, 1974; pp 1–68.

(291) Pattni, B. S.; Chupin, V. V.; Torchilin, V. P. New Developments in Liposomal Drug Delivery. *Chem. Rev.* **2015**, *115* (19), 10938–10966. https://doi.org/10.1021/acs.chemrev.5b00046.

(292) Allen, T. M.; Cullis, P. R. Liposomal Drug Delivery Systems: From Concept to Clinical Applications. *Adv. Drug Deliv. Rev.* **2013**, *65* (1), 36–48. https://doi.org/10.1016/j.addr.2012.09.037.

(293) Bozzuto, G.; Molinari, A. Liposomes as Nanomedical Devices. *Int. J. Nanomedicine* **2015**, *10*, 975–999. https://doi.org/10.2147/IJN.S68861.

(294) Routledge, S. J.; Linney, J. A.; Goddard, A. D. Liposomes as Models for Membrane Integrity. *Biochem. Soc. Trans.* **2019**, *47*, 919–932.

(295) Laouini, A.; Jaafar-Maalej, C.; Limayem-Blouza, I.; Sfar, S.; Charcosset, C.; Fessi, H. Preparation, Characterization and Applications of Liposomes: State of the Art. *J. Colloid Sci. Biotechnol.* **2012**, *1* (2), 147–168. https://doi.org/10.1166/jcsb.2012.1020.

(296) Kanásová, M.; Nesměrák, K. Systematic Review of Liposomes' Characterization Methods. *Monatshefte fur Chemie* **2017**, *148* (9), 1581–1593. https://doi.org/10.1007/s00706-017-1994-9.

(297) Chen, C.; Zhu, S.; Huang, T.; Wang, S.; Yan, X. Analytical Techniques for Single-Liposome Characterization Analytical Methods Accepted Manuscript. *Anal. Methods* **2013**, *5* (9), 1–18.

(298) Du Plessis, J.; Ramachandran, C.; Weiner, N.; Müller, D. G. The Influence of Lipid Composition and Lamellarity of Liposomes on the Physical Stability of Liposomes upon Storage. *Int. J. Pharm.* **1996**, *127* (2), 273–278. https://doi.org/10.1016/0378-5173(95)04281-4.

(299) Vorselen, D.; Marchetti, M.; López-Iglesias, C.; Peters, P. J.; Roos, W. H.; Wuite, G. J. L. Multilamellar Nanovesicles Show Distinct Mechanical Properties Depending on Their Degree of Lamellarity. *Nanoscale* **2018**, *10* (11), 5318–5324. https://doi.org/10.1039/c7nr09224e.

(300) Chan, K. L.; Gascoiyne, R. C.; Becker, F. F.; Pethig, R. Electrorotation of Liposomes: Verification of Dielectric Multi-Shell Model for Cells. *Biochim. Biophys. Acta* **1997**, *1349* (2), 182–196.

(301) Banquy, X.; Suarez, F.; Argaw, A.; Rabanel, J. M.; Grutter, P.; Bouchard, J. F.; Hildgen, P.; Giasson, S. Effect of Mechanical Properties of Hydrogel Nanoparticles on Macrophage Cell Uptake. *Soft Matter* **2009**, *5* (20), 3984–3991. https://doi.org/10.1039/b821583a.

(302) Yi, X.; Shi, X.; Gao, H. Cellular Uptake of Elastic Nanoparticles. *Phys. Rev. Lett.* **2011**, *107* (9), 1–5. https://doi.org/10.1103/PhysRevLett.107.098101.

(303) Hadady, H.; Montiel, C.; Wetta, D.; Geiger, E. J. Liposomes as a Model for the Study of High Frequency Dielectrophoresis. *Electrophoresis* **2015**, *36* (13), 1423–1428. https://doi.org/10.1002/elps.201400480.

(304) Gruber, H. J.; Schindler, H. External Surface and Lamellarity of Lipid Vesicles: A Practice-Oriented Set of Assay Methods. *BBA - Biomembr.* **1994**, *1189* (2), 212–224. https://doi.org/10.1016/0005-2736(94)90068-X.

(305) Edwards, K. A.; Baeumner, A. J. Analysis of Liposomes. *Talanta* **2006**, *68* (5), 1432–1441. https://doi.org/10.1016/j.talanta.2005.08.031.

(306) Bibi, S.; Kaur, R.; Henriksen-Lacey, M.; McNeil, S. E.; Wilkhu, J.; Lattmann, E.; Christensen, D.; Mohammed, A. R.; Perrie, Y. Microscopy Imaging of Liposomes: From Coverslips to Environmental SEM. *Int. J. Pharm.* **2011**, *417* (1–2), 138–150. https://doi.org/10.1016/j.ijpharm.2010.12.021.

(307) Robson, A. L.; Dastoor, P. C.; Flynn, J.; Palmer, W.; Martin, A.; Smith, D. W.; Woldu, A.; Hua, S. Advantages and Limitations of Current Imaging Techniques for Characterizing Liposome Morphology. *Front. Pharmacol.* **2018**, *9*, 1–8.

https://doi.org/10.3389/fphar.2018.00080.

(308) Kwok, R.; Evans, E. Thermoelasticity of Large Lecithin Bilayer Vesicles. *Biophys. J.* **1981**, *35* (3), 637–652. https://doi.org/10.1016/S0006-3495(81)84817-5.

(309) Akashi, K.; Miyata, H.; Itoh, H.; Kinosita, K. Preparation of Giant Liposomes in Physiological Conditions and Their Characterization under an Optical Microscope. *Biophys. J.* **1996**, *71* (6), 3242–3250. https://doi.org/10.1016/S0006-3495(96)79517-6.

(310) Wicher, D.; Gündel, J. Electrorotation of Multi- and Oligolamellar Liposomes. *J. Electroanal. Chem.* **1989**, *275* (3), 279–288. https://doi.org/10.1016/0022-0728(89)87229-8.

(311) Arinero, R.; Riedel, C.; Guasch, C. Numerical Simulations of Electrostatic Interactions between an Atomic Force Microscopy Tip and a Dielectric Sample in Presence of Buried Nano-Particles. *J. Appl. Phys.* **2012**, *112* (11). https://doi.org/10.1063/1.4768251.

(312) Jespersen, T. S.; Nygard, J. Mapping of Individual Carbon Nanotubes in Polymer/Nanotube Composites Using Electrostatic Force Microscopy. *Appl. Phys. Lett.* **2007**, *90* (18), 15–18. https://doi.org/10.1063/1.2734920.

(313) Thompson, H. T.; Barroso-Bujans, F.; Herrero, J. G.; Reifenberger, R.; Raman, A. Subsurface Imaging of Carbon Nanotube Networks in Polymers with DC-Biased Multifrequency Dynamic Atomic Force Microscopy. *Nanotechnology* **2013**, *24* (13). https://doi.org/10.1088/0957-4484/24/13/135701.

(314) Patel, S.; Petty, C. W.; Krafcik, K.; Loyola, B.; O'Bryan, G.; Friddle, R. W. Imaging Latex – Carbon Nanotube Composites by Subsurface Electrostatic Force Microscopy. *Nanotechnology* **2016**, *27*, 415705.

(315) Takano, H.; Porter, M. D. Monitoring Chemical Transformations at Buried Organic Interfaces by Electric Force Microscopy [3]. *J. Am. Chem. Soc.* **2001**, *123* (34), 8412–8413. https://doi.org/10.1021/ja016353v.

(316) Takano, H.; Wong, S. S.; Harnisch, J. A.; Porter, M. D. Mapping the Subsurface Composition of Organic Films by Electric Force Microscopy. *Langmuir* **2000**, *16* (12), 5231–5233. https://doi.org/10.1021/la0002334.

(317) Plonsey, R.; Barr, R. C. *Bioelectricity: A Quantitative Approach*; Plenum Press: New York, 1982.

(318) Ridolfi, A.; Brucale, M.; Montis, C.; Caselli, L.; Paolini, L.; Borup, A.; Boysen, A. T.; Loria, F.; Van Herwijnen, M. J. C.; Kleinjan, M.; et al. AFM-Based High-Throughput Nanomechanical Screening of Single Extracellular Vesicles. *Anal. Chem.* **2020**, *92* (15), 10274–10282. https://doi.org/10.1021/acs.analchem.9b05716.

(319) Jones, T. B. *Electromechanics of Particles*; Cambridge University Press: Cambridge, 1995.

(320) Giordano, S. Dielectric and Elastic Characterization of Nonlinear Heterogeneous Materials; *Materials* **2009**, *2* (4), 1417-1479 https://doi.org/10.3390/ma2041417.

(321) Loll, P. J. Membrane Protein Structural Biology : The High Throughput Challenge. *J. Struct. Biol.* **2003**, *142*, 144–153. https://doi.org/10.1016/S1047-8477(03)00045-5.

(322) Lin, Y. What's Happened over the Last Five Years with High-Throughput Protein Crystallization Screening ? *Expert Opin. Drug Discov.* **2018**, *13* (8), 691–695. https://doi.org/10.1080/17460441.2018.1465924.

(323) Shiu, P.; Ju, Y.; Chen, H.; Lee, C. Facile Isolation of Purple Membrane from Halobacterium Salinarum via Aqueous-Two-Phase System. *Protein Expr. Purif.* **2013**, *89* (2), 219–224. https://doi.org/10.1016/j.pep.2013.03.011.

(324) Popot, J.; Trewhella, J.; Engelman, D. M. Reformation of Crystalline Purple Membrane from Purified Bacteriorhodopsin Fragments. *EMBO J.* **1986**, *5* (11), 3039–3044. https://doi.org/10.1002/j.1460-2075.1986.tb04603.x.

(325) Wagner, N. L.; Greco, J. A.; Ranaghan, M. J.; Birge, R. R. Directed Evolution of Bacteriorhodopsin for Applications in Bioelectronics. *J. R. Soc. Interface* **2013**, *10* (84). https://doi.org/10.1098/rsif.2013.0197.

(326) Müller, D. J.; Heymann, J. B.; Oesterhelt, F.; Möller, C.; Gaub, H.; Büldt, G.; Engel, A. Atomic Force Microscopy of Native Purple Membrane. *Biochim. Biophys. Acta - Bioenerg.* **2000**, *1460* (1), 27–38. https://doi.org/10.1016/S0005-2728(00)00127-4.

(327) Hirai, T.; Subramaniam, S.; Lanyi, J. K. Structural Snapshots of Conformational Changes in a Seven-Helix Membrane Protein: Lessons from Bacteriorhodopsin. *Curr. Opin. Struct. Biol.* **2009**, *19* (4), 433–439. https://doi.org/10.1016/j.sbi.2009.07.009.

(328) Oesterhelt, D.; Stoeckenius, W. Functions of a New Photoreceptor Membrane. *Proc. Natl. Acad. Sci. U. S. A.* **1973**, *70* (10), 2853–2857. https://doi.org/10.1073/pnas.70.10.2853.

(329) Rico, F.; Su, C.; Scheuring, S. Mechanical Mapping of Single Membrane Proteins at Submolecular Resolution. *Nano Lett.* **2011**, *11* (9), 3983–3986. https://doi.org/10.1021/nl202351t.

(330) Voïtchovsky, K.; Contera, S. A.; Kamihira, M.; Watts, A.; Ryan, J. F. Differential Stiffness and Lipid Mobility in the Leaflets of Purple Membranes. *Biophys. J.* **2006**, *90* (6), 2075–2085. https://doi.org/10.1529/biophysj.105.072405.

(331) Kimura, Y.; Vassylyev, D. G.; Miyazawa, A.; Kidera, A.; Matsushima, M.; Mitsuoka, K.; Murata, K.; Hirai, T.; Fujiyoshi, Y. Surface of Bacteriorhodopsin Revealed by High-Resolution Electron Crystallography. *Nature* **1997**, *389* (6647), 206–211. https://doi.org/10.1038/38323.

(332) Philippsen, A.; Im, W.; Engel, A.; Schirmer, T.; Roux, B.; Müller, D. J. Imaging the Electrostatic Potential of Transmembrane Channels: Atomic Probe Microscopy of OmpF Porin. *Biophys. J.* **2002**, *82* (3), 1667–1676. https://doi.org/10.1016/S0006-3495(02)75517-3.

(333) Heinz, W. F.; Hoh, J. H. Relative Surface Charge Density Mapping with the Atomic Force Microscope. *Biophys. J.* **1999**, *76* (1 I), 528–538. https://doi.org/10.1016/S0006-3495(99)77221-8.

(334) Johnson, A. S.; Nehl, C. L.; Mason, M. G.; Hafner, J. H. Fluid Electric Force Microscopy for Charge Density Mapping in Biological Systems. *Langmuir* **2003**, *19* (24), 10007–10010. https://doi.org/10.1021/la035255f.

(335) Zhong, S.; Li, H.; Chen, X. Y.; Cao, E. H.; Jin, G.; Hu, K. S. Different Interactions between the Two Sides of Purple Membrane with Atomic Force Microscope Tip. *Langmuir* **2007**, *23* (8), 4486–4493. https://doi.org/10.1021/la0631062.

(336) Butt, H. J. Measuring Local Surface Charge Densities in Electrolyte Solutions with a Scanning Force Microscope. *Biophys. J.* **1992**, *63* (2), 578–582. https://doi.org/10.1016/S0006-3495(92)81601-6.

(337) Heymann, J. B.; Müller, D. J.; Landau, E. M.; Rosenbusch, J. P.; Pebay-Peyroula, E.; Büldt, G.; Engel, A. Charting the Surfaces of the Purple Membrane. *J. Struct. Biol.* **1999**, *128* (3), 243–249. https://doi.org/10.1006/jsbi.1999.4180.

(338) Fitter, J.; Lechner, R. E.; Dencher, N. A. Interactions of Hydration Water and Biological Membranes Studied by Neutron Scattering. *J. Phys. Chem. B* **1999**, *103*, 8036–8050.

(339) Ermolina, I.; Lewis, A.; Feldman, Y. Dielectric Properties of the BR Membrane. *J. Phys. Chem* **2003**, *107*, 14537–14544.

(340) Yokoyama, Y.; Yamada, K.; Higashi, Y.; Ozaki, S.; Wang, H.; Koito, N.; Watanabe, N.; Sonoyama, M.; Mitaku, S. Dependence of Purple Membrane Bump Curvature on PH and Ionic Strength Analyzed Using Atomic Force Microscopy Combined with Solvent Exchange. *J. Phys. Chem. B* **2014**, *118* (31), 9322–9328. https://doi.org/10.1021/jp5036234.

(341) Baumann, R. P.; Eussner, J.; Hampp, N. PH-Dependent Bending in and out of Purple Membranes Comprising BR-D85T. *Phys. Chem. Chem. Phys.* **2011**, *13* (48), 21375–21382. https://doi.org/10.1039/c1cp22098e.

(342) Baumann, R. P.; Schranz, M.; Hampp, N. Beniding of Purple Membranes in Dependence on the PH Analyzed by AFM and Single Molecule Force Spectroscopy. *Phys. Chem. Chem. Phys.* **2010**, *12* (17), 4273–4274. https://doi.org/10.1039/c004746p.

(343) Rhinow, D.; Hampp, N. Curvature of Purple Membranes Comprising Permanently Wedge-Shaped Bacteriorhodopsin Molecules Is Regulated by Lipid Content. *J. Phys. Chem. B* **2010**, *114* (1), 549–556. https://doi.org/10.1021/jp908408d.

(344) Müller, D. J.; Engel, A. The Height of Biomolecules Measured with the Atomic Force Microscope Depends on Electrostatic Interactions. *Biophys. J.* **1997**, *73* (3), 1633–1644. https://doi.org/10.1016/S0006-3495(97)78195-5.

(345) Müller, D. J.; Fotiadis, D.; Scheuring, S.; Müller, S. A.; Engel, A. Electrostatically Balanced Subnanometer Imaging of Biological Specimens by Atomic Force Microscope. *Biophys. J.* **1999**, *76* (2), 1101–1111. https://doi.org/10.1016/S0006-3495(99)77275-9.

(346) Butt, H. J.; Jaschke, M.; Ducker, W. Measuring Surface Forces in Aqueous Electrolyte Solution with the Atomic Force Microscope. *Bioelectrochemistry Bioenerg.* **1995**, *38* (1), 191–201. https://doi.org/10.1016/0302-4598(95)01800-T.

(347) Rotsch, C.; Radmacher, M. Mapping Local Electrostatic Forces with the Atomic Force Microscope. *Langmuir* **1997**, *13* (10), 2825–2832.

(348) Chiodini, S.; Ruiz-Rincón, S.; Garcia, P. D.; Martin, S.; Kettelhoit, K.; Armenia, I.; Werz, D. B.; Cea, P. Bottom Effect in Atomic Force Microscopy Nanomechanics. *Small* **2020**, *16* (35).

(349) Wei, H.; Vejerano, E. P.; Leng, W.; Huang, Q.; Willner, M. R.; Marr, L. C.; Vikesland, P. J. Aerosol Microdroplets Exhibit a Stable PH Gradient. *Proc. Natl. Acad. Sci. U.S.A.* **2018**, *115* (28), 7272–7277. https://doi.org/10.1073/pnas.1720488115.

(350) Khodagholy, D.; Doublet, T.; Quilichini, P.; Gurfinkel, M.; Leleux, P.; Ghestem, A.; Ismailova, E.; Hervé, T.; Sanaur, S.; Bernard, C.; et al. In Vivo Recordings of Brain Activity Using Organic Transistors. *Nat. Commun.* **2013**, *4*, 1575.

(351) T. Cramer, B. Chelli, M. Murgia, M. Barbalinardo, E. Bystrenova, D. M. de Leeuw, F. B. Organic Ultra-Thin Film Transistors with a Liquid Gate for Extracellular Stimulation and Recording of Electric Activity of Stem Cell-Derived Neuronal Networks. *Phys. Chem. Chem. Phys.* **2013**, *15*, 3897.

(352) S. Casalini, F. Leonardi, T. Cramer, F. B. Organic Field-Effect Transistor for Label-Free Dopamine Sensing. *Org. Electron.* **2013**, *14*, 156–163.

(353) Macchia, E.; Manoli, K.; Holzer, B.; Franco, C. Di; Ghittorelli, M.; Torricelli, F.; Alberga, D.; Mangiatordi, G. F.; Palazzo, G.; Scamarcio, G.; et al. Single-Molecule Detection with a Millimetre-Sized Transistor. *Nat. Commun.* **2018**, *9*, 3223.

(354) Picca, R. A.; Manoli, K.; Macchia, E.; Sarcina, L.; Franco, C. D. .; Cioffi, N.; Blasi, D.; Österbacka, R.; Torricelli, F.; Scamarcio, G.; et al. Ultimately Sensitive Organic Bioelectronic Transistor Sensors by Materials and Device Structure Design. *Adv.*

Funct. Mater. **2020**, *30*, 1904513.

(355) Berto, M.; Diacci, C.; D'Agata, R.; Pinti, M.; Bianchini, E.; Lauro, M. D. .; Casalini, S.; Cossarizza, A.; Berggren, M.; Simon, D.; et al. EGOFET Peptide Aptasensor for Label-Free Detection of Inflammatory Cytokines in Complex Fluids. *Adv. Biosyst.* **2018**, *2*, 1700072.

(356) Diacci, C.; Berto, M.; Lauro, M. D. .; Bianchini, E.; Pinti, M.; Simon, D. T.; Biscarini, F.; Bortolotti, C. A. Label-Free Detection of Interleukin-6 Using Electrolyte Gated Organic Field Effect Transistors. *Biointerphases* **2017**, *12* (5), 05F401.